

Development of stencil lithography for stretchable interconnects

Présentée le 21 juillet 2022

Faculté des sciences et techniques de l'ingénieur
Laboratoire de microsystemes 1
Programme doctoral en microsystemes et microélectronique

pour l'obtention du grade de Docteur ès Sciences

par

Yi-Chiang SUN

Acceptée sur proposition du jury

Prof. L. G. Villanueva Torrijo, président du jury
Prof. J. Brugger, directeur de thèse
Prof. F. Niklaus, rapporteur
Prof. B. Kim, rapporteur
Dr D. Briand, rapporteur

The greatest glory in living lies not in never falling,
but in rising every time we fall.
— Nelson Mandela

To my parents...

Acknowledgements

The PhD is a long journey with lots of up and down times. In the end, the moments I have been through in the past years all became unique experiences in my life. This journey would not have been completed without the support from people who have helped me.

First of all, I would like to express my deep gratitude to Prof. Jürgen Brugger for providing me an opportunity to work in LMIS1, for his guidance and support along with my PhD as well as the encouragement when I was lost in a mid way. I would also like to thank Dr. Giovanni Boero for the invaluable scientific advice and relevant comments. Your passion in science always drives me back to the right track.

I am also grateful to Prof. Guillermo Villanueva, Prof. Frank Niklaus, Prof. Beomjoon Kim and Dr. Danick Briand for accepting to be jury members for reviewing my thesis work. The comments you have provided greatly improve the quality of my thesis.

It is my pleasure to work in a group having a great atmosphere in the office and the lab with inspiring colleagues. I would like to thank the current members, Ana, Mohammad, Xia, André, Berke, Reza, Lorenz, Jongeon, Roberto, Nergiz, Zhiwei and Henry as well as the former members, Ya, Thomas, Jongmoon, Alessandro, Claudio, Matthieu and Samuel for making my PhD journey enjoyable with memorable work and after-work times. A special thank goes to Chris for proofreading my thesis and for the drinking and dinner times we have shared, especially when I was in tough moments during my PhD.

I would like to warmly thank all the staff members from the Center of MicroNanoTechnology (CMi) and the IPHYS cleanroom for their expertise and services. Without the great facilities you have provided and maintained day after day, I would not have been able to complete my thesis.

Throughout my PhD life, I had the pleasure to connect deeply with the Taiwanese community here in Lausanne. Without these delighting and cheering moments we had, my Swiss life would have become less enjoyable.

Last but not least, I would like to thank my family for allowing and supporting me to do whatever things I would like to do. I would also like to express my deepest gratitude to my girlfriend, Sophie Chien and her godparents in Fribourg. I would not have finished this journey without your heart-warming and endless support.

Lausanne, June 08 2022

Jack Yi-Chiang Sun

Abstract

The growing needs for human healthcare have driven the development of wearable devices for monitoring the health status of an individual. Polymers represent a promising platform for such devices due to their ability to form an intimate contact between soft organs and rigid electronic components. Stencil lithography (SL), which uses patterned membranes as a mask to locally deposit materials on substrates, provides a simple but versatile fabrication platform for realizing wearables. However, no studies have explored the deposition of materials on polymer substrates through this technique, impeding further development. Additionally, the freestanding membranes in stencils limit the geometrical design flexibility of apertures. This thesis aims to overcome such limitations, extend the use of SL for structuring stretchable liquid metal (LM) and finally demonstrate the connection of LM to silicon nanomembrane (Si NM) for stretchable Si conductors.

This thesis starts by providing a systematic study on the deposition of metals on various polymers including biocompatible and biodegradable materials using SL. The metallic patterns are successfully fabricated on the polymer substrate used by SL. The geometrical and electrical characterizations are performed and discussed.

Next, we propose a concept of introducing bridges on stencil membranes to extend the geometrical design flexibility of SL. The applied bridges stabilize the suspended membrane to enable arbitrary apertures. Continuous material traces are produced by taking advantage of the blurring effect. When the stencil is lifted to an appropriate distance above the substrate, the line-of-sight evaporation process results in the material deposition under the shadowed bridge region. The proposed bridge stencils allow the realization of spiral and meandering structures at the micrometer and sub-micrometer scales. The deposition on a variety of substrate materials reveals the versatility of the proposed bridge stencil.

We further extend the use of SL for the realization of stretchable LM electronics. A hybrid process combining SL and centrifugal force-assisted patterning of LM is presented. The selective wetting behaviour of oxide-removed eutectic gallium-indium (EGaIn) on metal patterns defined by SL enables micrometer LM patterns on elastomeric substrates. Microscale LM patterns are achieved by efficiently removing the excess material by the centrifugal forces experienced from spinning the substrate. The geometrical and electrical properties of LM patterns on stretchable substrates are characterized. Utilizing bridge stencils, EGaIn serpentine conductors and interdigitated capacitors are fabricated and characterized.

Abstract

Lastly, we translate the LM patterning technique to realize stretchable Si NM conductors using LM as interconnections. Si NM provides exceptional mechanical flexibility and electrical properties, an excellent candidate for wearable electronic applications. The use of LM significantly reduces the need for complex wiring while providing excellent stretchability. PI films are added underneath Si NMs to allow the device to sustain large mechanical deformation. The simulations detail the design strategy of the proposed device configuration. The fabrication methods, including the transfer of single-crystalline Si NMs to polymers and the integration of LM to Si NMs, are developed. The electrical characterizations under mechanical deformation are performed and the results are discussed.

Keywords: Stencil lithography, Biocompatible, Biodegradable, Stretchable conductor, Liquid metal, Si nanomembrane

Résumé

Les besoins croissants en matière de soins de santé ont conduit au développement de dispositifs portables permettant de surveiller l'état de santé d'un individu. Les polymères représentent une plateforme prometteuse pour ces dispositifs en raison de leur capacité à former un contact intime entre les organes mous et les composants électroniques rigides. La lithographie au pochoir (SL), qui utilise des membranes à motifs comme masque pour déposer localement des matériaux sur des substrats, constitue une plateforme de fabrication simple mais polyvalente pour la réalisation de dispositifs portables. Cependant, aucune étude n'a exploré le dépôt de matériaux sur des substrats polymères par cette technique, ce qui empêche tout développement ultérieur. De plus, les membranes autoportantes des pochoirs limitent la flexibilité de la conception géométrique des ouvertures. Cette thèse vise à surmonter ces limitations, à étendre l'utilisation de SL pour structurer le métal liquide étirable (LM) et enfin à démontrer la connexion de LM à la nanomembrane de silicium (Si NM) pour des conducteurs de Si étirables.

Cette thèse commence par une étude systématique du dépôt de métaux sur divers polymères, y compris des matériaux biocompatibles et biodégradables, à l'aide de SL. Les motifs métalliques sont fabriqués avec succès sur le substrat polymère utilisé par SL. Les caractérisations géométriques et électriques sont réalisées et discutées.

Ensuite, nous proposons un concept d'introduction de ponts sur les membranes de pochoir pour étendre la flexibilité de conception géométrique de SL. Les ponts appliqués stabilisent la membrane suspendue pour permettre des ouvertures arbitraires. Des traces matérielles continues sont produites en profitant de l'effet de flou. Lorsque le pochoir est soulevé à une distance appropriée au-dessus du substrat, le processus d'évaporation en visibilité directe entraîne le dépôt de matériau sous la région ombragée du pont. Les pochoirs à pont proposés permettent de réaliser des structures en spirale et en méandres à l'échelle du micromètre et du sous-micromètre. Le dépôt sur une variété de matériaux de substrat révèle la versatilité du pochoir de pont proposé.

Nous étendons encore l'utilisation de SL pour la réalisation de l'électronique LM étirable. Nous présentons un procédé hybride combinant le SL et le modelage de LM assisté par la force centrifuge. Le comportement de mouillage sélectif du gallium-indium eutectique sans oxyde (EGaIn) sur les motifs métalliques définis par SL permet de réaliser des motifs LM micrométriques sur des substrats élastomères. Les motifs LM à l'échelle microscopique sont obtenus en éliminant efficacement l'excès de matériau grâce aux forces centrifuges exercées

Abstract

par la rotation du substrat. Les propriétés géométriques et électriques des motifs LM sur les substrats étirables sont caractérisées. En utilisant des pochoirs de pont, des conducteurs serpents en EGaIn et des condensateurs interdigités sont fabriqués et caractérisés.

Enfin, nous appliquons la technique de modelage LM pour réaliser des conducteurs Si NM étirables en utilisant LM comme interconnexions. Le Si NM offre une flexibilité mécanique et des propriétés électriques exceptionnelles, ce qui en fait un excellent candidat pour les applications électroniques portables. L'utilisation de LM réduit considérablement la nécessité d'un câblage complexe tout en offrant une excellente extensibilité. Des films PI sont ajoutés sous les Si NMs pour permettre au dispositif de supporter une grande déformation mécanique. Les simulations détaillent la stratégie de conception de la configuration du dispositif proposé. Les méthodes de fabrication, y compris le transfert de Si NMs monocristallins aux polymères et l'intégration de LM aux Si NMs, sont développées. Les caractérisations électriques sous déformation mécanique sont effectuées et les résultats sont discutés.

Mots-clés : Lithographie au pochoir, biocompatible, biodégradable, conducteur extensible, métal liquide, nanomembrane de Si

Contents

Acknowledgements	v
Abstract (English/Français)	vii
List of figures	xiii
List of tables	xvii
List of abbreviations	xix
1 Introduction	1
1.1 Background and motivation	2
1.2 State-of-the-art	6
1.2.1 Wearable and implantable devices	6
1.2.2 Stretchable conductors	10
1.2.3 Non-conventional fabrication process on polymers	15
1.3 Thesis outline	22
2 Stencil lithography on polymer substrate materials	25
2.1 Introduction	26
2.2 Results and discussions	26
2.2.1 Stencil fabrication method and results	26
2.2.2 Stencil lithography on polymer substrates	29
2.3 Conclusion	37
3 Bridge stencil enabling high resolution arbitrarily shaped metallic thin films on polymer substrates	39
3.1 Introduction	40
3.2 Results and discussions	42
3.2.1 Microbridge stencil	42
3.2.2 Nanobridge stencil	53
3.3 Conclusion	66
	xi

Contents

4 Stretchable conductors fabricated by SL and centrifugal force-assisted patterning of LM	67
4.1 Introduction	68
4.2 Results and discussions	70
4.2.1 Microfabrication based on a hybrid process	70
4.2.2 Electrical characterization of the patterned EGaIn	78
4.2.3 Microbridge stencil for more complex patterns	85
4.3 Conclusion	89
5 Stretchable silicon nanomembrane conductors enabled by liquid metal interconnections	91
5.1 Introduction	92
5.2 Results and discussion	96
5.2.1 Simulation of the mechanical responses of stretchable Si NM conductors	96
5.2.2 Transfer printing of Si NMs to polymer substrates	101
5.2.3 Microfabrication of silicon NM conductors with LM interconnections . .	105
5.2.4 Electrical characterization	111
5.3 Conclusion	116
6 Conclusion and perspectives	117
6.1 Conclusion	117
6.2 Perspectives	119
Bibliography	123
Curriculum Vitae	147

List of Figures

1.1	Elastic moduli of human organs and common materials.	3
1.2	Skin serves as an excellent interface for accessing biological signals.	4
1.3	Schematic drawings showing the principle of digital printing methods, transfer printing technique and stencil lithography.	6
1.4	Wearable systems for human healthcare.	9
1.5	Stretchable conductors realized by structuring rigid metal films and using nano-materials.	12
1.6	Stretchable conductors using intrinsically stretchable materials.	14
1.7	The use of polymer stencils for structuring various materials on different substrates.	17
1.8	The application of rigid film stencils.	19
1.9	The blurring and the clogging effect in SL.	20
2.1	Fabrication flow of stencils.	28
2.2	Stencil fabrication results with square aperture openings.	28
2.3	Stencil fabrication results with 4-point probe apertures.	29
2.4	Geometrical characterization of square arrays evaporation deposited on different substrate materials.	32
2.5	Surface roughness of parylene C films deposited on Si substrates.	33
2.6	Comparison between the evaporation and the sputter deposition results on PLGA substrates.	34
2.7	Resistivity characterization of Au films deposited on different polymer substrates.	35
3.1	The concept of bridge stencils and the blurring effect.	41
3.2	Detailed microbridge study with cantilever stencils.	43
3.3	Calculated and measured cantilever bending.	44
3.4	Microbridge study with cantilever stencils having a width of 15 μm with bridges.	44
3.5	Microbridge study with cantilever stencils having a width of 50 μm with bridges.	46
3.6	Summary of bending induced deposition length α with cantilever stencils.	46
3.7	SEM images of the fabricated bridges on stencils.	47
3.8	Bridge stencil applied to the fabrication of spiral structures.	47
3.9	Optical and confocal images of the released SiN stencils.	49
3.10	Schematic drawing showing stencil lithography and the parameters.	49

List of Figures

3.11	The fabricated spiral structures on a Si substrate by using a microbridge stencil.	50
3.12	Fabrication results on a biodegradable PLGA substrate.	52
3.13	Nanobridge stencil with meandering pattern.	54
3.14	Fabrication results on a Si substrate with different gap distances.	55
3.15	AFM characterizations of the metal structures deposited through nanoapertures.	56
3.16	AFM characterizations of the metal structures deposited through large apertures.	57
3.17	Schematic drawing showing the varying effective evaporation source size. . . .	57
3.18	Measured electrical resistance of the meandering metal patterns deposited by placing stencils at different gap distances.	58
3.19	SEM images of the fabricated meandering patterns on parylene and PLGA substrates.	59
3.20	SEM images of the fabricated meandering patterns on PI and PPA substrates. .	60
3.21	AFM images and electrical characterization results of the fabricated nanostructures on various polymer substrates.	60
3.22	Meandering patterns deposited on PLGA substrates under different evaporation deposition parameters.	62
3.23	Demonstration of the use of nanoscale meandering patterns as heaters.	63
3.24	Demonstration of the use of nanobridge stencil on a stretchable substrate with stiffness gradients.	65
4.1	Hybrid process for the fabrication of EGaIn stretchable conductors.	71
4.2	Images showing the detailed procedure during the removal of EGaIn.	72
4.3	Re-collection of the removed excess EGaIn after spinning.	72
4.4	Various EGaIn patterns obtained by the proposed process.	74
4.5	The irregular EGaIn patterns due to the corrosion of Au by EGaIn.	74
4.6	High resolution EGaIn patterns fabricated by the presented method.	75
4.7	Patterned EGaIn on POMaC, a flexible and biodegradable substrate	75
4.8	Geometrical analysis of the patterned EGaIn on a PDMS substrate.	77
4.9	Measured heights of the EGaIn square patterns fabricated with different spinning speed.	77
4.10	Electrical characterization of the sputter deposited Au structures on a PDMS substrate.	79
4.11	Optical image of the sputtered Au surface on a PDMS substrate.	79
4.12	Electrical characterization of the patterned EGaIn on a PDMS substrate.	80
4.13	Resistance versus applied currents.	81
4.14	Simulation of the Joule heating effect.	81
4.15	Electrical characterization of the patterned EGaIn on a PDMS substrate under strain.	83
4.16	A LED chip connected with EGaIn/Au stretchable conductors.	84
4.17	The use of a microbridge stencil for patterning EGaIn.	85
4.18	Optical and confocal images of stencils with and without microbridges.	86
4.19	Schematic drawings showing the blurring effect.	86

4.20	The fabrication results by the use of a microbridge stencil for patterning EGaIn.	88
4.21	The use of a microbridge stencil with interdigitated apertures for an interdigitated EGaIn capacitor.	88
5.1	Properties of Si nanomembranes (NMs).	93
5.2	Schematic drawings of the proposed stretchable Si NM conductors.	95
5.3	FEA of the local mechanics of Si NM conductors with varying PI thickness. . . .	97
5.4	FEA of the local mechanics of Si NM conductors with varying Si NM thickness. .	99
5.5	FEA of the mechanical responses of Si NM conductors under the applied strain. .	100
5.6	Transfer printing of Si NMs to a PI substrate.	101
5.7	Optical images showing the process of transferring Si NMs to a PI substrate. . .	102
5.8	Transfer printing of Si NMs to a PI substrate with PR-surrounded anchors. . . .	103
5.9	Optical images showing the process of transferring Si NMs to a PI substrate with PR-surrounded anchors.	103
5.10	Transfer printing of Si NMs to a PI substrate with strip-shaped PR anchors. . . .	104
5.11	Optical images showing the process of transferring Si NMs to a PI substrate with strip-shaped PR anchors.	104
5.12	Fabrication process of stretchable Si NM conductors with LM interconnections. .	107
5.13	Optical images showing the failures during the patterning of EGaIn.	108
5.14	Schematic drawings and the corresponding optical images showing the detailed process steps.	110
5.15	Profile of Si NM/PI islands.	110
5.16	Resistance measurements of Si NM ribbons with LM interconnections.	112
5.17	Measurement setup for electromechanical characterization of stretchable Si NM conductors.	113
5.18	Electromechanical characterization of the fabricated Si NM conductors.	115
6.1	Schematic drawing showing a customized tool for transfer printing.	120



List of Tables

2.1	Material properties of polymer thin films.	31
4.1	Comparison of the reported selective wetting process	89

List of abbreviations

- AFM: atomic force microscope
- CNT: carbon nanotube
- CTE: thermal expansion coefficient
- CVD: chemical vapor deposition
- DEP: dielectrophoresis
- DUV: deep ultraviolet
- EBL: electron beam lithography
- ECG: electrocardiogram
- EEG: electroencephalogram
- EGaIn: eutectic gallium-indium
- EMG: electromyography
- FEA: finite element analysis
- IPA: isopropyl alcohol
- LM: liquid metal
- LS-SiN: low stress silicon nitride
- LPCVD: low pressure chemical vapor deposition
- NFC: near-field communication
- NM: nanomembrane
- NW: nanowire
- Pa: pascals

List of Tables

- PCB: printed circuit board
- PDMS: polydimethylsiloxane
- PEN: polyethylenaphthalat
- PET: polyethylenterephthalat
- PI: polyimide
- PLGA: poly(lactic-co-glycolic acid)
- PMMA: poly(methyl methacrylate)
- POMaC: poly(octamethylene maleate (anhydride) citrate)
- PPA: poly(phthalaldehyde)
- PR: photoresist
- PSG: phosphosilicate glass
- PUA: polyurethaneacrylate
- PVA: polyvinyl alcohol
- PVD: physical vapor deposition
- PVDF: polyvinylidene fluoride
- RIE: reactive ion etching
- SEM: scanning electron microscope
- SOI: silicon-on-insulator
- SL: stencil lithography
- TENG: triboelectric nanogenerator
- TMCS: trimethylsilyl chloride silane

1 Introduction

Disclaimer: This chapter (1) is adapted from the following articles with permissions of all co-authors and journal:

Y.-C. Sun, G. Boero and J. Brugger, "Stretchable Conductors Fabricated by Stencil Lithography and Centrifugal Force-Assisted Patterning of Liquid Metal", *ACS Applied Electronic Materials*, 2021, 3, 5423-5432.

Y.-C. Sun, G. Boero and J. Brugger, "High resolution meandering metal patterns enabled by nano-bridge stencil ", *47th international Conference on Micro and Nano Engineering (MNE2021)*, Turin, Italy, September 20-23, 2021.

Y.-C. Sun, G. Boero and J. Brugger, "Nanobridge stencil enabling high resolution arbitrarily shaped metallic thin films on polymer substrates", *In preparation*

My contribution: conceptualization, design, fabrication, experiments, figures and writing.

This chapter aims to define the problems to be addressed and the challenges behind the aims of this thesis. First, an overview of wearable and stretchable systems is introduced, followed by presenting the recent progress of stretchable conductors, an enabling step for such systems. Last, fabrication strategies for producing wearable and stretchable sensors using non-conventional fabrication processes are described.

1.1 Background and motivation

In recent years, increased demand in human healthcare has driven the development of a system enabling real-time monitoring of user's biosignals. Monitoring physiological biosignals in the human body can enable earlier detection and treatment of cardiovascular diseases, manage the activities of professional athletes and improve public health. Modern wearable sensors have been commercialized in the forms of watches [1], wristbands [2] and tiny stickers [3] to monitor blood oxygen level, heart rate, body temperature or biomarkers in sweat. These systems provide robust and reliable measurements of biosignals and allow transmitting data to their mobile devices for an immediate response to health status. However, cumbersome electronic components and rigid circuit boards limit long-term, comfortable and continuous monitoring. In particular, the mismatch in the mechanical properties at the sensor/organ interface prevents intimate contact for such systems for better biosignal detection. The elastic moduli of natural soft tissues and organs ranges from a few Pascals (Pa) (e.g., neural) to few tens of kPa (e.g., cartilage) (Figure 1.1a) [4]. Therefore, the selection of substrate materials whose elastic modulus matches the organs' is of great importance. Polymers represent a promising platform for soft and stretchable technologies due to their lower mechanical stiffness comparing to other materials such as Silicon (Si) and their biocompatibility (Figure 1.1b) [5].

Significant progress in the development of soft, flexible and stretchable devices combining different polymer substrates and conductors has been achieved. These soft devices allow the formation of an intimate interface between functional electronic devices (e.g., sensor, memory, communication components, etc.) and soft organs (e.g., skin, heart, etc.). The configuration eliminates signal artifacts associated with relative movements, thereby providing a precise measurement of biosignals for a long period of time. Skin is the largest organ in the human body and an ideal interface for accessing vital biological signals from muscles, blood vessels and epidermis (Figure 1.2) [6]. In the muscle layer, a muscle is interwoven by branches of nerve cells, which trigger the muscle to stimulate physical contraction [6]. It produces electrical signals that can be recorded by electrodes placed close to the target muscles. For instance, electrocardiogram (ECG) determines heart activity by measuring electrical signals from the electrodes placed on the chest. Electroencephalogram (EEG) captures brain activity from the electrodes attached to the forehead. Electromyography (EMG) records muscle activity by placing the electrodes on specific muscle regions [7]. Analyzing the condition of blood vessels provides information including blood pressure, oxygen level and heart rate, etc. The results can be used to prevent vascular diseases such as hypertension and stroke, etc. Sweat is also a great source of information, rich in biomarkers such as PH, lactate and glucose, etc, which are essential for the early detection of diseases. For instance, lactate can be detected for preventing ischaemia [8] and glucose level can be measured for continuous monitoring of diabetes [9]. Each of the biosignals mentioned above represents a driving force for the development of application-specific wearable sensors utilizing soft materials as supporting platforms.

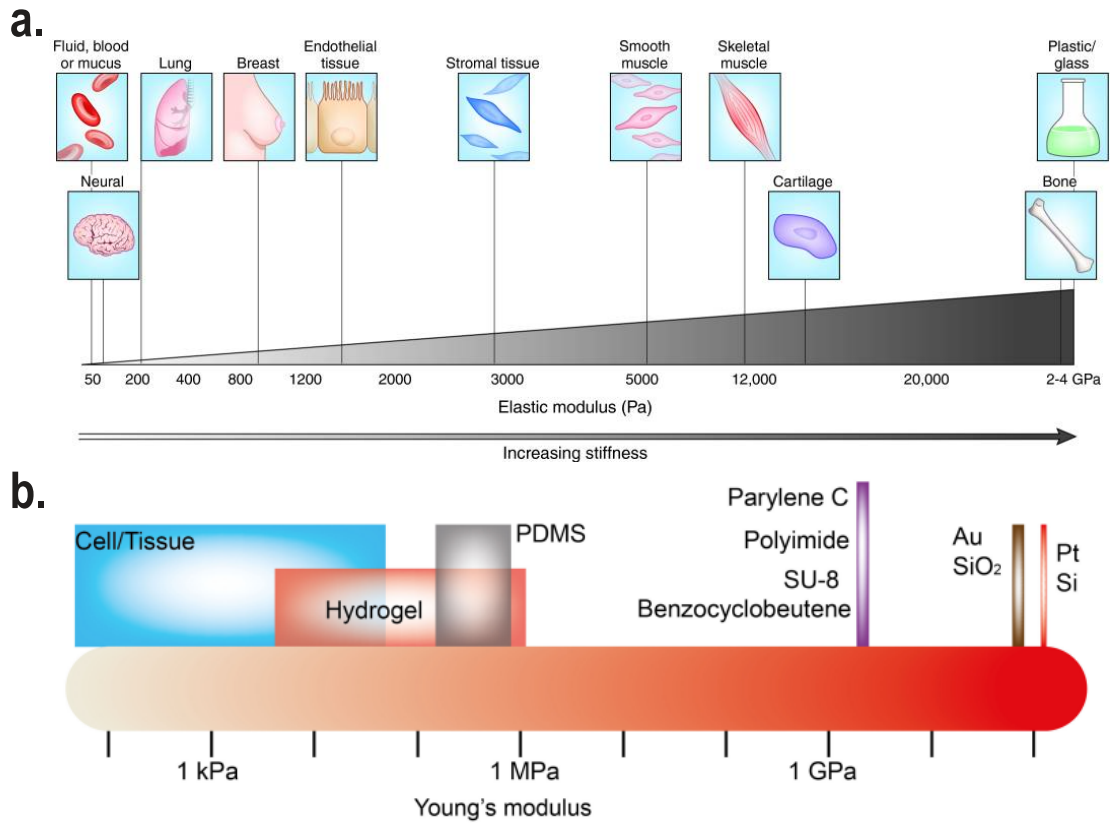


Figure 1.1: **Elastic moduli of human organs and common materials.** **a.** Elastic moduli of human tissues and organs ranging from 50 Pa (e.g., neural) to few tens of KPa (e.g., cartilage). Reprinted with permission from [4]. **b.** Elastic moduli among various polymer materials. A lower Young's modulus of polymers comparing to rigid materials such as Si demonstrates a better mechanical compatibility with human tissues and organs. Reprinted with permission from [5].

Thanks to the advances in material science, a diverse array of polymer materials have been developed to enable systems that can be intimately attached to soft human organs. With respect to compatible materials, few polymers having elastic moduli around a few GPa (e.g., polyimide (PI), parylene, polyethylenephthalat (PEN), etc.) have been widely used as substrate materials for flexible electronics [10–13]. These materials possess ultraflexibility that allows intimate contact with soft organs having different shapes. For example, applying water-dissolvable silk as an intermediate layer, thin PI films were implemented as supporting substrates for flexible electronics to monitor brain activity [10]. Quantum dot displays were realized on ultrathin parylene substrates for real-time visualization of measured biosignals [12]. Ultrathin PEN substrates enabled light-weight flexible electronics that can be attached to arbitrary objects [13]. In addition to polymers that provide ultraflexibility for intimate contact with arbitrary shapes for sensing, there are specific applications (e.g., prosthetic skin or detecting motions on a human body) requiring polymers to be elastically stretched while maintaining their elastic properties. Among all the stretchable polymers, polydimethylsiloxane (PDMS)

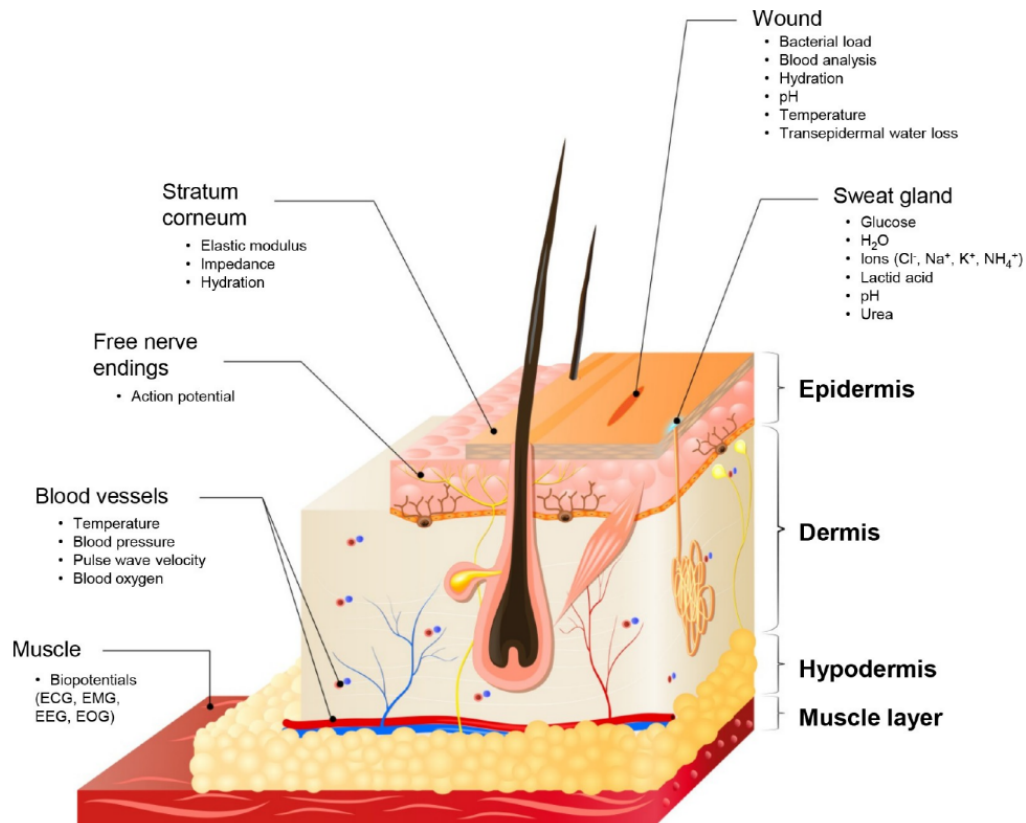


Figure 1.2: **Skin serves as an excellent interface for accessing biological signals.** Schematic drawing showing the access to various biological signals through skin. Reprinted with permission from [6].

(Sylgard 184, Dow, Inc.) and Ecoflex (Smooth-On, Inc.) are the most common candidates for stretchable electronics due to their low elastic moduli. They are crosslinked elastomers and the crosslinking process is assisted by crosslinking agents (i.e., curing agents). Polymer chains are joined together by covalent bonds and thus, the physical properties of the polymers can be adjusted. Their mechanical properties can be tailored by modulating the ratios between the base polymer and the curing agent as well as the curing temperature [14, 15]. For commonly used PDMS with a mixing ratio of 10:1 (base polymer: curing agent), it has a Young's modulus of 0.5-3 MPa and an elastic limit of $\approx 200\%$ [16]. In comparison, Ecoflex possesses the lower Young's modulus of 50-100 kPa and the larger elastic limit of $\approx 1000\%$ [16]. Additionally, another type of polymers that degrades via the reaction of water (i.e., hydrolysis) has received enormous attention for implantable or biodegradable electronics. These polymers, such as silk, polyvinyl alcohol (PVA) and poly(lactic-co-glycolic acid) (PLGA), undergo chemical degradation via hydrolysable covalent bonds with the presence of water [17, 18].

Conventional microfabrication processes commonly used in producing integrated circuits on rigid substrates (e.g., Si or glass) employ high temperature baking and harsh chemicals to define patterns on photo-sensitive resists. The patterns are then transferred to conducting

or semiconducting materials using high power plasma or chemicals. These processes have been utilized in producing functional devices on certain polymers such as PI, PEN, etc [13, 19]. However, due to the different mechanical and chemical properties of a wide range of polymers, for some polymer substrate materials, these processes deteriorate the supporting polymer substrates and the patterned materials. To elaborate, a huge difference in the thermal expansion coefficient (CTE) between stretchable polymers and metal conductors (e.g., CTE of PDMS and Au are 310 ppm/°C [20] and 14 ppm/°C [21], respectively) results in wrinkles or cracks in the metal film during the metal deposition process or after high temperature treatment, which deteriorate the electrical conductivity of the fabricated conductors [22]. The conductors having a low electrical conductance would lead to unwanted heating of the device. For some polymers, such as biodegradable polymers that are degraded in aqueous solution, conventional resist-based processes are not suitable due to the use of aqueous solution in defining photo-sensitive resists and transferring patterns to the functional metal films.

To overcome the aforementioned limitations, the employed fabrication process needs to avoid harsh chemicals, aqueous solution and high temperature treatment. Three main streams of the fabrication process are developed to fulfill the requirements: digital printing methods, transfer printing technique and stencil lithography (SL). Digital printing methods such as inkjet printing and 3D printing are working with the principle of direct printing of functional inks to substrates through a dispensing nozzle (Figure 1.3a) [23]. The transfer printing technique is based on the principle of transferring the devices prefabricated on a rigid substrate to another substrate using a viscoelastic stamp (Figure 1.3b) [24]. The other strategy involves the development of resistless processes such as SL, which uses a freestanding membrane with opening apertures to locally deposit or etch materials on substrates (Figure 1.3c). In contrast to digital printing methods and the transfer printing technique, SL provides a clean and cost-efficient way to directly fabricate devices on substrates while maintaining excellent electrical performance and high feature resolution down to the nanometer scale. However, no systematic studies have explored the deposition of metals on various polymer substrates using SL, impeding further development. Additionally, the freestanding membranes in stencils limit the geometrical design flexibility of apertures.

The motivation of this work is to address the aforementioned challenges and further extend the use of SL for stretchable interconnects. We aim to explore the capability of applying SL to a wide range of substrate materials, especially soft polymer materials and improve the use of SL by addressing the limitations in stencil designs. In addition, we target to extend the use of SL for structuring intrinsically stretchable conductors (e.g., liquid metals, LMs) to realize stretchable liquid electronics and demonstrate the connection of LMs to Si nanomembranes (NMs) for the prospective applications in stretchable Si conductors.

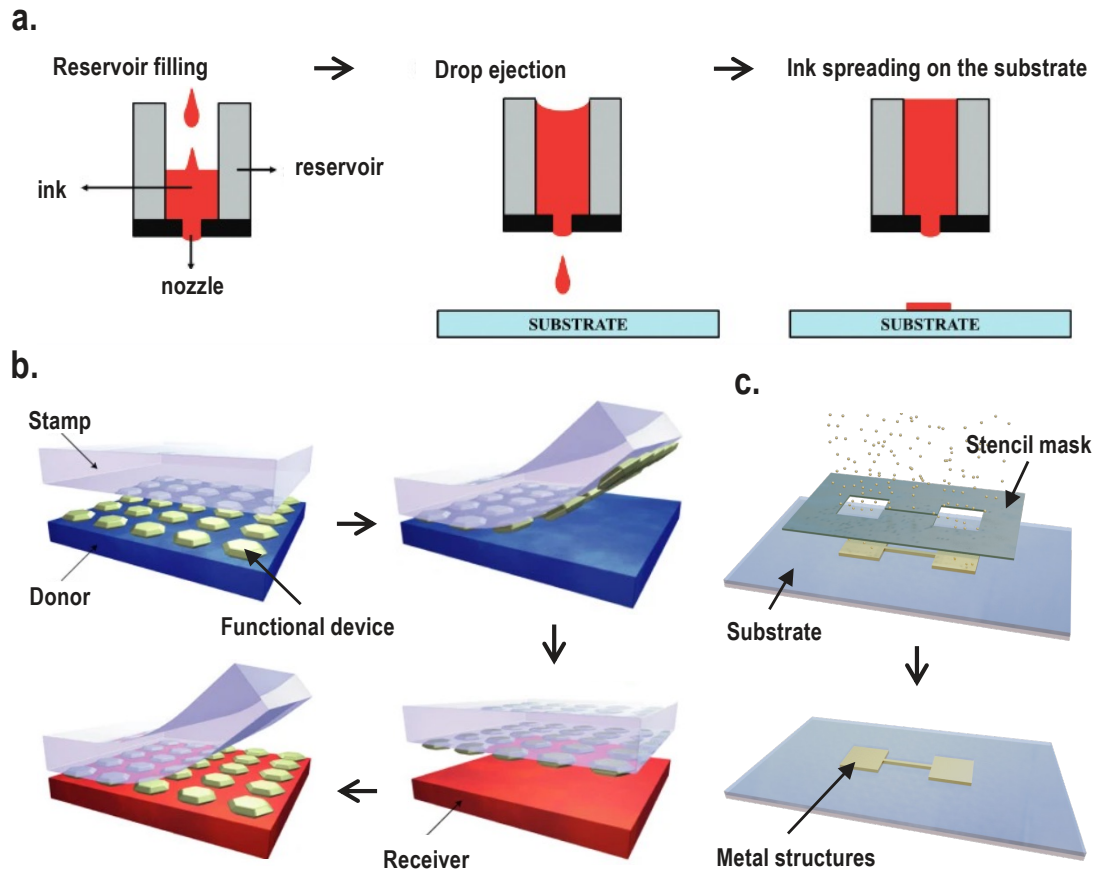


Figure 1.3: **Schematic drawings showing the principle of digital printing methods, transfer printing technique and stencil lithography.** **a.** Digital printing methods utilize a dispensing nozzle to directly print functional inks to the substrates. Reprinted with permission from [23]. **b.** The transfer printing technique employs a viscoelastic stamp to transfer the prefabricated functional devices to the substrates. Reprinted with permission from [24]. **c.** Stencil lithography adapts a patterned thin membrane as a hard mask to locally deposit or etch materials on the target substrates.

1.2 State-of-the-art

In this chapter, a brief overview of the state-of-the-art of wearables for human healthcare is firstly introduced. Next, stretchable conductors, which are essential enabling steps towards wearables, are discussed. Lastly, research interests in non-conventional processes to realize stretchable conductors are presented.

1.2.1 Wearable and implantable devices

Wearable devices interfacing with epidermis Enormous wearable systems have been realized to monitor biophysical, biochemical and environmental signals for human healthcare.

One of the important requirement for wearable sensors is clean signal detection through intimate contact between sensors and epidermis, eliminating motion and environment artifacts and providing a precise and comfortable monitoring environment. Such requirement piques interest for the development of ultrathin sensors. Taking advantage of the semiconducting properties of Si nanomembranes (NMs), the fabricated ultrathin Si NM temperature sensors allowed precise and continuous monitoring of human skin temperature (Figure 1.4a) [19]. By depositing thin Au on electrospun PVA fibers, the resulting Au nanomesh enabled ultrathin capacitive pressure sensors for monitoring finger manipulation without detectable effects on human sensation [25]. The same method was developed as ultrathin electrodes for monitoring the skin resistance without inhibiting water evaporation, such as sweating for a long period of time [26].

The integration of multifunctional sensors with wireless transmission modules for real-time sensing applications to avoid the need for complex wiring has also received great attention for wearable sensors. The collected data can be immediately transmitted to mobile phones to take prompt action. Combining with an intrinsically stretchable LM (e.g., GaInSn) for strain sensing and near-field-communication (NFC) chips for wireless power and data transfer, wireless stretchable sensors were developed for monitoring various human motions [27]. Integrating commercial wireless communication chips, motion sensors (e.g., accelerometer and gyroscope) and metal electrodes on a breathable elastomer, the integrated wearable patches were capable of continuously measuring ECG, heart rate and human activities [28]. Incorporating commercial chips and sensors such as NFC chips, temperature sensors and self-made pressure sensors on a flexible printed circuit board (PCB), the assembled systems provided capabilities for continuous measurements of pressure and temperature from patients having a high risk of pressure injuries (Figure 1.4b) [29]. Following the similar approach, integrated wearable sensors comprising mesh-patterned Au and electronic components were demonstrated for wirelessly measuring the variation in skin conductance (i.e., galvanic skin response) for daily stress monitoring [30].

In order to obtain a comprehensive assessment of the health status of an individual, collecting and analysing biochemical signals are another crucial aspect. Sweat represents a promising non-invasive platform for obtaining a wealth of biochemical targets that can be employed for monitoring human health. More information about sweat composition and the corresponding applications for disease diagnosis can be found in review papers [31, 32]. Recently, multiple chemical sensors coupled with electronic circuits for signal processing and wireless transmission were realized on a flexible PCB for selectively and concurrently measuring the concentrations of sweat metabolites (e.g., glucose and lactate) and electrolytes (e.g., Na and K ions) (Figure 1.4c) [33]. In one example, sensors were configured as a headband and were demonstrated for real-time monitoring of the health status during running [33]. Incorporating with thermoresponsive polymer microneedles, the produced chemical sweat sensors were capable of not only monitoring the concentrations of biomarkers but also releasing drugs by thermal-activation [34]. Monitoring sweat rate, a crucial indicator that provides information about hydration state, stress and other body characteristics, however, remains challenging

due to low secretion rates and the evaporation of sweat. One promising approach exploited microfluidic channels to overcome the challenges and further enabled collecting and analyzing sweat rates under different activities [35,36]. With a transdermal patch, the wearable devices allowed not only measuring nutrients in sweat but also supplying vitamins through thermal-activation [37].

Wearable devices interfacing with eyes In addition to the human epidermis, the development of wearables interfacing with human eyes has also attracted great attention. The main focus is on the integration of sensors on contact lenses for detecting intraocular pressure and the concentrations of glucose. The use of contact lenses provides a non-invasive platform for long-term and continuous measurements of biosignals for the diagnosis of eye diseases [38]. In contact lenses, the used materials require not only to be mechanically flexible for wearing comfort and permeable to oxygen but also to be transparent. To fulfill these criteria, nanomaterials such as 2D materials and nanowires (NWs) are often used. A hybrid structure composed of graphene and AgNWs was developed and implemented as electrodes to realize field-effect transistors using graphene as the channel material. The electronic components were integrated into soft contact lenses for wireless ocular diagnostic applications [39]. Adapting MoS₂ as a semiconducting channel material, thin-film transistors were fabricated on contact lenses for the detection of light and concentrations of glucose [40]. Combining with conducting (e.g., Ag nanofibers) and semiconducting (e.g., Si NM) materials, the smart contact lenses comprised of wireless displays, rectifier circuits and glucose sensors were demonstrated (Figure 1.4d) [41]. Apart from the intraocular pressure and glucose sensing, a graphene microelectrode array was fabricated on transparent substrates for recording a full-cornea electroretinography [42].

Implantable devices Realizing functional devices on biodegradable substrate materials for biomedical implants has opened a new field for human healthcare. Such devices can be naturally dissolved in biofluids, avoiding not only the need for additional surgery to remove the device but also physiologically harmful by-products in body environments. Utilizing biodegradable electronic materials such as Si, Tungsten and SiO₂, fully biodegradable complementary metal-oxide-semiconductor (CMOS) devices and circuits were demonstrated on biodegradable PLGA substrates [43]. A soft, biodegradable and battery-less device that can wrap around an artery was realized for the wireless monitoring of blood flow [44]. Functionalizing doped Si NMs with 3-aminopropyltriethoxysilane (APTES), the fabricated biodegradable sensor was able to detect pH for biomedical applications [45]. A biodegradable spectrometer made of a biodegradable photodetector on a biodegradable fibre optic probe was realized to spectroscopically characterize biological tissues. The devices were demonstrated to be capable of continuous characterization of biological tissues in freely moving mice [46]. To interface with the brain, a biodegradable sensor platform comprising pressure and strain sensors, a temperature sensor, a flow rate sensor and a pH sensor was produced on a biodegradable PLGA substrate for continuous monitoring of biosignals within the brain (Figure 1.4e) [47].

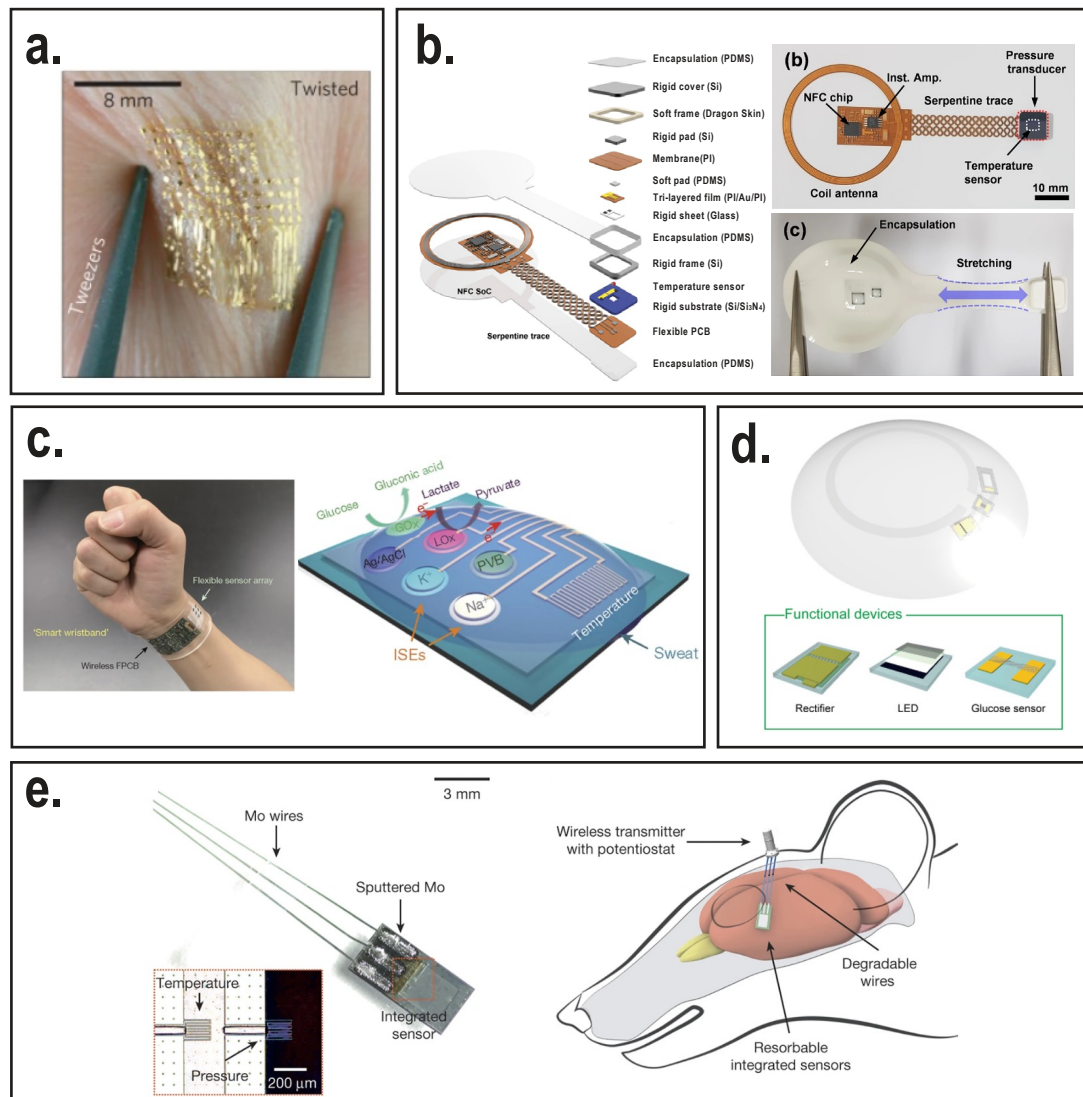


Figure 1.4: Wearable systems for human healthcare. **a.** Temperature sensor array made from Si NMs on an ultrathin PI substrate enabling precise measurements of human skin temperature. Reprinted with permission from [19]. **b.** Integrated system comprising commercial NFC chips, temperature sensors and self-made pressure sensors on a flexible printed circuit board (PCB) for continuous monitoring of pressure and temperature from patients having a high risk of pressure injuries. Reprinted with permission from [29]. **c.** Smart wristband consists of electronic circuits, chemical analytes and wireless modules on a flexible PCB for analysing biomarkers from human sweat. Reprinted with permission from [33]. **d.** Smart contact lens composed of Si NM electronic devices, wireless displays and glucose sensors. Reprinted with permission from [41]. **e.** A biodegradable sensor platform for continuous monitoring of biosignals within the brain. Reprinted with permission from [47].

1.2.2 Stretchable conductors

Among all the essential elements for wearable devices, stretchable conductors that remain mechanically intact and electrically functional under mechanical deformation are particularly important. In this section, the state-of-the-art of strategies for realizing stretchable conductors is introduced.

Structuring rigid metal films The engineering of thin metal films has been intensively studied to enable stretchable conductors. Structuring rigid metal films into deterministic fractal motifs in 2D [48, 49] or 3D forms [50, 51] has increased the strain limit of rigid metal films (Figure 1.5a). For example, a stretchability of 800% was demonstrated by shaping thin Ag films into meanders (Figure 1.5b) [49]. A self-similar serpentine structure was shown to have over 200% stretchability with a smaller form factor [52]. Thin Au films were capable of enduring over 100% strain with 3D helical structures produced by printing patterned flat metal films to a prestrained polymer substrate with designed bonding sites [51]. The compressive forces induced during the release of the polymer resulted in buckled 3D metal patterns. Mesh structures having apertures of various shapes offer superior stretchability over non-patterned rigid metal films. The high stretchability of up to ~500% was reported by using a Kirigami structure where several line cuts were introduced [53]. Kirigami is originally the Japanese art of paper cutting. It is now generally referred to as a structure created by introducing several cuts in a film. The limit of elastic deformation in Kirigami structures relies strongly on the geometrical design of cuts. Therefore, optimizing the cut geometries allows the conductors to remain functional over a wide range of mechanical deformation [54]. Incorporating hierarchical Kirigami designs, 2D deformed and 3D buckled Kirigami patterns were triggered, allowing the produced structures to endure mechanical deformation in different directions [55]. Kirigami structures having cuts with different shapes have also been explored to advance their mechanical performance. For instance, adapting Y-shaped motifs and engineering the opening tip profiles probed the stress concentration issue and further improved the mechanical robustness [56].

Instead of structuring metal films into serpentine or mesh patterns, forming microcracks in metal films is also capable of extending their stretchability. Microcracks are usually produced by metal films (e.g., Au) deposited in a vacuum environment on a polymer substrate with high CTE (e.g., PDMS). The CTE mismatch between metals and polymers leads to micrometer cracks [57, 58]. The presence of microcracks forms a Kirigami-like structure and enables a certain degree of stretchability [59, 60]. The initial crack formation could be controlled by modulating the metal deposition parameters to enlarge the stretchability and to enable a stable electrical output under large strain (Figure 1.5c) [61]. Another strategy to turn rigid metal films into a stretchable form is to create a wavy structure on the films. A common approach is to deposit or laminate flat metal films on a prestrained elastomer substrate. The wavy patterns are determined by the applied strain, mechanical properties of polymers, film thickness and adhesion strength between polymers and metals [62, 63]. This method allowed

metal films to be stretched reversibly with strains of up to 275% [64]. Depositing metal films on a silk protein substrate, of which the mechanical properties could be tailored by adding different amounts of Ca^{2+} ions, to form wrinkle patterns was demonstrated as stretchable electrodes [65]. Utilizing elastomer as a dielectric layer, stretchable capacitive strain sensors with high sensitivity were realized via wrinkled metal films, capable of sustaining strain up to 100% (Figure 1.5d) [66].

Even though engineering metal films into stretchable forms has enabled surpassing the stretching limit of metals, the usable density of electronic components is limited. In this type of stretchable conductor, the stretchability is dominated by meandering, helical wiring routing or wrinkles, which consume a large portion of space in the system. In addition, the required sophisticated patterns increase the process complexity and the electrical resistance of wires.

Nanomaterial-polymer composites Embedding non-stretchable conductive nanomaterials into stretchable insulating polymer matrix provides another design strategy to overcome the limitations in structured metal films. It is working with the principle of percolation of the conductive nanomaterials. The solid-state material is not stretched but displaced so it provides good stretchability and an acceptable electrical resistivity [67, 68]. Stretchable conductors produced by spray-coating carbon nanotubes (CNTs) on PDMS surfaces via a shadow mask enabled the realization of stretchable transistors that can sustain strain up to 100% for at least 1000 stretching cycles [68]. Embedding CNTs in PDMS elastomer with a specific orientation, the formed conductive composite behaved with enhanced sensitivity for directional strain sensing [69]. CNT-PDMS composites prepared by printing CNT inks on PDMS surfaces enabled stretchable strain sensors with adjustable sensitivity. The gauge factors were modulated by the numbers of CNT printing cycles for various applications [70]. CNT is also an excellent candidate for high performance supercapacitors due to its high charge transport capability and chemical stability. CNT-PDMS structures were demonstrated as stretchable supercapacitors for wearable energy storage devices [71]. In addition to CNTs, AgNW is another excellent candidate for stretchable conductors due to its high electrical conductivity, high optical transparency and mechanical flexibility. Drop-casting AgNWs on a PDMS substrate having surface energy contrasts allowed structuring Ag NWs on the surface for the realization of stretchable and transparent electrodes for electroluminescent devices (Figure 1.5e) [72]. Patterning AgNWs via laser ablation enabled capacitive sensor arrays for touch sensing [73]. Biaxially stretchable strain-insensitive heaters based on AgNWs were achieved by laser cutting AgNW-PI composites into Kirigami patterns and subsequently bonding the composites to a stretchable textile [74]. Combining with CNTs, AgNW/CNT hybrid electrodes showed enhanced electrical conductivity and the ability to sustain strain up to 490% [75].

Nevertheless, the most commonly used manufacturing method for this type of conductor is spray-coating, which results in a relatively low resolution in the order of tens of micrometers

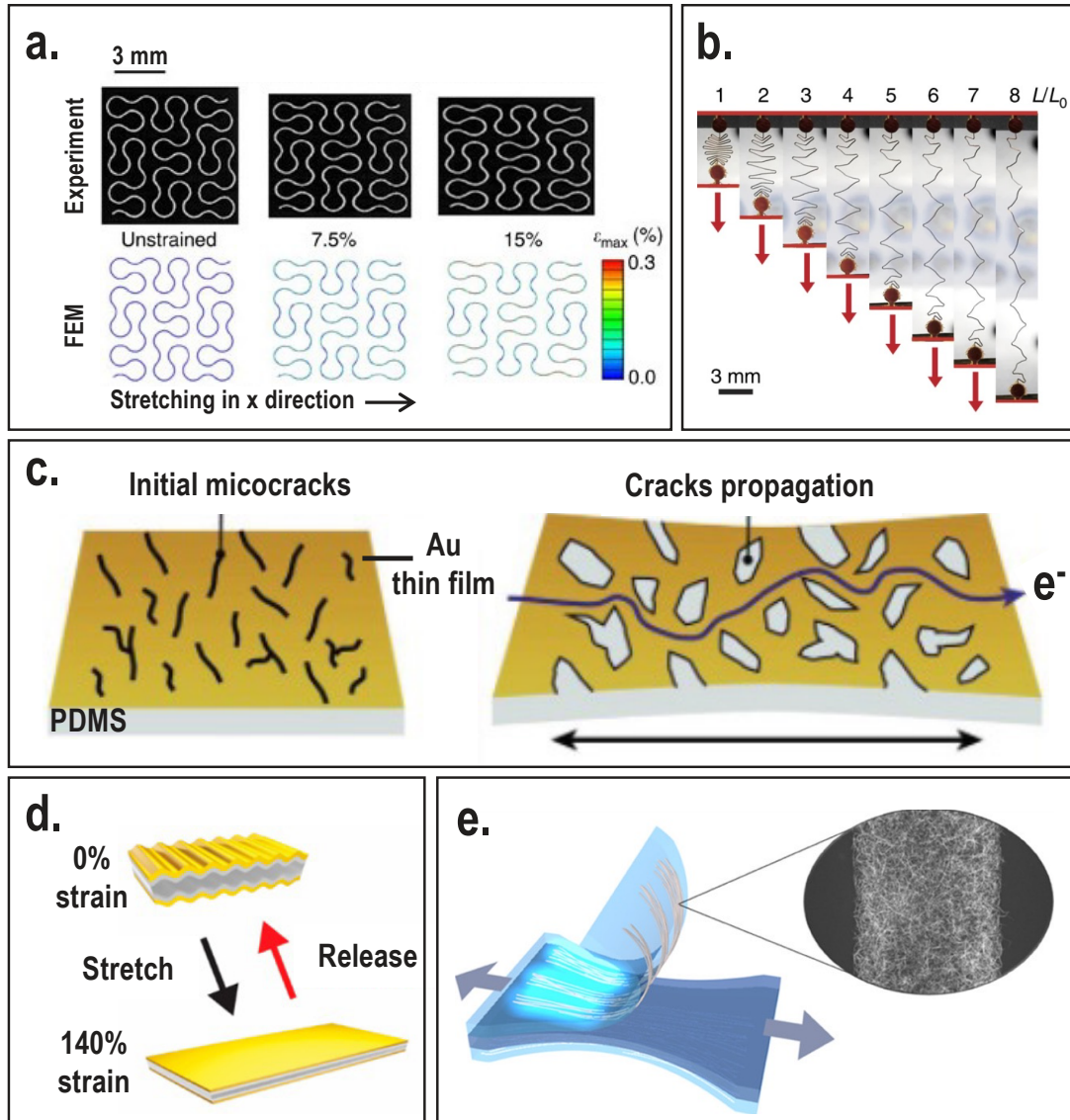


Figure 1.5: **Stretchable conductors realized by structuring rigid metal films and using nano-materials.** **a.** Patterning rigid Au films into 2D fractal motifs enlarged their stretchability. Reprinted with permission from [48]. **b.** Meander-patterned Ag thin films enabled stretchability up to 800%. Reprinted with permission from [49]. **c.** Microcracked Au films whose cracks were modulated using different deposition parameters presented improved stretchability. Reprinted with permission from [61]. **d.** Capacitive stretchable strain sensors enabled by wrinkled Au films. Reprinted with permission from [66]. **e.** Embedding Ag NWs into polymer matrix allowed the realization of stretchable transparent electrodes for electroluminescent devices. Reprinted with permission from [72].

due to the size of spray nozzles [68]. The relatively low resolution limits their use in high density electronic devices.

Intrinsically stretchable conductors Another strategy involves using intrinsically stretchable materials as stretchable conductors. The immobilization of ions or ionic conducting liquids into polymer matrix offers excellent stretchability and high transparency, which has attracted interest in the development of stretchable conductors [76, 77]. Owing to its high transparency, ionic conducting polymers were utilized as several transparent devices such as highly deformable actuators [76], touch panels [78] and energy harvesters [79]. Stretchable electroluminescent devices using ionic conductors were demonstrated to have stable device performances under the maximum strain of 400% over 1000 cycles (Figure 1.6a) [77]. Introducing lithium salt into polymer matrix enabled an ionic elastomer that was highly stable in air and high temperature environment [80]. However, a high electrical resistivity of ionic polymers (in the order of $10^7 \Omega \cdot \mu\text{m}$) hinders their use as electrical conductors.

On the other hand, LMs provide an excellent opportunity for their use as stretchable conductors due to the lower electrical resistivity ranging from $0.29 \Omega \cdot \mu\text{m}$ (eutectic gallium-indium, EGaIn) to $1 \Omega \cdot \mu\text{m}$ (Hg) [85] compared to the above-mentioned materials and an intrinsically unlimited strain limit without the need of complex wire routing [86]. Among all the LM candidates, Ga-based alloys have attracted enormous attention due to their low electrical resistivity and low toxicity. In spite of their excellent electrical properties and high stretchability, the main challenge remains in patterning LMs due to their ability to flow. The overview of the fabrication of LMs is detailed in Chapter 4. Here, a general introduction to LM-based wearable applications is presented.

One of the promising strategies of using LM is to embed it into microfluidic channels. When a LM device experiences mechanical deformation, the geometrical changes in the LM channel result in different electrical signal outputs, thereby enabling strain [87] or pressure sensing [88]. LM-based TENGs were demonstrated by embedding LM into silicone rubber for energy harvesting [89]. Stretchable heaters for wearable thermotherapy [81] and stretchable antennas for wireless power transmission [82] were reported by embedding LMs into channels with various structures (Figure 1.6b,c). Coating LM on an electrospun superelastic fibre mat enabled permeable, biocompatible and stretchable electronics [90]. Owing to the ability of LMs to flow, stretchable and self-healable electronics were introduced by embedding LMs into self-healable hydrogels [91].

Another approach involves incorporating LM microparticles into elastomers to form a new type of stretchable conductive material. Conductive LM pathways are created by means of rupturing the native oxide skin of LM microparticles to allow oxide-removed microparticles to merge and form continuous traces (Figure 1.6d). It can be realized by mechanical pressure [92] or laser sintering [93]. One of the most promising characteristics of LM-elastomer composites is an autonomously self-healing capability without the need for external stimuli such as heat or mechanical energy. The conductive traces self-reconfigure around the damaged region to reroute the electrical conductance (Figure 1.6d) [83]. Modifying the surface property of LM microparticles prevents them from oxidation. As a result, an entirely conductive LM-elastomer was produced and could be patterned into various shapes via screen printing for

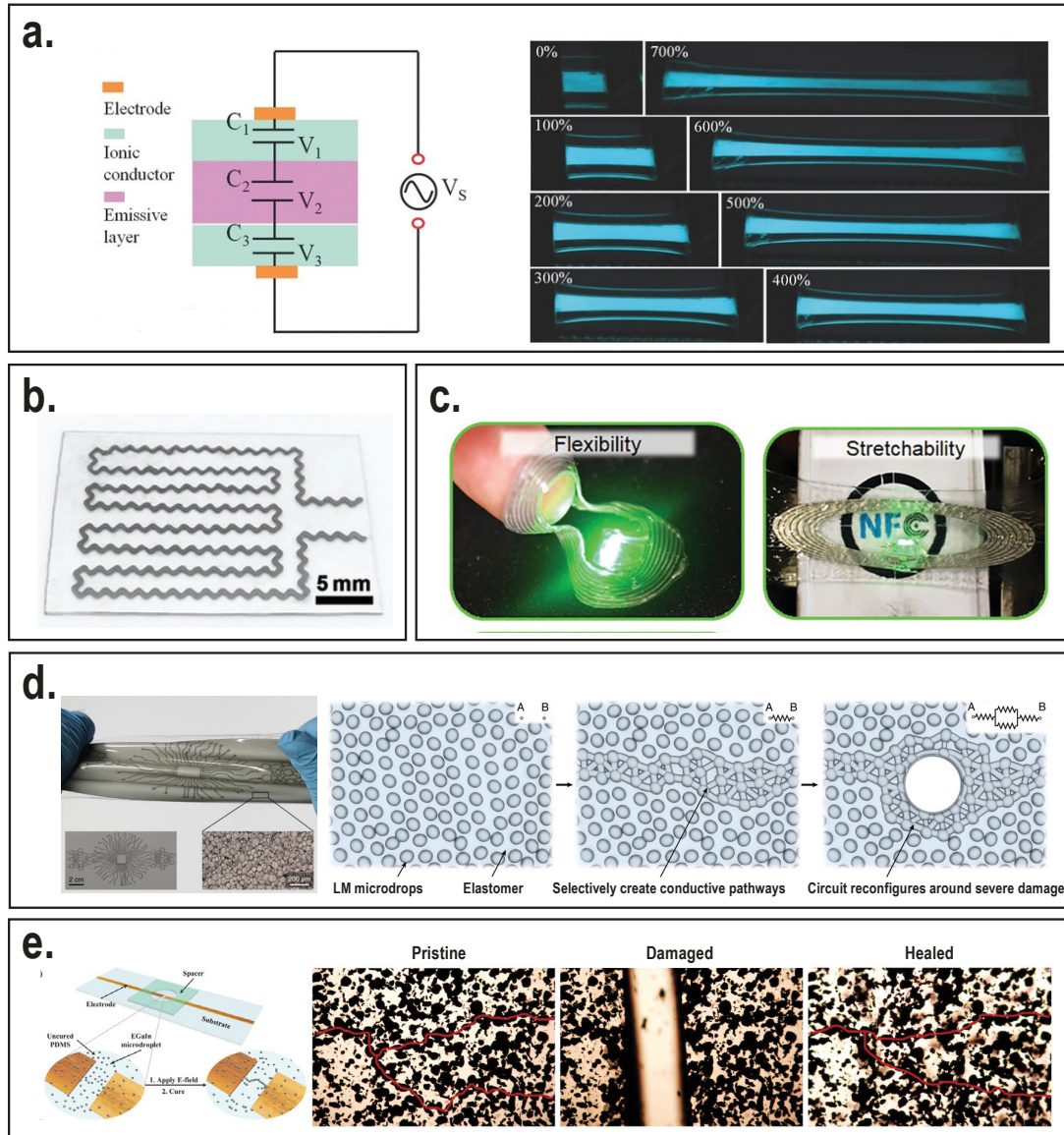


Figure 1.6: Stretchable conductors using intrinsically stretchable materials. **a.** Stretchable electroluminescent devices made from ionic conductors that can sustain strain up to 400%. Reprinted with permission from [77]. **b.** Sinusoidal-structured LM heaters for wearable thermotherapy. Reprinted with permission from [81]. **c.** LM embedded in coil-shaped microchannels for wireless power transmission of light-emitting devices. Reprinted with permission from [82]. **d.** LM-elastomer composite for stretchable and self-healable conductors. The selective conductive pathways were created by mechanical stimuli. The circuit spontaneously reconfigured around the damages. Reprinted with permission from [83]. **e.** LM conductive pathways created by using DEP without high loading of LM microparticles. The circuit was recovered by filling the damaged area with uncured LM-elastomer mixture and performing additional DEP to realign the LM particles. Reprinted with permission from [84].

stretchable and self-healable electronic applications [94]. However, LM-elastomer composites activated by mechanical pressure or laser sintering require a huge amount of particles in the polymer matrix, which makes them not cost-efficient. Additionally, mechanical loadings applied unintentionally during handling would result in inevitable mechanical sintering to form unwanted conductive paths in regions where they should remain insulating. Therefore, aligning LM microparticles using dielectrophoresis (DEP) provided an approach to creating stretchable and healable conductors without high loading of LM microparticles, which kept the process cost-efficient and avoided unwanted sintering (Figure 1.6e) [84].

1.2.3 Non-conventional fabrication process on polymers

Conventional resist-based processes which require high temperature and harsh chemicals are not suitable for realizing functional devices on polymer substrates because most polymers are not resistant to acidic, basic or aqueous solution and have large CTE mismatch to metal films. The CTE mismatch would result in the deterioration of the performance of sensors due to cracks in metal films produced during the metal deposition process. Therefore, the innovations in non-conventional fabrication processes avoiding using resists receive enormous attention. In the following, the state-of-the-art of fabrication platforms without the use of resists is presented.

Digital printing methods Digital printing methods such as inkjet printing and 3D printing are working with the principle of direct printing of functional inks through a dispensing nozzle. These printing techniques avoid the need for moulds, stencils or cleanroom lithography and can be automated for rapid and mass production, which have received great attention for the realization of flexible and stretchable electronics [95] or biodegradable electronics [96]. For instance, by layer-by-layered printing of different materials on a polyethyleneterephthalat (PET) film, flexible organic light-emitting diode (LED) displays were realized [97]. This study demonstrated the capability of using printing methods to pattern not only electrical components (e.g., silver nanoparticle (AgNP) inks and EGaIn) but also polymers (e.g., light-emitting poly(2-methoxy-5-(3',7'-dimethyloctyloxy)-1,4-phenylenevinylene) (MDMO-PPV) and silicone) for diverse applications. Since the printing of functional inks is processed in non-contact mode, it enables the patterning of inks on 3D surfaces. By taking advantage of this unique property, 3D antennas were produced by conformal printing of AgNP inks onto the concave and convex surfaces of hemispherical glass substrates [98]. The printing method also allows for the reconfiguration of intrinsically stretchable EGaIn conductors in 3D architecture, which enables the modification of the resonant frequency of an EGaIn antenna and the switch of LEDs [99]. A more detailed summary regarding the printing process performance and its applications can be found in review papers [95, 100]. In spite of the broad capabilities of the printing methods, the pattern resolution strongly relies on the size of nozzles and it remains challenging to further scale down to the sub-micrometer scale. Additionally, the electrical

performance of printed conductors stays worse than evaporation or sputter-deposited thin metal films due to the relatively low electrical conductivity of formulated printable inks.

The transfer printing technique The transfer printing technique is based on the principle of transferring prefabricated devices from a rigid substrate to a polymer substrate. It is a significant milestone in flexible and stretchable devices [101, 102] and biodegradable electronics [103, 104]. Since the devices are prefabricated on a rigid substrate (e.g., Si), transfer printing allows the use of a wide range of materials and well-established semiconductor processes to realize high performance electronic devices on various substrate materials. For example, stretchable strain and temperature sensors based on single crystalline Si were monolithically integrated on a stretchable PDMS substrate by transferring the prefabricated devices onto the substrate for epidermal electronic applications [105]. Structuring the stamp geometry enabled full-color quantum dot displays via sequential transfer printing of red, blue and green quantum dots [106]. Additionally, the advances in the stamp design enabled the realization of functional devices on arbitrary 3D substrates [107, 108]. By using the soft balloon stamp, Si NM-based photodetectors and solar cells were successfully fabricated on multidimensional substrates [107]. Moreover, printing prefabricated devices to a prestretched substrate has opened a new route to achieving functional devices in 3D architecture [109, 110]. Combining the structure designs in 2D precursors and bonding sites, the compressive forces generated by releasing prestressed elastomer substrates enabled functional electronics in 3D [110]. However, despite the great achievements in the transfer printing technique, realizing sub-micrometer or nanometer scale features by utilizing this technique is still challenging.

Stencil lithography An alternative approach to transfer printing consists of the use of a shadow mask technique (i.e., SL) to directly fabricate the designed structures on substrates. It provides the ability to produce high resolution patterns without the need for complex processes. The history of using stencils can be traced back to thousands of years ago when people used animal bodies or human hands to create decorative paintings [111]. The same working principle was extended to transfer features through a patterned thin sheet of paper, polymer or steel to the underlying substrates. In micro- and nanomachining, SL employs a suspended thin membrane with open apertures to locally deposit or etch materials. By having a prefabricated stencil mask placed on the substrate, materials can be locally deposited using PVD, avoiding potential resist contamination, high temperature and chemical treatments [112]. Localized etching and implantation can also be achieved using stencils in resist-free procedures [113–115]. Stencils have been widely applied on a variety of polymer substrate materials for flexible and stretchable plasmonic biosensing [116, 117], flexible organic transistors [118] and transient electronics [119, 120]. Due to its resistless characteristic, SL was applied to fabricate electrical contacts on 2D materials for its much lower impact on the material properties when compared to electron beam lithography (EBL) [121]. A full wafer stencil was demonstrated to produce full wafer organic thin film transistors on a flexible PI substrate [122].

Based on the membrane materials, stencils can be categorized into polymer stencils and rigid film stencils. Polymer stencils utilize structured flexible polymer thin films as a mask to define patterns. Thanks to the flexibility of polymer films, polymer stencils are able to form an intimate contact with the substrate, thereby enabling the structuring of not only solid but also liquid materials. PI is one of the most widely used membrane materials due to its mechanical robustness and high resistance against high temperature and chemicals. PI stencils were applied to pattern biodegradable metals via physical vapor deposition (PVD) (Figure 1.7a) [47, 119] and structuring AgNWs via spray coating [123]. Stretchable LM electronics were achieved by screen printing LMs through PET stencil masks (Figure 1.7b) [124]. UV curable polyurethaneacrylate (PUA) films were applied as stencil masks for the realization of flexible microsupercapacitors [125] and stretchable LM conductors [126]. Besides the commonly used polymer materials, an E-beam resist has also received great attention. The resist patterned by electron beam can be directly used as a stencil for nanofabrication by transferring the mask to various substrates. For instance, poly(methyl methacrylate) (PMMA) was applied as a stencil mask to enable nanostructures with resolution down to 40 nm (Figure 1.7c) [127]. The soft nature of resist stencils also allows the production of multidimensional structures on curved surfaces [128].

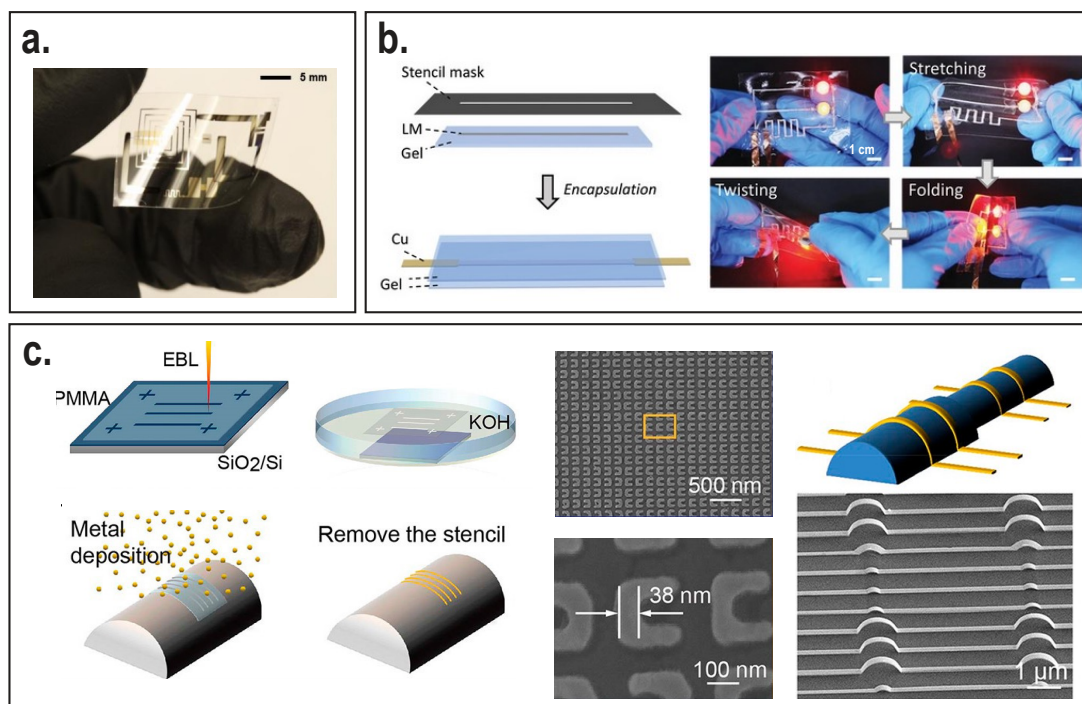


Figure 1.7: The use of polymer stencils for structuring various materials on different substrates. **a.** Patterned PI film was utilized as a stencil for structuring biodegradable conductors on biodegradable silk substrates. Reprinted with permission from [119]. **b.** Laser-patterned PET film was used as a mask to pattern liquid conductors on hydrogels. Reprinted with permission from [124]. **c.** Resist used for EBL was applied as soft stencil masks for the fabrication of nanostructures on curved substrates. Reprinted with permission from [127].

Rigid, uniform and chemically resistant stencils are commonly fabricated using SiN as membrane material. SiN is broadly used in semiconductor processes because it can be grown by using chemical vapor deposition (CVD), allowing conformal deposition of high quality dielectric films with precise thickness control for electrical insulation. In addition, the stress of the grown SiN film can be adjusted by modulating CVD parameters such as deposition temperature and the ratio between the used precursors, which enables a low stress SiN (LS-SiN) film, an excellent candidate material for stencil application. Compared to polymer stencils, suspended SiN membranes supported by a rigid Si frame make the handling easier and thus can be simply attached to various substrate materials. This property enables dynamic SL where the applied stencil moves with respect to the substrate during the deposition process, allowing multimaterial deposition and also the production of close-loop patterns (Figure 1.8a) [129]. Utilizing SiN stencils with apertures patterned by EBL, sub-100 nm patterns were produced on polymer substrates for plasmonic biosensing (Figure 1.8b) [116, 117]. Another important merit of SiN stencils is the capability of full wafer patterning, making the process more cost-efficient. The easy-to-handle SiN stencil enables structuring nanometer features at the full wafer scale as well as fine-pitch alignment [130]. SiN stencils are well-suited for patterning high quality thin films of materials that require to be deposited in ultrahigh vacuum and high temperature environments (e.g., superconducting thin films grown by molecular-beam epitaxy) for quantum devices [131]. To further improve the resolution of SL, shadow masks with apertures defined by stress-induced cracks were proposed. Nanowires featuring 20 nm resolution were realized using crack-defined TiN stencils (Figure 1.8c) [132].

One of the particular features of SiN stencils is the inherent gap existing between the stencil mask and the substrate. The gap is a result of several reasons such as the wafer curvature, stress-induced bending of the stencil membrane and the substrate topography. Compared to conventional resist-based processes, where a photoresist adheres to the substrate, the inherent gap in SL allows producing structures on fragile substrates that could be damaged by resist-based processes due to UV radiation, energetic electrons or mechanical contact. However, the gap results in pattern enlargement of the deposited structures (i.e., the blurring effect) (Figure 1.9a,b). The blurring effect is affected not only by the intrinsic gap between the stencil mask and the substrate but also by the properties of the deposited materials and the substrate. The blurring effect is due to the geometrical trajectory of the incoming atoms (geometrical blurring) and the surface diffusion of the deposited atoms (halo blurring) [133]. The geometrical blurring has been thoroughly studied and can be approximately estimated by considering the aperture size, the stencil/substrate gap, the substrate/source distance and the source size [133]. Equation 1.1 describes the relationship between these parameters where B_G is the resulting blurring length, W_c is the width of the deposited structure, A is the aperture size, G is the gap distance between the stencil and the substrate, S is the evaporation source size and D is the distance between the substrate and the evaporation source. When the substrate/source distance is much larger than the stencil/substrate gap ($D \gg G$) and the source size is much larger than the aperture size ($S \gg A$), the blurring length can be approximately estimated as $B_G \approx (G \cdot S)/D$. The halo blurring length is affected by the

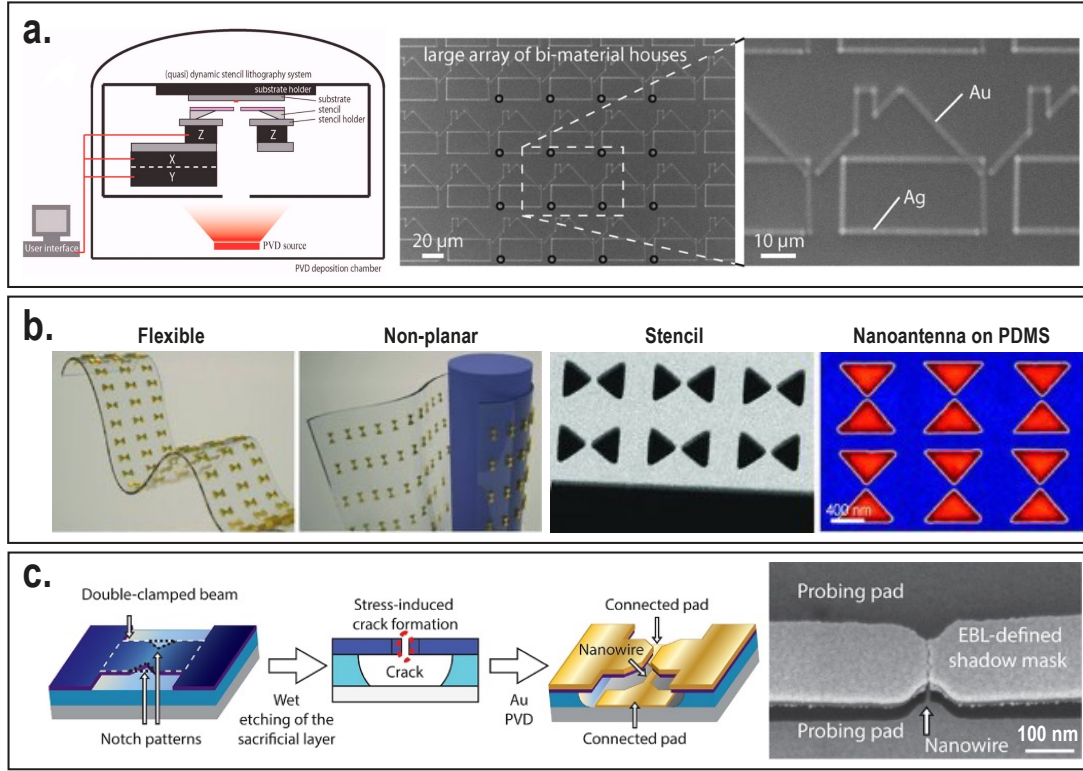


Figure 1.8: **The application of rigid film stencils.** **a.** Si-supported SiN stencils moved respect to the substrate during the deposition process, enabling the production of multimaterial structures. Reprinted with permission from [129]. **b.** Nanostencils with apertures created by using EBL permitted the fabrication of nanostructures on stretchable polymer substrates for tunable plasmonic biosensing. Reprinted with permission from [116]. **c.** Scalable fabrication of nanowires using nanostencils with apertures defined by stress-induced cracks. Reprinted with permission from [132].

differences in the diffusion constant among different materials [134]. Although the blurring effect leads to a typically undesired pattern enlargement (i.e., limits the pattern resolution), it was utilized to control the crystallization of organic thin films through the surface diffusion of absorbed molecules [135] and also to form continuous films with a well-controlled grain size. Through well-designed nanosieve stencils, continuous organic semiconductor thin films with a crystalline domain size of $5\ \mu\text{m}$ were successfully demonstrated by taking advantage of the blurring effect resulting from the inherent gap [136].

$$B_G = W_c - A = \frac{G(S + A)}{(D - G)} \quad (1.1)$$

A straightforward solution to mitigate the blurring effect is to reduce the gap distance between the stencil and the substrate. Different strategies have been proposed. For instance, the

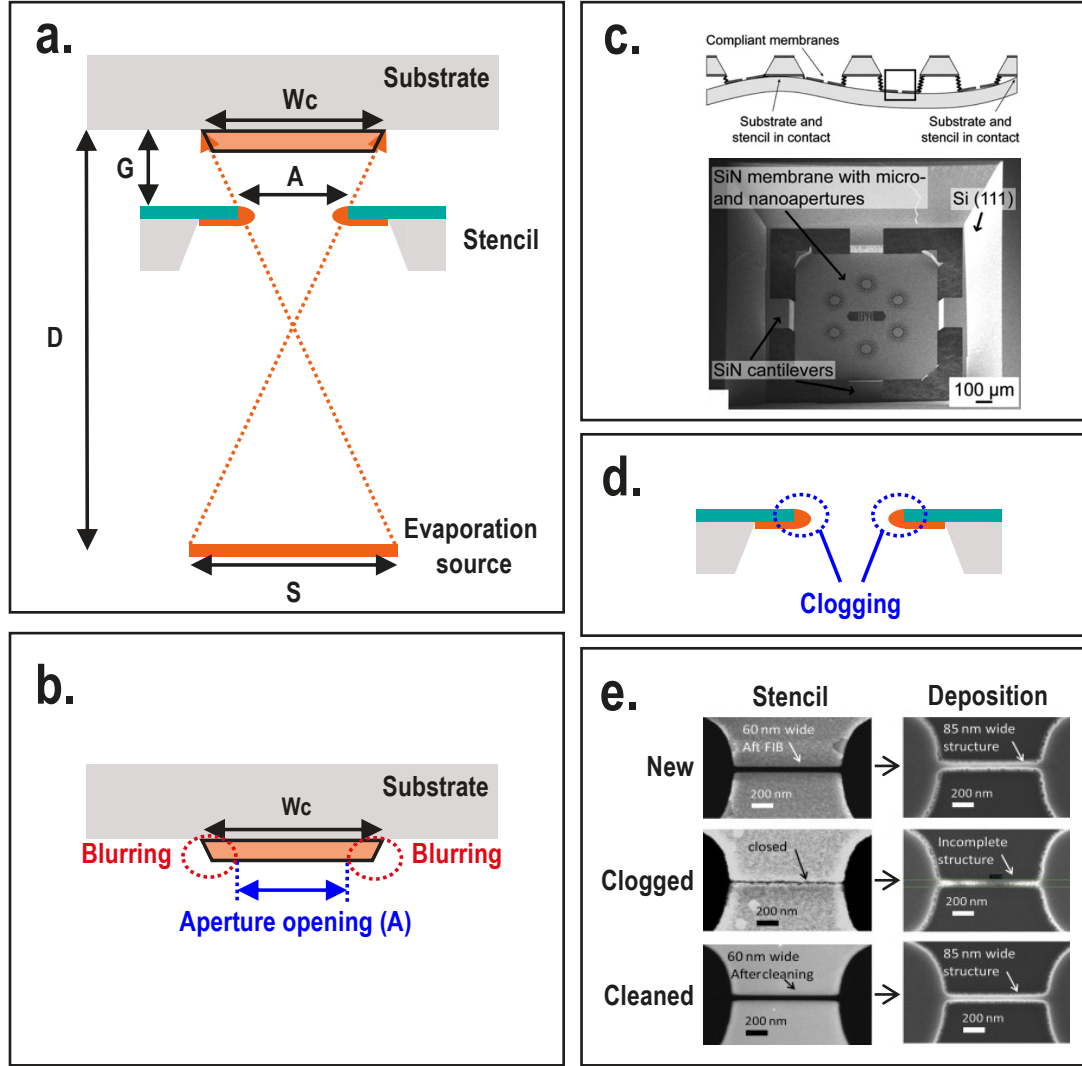


Figure 1.9: **The blurring and the clogging effect in SL.** **a.** Schematic drawing showing the working principle of SL. The stencil having an aperture size of A is placed above the substrate with a gap distance of G . The evaporation source having a size of S is located at a distance of D from the substrate. W_c is the width of the deposited structure. **b.** Detailed schematic view of the blurring effect, where the resulting structure width W_c is larger than the design aperture size A due to the gap distance G between the stencil and the substrate and the line-of-sight evaporation process. **c.** The concept of using compliant stencils to reduce the gap between the stencil and the substrate, resulting in less blurring length. Reprinted with permission from [137]. **d.** Detailed schematic view of the clogging effect resulting from the materials deposited on the stencil apertures. **e.** Cleaning of the stencils using metal wet etchants to prevent the clogging effect. Reprinted with permission from [138].

gap was reduced by designing compliant stencils where the membrane with apertures was supported by several cantilevers. The cantilevers were used as springs to enable conformal

contact between the membrane and the substrate (Figure 1.9c) [137]. Incorporating heaters on the stencil membrane allowed in-situ actuation of the membrane to reduce the gap distance [139]. Intimate contact can also be achieved by utilizing soft polymer stencils. The soft nature of polymer films allowed close contact with the substrate surface [140].

During the deposition process, materials are deposited not only on the substrate surface but also on the sidewall of the aperture openings, which results in the clogging of the apertures after multiple uses (Figure 1.9d). Clogging leads to the reduced lifetime of stencils and non-repeatable deposition results. The strategies applied to mitigate clogging involve using heaters to re-evaporate the deposited materials on stencils [141], coating stencils with a self-assembled layer to reduce the metal adhesion to the membrane [142] or removing the materials deposited on stencils using proper wet etchants (Figure 1.9e) [138]. Interestingly, despite the mentioned disadvantages of the clogging effect, it has been applied to produce 3D nanostructures. With the appropriate designs of aperture openings, materials continue to be deposited on the substrate through larger apertures after smaller apertures are clogged, thereby enabling 3D structures. This particular characteristic was adapted to produce various 3D nanostructures [143].

Since stencils are composed of freestanding thin membranes, membrane stability has long been a major parameter that needs to be considered. Due to stress-induced bending and breaking, thin and large suspended membranes in stencils are, in practice, not possible. This restricts the geometrical design flexibility of SL and sets a limit on their potential applications.

1.3 Thesis outline

The overall objective of this thesis is to explore the application of SL on a variety of substrate materials, aiming to realize flexible and stretchable devices. To this end, a systematic study on the deposition of metals on various polymer substrates using SL is firstly investigated. To overcome the limitations in the geometrical design flexibility of SL, a new stencil concept utilizing bridge supports is proposed. Combining with a DUV stepper, several structures are realized on various substrate materials with resolution down to the sub-micrometer scale. The application of SL is further extended to pattern intrinsically stretchable material (e.g., LM) for stretchable electronic applications. Lastly, the LM patterning technique is applied to realize stretchable Si NM conductors. The content of this thesis is divided into 5 chapters.

Chapter 2 presents the detailed study of the deposition of metal films on a variety of substrate materials using SL. The investigated polymer substrates include biocompatible PI, parylene, biodegradable PLGA and metastable poly(phthalaldehyde) (PPA). The geometrical and electrical characterization of the patterned metal structures are examined.

Chapter 3 describes a new stencil design concept to enable almost arbitrary aperture openings on stencil membranes. The proposed design employs several bridges to support and stabilize the suspended membrane. Continuous metal traces are produced by taking advantage of the blurring effect. When the stencil is lifted at an appropriate gap distance above the substrate, the line-of-sight evaporation process results in the material deposition under the shadow bridge regions. The effect of utilizing narrow bridges to stabilize the suspended membrane is studied using stencils composed of several cantilevers. Spiral structures at the micrometer scale are fabricated on various polymer substrates. With the use of a DUV stepper, sub-micrometer meandering structures are realized. The geometrical and electrical properties of the fabricated metal structures are discussed in detail.

Chapter 4 explores the application of SL to shape LMs (e.g., EGaIn). Adapting the selective wetting properties of oxide-removed EGaIn, fine-pitch EGaIn patterns are achieved by combining SL and the centrifugal force-assisted patterning technique. Metal traces that EGaIn wets are produced by using SL on a stretchable polymer substrate. The well-controlled centrifugal force is introduced to selectively remove excess EGaIn, thereby remaining high resolution EGaIn patterns on the substrate. The developed bridge stencil concept is applied to shape EGaIn into long serpentine and interdigitated patterns. The geometrical and electrical characterizations of the fabricated EGaIn structures are thoroughly presented.

Chapter 5 demonstrates a concept of stretchable Si NM conductors enabled by LM interconnections. The proposed device scheme comprises single crystalline Si NMs supported by PI films and EGaIn on a stretchable substrate. In this configuration, Si NMs are used as functional materials, PI films are applied as a strain-isolation layer for Si NMs and EGaIn is utilized as stretchable interconnections. As a proof of concept, stretchable Si conductors are demonstrated using highly doped Si NM as a functional material. Finite element analysis (FEA) details the design consideration of the proposed device configuration. A fabrication platform

for the realization of such devices is proposed and demonstrated. Electrical behaviour of the fabricated devices under mechanical deformation is characterized and discussed.

Chapter 6 summarizes the contribution of this these and provides a brief outlook for future works.

2 Stencil lithography on polymer substrate materials

Disclaimer: This chapter (2) is adapted from the following article with permissions of all co-authors and journal:

Y.-C. Sun, G. Boero and J. Brugger, "Nanobridge stencil enabling high resolution arbitrarily shaped metallic thin films on polymer substrates", *In preparation*

My contribution: conceptualization, design, fabrication, experiments, figures and writing.

The purpose of this chapter is to present the systematic study on the deposition of metals on various polymer substrates using stencil lithography (SL). The fabrication and the implementation of stencils are firstly introduced. Geometrical and electrical characterizations of the fabricated metal structures are performed and discussed in detail, followed by the conclusion of this chapter.

2.1 Introduction

Shaping metal films on polymer substrates has enabled a wide range of applications. For instance, heterogeneous integration of various metallic materials and structures on a single polymer substrate allowed the realization of multifunctional wearable devices for light, magnetic field, temperature and strain sensing [49]. Patterning thin metal films into interdigitated structures on an ultrathin PEN foil was demonstrated as an ultralightweight tactile sensing array [13]. Combining with biodegradable metals and polymers, numerous biodegradable devices that can be naturally dissolved in body fluids were demonstrated for a variety of applications such as electrocorticography systems [144], wireless power transfer [145], in-plane strain and pressure sensors [146] and self-powered pressure sensors [147], etc. Stencil lithography (SL) represents an excellent fabrication platform for the realization of such devices due to its resistless characteristics.

The further development of SL requires a thorough exploration of the deposition of materials on different substrates using this technique. Previous studies have reported the geometries of metal structures fabricated on several polymer substrates using SL [117] and the electrical properties of metals deposited on biocompatible PI using stencil masks [148]. However, a systematic study on the geometrical and electrical behaviour of the metals deposited on various commonly used polymer substrates using SL has not yet been reported.

In this chapter, we report a detailed study on the deposition of metals on various polymer substrates using SL. The investigated substrate materials include biocompatible PI, parylene, biodegradable PLGA and widely used metastable PPA. The geometrical and electrical properties of the produced metal structures are studied. The results presented here pave an enabling step towards the realization of wearable and implantable systems using SL.

2.2 Results and discussions

2.2.1 Stencil fabrication method and results

Stencil fabrication Stencils, which contain freestanding membranes supported by bulk materials, can be realized with combinations of different thin film materials. In this thesis, SiN is used as a membrane material due to the following reasons:

1. The stress of SiN films can be tuned by modulating CVD deposition parameters such as the ratio between precursors and the deposition temperature to have a low stress thin film.
2. SiN is a commonly used material in micro- and nanofabrication with a well-established deposition process for precise thickness and uniformity control across the entire wafer.
3. SiN can resist most chemicals and endure high temperature, excellent properties to be used as a mask for material deposition, etching and implantation.

The fabrication of SiN stencils starts by growing low stress SiN (LS-SiN) films on both sides of a 100 mm Si wafer by low-pressure CVD (LPCVD) (Figure 2.1a). The stress of the deposited LS-SiN film is about 200 MPa by measuring wafer curvatures before and after SiN film deposition and removing one side of the film. The determination of the membrane thickness depends on the sizes of aperture openings and suspended membranes. In this chapter, the minimum aperture size is 2 μm so the membrane with a thickness of 500 nm is used. The frontside aperture designs are defined by the lithography process and the patterns are transferred to the SiN by reactive ion etching (RIE) with a mixture of C_4H_8 , H_2 and He (Figure 2.1b). Subsequently, a second lithography process with an alignment to the frontside layer is performed on the wafer backside to define the size of the freestanding membrane and cleaving lines, which are defined to enable the cleaving of the wafer into chips at the last step (Figure 2.1c). RIE is then conducted to transfer the patterns. Next, the open area is dry-etched using the Bosch process for $\sim 300 \mu\text{m}$, followed by etching the remaining Si using KOH wet etching to release the membrane (Figure 2.1d,e).

Here, a combined dry and wet process is applied to release the membrane for certain process concerns. First, the etching rate in KOH wet etching is relatively slow ($\sim 20 \mu\text{m/hr}$) comparing to the Bosch process ($\sim 300 \mu\text{m/hr}$). Another reason is that long etching in a KOH bath would lead to the potential contamination on the surface due to the etched debris. Last, because KOH also etches Si from the periphery of wafers due to the lack of protection from the wafer edge, performing etching in a KOH bath for a long period of time might result in a very rough wafer edge, making the handling difficult. Incorporating the Bosch process to reduce the processing time in a KOH bath can effectively resolve the concerns. However, utilizing the Bosch process to etch all the backside Si might lead to the breaking of the membrane because the Bosch process requires an electrostatic clamp and He flow to control the temperature during etching. The He flow sometimes causes damage to the membrane during the declamping procedure. The aperture openings would also lead to a He flow leak failure after the membrane is fully released. Therefore, a combined dry and wet process ensures the successful release of the stencil membrane without damage. When the cleaving lines are relatively narrow (e.g., 15 μm), the rate of anisotropic KOH etching becomes significantly slow when $\langle 100 \rangle$ planes inside the lines are fully etched. It prevents the wafer from splitting during the process but enables the cleaving of the wafer into chips by gently pressing the wafer along the lines with tweezers. The released stencil is then placed in a fume hood for at least 4 hrs for drying.

Stencil fabrication results Two types of stencils are designed and fabricated to study the geometries and the electrical properties of the fabricated metal structures on various polymers. The stencil for geometry study contains a square array with widths from 2 to 20 μm and gap distances from 2 to 20 μm . Figure 2.2a shows that the designed square array is successfully fabricated without damage. The magnified optical image shows the square apertures with different widths and gap distances (Figure 2.2b). With the use of a laser writer, a square array with a width and a gap distance of 2 μm is successfully realized (Figure 2.2c). It is noted that the resolution can be further improved by using different lithography techniques (e.g.,

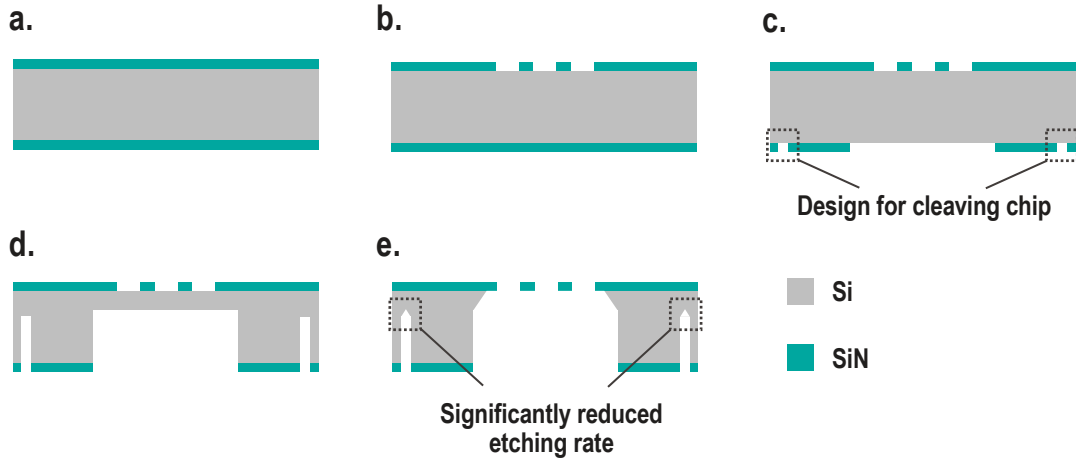


Figure 2.1: **Fabrication flow of stencils.** **a.** Low-stress SiN films are grown on both sides of a Si wafer using LPCVD. **b.** Frontside aperture openings are defined by the lithography process and are transferred to the SiN layer using RIE. **c.** Backside opening windows and cleaving lines are defined using the same method. **d.** The Bosch process is used to anisotropically etch the Si backside for $\sim 300 \mu\text{m}$. **e.** The SiN membrane is fully released using KOH wet etching.

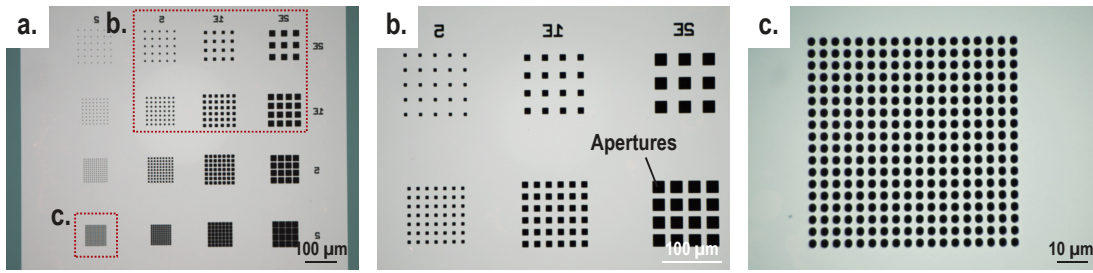


Figure 2.2: **Stencil fabrication results with square aperture openings.** Optical images showing **a.** the overview of square arrays and **b.,c.** the zoom-in views of the dashed squares in **a.** **b.** Square arrays with sides of 5, 10 and 20 μm and gap distances of 10 and 20 μm . **c.** The detailed view of the array with a width and a gap distance of 2 μm each.

deep ultraviolet (DUV) or E-beam lithography (EBL)). In this chapter, we aim to discuss the geometry of the deposited structures, so a square array with a width of 2 μm is sufficient. The other type of stencil consists of aperture openings with 4 point probe configuration having a width of 10 μm and lengths of 50, 100 and 150 μm (Figure 2.3a). The magnified views indicate the successful fabrication of stencils having apertures of 4-point probe structure design (Figure 2.3b,c). Noticeably, we observe membrane bending after the SiN membrane is fully released. The membrane bending results from stresses built during the stencil fabrication process and mainly come from the intrinsic stress of SiN film deposited at high temperature. The bending depends on the design of aperture openings, which turn the square suspended membrane into several cantilevers. When the membrane is released, the cantilevers deform due to the release of stresses. In some extreme cases, the deformation in the membrane would

lead to serious blurring effects on the deposited structures. However, in the presented case, the bending does not significantly affect the resulting patterns.

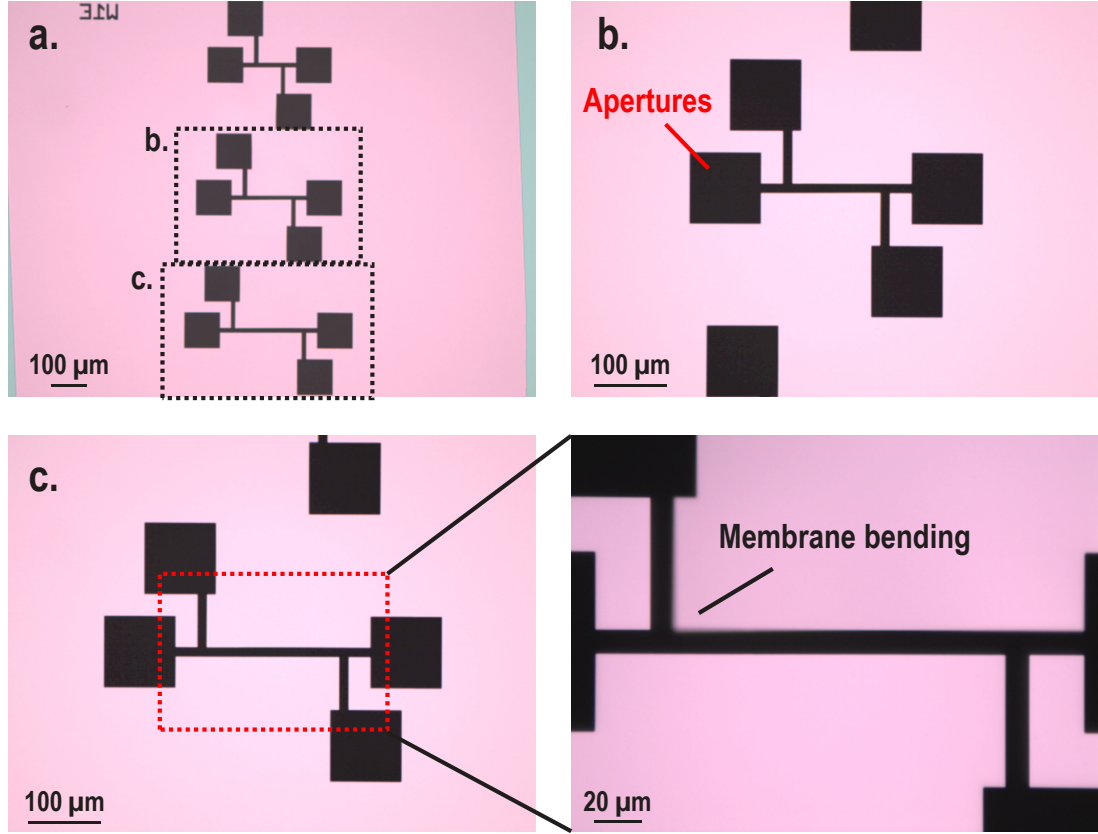


Figure 2.3: **Stencil fabrication results with 4-point probe apertures.** **a.** Optical images showing the overview of 4-point probe apertures with a line width of 10 μm and lengths of 50, 100 and 150 μm . **b.,c.** The zoom-in views of the apertures with line lengths of **b.** 100 μm and **c.** 150 μm (shown as the dashed squares in a.). The detailed view of c. indicates the membrane bending after the SiN membrane is released.

2.2.2 Stencil lithography on polymer substrates

Experimental method for SL

The experiment starts by placing stencils on polymer substrates with SiN membrane facing down (i.e., the membrane is in contact with the substrate) to have a minimum gap between the stencil and the substrate to mitigate the blurring effect. The stencil is fixed on the substrate using Kapton tape attached to the corners of the stencil. Subsequently, the sample is brought into an evaporation chamber and 5 nm Cr and 50 nm Au are deposited on the substrate using an E-beam evaporation process. Here, an E-beam evaporation process is used due to the better control of the resulting geometries thanks to the line-of-sight trajectory of the material flux. Last, the stencil is gently removed from the substrates to have the metal patterns for

further analysis. For certain substrate materials (e.g., PLGA), we observed that the applied stencil adheres to the polymer surface after the evaporation deposition process. The sticking issue is tentatively attributed to the low glass transition temperature (T_g) of PLGA (45 to 60 °C) [149]. The evaporated metal sources heat the polymer surface above its T_g during the deposition process, leading to temporary reflow of the polymer. The stencil adheres to the polymer surface after the temperature cools down to room temperature. Hence, in the case of PLGA, we deliberately introduce a gap between the stencil and the substrate by inserting a thin Kapton foil having a thickness of 25 μm in between to avoid direct contact.

Polymer properties and substrate preparation

Polyimide (PI) PI has long been used as insulation and passivation layers for electronic devices due to its high chemical and thermal resistance, a high T_g of 350 °C and low CTE of 3 ppm/°C, which is close to the value of Si (2.6 ppm/°C) [150, 151]. Because of such excellent properties, it is considered an interesting substrate material for flexible electronics. The preparation of PI begins with cleaning a fresh Si wafer with O_2 plasma for 7 mins. Then, a PI liquid precursor (PI 2611, HD Microsystems) is poured at the center of the wafer, followed by spinning the wafer at the maximum speed of 2700 rpm to form a continuous film having a thickness of $\sim 5 \mu\text{m}$. Last, the film is soft-baked at 65 °C and 105 °C for 3 mins each, then the film is cured in an oven at the maximum temperature of 300 °C for 1 hr.

Poly(phthalaldehyde) (PPA) PPA is a metastable polymer and the transience of the polymer can be triggered by specific stimuli such as heat, light or mechanical stress by tuning its material composition. The tunable transience property has received enormous interest for triggered transient electronics [152–154]. The fabrication of PPA films begins with spin-coating PPA (Allresist DE) solution (1.3 wt% in anisole) on a bare Si substrate at the maximum speed of 1500 rpm, followed by baking the wafer at 90°C for 3 mins to form a film having a thickness of $\sim 20 \text{ nm}$.

Parylene C Parylene C is a chemical vapor deposited polymer so it can be conformally coated on substrates and can be easily etched using O_2 plasma. It has an excellent chemical resistant property and biocompatibility [155]. Such properties enable parylene C to be used as encapsulation layers for medical implants [156] or substrates and dielectric layers for microelectronics [157]. A parylene C film is deposited on a bare Si substrate using a commercial CVD tool (Comelec C-30-S, Comelec SA) to form a uniform film having a thickness of 5 μm .

Poly(lactic-co-glycolic) acid (PLGA) PLGA is a synthetic biodegradable polymer that is co-polymerized with poly(lactic acid) (PLA) and polyglycolide (PGA). It is one of the most commonly used biodegradable polymers for transient electronics because of its tunable transient properties. PLGA degrades in the presence of water via hydrolysis and the dissolution rate can

be modulated using different ratios of lactide to glycolide, which changes its hydrophobicity and swelling. Such a property receives enormous interest for controlled transient electronics [158–160]. The fabrication of PLGA film starts by dissolving 0.1 g PLGA (PLGA 50:50, Vornia Biomaterials, Ireland) in 4 ml Ethyl Acetate (Sigma-Aldrich, Switzerland). Then, the solution is drop-casted on a bare silicon wafer coated with a self-assembled trimethylsilyl chloride silane (TMCS) (Sigma-Aldrich) layer to facilitate the removal of the film. For a 4-inch Si wafer, 4 ml solution is required to cover the whole wafer surface to form a $\sim 7.5 \mu\text{m}$ thick PLGA film. Last, the solvent is evaporated in ambient conditions for at least 6 hrs.

Table 2.1 summarizes the mechanical and thermal properties of the listed polymers. It is noted that the low Young's modulus of the used polymers allows them to be used as substrates for flexible electronic applications. However, the lower yield strain of less than 10% hinders their use for stretchable applications. It is indicated that the low T_g of PLGA of less than 60°C might lead to different geometries of the resulting structures when using the evaporation deposition process because the surface temperature is known to be increased during the deposition by the evaporated source atoms [161].

Table 2.1: **Material properties of polymer thin films.** The values would vary using different synthesis parameters. The listed values are captured from literature with synthesis conditions close to our experiment.

	PI-2611	PPA	Parylene C	PLGA
Young's modulus (GPa)	8.5	0.4	2.8	0.002
Yield strain (%)	4	10	2.9	3-10
Melting point ($^\circ\text{C}$)	N.A.	150-200*	290	262
T_g ($^\circ\text{C}$)	360	110-130	80-100	45-60
Reference	[150, 151]	[154, 162, 163]	[164, 165]	[149, 166, 167]

*PPA thermally decomposes instead of melting

Geometrical characterization

The geometries of the deposited metal structures are probed by atomic force microscope (AFM) and optical microscope. In addition to the four polymer substrates introduced above, a rigid SiN substrate is applied as a reference. A square array with a square side and a gap distance of $2 \mu\text{m}$ each is investigated. AFM cross-section and 3D views show similar metal profiles on SiN, PI, PPA and parylene C substrates (i.e., similar height and pitch) (Figure 2.4a,b). The rough metal surface on parylene substrates comes from the roughness of parylene layers after being deposited on Si substrates using CVD (Figure 2.5). The measured roughness shows a root mean square of the roughness of $\sim 8 \text{ nm}$ from two reference wafers. Interestingly, we notice that the deposited metal structures on PLGA substrates show a different behaviour, where the deposited metals are surrounded by PLGA fences built during the evaporation deposition process. The cross-section view of the AFM images indicates that the deposited metals are inside the created PLGA holes (Figure 2.4a,b). By investigating the material properties of polymer thin films (Table 2.1), we tentatively attribute the observed phenomenon to the low

T_g of PLGA (~45 to 60 °C [149]). It has been widely studied that when a polymer is heated above its T_g , the polymer experiences reflow behaviour due to reduced viscosity [168]. For example, with an ion-beam source, localized polymer reflow due to ion-beam heating was observed and utilized for self-assembly [169]. Furthermore, during the electron-beam evaporation deposition process, it was reported that the evaporated metal source atoms heated substrate materials, thereby inducing a temperature increase on the substrate surface [161]. In the presented observation, PLGA surfaces might experience local heating in the stencil aperture regions, resulting in polymer deformation during the metal deposition process. It is important to note that we deliberately introduce a gap between the stencil and the PLGA surface during the metal deposition process because of the stencil adherence issue. The gap creates a free space where PLGA could undergo polymer reflow during the process and form fences. The optical images reveal the successful fabrication of square arrays having a minimum pitch of 4 μm on different substrate materials (Figure 2.4c).

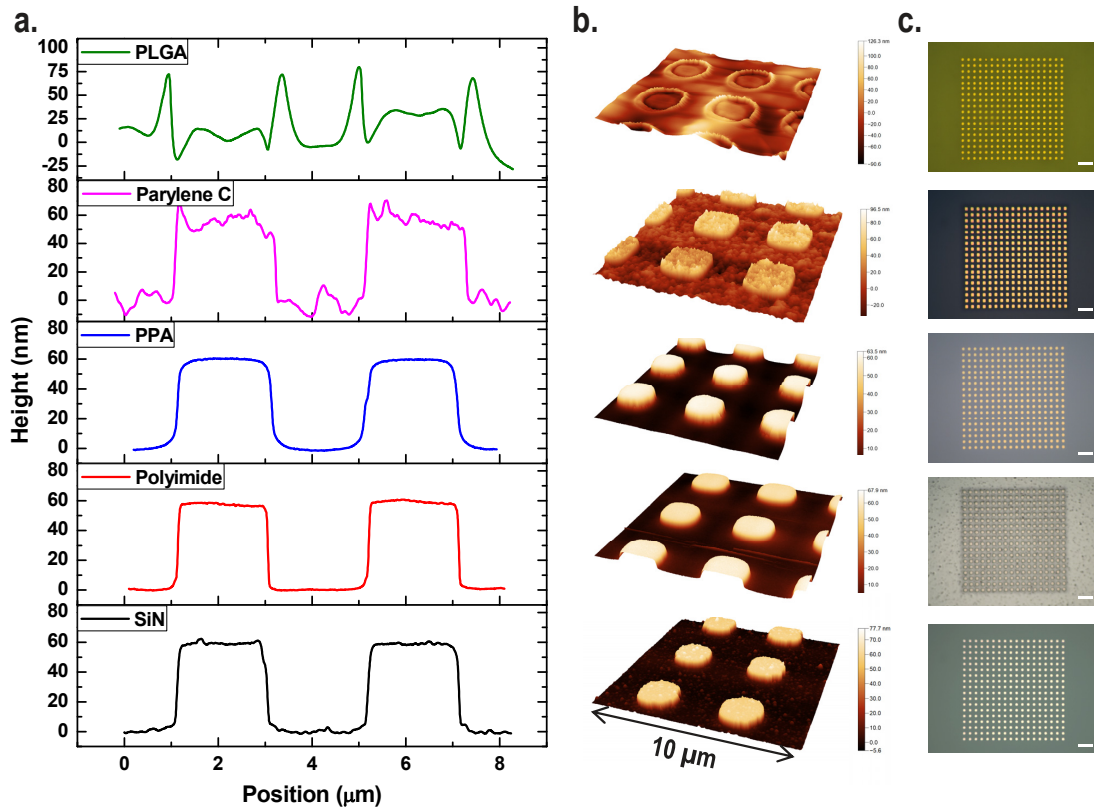


Figure 2.4: **Geometrical characterization of square arrays evaporation deposited on different substrate materials.** AFM images showing **a.** the cross-section profile of the deposited Cr (5 nm)/ Au (50 nm) structures on different substrate materials and **b.** their corresponding 3D views. **c.** Optical images showing the deposited square arrays on different substrate materials. Scale bar: 10 μm . A square array having a square side and a gap of 2 μm each is investigated. On PLGA substrates, thin Kapton foils with a thickness of 25 μm are introduced between the stencil and the substrate during the metal deposition process. For the other substrates, the stencils are placed in contact with the substrates.

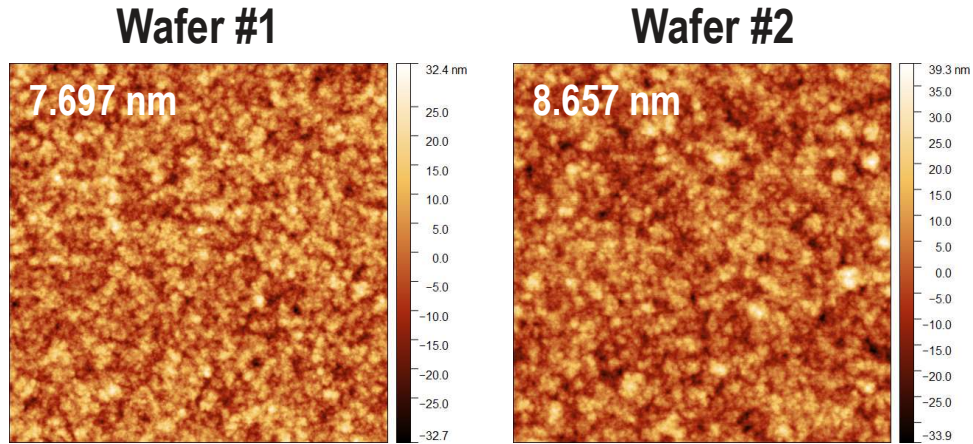


Figure 2.5: **Surface roughness of parylene C films deposited on Si substrates.** AFM images showing the roughness of parylene C surfaces after being deposited on Si substrates using CVD. The number indicates a root mean square of the surface roughness.

To elaborate on the observed reflow behaviour on PLGA substrates, we conduct experiments using the sputter deposition process. The sputter deposition applies high energy plasma ions (e.g., Ar) to physically eject atoms from the target material. The ejected atoms are then deposited on the substrate to form a film. Because the target material is not thermally evaporated, the surface temperature during the deposition is considered to be lower than using the evaporation deposition process. Optical and AFM images clearly show different geometries of the deposited metal structures when using the evaporation and sputter deposition (Figure 2.6a-d). Several observations are noticed and discussed as follows. First, compared to the evaporation deposition process, there is no stencil adherence issue using the sputter deposition process when the stencil is placed in contact with the PLGA surface during the process, allowing the successful removal of the stencil (Figure 2.6c). The observation is attributed to the fact that since PLGA is not heated above its T_g , no polymer reflow is triggered. As a result, the applied stencil does not adhere to the PLGA surface after the deposition process. Another point is that the AFM images of the sputter deposited structures show a mesa-like profile (i.e., no significant PLGA fence is observed), which might be due to the less heating of the PLGA surface during the metal deposition process (Figure 2.6d). However, since the sputter deposition has a random trajectory of atoms during the deposition process, the more significant blurring effect is noticed (Figure 2.6c,d). The blurring results from the existing gap between the stencil and the substrate because the stencil membrane and the PLGA surface are not perfectly flat. Owing to the random trajectory of atoms during the sputter deposition process, introducing a gap of 25 μm between the stencil and the substrate leads to a blurred pattern, which cannot be further analyzed (Figure 2.6e).

In short, the observed different geometries of metal structures produced using the sputter deposition method are ascribed to the fact that the temperature of PLGA surfaces remains below its T_g during the process. Therefore, no significant polymer reflow is triggered. On

the other hand, during the evaporation deposition process, the high temperature evaporated source atoms would increase the surface temperature of PLGA above its T_g , resulting in the irregular metal structures as observed in Figure 2.4.

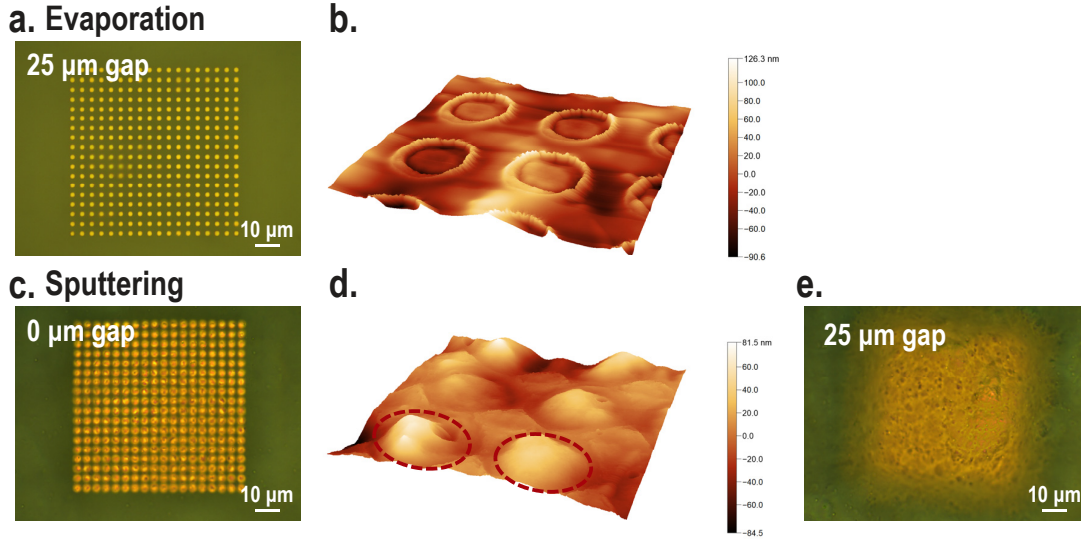


Figure 2.6: **Comparison between the evaporation and the sputter deposition results on PLGA substrates.** **a.,b.** Optical and AFM images showing the evaporation deposition results with a gap distance of $25\ \mu\text{m}$ between the stencil and the substrate. **c.,d.** Optical and AFM images showing the sputter deposition results with zero gap distance between the stencil and the substrate. The red circles in d. indicate the deposited metal squares (i.e., the regions where the stencil apertures are). **e.** Optical image showing the sputter deposition results with a gap distance of $25\ \mu\text{m}$ between the stencil and the substrate. The resulting structure is seriously blurred due to the random trajectory of sputtered source atoms.

Electrical characterization

Next, we characterize the electrical properties of metal films deposited on different polymer substrates using SL. The measured structure contains 4-point probe patterns having a width of $10\ \mu\text{m}$ and lengths of 50, 100 and $150\ \mu\text{m}$. The measurement follows the conventional 4-point probe method to eliminate the contact resistance. A constant current is applied on the outer two pads and a voltage drop is measured on the inner two pads. Resistivity values are calculated by considering the deposited metal geometry (width, length and thickness) measured by optical microscope and AFM. Here, the contribution of Cr to the electrical conductance is neglected in the calculation because the thickness of Cr (5 nm) is 10 times thinner than Au (50 nm) and Cr is 6 times more resistive than Au (the resistivity of Cr and Au are $0.12\ \Omega\cdot\mu\text{m}$ [170] and $0.02\ \Omega\cdot\mu\text{m}$ [171], respectively). The characterization results show similar resistivity values of Au films deposited on different polymer substrates (Figure 2.7). The extracted resistivities are 0.036 ± 0.001 , 0.037 ± 0.001 , 0.042 ± 0.002 , 0.041 ± 0.001 and $0.043\pm0.001\ \Omega\cdot\mu\text{m}$ for SiN, PI, PPA, parylene C and PLGA substrates, respectively. The measured resistivity values are all

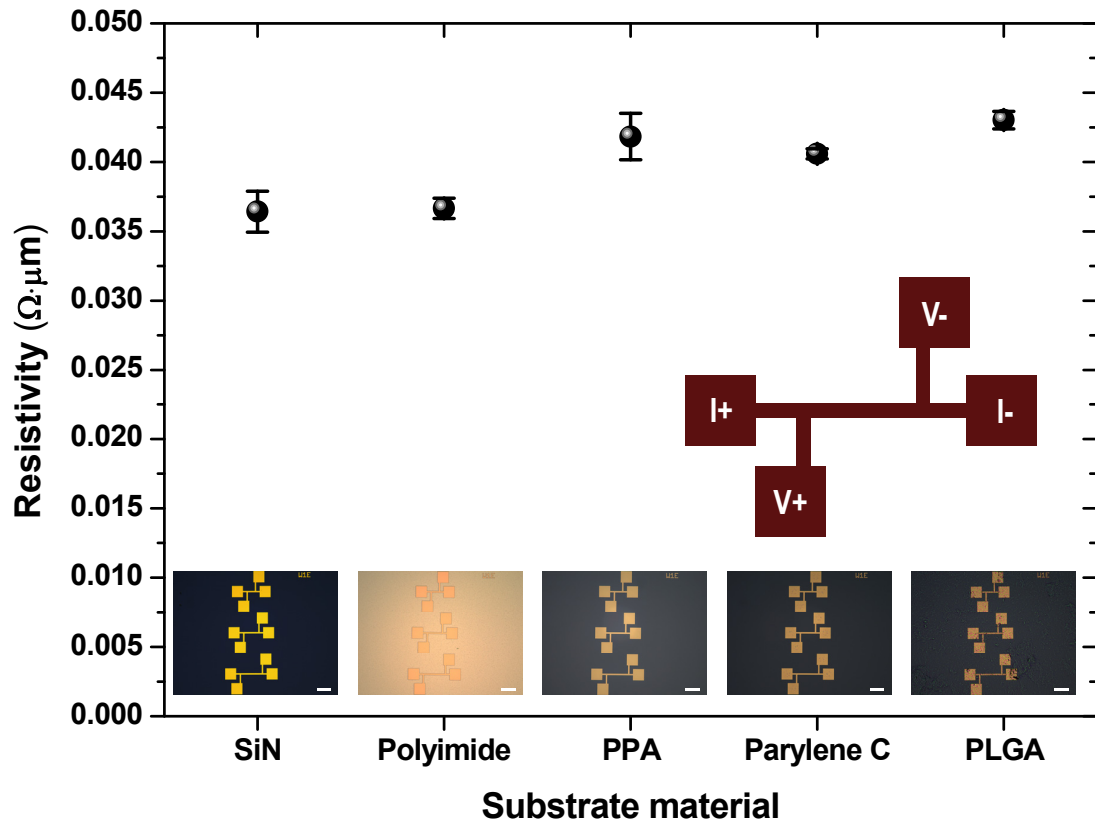


Figure 2.7: **Resistivity characterization of Au films deposited on different polymer substrates.** The extracted resistivity values of Au films on different substrate materials. Error bar presents the standard deviation from more than 8 data sets. Insets show the corresponding optical images of the fabricated 4-point probe structures and the schematic drawing of the placement of measurement probes. Scale bar: 100 μm .

higher than the reported thin Au film value ($0.02 \Omega \cdot \mu\text{m}$ [171]). The deviation might come from the used deposition method and tools, which would lead to different grain sizes and result in different resistivity values. It is worth mentioning that the extracted resistivity value of Au on PLGA substrates is close to the values on the other substrates, indicating that the observed irregular metal patterns on PLGA substrates do not influence the electrical functionalities.

2.3 Conclusion

In this chapter, we present the implementation of stencil lithography on a wide range of polymer substrate materials, including biocompatible PI, parylene C to biodegradable PLGA and metastable PPA. The geometries of deposited metal structures are probed using optical microscope and AFM. The results reveal the successful fabrication of metal patterns on various polymer substrates without damage. The minimum resolution presented here is $2\text{ }\mu\text{m}$ but can be further improved using nanostencils fabricated with DUV or EBL. The observed irregular metal patterns on PLGA substrates are hypothesized to result from polymer reflow during the evaporation deposition process. The evaporated metal source atoms heat the PLGA surface above its T_g , leading to the local reflow of the polymer. Additional experiments using the sputter deposition method provide certain observations to support the proposed hypothesis. Electrical characterizations show similar resistivity values of Au films deposited on all the used polymer substrates. The results indicate that the observed irregular metal patterns on PLGA substrates do not influence the electrical functionalities. Here, we report on a case study of using Au films having a thickness of 50 nm. The presented results can be generalized for different kinds of metals that can be evaporation deposited on substrates. The thickness of metal films is limited by the mechanical robustness of the suspended membranes in stencils and the clogging of stencil apertures. Based on our experimental results, the stencils remain intact after the deposition of 150 nm-thick Au films on substrates. The study reported in this chapter lays a solid foundation for the realization of wearable or transient devices using simple and cost-efficient resistless stencil lithography.

3 Bridge stencil enabling high resolution arbitrarily shaped metallic thin films on polymer substrates

Disclaimer: This chapter (3) is adapted from the following article with permissions of all co-authors and journal:

Y.-C. Sun, G. Boero and J. Brugger, "High resolution meandering metal patterns enabled by nano-bridge stencil", *47th international Conference on Micro and Nano Engineering (MNE2021)*, Turin, Italy, September 20-23, 2021.

Y.-C. Sun, G. Boero and J. Brugger, "Nanobridge stencil enabling high resolution arbitrarily shaped metallic thin films on polymer substrates", *In preparation*

My contribution: conceptualization, design, fabrication, experiments, figures and writing.

This chapter aims to present a new bridge stencil concept to address the limitation in the geometrical design flexibility of stencils. The concept of bridge stencil is introduced, followed by discussing the strategy of applying narrow bridges to stabilize the suspended membrane. Next, the fabrication of micro- and nanobridge stencils and the characterization of the resulting metal structures are presented.

3.1 Introduction

In the conventional approach to the design of stencils, the apertures in the membrane cannot have an arbitrary geometry. For example, close-loop apertures (e.g., O shapes) in stencils are practically not possible due to the lack of supports in the remaining membrane structures (Figure 3.1a). Applying SL in a dynamic mode where the stencil moves with respect to the substrate during the deposition process allowed the production of close-loop patterns [129, 172]. However, dynamic SL leads to a huge waste of materials, making it not cost-efficient. In addition, the residual stress built up during the stencil fabrication process results in membrane bending after it is released from the Si substrate (Figure 3.1b). The membrane bending results in an inaccurate pattern definition of the material deposited on the substrate. Therefore, structures such as meanders and long slits aiming for an accurate pattern definition using SL are practically not possible. These challenges constrain the geometrical design flexibility of SL and set a limit on potential applications. Strategies applied to solve these challenges focused on increasing the cross sectional moment of inertia of stencil membranes by incorporating additional Si supports [173, 174] or introducing corrugations [175, 176]. However, the reported methods require additional fabrication steps and relatively complicated patterns such as spiral and meandering patterns have not yet been demonstrated. Another strategy involves the use of bridges to connect isolated islands to enable doughnut-shape-like apertures on stencil membranes. Using bridges having a width in the range from 5 to 35 μm , various close-loop metallic structures were realized on Si substrates [177].

Here, we report on the extended use of bridges to overcome the limitation of geometrical design flexibility of stencils to realize high resolution arbitrarily shaped metallic patterns on a variety of polymer substrate materials. Comparing to the previous literature [177], we demonstrate the use of narrower bridges (1 μm and 250 nm) to enable high resolution metallic patterns. Additionally, we study the use of bridge stencils not only on biocompatible but also on biodegradable polymer substrates, enabling devices for wearable and implantable applications. The bridge stencils presented here utilize uniformly distributed bridges on stencils to stabilize the freestanding membranes, thereby enabling a variety of aperture openings (Figure 3.1a,b). The suspended membrane is bounded to remain in the same plane as the surrounding membrane by narrow bridges. The applied narrow bridges allow not only the realization of conventionally unfeasible geometries on stencils (e.g., close-loop apertures) (Figure 3.1a), but also the suppression of membrane bending for meandering apertures (Figure 3.1b). The blurring effect, which has long been a disadvantage in SL is converted into a solution for creating continuous material traces. By lifting the stencil at an appropriate gap distance above the substrate, the enhanced blurring effect leads to the material deposition under the shadowed bridge region (Figure 3.1c). Due to the line-of-sight evaporation process, high resolution patterns can be produced by properly designing the gap distance between the stencil and the substrate (Figure 3.1d). As demonstrative examples, we fabricated continuous spiral structures at the micrometer scale and meandering structures at the sub-micrometer scale on both rigid and soft substrate materials. The geometrical and electrical characteriza-

tions demonstrate the success of applying bridge stencils for direct fabrication of functional metal structures on a variety of substrate materials, an important step towards the use of this approach for the fabrication of soft and implantable devices with resolution down to sub-micrometer range.

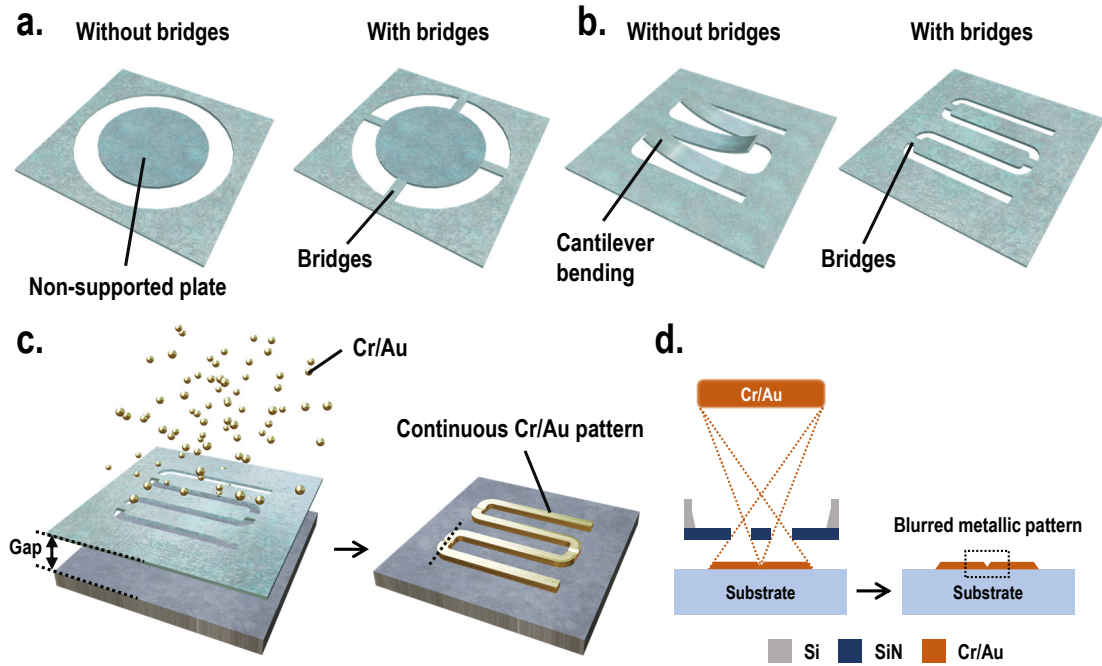


Figure 3.1: The concept of bridge stencils and the blurring effect. **a.,b.** Schematic drawings showing the use of bridges for **a.** realizing close-loop circular apertures and **b.** suppressing the bending of cantilevers for meandering apertures. **c.,d.** Schematic drawing showing the beneficial use of the blurring effect. When the stencil is lifted at an appropriate gap distance above the substrate, the blurring effect resulting from the line-of-sight evaporation process causes material deposition under the shadowed bridge region. The black dashed line indicates where the cross-section profile is extracted.

3.2 Results and discussions

In the following, we report and discuss the results of experiments performed to demonstrate the key features of the proposed bridge stencil approach. The experiments have been performed with stencils having features down to 1 μm (microbridge stencil) and down to 250 nm (nanobridge stencil).

3.2.1 Microbridge stencil

We begin by investigating the effects of applying narrow bridges as a countermeasure to the stress built up on stencil membranes using a cantilever as a proof structure. After a film is deposited on a cantilever, the cantilever is subjected to bending due to stresses built on the structure. The origin of the stresses is mainly from the CTE differences and the lattice mismatch of materials. In a bilayer structure, the stress can be estimated by measuring radius of curvature of the structure using the Stoney's equation as shown in Equation 3.1, where σ is the stress, R is the radius of curvature of the structure, E is the Young's modulus, t is the thickness and ν is the Poisson's ratio. The subscripts s and f indicate the substrate and the film, respectively. The quantitative estimation of the stress-induced bending of a bilayer cantilever can be derived using Equation 3.2, where δ is the bending of the cantilever and l is the length of the cantilever. Substituting Equation 3.2 into the Stoney's equation, the bending of the cantilever can be obtained in Equation 3.3 [178]. Larger cantilever bending arises when a film having large thin film stress is deposited on the structure. The bending also increases with a longer cantilever.

$$\sigma_f = \frac{1}{6R} \frac{E_s t_s^2}{(1 - \nu_s) t_f} \quad (3.1)$$

$$\delta = \frac{l^2}{2R} \quad (3.2)$$

$$\delta = \frac{3\sigma_f(1 - \nu_s) t_f l^2}{E_s t_s^2} \quad (3.3)$$

We fabricate on stencils several cantilevers having a width of 15 μm and lengths ranging from 50 to 900 μm with and without microbridges (Figure 3.2a). The stencil used here consists of freestanding 500 nm-thick LS-SiN membranes supported by a Si frame. The fabrication starts from defining apertures on the front side LS-SiN, followed by backside etching of the Si to release the membrane. The microbridges having a width of 1 μm are placed at different

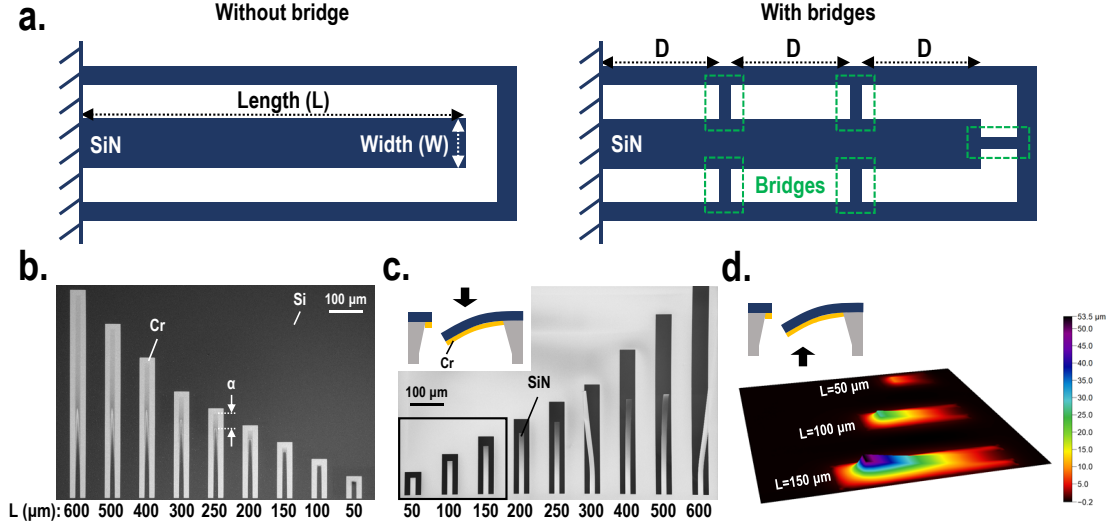


Figure 3.2: **Detailed microbridge study with cantilever stencils.** **a.** Schematic drawings showing the design of the cantilever stencils. **b.,c.** SEM images showing the deposition results of 25 nm Cr by cantilever stencils without bridges and the corresponding cantilever stencil images after metal deposition. A parameter α is defined as the length of the unwanted Cr structures deposited on a substrate due to the bending of cantilevers. **d.** Confocal image showing the bending of the cantilever stencil after metal deposition. Insets in c. and d. show the schematic drawings of the structures and arrows indicate the direction where the images are taken.

interdistances ranging from 25 to 900 μm (i.e., D shown in Figure 3.2a). To gain quantitative understanding of the efficacy of the bridge placement, we characterize the accuracy of the resulting patterns transferred through the apertures of cantilever stencils. The stencils are firstly placed in contact with a Si substrate, followed by evaporation deposition of 25 nm Cr. Here, Cr is selected to enhance the bending of cantilevers during the metal deposition because it is known to have a high thin film stress. In the experiment, the thin film stress of the deposited 25 nm Cr is about 2750 MPa, obtained by measuring the wafer curvature before and after metal deposition on a reference wafer. After Cr deposition and removal of the stencil, 60 nm of Si is etched using the deposited Cr as a hard mask to enhance the contrast of the resulting structures. As expected, using the stencil without bridges, we observe inaccurate pattern transfer of the membrane apertures, especially with longer cantilevers (Figure 3.2b). To quantify the accuracy of the transferred patterns, we define a parameter α , which is the length of the unwanted Cr structures deposited on the substrate due to the bending of the cantilevers. The SEM and confocal images indicate significant bending of the cantilevers after the deposition of a 25 nm thick Cr layer (Figure 3.2c,d). For example, bending of around 50 μm is observed on the 150 μm long cantilever. The measured bending of the cantilever is in agreement with the calculated values obtained using Equation 3.3 (Figure 3.3).

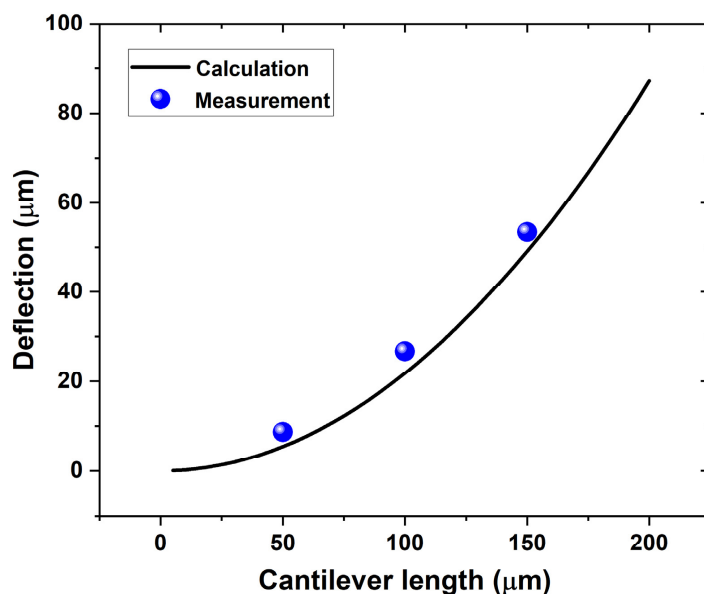


Figure 3.3: **Calculated and measured cantilever bending.** Cantilever bending calculated using Equation 3.3, assuming thin film stresses of 200 MPa and 2750 MPa for SiN and Cr, respectively. The thin film stress of SiN is obtained in Chapter 2.

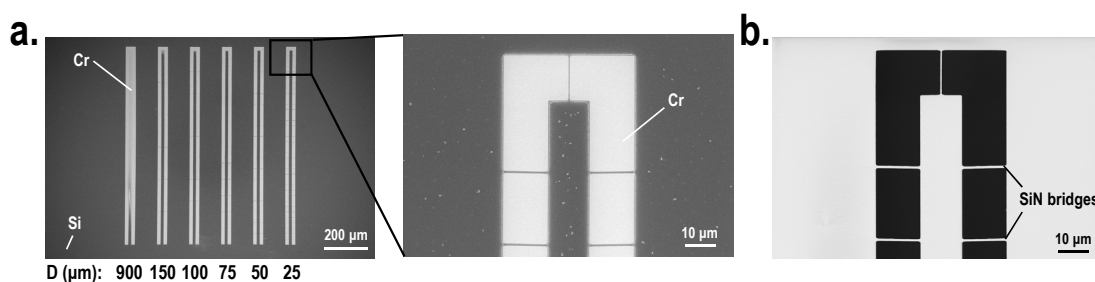


Figure 3.4: **Microbridge study with cantilever stencils having a width of 15 μm with bridges.** **a.** SEM images showing the deposition results of 25 nm Cr by cantilever stencils with bridges. The stencil contains cantilevers having a width of 15 μm and a length of 900 μm , supported by several bridges having different interdistances D . **b.** SEM image of the cantilever stencil having an interdistance D of 25 μm between the bridges after metal deposition.

On the other hand, with the stencil with microbridges, α is significantly reduced (Figure 3.4a). For instance, on the cantilever having a width of $15\text{ }\mu\text{m}$ and a length of $900\text{ }\mu\text{m}$, microbridges with an interdistance (i.e., D in Figure 3.2a) of $25\text{ }\mu\text{m}$ result in a value of α of less than $1\text{ }\mu\text{m}$. The SEM image also shows that the stencil remains intact after the metal deposition (Figure 3.4b). We apply the same design to cantilevers having a width of $50\text{ }\mu\text{m}$ and a length of $900\text{ }\mu\text{m}$. The results indicate that the $1\text{ }\mu\text{m}$ wide microbridges are capable of stabilizing the long and wide cantilevers (Figure 3.5). We observe that the bridge connected at the end of the cantilever is broken after the metal deposition. However, thanks to presence of other intact bridges, the value of α is less than $1\text{ }\mu\text{m}$ (Figure 3.5c,d). Wider cantilevers can be better stabilized by connecting more bridges at the end of the structures. To sum up, without microbridges, the fabricated cantilevers lead to significantly larger values of α on the deposited metal structures. The measured α can be up to $85\text{ }\mu\text{m}$ for the cantilever having a width of $50\text{ }\mu\text{m}$ and a length of $300\text{ }\mu\text{m}$ (Figure 3.6a). Whereas, by applying microbridges uniformly distributed across the cantilever structures, α is significantly reduced (Figure 3.6b). As expected, smaller values of α are observed with reduced interdistances between each bridge (i.e., more bridges in one cantilever) (Figure 3.6b). In the presented case, α can be reduced to less than $1\text{ }\mu\text{m}$ by having bridges placed at an interdistance of $25\text{ }\mu\text{m}$ across the $900\text{ }\mu\text{m}$ long cantilever. Moreover, we also investigate the limitations of the microbridge structure. Several microbridges with a width of $1\text{ }\mu\text{m}$ and lengths ranging from 80 to $500\text{ }\mu\text{m}$ are fabricated. The results show that bridges having a length of up to $500\text{ }\mu\text{m}$ are successfully fabricated without damage (Figure 3.7).

Chapter 3. Bridge stencil enabling high resolution arbitrarily shaped metallic thin films on polymer substrates

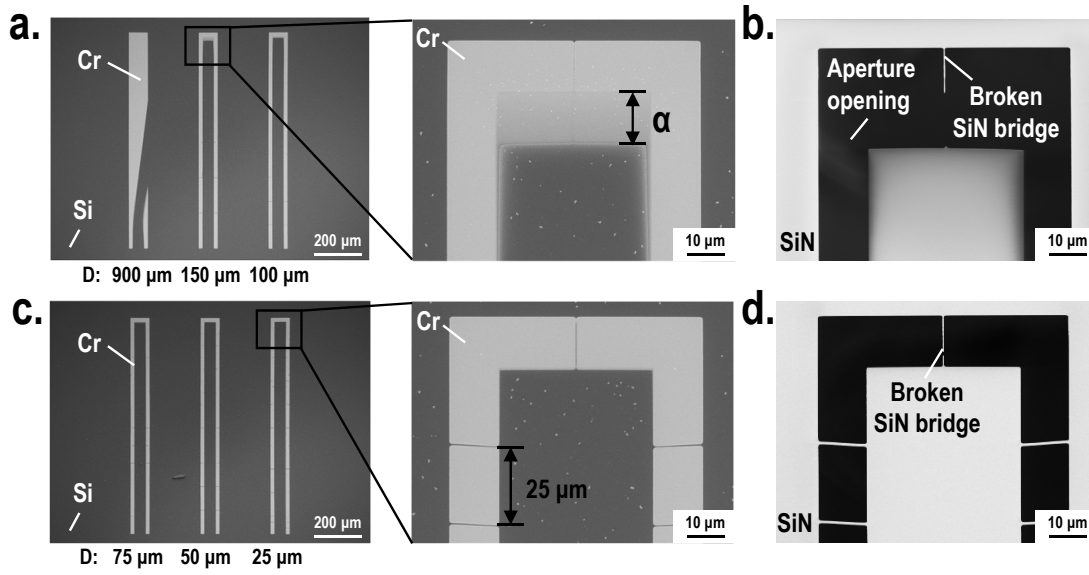


Figure 3.5: **Microbridge study with cantilever stencils having a width of 50 μm with bridges.** SEM images showing the deposition results of 25 nm Cr by cantilever stencils with bridges. The stencil contains cantilevers having a width of 50 μm and a length of 900 μm , supported by several bridges having a width of 1 μm and different interdistances D between each bridge. Magnified view of the SEM images showing the deposited 25 nm Cr by cantilever stencils having interdistances D of **a.** 150 μm and **c.** 25 μm between each bridge and **b.,d.** their corresponding stencils after metal deposition.

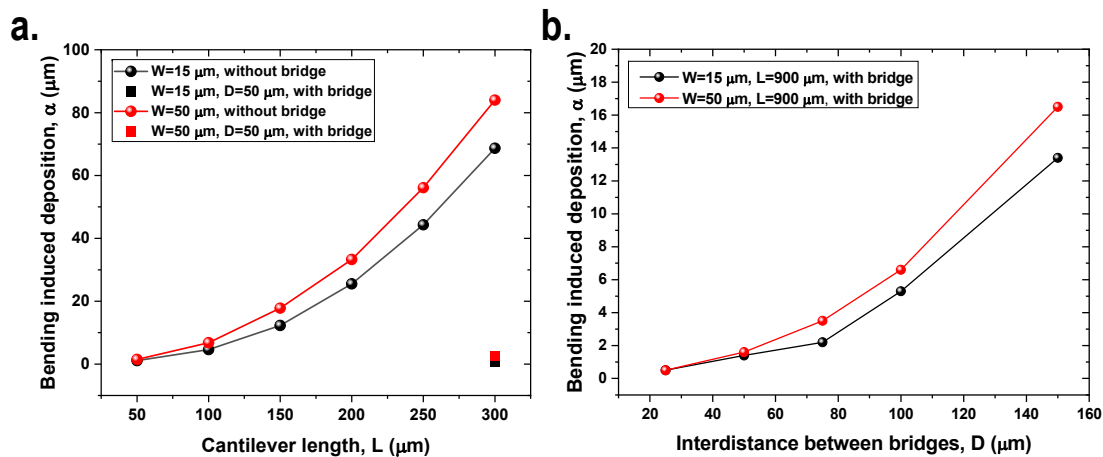


Figure 3.6: **Summary of bending induced deposition length α with cantilever stencils.** Bending induced deposition length α **a.** without and **b.** with microbridges. In **b.**, the length α is plotted as a function of the interdistances D between each bridge.

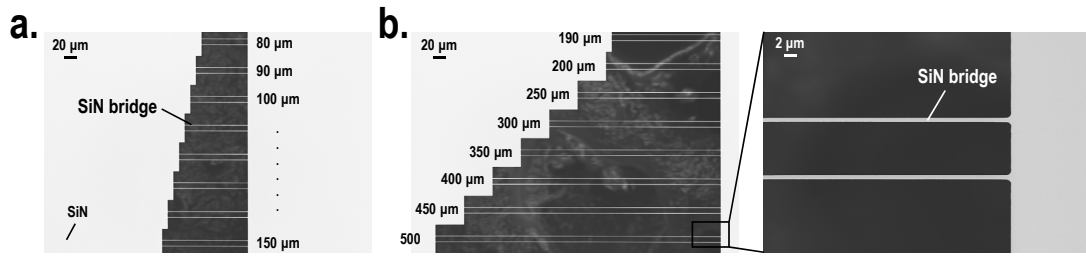


Figure 3.7: **SEM images of the fabricated bridges on stencils.** The stencils consist of several suspended bridges having a width of 1 μm and lengths ranging from 80 to 500 μm .

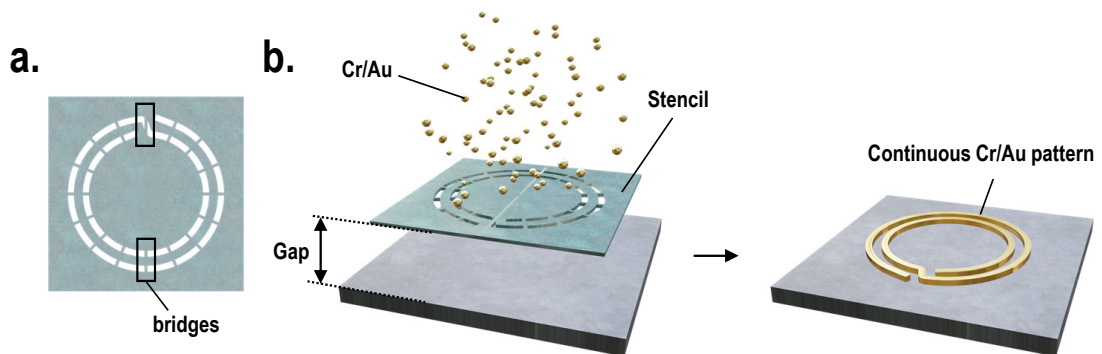


Figure 3.8: **Bridge stencil applied to the fabrication of spiral structures.** **a.** Schematic drawing illustrating the bridge stencil concept where several bridges are uniformly distributed on the suspended stencil membrane. **b.** Schematic drawings of the fabrication process. The stencil is lifted at a certain distance above the substrate, followed by evaporation deposition of Cr (5 nm) / Au (50 nm) on the substrate. Thanks to the blurring effect, the resulting metallic spiral is continuous.

Chapter 3. Bridge stencil enabling high resolution arbitrarily shaped metallic thin films on polymer substrates

As a proof of concept for the bridge stencil approach proposed here, we demonstrate a spiral structure, a geometry previously used as wireless heating elements for biomedical implants [179]. Microbridges with a width of $1\ \mu\text{m}$ uniformly distributed across the entire structure force the suspended membrane to remain in the same plane as the surrounding membrane (Figure 3.8a). Continuous patterns are achieved by taking advantage of the blurring effect, where the line-of-sight evaporation process results in the material deposition under the bridge shadow region when the stencil is placed at an appropriate distance from the substrate (Figure 3.8b). With the applied microbridges, stencils with spiral apertures are successfully fabricated and the confocal image shows that the membrane bending induced by the intrinsic stress is less than $1.5\ \mu\text{m}$ (Figure 3.9a,b). On the other hand, without microbridges, the membrane breaks during the membrane release process (Figure 3.9c). The fabricated stencil is placed on a Si substrate and lifted above the substrate to a gap distance of $70\ \mu\text{m}$, which is introduced by inserting a Kapton tape in between, followed by the evaporation deposition of $5\ \text{nm}$ Cr and $50\ \text{nm}$ Au onto the substrate. Here, a $70\ \mu\text{m}$ gap distance is chosen based on the calculated blurring length of $1.1\ \mu\text{m}$ (Equation 3.4 and Figure 3.10). In the presented case of a spiral structure, the parameters used for the calculation are listed as follows: $G = 70\ \mu\text{m}$, $S = 16000\ \mu\text{m}$, $A = 65\ \mu\text{m}$ and $D = 10^6\ \mu\text{m}$. The resulting blurring length is large enough to fill the shadowed bridge area. Next, $5\ \text{nm}$ Cr and $50\ \text{nm}$ Au are evaporation deposited onto the substrate. The optical microscope images show that the designed spiral structure is successfully obtained (Figure 3.11a). The SEM images indicate that the metals (Cr/Au) are deposited under the bridge area due to the blurring effect (Figure 3.11b). The measured width of the deposited structure without considering the halo of materials (i.e., the scattered particles) is about $67\ \mu\text{m}$, which is in agreement with the calculated value ($66.1\ \mu\text{m}$). The scattered particles are induced by the surface diffusion of the deposited materials [133]. In Equation 3.4, the blurring length is estimated based on the trajectory of the incoming flux of atoms in the line-of-sight evaporation process. Thus, the halo blurring due to material diffusion is not considered in the calculation. To measure the deposition profile under the bridge region, AFM characterizations are performed. The results indicate a metal thickness of about $55\ \text{nm}$ on the stencil aperture area and of about $25\ \text{nm}$ under the shadowed bridge region (Figure 3.11c-e). The measured thickness of the metals deposited through the aperture openings agrees well with the expected thickness value. The thinner layer obtained under the shadowed bridge region is expected due to the smaller flux of atoms arriving under the bridge area.

$$B_G = W_c - A = \frac{G(S + A)}{(D - G)} \quad (3.4)$$

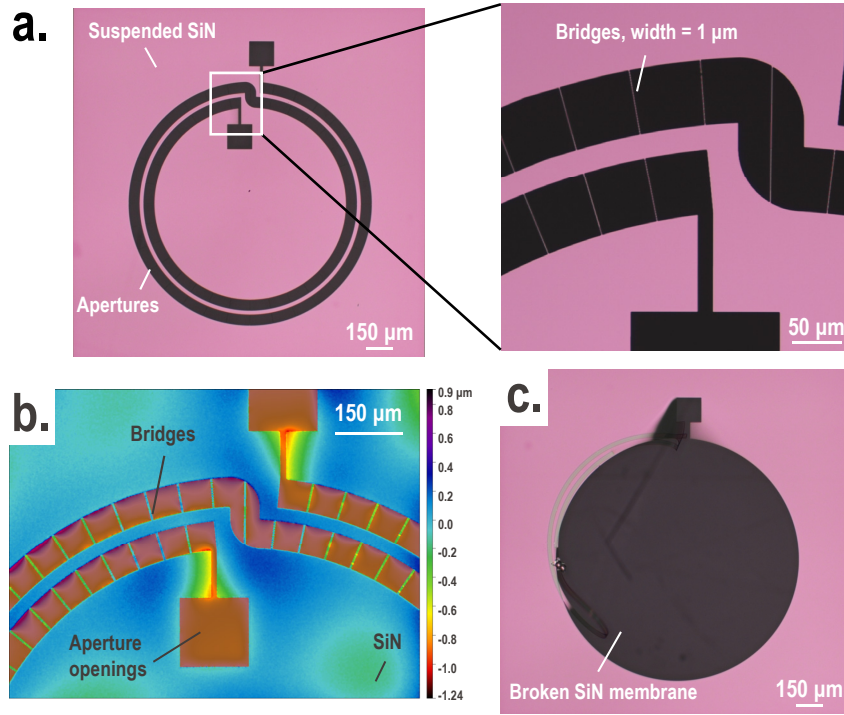


Figure 3.9: **Optical and confocal images of the released SiN stencils.** **a.** Optical and **b.** confocal images of the released stencil with bridges. **c.** Optical image of the released stencil without bridges. Without the supports of microbridges, the freestanding SiN membrane is damaged.

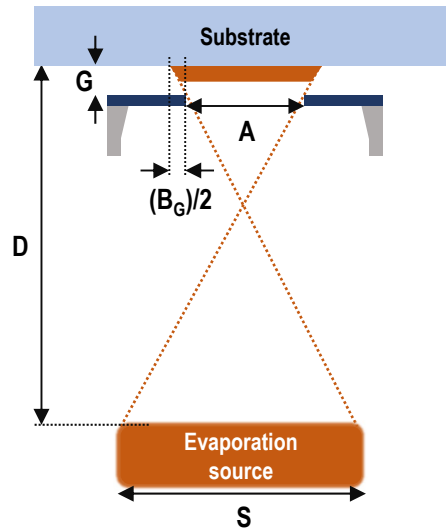


Figure 3.10: **Schematic drawing showing stencil lithography and the parameters.** Equation 3.4 showing the quantitative estimation of the blurring length, where G indicates the gap between the stencil and the substrate, S the size of the evaporation source, A the aperture size on stencil and D the distance between the evaporation source and the substrate.

Chapter 3. Bridge stencil enabling high resolution arbitrarily shaped metallic thin films on polymer substrates

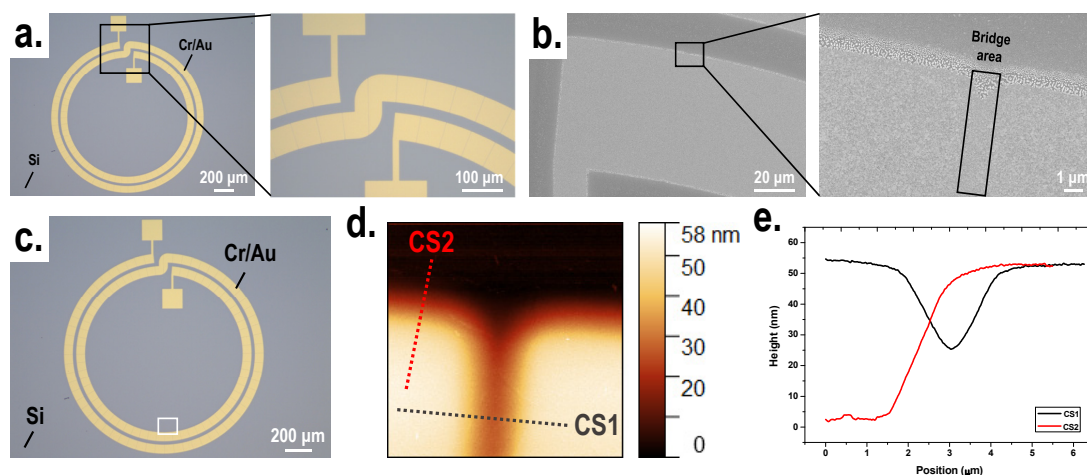


Figure 3.11: **The fabricated spiral structures on a Si substrate by using a microbridge stencil.** **a.,b.** Optical and SEM images of the deposited Cr/Au structures on the Si substrate. The SEM images clearly show that the material is successfully deposited under the shadowed bridge region due to the blurring effect. **c.-e.** AFM characterization results presenting the profile of the deposited metal structures. **c.** Optical image showing the sample used for AFM characterization. The white square indicates the region where an AFM image is taken. **d.,e.** AFM image and cross-section profile of the deposited structure along the dashed lines. A reduced thickness of about 25 nm is observed under the bridge region.

To validate the use of the proposed bridge stencil approach on a variety of substrate materials, we apply the bridge stencils on a biodegradable PLGA substrate. In Section 3.2.2, we will discuss experiments performed also on polyimide, PPA, and parylene C substrates. The stencil is attached to a PLGA substrate with a gap distance of $70\text{ }\mu\text{m}$, followed by evaporation deposition of 5 nm Cr and 50 nm Au. The optical images reveal that the spiral structures are successfully fabricated on the PLGA substrate (Figure 3.12a). Next, we perform electrical measurements not only on the PLGA substrate but also on a reference glass substrate to characterize the functionality of the deposited structures. The results show similar resistance values on both substrates with a value of $120\text{ }\Omega$ (Figure 3.12b). The measured resistance values are within 15% deviation from the calculated values, assuming gold resistivities of $0.036\text{ }\Omega\cdot\mu\text{m}$ on glass and $0.043\text{ }\Omega\cdot\mu\text{m}$ on PLGA and a cross-section of $3.3\text{ }\mu\text{m}^2$. The resistivity values of gold on different substrates are obtained in Chapter 2. The width and the thickness of the deposited metal lines are obtained by optical imaging and AFM, respectively. To demonstrate its applicability as heaters for biomedical implants, a meandering structure is incorporated in the spiral design, which produces a local hot spot due to the increased current density in the meander (Figure 3.12c) [179]. As a demonstration, an increasing voltage is applied as a heating source until electrical breakdown. It is observed that the device is burnt with an applied voltage of 6.5 V due to the damages in the incorporated meandering pattern (Figure 3.12d), which corresponds to a current density of $7.5 \times 10^{10}\text{ A/m}^2$. The optical images reveal that the incorporated meandering structure and the underlying PLGA surface are damaged due to the increased temperature (Figure 3.12e).

Chapter 3. Bridge stencil enabling high resolution arbitrarily shaped metallic thin films on polymer substrates

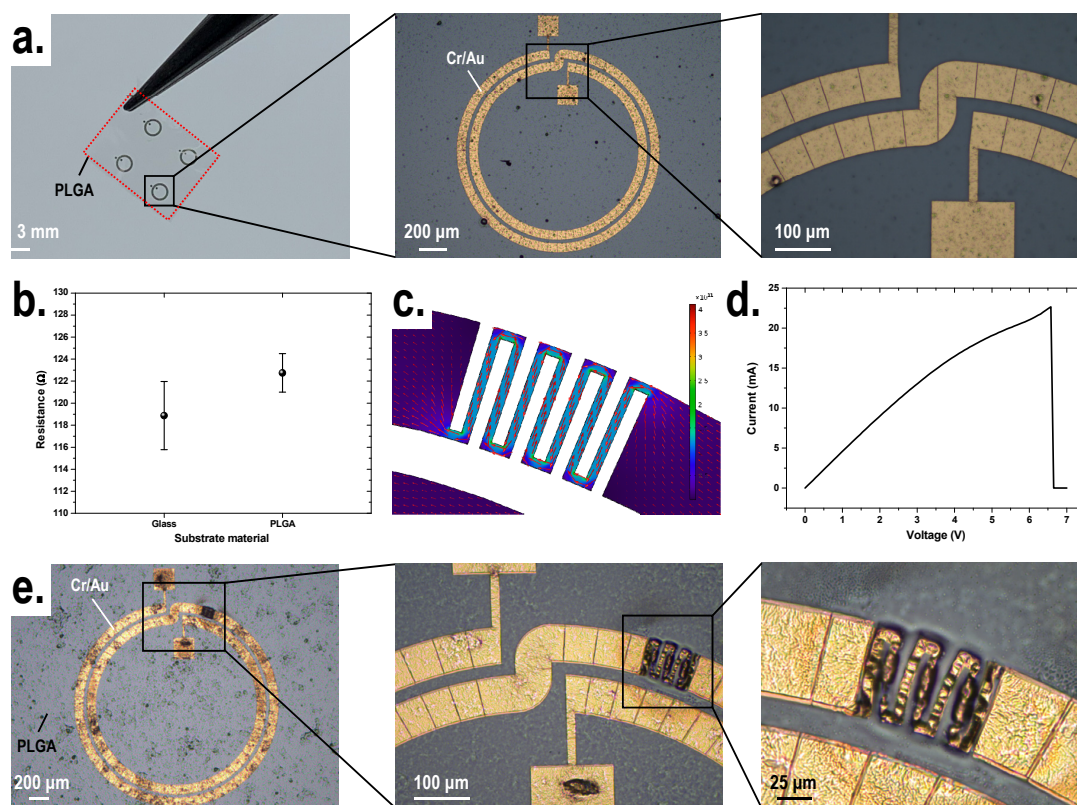


Figure 3.12: **Fabrication results on a biodegradable PLGA substrate.** **a.** Optical images showing the Cr/Au spiral structures on the biodegradable PLGA film. **b.** Resistance of the deposited structures on glass and PLGA substrates. Each data point contains measurement results from five nominally identical devices. The error bar represents the standard deviation. **c.** Finite element analysis indicating an increased current density on the incorporating meanders. **d.** IV curve showing an electrical breakdown at 6.5 V. **e.** Optical images showing the fabricated spiral structure device after being electrically damaged by applying a voltage of 6.5 V.

3.2.2 Nanobridge stencil

To take a step further, we scale down the proposed bridge stencil concept to the nanometer scale. A meandering pattern is demonstrated in this work as a proof of concept. The stencil used here contains 100 nm-thick LS-SiN membranes supported by a Si frame and nanoscale apertures are defined by a deep-ultraviolet (DUV) stepper. The rest of the fabrication process is the same as the one for microbridge stencils. The nanobridge stencil consists of meander apertures having a width of 350 nm and several 250 nm wide bridges uniformly distributed across the apertures. The membrane bending due to the intrinsic stress of the suspended SiN film is markedly reduced for the bridge stencil compared to the reference stencil without bridges (Figure 3.13a,c). The confocal images show that the SiN membrane with nanobridges is nearly flat, whereas the one without bridges has a bending of $2.5\ \mu\text{m}$ (Figure 3.13e). Additionally, in the highlighted region near the aperture openings, the bridge-supported stencil possesses a nearly flat membrane. In contrast, the one without bridge supports has a membrane bending of $0.5\ \mu\text{m}$, which would lead to an inaccurate pattern definition (Figure 3.13f). We then place the stencil in contact with a Si substrate, followed by evaporation deposition of 5 nm Cr and 50 nm Au. Using stencils without nanobridges, we observe irregular patterns due to the mechanical stress being built by the added metal layers. In contrast, the use of the nanobridge stencil allows for obtaining well-defined patterns (Figure 3.13b,d). To elucidate the blurring induced pattern enlargement, we perform the deposition with three different gap distances (0, 25 and $50\ \mu\text{m}$) on a SiN substrate. The SEM images indicate a width of the deposited metals of around 350, 650 and 950 nm for gap distances of 0, 25 and $50\ \mu\text{m}$, respectively (Figure 3.14), which is within 20% deviation from the calculated blurring lengths (Equation 3.4).

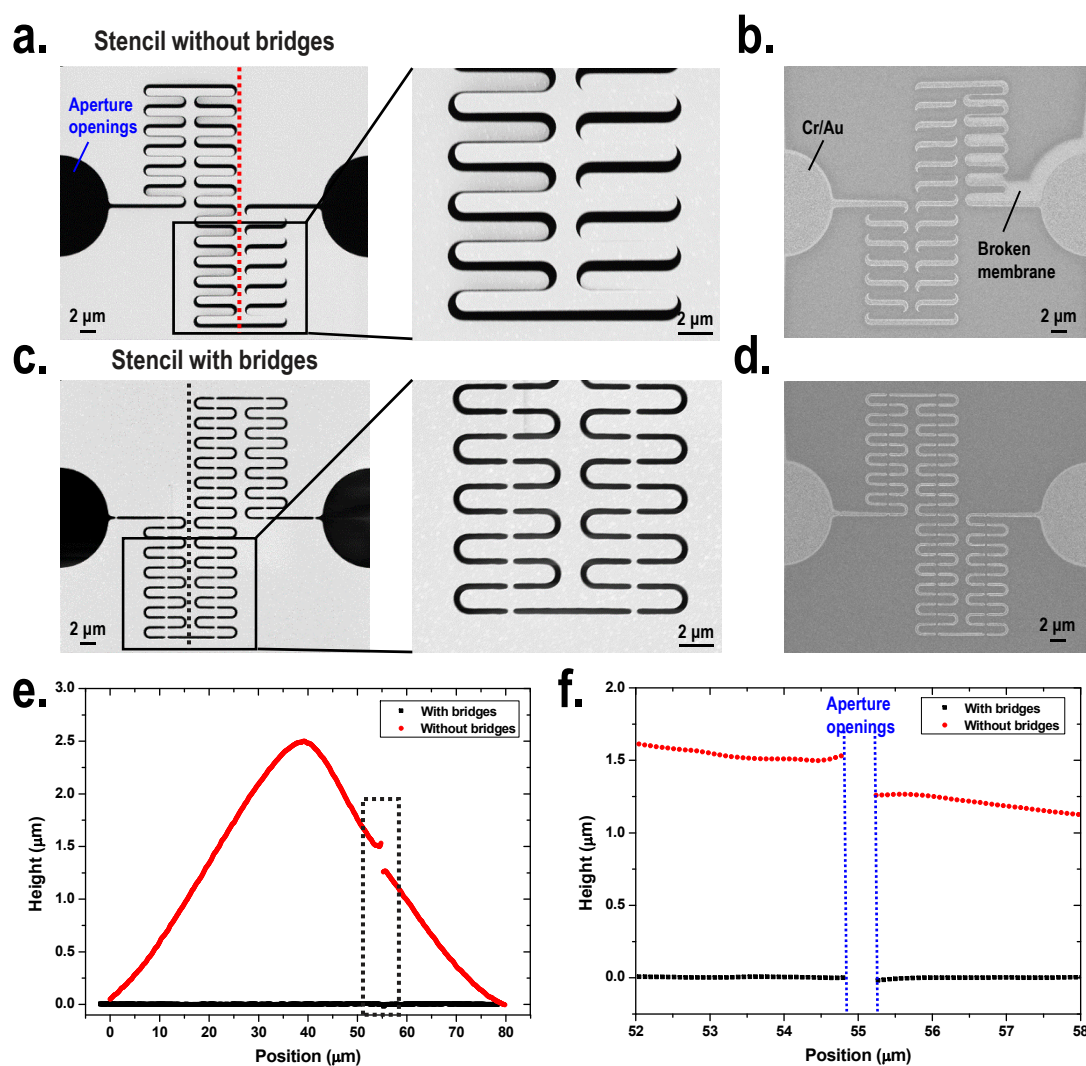


Figure 3.13: **Nanobridge stencil with meandering pattern.** SEM images showing the stencils **a.** without and **c.** with nanobridges and **b.,d.** their corresponding Cr(5 nm)/ Au(50 nm) deposition results on a Si substrate with zero gap distance. **e.** Stencil membrane bending measured by confocal microscopy along the dashed lines in **a.** and **c.** **f.** Zoom-in view of the dashed black rectangle in **e.**, highlighting the region where is located the aperture opening.

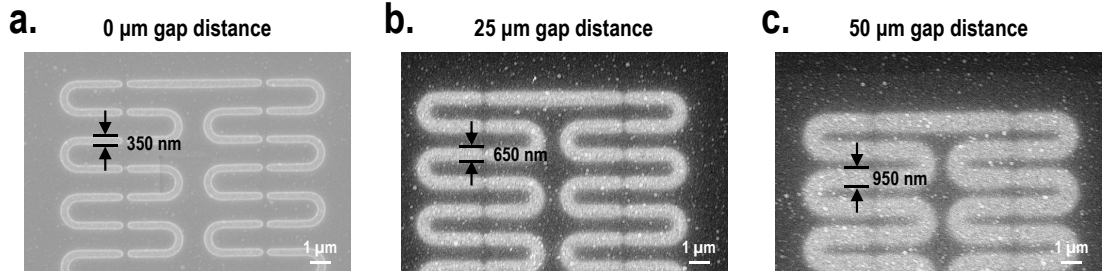


Figure 3.14: **Fabrication results on a Si substrate with different gap distances.** SEM images of the deposited Cr(5 nm)/ Au(50 nm) meandering patterns on a silicon substrate with different gap distances between the stencil and the substrate. The contrasts of image b. and c. are enhanced by postprocessing the original SEM images using a commercial image processing software (imageJ).

Noticeably, we observe a thickness reduction of the deposited metals not only under the bridges, but also in the regions under the aperture openings. The AFM images reveal thickness reductions of around 35% (i.e., 35 nm instead of 55 nm) and 70% (i.e., 15 nm instead of 55 nm) for gap distances of 25 and 50 μm , respectively (Figure 3.15). Meanwhile, no thickness reduction is observed in the large aperture opening regions (i.e., a square electrical pad having a side of 80 μm) (Figure 3.16). The phenomenon is attributed to the fact that when the stencil is lifted to a certain gap distance, it blocks a significant fraction of the incoming flux of atoms [133]. The different placement of stencils results in different effective source sizes, which influences the actual amount of atoms deposited on the substrate (Figure 3.17). The reduced amount of atoms reaching the substrate is mainly affected by the stencil/substrate distance, the source/substrate distance, the source size and the aperture openings in the stencil. The reduction can be approximately estimated by calculating the effective source size $S' = \frac{A \times D}{G}$, where A is the stencil aperture opening size, D is the substrate/source distance and G is the substrate/stencil gap. The equation is derived by considering the geometrical relation of the stencil and the line-of-sight trajectory of the evaporant. When the calculated effective source size is smaller than the evaporation source size, the substrate receives less atoms coming from the source, leading to less material deposited on it. Based on the equation above, we obtain 25% and 80% of area reduction in the effective source size using $1 - (\frac{S'}{S})^2$ for the cases of 25 and 50 μm gap distances, respectively. An accurate estimation of the thickness reduction remains challenging due to the difficulties in calculating the angular distribution of the evaporated atoms in the evaporation chamber. Furthermore, because the substrate is rotating during the evaporation deposition process to enhance the blurring effect, it makes this estimation even more challenging. Here, we aim at providing a rough estimation to explain the phenomenon of the observed thickness reduction. For the presented cases of 25 and 50 μm gap, the calculated effective source sizes are all smaller than the real source size of 16000 μm . Therefore, the observed thickness reduction in both cases is in agreement with the proposed hypothesis. The measured resistance is infinite for a metal pattern produced with the stencil placed in contact with the substrate (zero gap) and therefore having an interrupted metal film, and 1600 Ω and 1400 Ω for gap distances of 25 and 50 μm , respectively, where the

Chapter 3. Bridge stencil enabling high resolution arbitrarily shaped metallic thin films on polymer substrates

blurring has created a conducting path under the bridge shadow. Based on the deposited metal geometries measured by SEM and AFM, the measured resistance values are 45% higher than the calculated values, assuming a resistivity of $0.036 \Omega \cdot \mu\text{m}$ (Figure 3.18). The deviation presumably comes from the inaccurate estimation of the deposited metal geometries under the bridges.

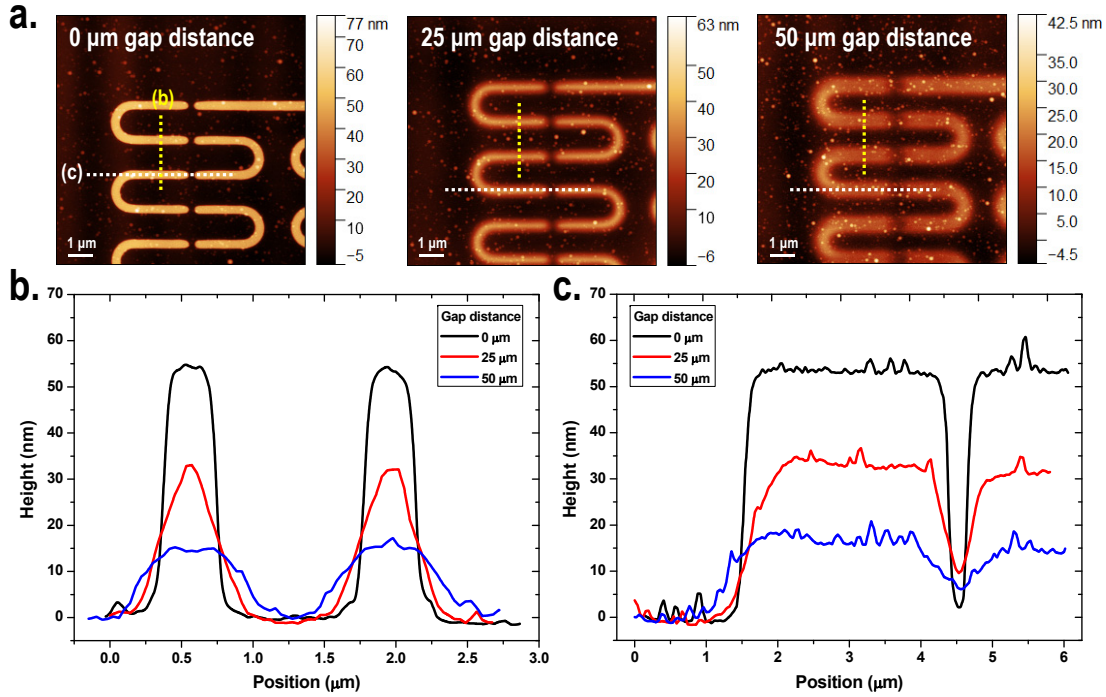


Figure 3.15: **AFM characterizations of the metal structures deposited through nanoapertures.** **a.** AFM images showing the meandering metal patterns deposited with gap distances of 0, 25 and 50 μm between the stencil and the substrate. The white and yellow lines indicate where the cross-section profiles are extracted. **b.,c.** Cross-section profile of the Cr/Au structures deposited with different gap distances between the stencil and the substrate.

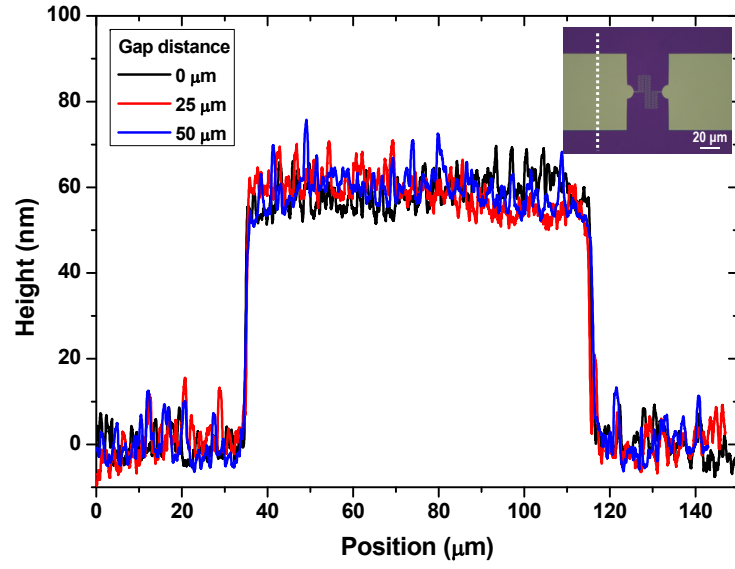


Figure 3.16: **AFM characterizations of the metal structures deposited through large apertures.** Cross-section profile of a large square electrical pad having a side of $80\ \mu\text{m}$. Inset shows the optical image of the deposited structure. The white dashed line indicates where the profile is extracted.

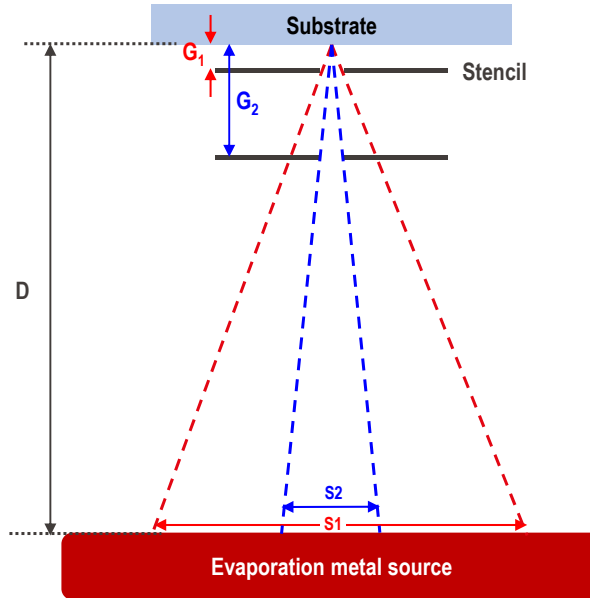


Figure 3.17: **Schematic drawing showing the varying effective evaporation source size.** Schematic drawing showing two effective evaporation source sizes (S_1 and S_2) resulting from the placement of the stencils above the substrate at different gap distances (G_1 and G_2).

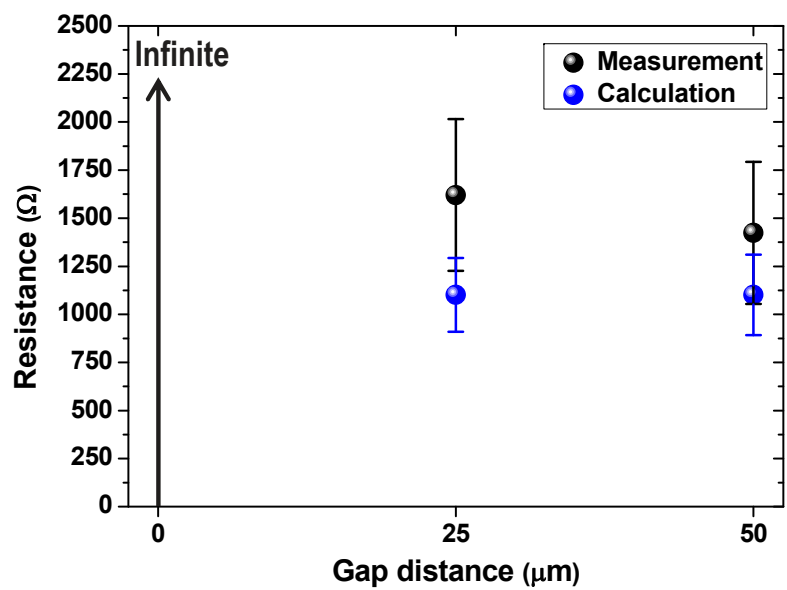


Figure 3.18: **Measured electrical resistance of the meandering metal patterns deposited by placing stencils at different gap distances.** The calculated resistance is obtained by assuming a resistivity value of $0.036 \, \Omega \cdot \mu\text{m}$. The error bar in the measurement indicates the standard deviation from at least seven nominally identical devices. The error bar in the calculation comes from considering $\pm 20\%$ of deviations in the effective cross-section of the metallic wire.

In the following, we apply the proposed nanobridge stencil on a wide range of substrate materials such as PI, parylene, PPA and biodegradable PLGA to underline its potential for a large variety of applications. 5 nm Cr and 50 nm Au are evaporation deposited on the polymer substrates with a fixed gap distance of 25 μm between the stencil and the substrate. The SEM images on the parylene and PLGA substrates clearly show that the metals are deposited not only on the stencil aperture regions but also under the shadowed bridge region due to the blurring effect (Figure 3.19a,b). SEM images of the deposited structures on the other substrates are presented in Figure 3.20. The fabricated meandering pattern having a line width of about 600 nm agrees well with the calculated blurring length. The AFM images show the geometries of the deposited metal structures on different substrate materials (Figure 3.21a). On PI, PPA, and parylene substrates, meandering patterns are successfully produced as expected. The rougher geometry observed on the parylene substrate comes from the roughness of the parylene layer after it is chemical vapor deposited on a bare Si substrate, as discussed in Chapter 2. Interestingly, we notice a different behaviour in the deposited metal structure on the PLGA substrate. The deposited metal is surrounded by a PLGA fence built during the evaporation deposition process. The cross-section view of the AFM images indicates that the deposited metals are inside the resulting PLGA channels (Figure 3.21b). The observed behaviour agrees well with the phenomenon presented in Chapter 2, which is attributed to the local reflow of PLGA due to the low T_g of PLGA and a high temperature of the evaporated source atoms. Last, the electrical characterization shows that similar resistance values are measured for all metal structures deposited on different polymeric substrate materials (Figure 3.21c). These results point out that the observed reflow behaviour on the PLGA surface has no significant influence on the electrical characteristics of the deposited metal structures, in agreement with the results presented in Chapter 2.

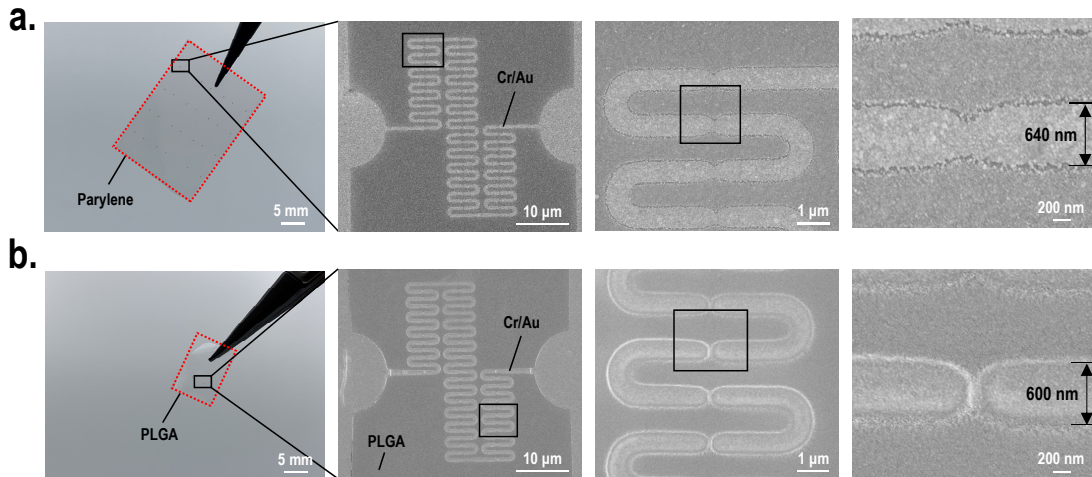


Figure 3.19: **SEM images of the fabricated meandering patterns on parylene and PLGA substrates.** Nanometer meandering patterns on **a.** biocompatible parylene and **b.** biodegradable PLGA substrates. The black squares show where the zoom-in images are taken.

Chapter 3. Bridge stencil enabling high resolution arbitrarily shaped metallic thin films on polymer substrates

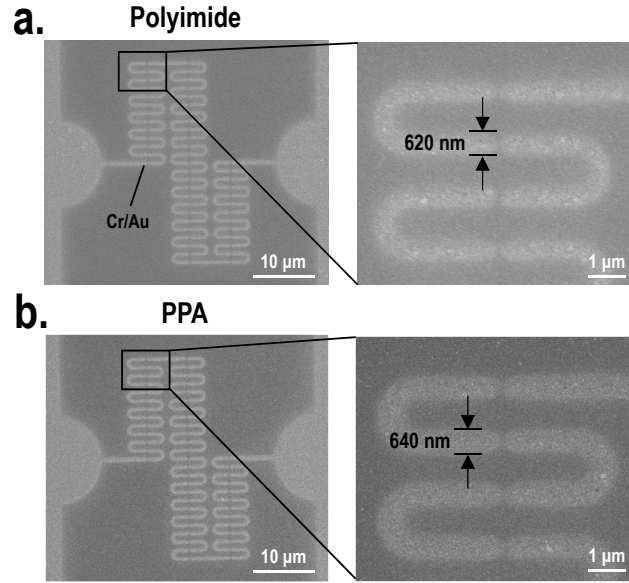


Figure 3.20: SEM images of the fabricated meandering patterns on PI and PPA substrates. Nanometer meandering patterns on **a.** PI and **b.** PPA substrates.

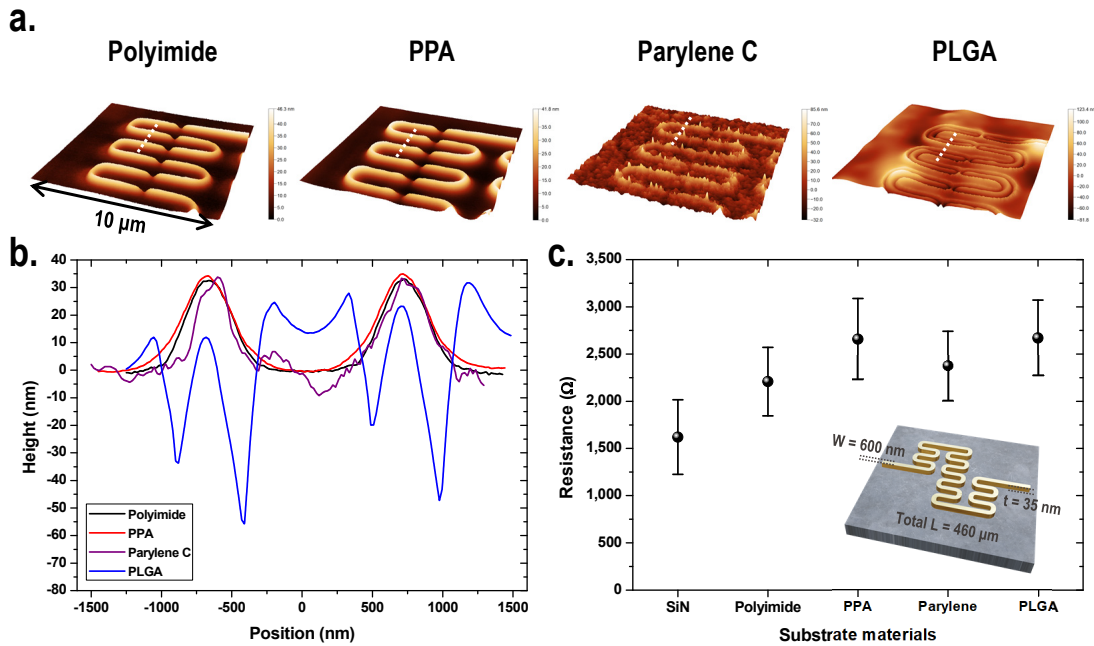


Figure 3.21: AFM images and electrical characterization results of the fabricated nanostructures on various polymer substrates. **a.** AFM images showing the geometries of the fabricated metal structures. **b.** Cross-section profile of the metal structures along the white dashed lines in **a.** **c.** Summary of measured electrical resistance values on different substrate materials. Each data point contains measurement results from at least ten samples. The error bar represents the standard deviation. Inset shows the schematic drawing of the meandering patterns and the corresponding dimensions.

To elaborate on the reflow behaviour observed on PLGA substrates, we perform additional experiments with different evaporation deposition parameters, including an increased target thickness and a reduced deposition rate. Both parameters lead to an increased deposition time, thereby increasing the level of thermal treatment on the PLGA surface. 3D view of the AFM images indicates the different profiles of metal structures deposited under different deposition parameters (Figure 3.22a). Cross-section views detail different levels of polymer reflow when the PLGA surface is exposed to the evaporated source atoms for a different amount of time (Figure 3.22b). For the deposition performed at the same deposition rate but longer deposition time (i.e., a thicker thickness), a deeper trench is obtained. Especially, under a deposition rate of 0.5 \AA/s (i.e., a quarter of the others), a much deeper trench is observed. The different profiles of the resulting patterns are attributed to different amounts of thermal energy transferred from the evaporated metal source to the substrate. More prolonged exposure of the PLGA surface to the evaporated source atoms results in more significant reflow behaviour (e.g., under a deposition rate of 0.5 \AA/s). The electrical characterization results show a slightly smaller deviation from the calculated value when a thicker structure is deposited on the substrate (Figure 3.22c), but no significant improvement is observed. It is noted that no conductive sample is obtained using a deposition rate of 0.5 \AA/s . The results show that the observed irregular metal patterns on PLGA substrates might result from the high temperature evaporated material flux. Different geometries of structures are obtained when the PLGA surface is exposed to the evaporated source atoms for a different amount of time. Longer exposure to the evaporation source increases the surface temperature of PLGA and induces local reflow behaviour under stencil aperture regions.

Chapter 3. Bridge stencil enabling high resolution arbitrarily shaped metallic thin films on polymer substrates

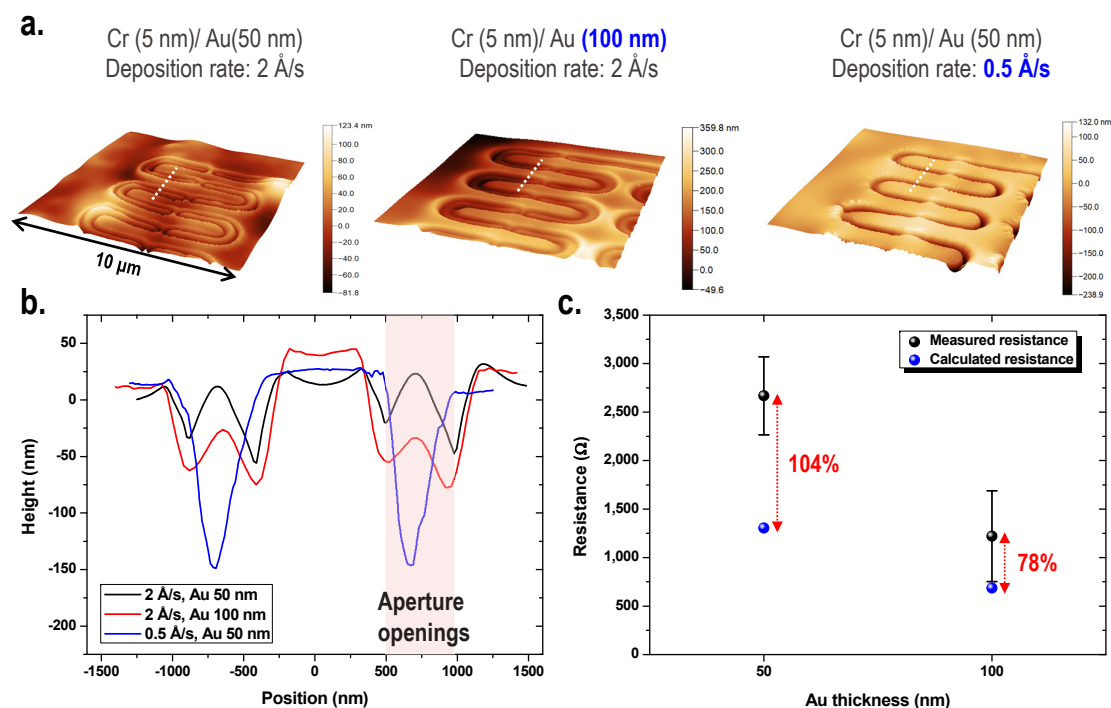


Figure 3.22: **Meandering patterns deposited on PLGA substrates under different evaporation deposition parameters.** **a.** 3D AFM images showing the deposited structures under different deposition parameters, including an increased deposition thickness and a reduced deposition rate. **b.** Cross-section view of the structures along the white dashed lines in **a**. More prolonged exposure of the PLGA surface to the evaporated source atoms leads to a deeper trench. **c.** Electrical characterization results of the meandering patterns with different Au thicknesses deposited at the same deposition rate. No conductive sample is obtained using a deposition rate of 0.5 Å/s.

Next, to demonstrate the potential application of fabricated nanomeandering patterns as implantable heaters, an increased voltage is applied as a Joule heating source. The results show that the meandering pattern fabricated on a PLGA substrate experiences an electrical breakdown at an applied voltage of 3.7 V, which corresponds to a maximum current density of about $6.5 \times 10^{10} \text{ A/m}^2$ (Figure 3.23a). The temperature is then extracted by converting the measured resistance value to the temperature using Equation 3.5, where α is the temperature coefficient of resistivity (TCR). The results indicate a maximum temperature of about 120 °C on the fabricated meandering pattern by considering a TCR of Au of 0.003 /°C (Figure 3.23b). Even though the structures presented here are made of biocompatible Au, the proposed nanobridge stencil can also be used to pattern biodegradable metals such as Mg to realize a fully biodegradable system.

$$R = R_0[1 + \alpha(T - T_0)] \quad (3.5)$$

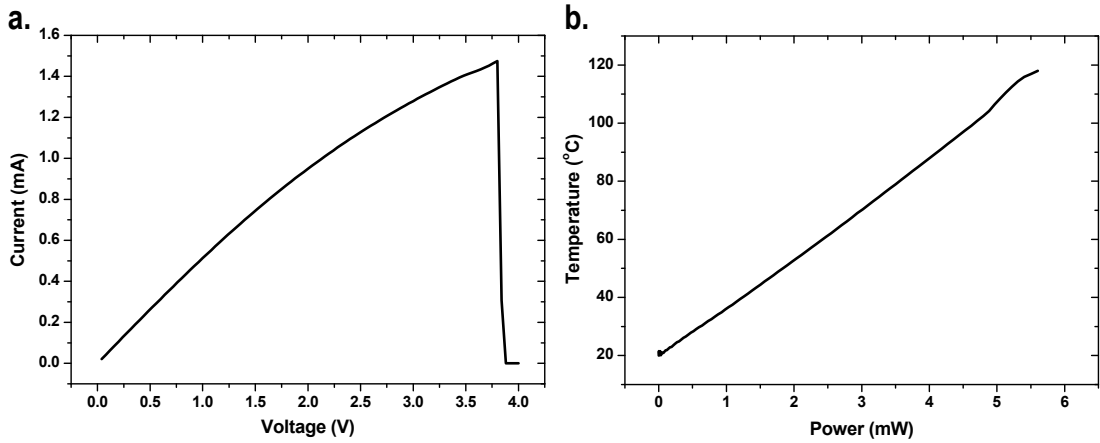


Figure 3.23: **Demonstration of the use of nanoscale meandering patterns as heaters.** **a.** IV curve showing an electrical breakdown at 3.7 V on the metal patterns fabricated on a PLGA substrate. **b.** Calculated power/temperature relation. A maximum temperature of about 120 °C is achieved on the device by Joule heating.

Lastly, we apply the proposed nanobridge stencil on a stretchable substrate composed of materials with different stiffness. By having stiffness gradients on a polymer substrate, the substrate is capable of sustaining a much larger strain before delamination occurs [180, 181]. The functional device fabricated on the material having the highest stiffness is insensitive to strain and thus can be decoupled from the strain influence and remains functional under large deformation [182]. Taking advantage of the controllable stiffness of PDMS, two types of PDMS prepared with ratios of 5:1 and 20:1 between PDMS base and curing agent are used as the first level of material gradients. A commercial Kapton film is applied on the top as the stiffest layer, where metal structures are deposited (Figure 3.24a). To realize such substrates, two types of PDMS are assembled by placing a semi-cured 5:1 PDMS cube on a non-cured 20:1

Chapter 3. Bridge stencil enabling high resolution arbitrarily shaped metallic thin films on polymer substrates

PDMS surface, followed by baking the assembled substrate at 80°C for 2 hrs. Subsequently, a Kapton film whose backside is sputter deposited with Ti/SiO₂ is bonded to the assembled PDMS substrate by activating the bonding interfaces with UV-ozone for 3 mins. The bonded substrate is then subjected to 2 hours of baking at 80 °C (Figure 3.24b). A stretching test on a reference sample demonstrates the excellent strain isolation capability of the fabricated substrate. The Kapton film is not stretched and no delamination is observed under an applied global strain of 45% (Figure 3.24c). Next, a nanobridge stencil is placed on the top of the Kapton surface with a gap distance of 25 μm between the stencil and the surface. Then, 5 nm Cr and 50 nm Au are evaporation deposited on the substrate.

An optical image details the composition of the fabricated stretchable substrate, consisting of two PDMS layers having different rigidity and a Kapton film. A SEM image indicates that nanomeandering patterns are successfully fabricated on the Kapton surface (Figure 3.24d). An electrical characterization result verifies that a continuous metal trace is produced on the substrate with a resistance value of about 1800 Ω (Figure 3.24e). In order to demonstrate the ability to sustain mechanical deformation, two big droplets of EGaIn are administered to the large electrical pads at both ends of the meandering pattern. Cu wires are inserted into the EGaIn droplets and covered with RTV silicone sealant (734, Dow Corning). After curing the silicone sealant at room temperature for 4 hours, the device is clamped on a commercial stretcher with a movable jar moving in one direction. The electrical resistance is measured at a sampling rate of 1 s. The measurement results from the produced 3 samples show minor resistance changes with applied strains up to 45%, which features the strain isolation characteristic of the produced stretchable gradient substrate (Figure 3.24f). The observed unstable changes in the measured resistance might be due to the poor fixation between Au pad, EGaIn and Cu wires and inadequate adhesion between the Kapton film and PDMS, contributing to non-negligible measurement noise. However, the results indicate that the device can sustain strain to at least 45% without electrical failure. The results reported here are a proof of concept demonstrating the possibility of realizing nanoscale features on a stretchable substrate with stiffness gradients using the proposed nanobridge stencil.

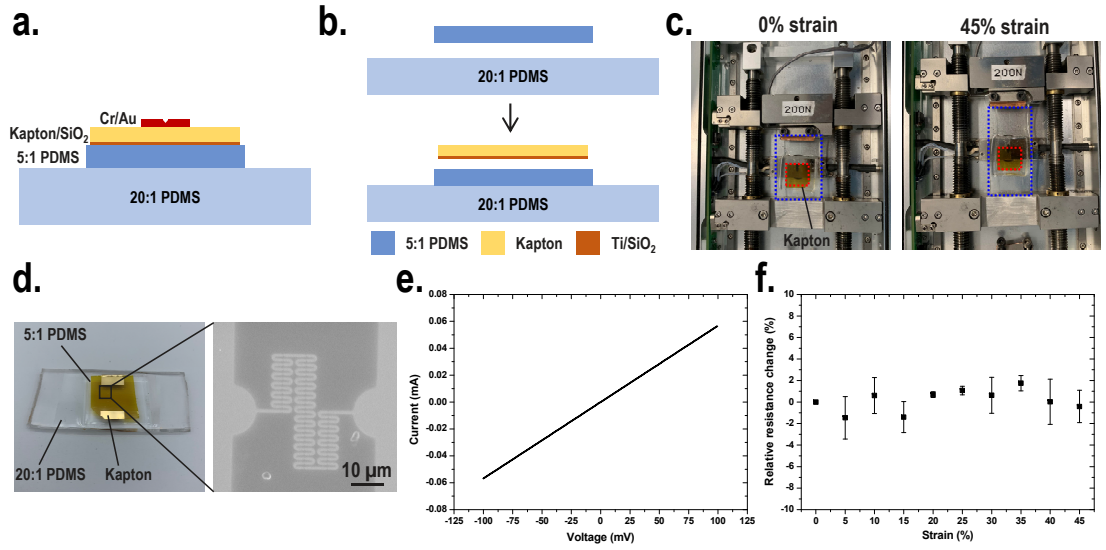


Figure 3.24: **Demonstration of the use of nanobridge stencil on a stretchable substrate with stiffness gradients.** **a.** Schematic drawing showing the cross-section of the fabricated Cr/Au patterns and a stretchable substrate with stiffness gradients. The substrate contains two types of PDMS having different rigidity and a Kapton layer. **b.** The fabrication process for a stretchable substrate with stiffness gradients. **c.** Stretching test on a reference sample with an applied global strain of 45%. The Kapton film is not stretched and no delamination is observed due to the presence of the stiffness gradients. The blue dashed square indicates the fabricated stretchable substrate and the red dashed square shows the Kapton film. **d.** Optical and SEM images of the nanoscale meandering patterns on the substrate. **e.** IV curve showing that a continuous metal trace is successfully produced. **f.** Demonstration of the strain isolation capability of the fabricated devices. Error bar shows the standard deviation of the measured 3 samples.

3.3 Conclusion

This work demonstrates a bridge stencil concept for the realization of complex, continuous metallic patterns on various substrate materials. The suspended membrane is bounded to remain in the same plane as the surrounding membrane by bridges uniformly distributed across the stencil, which enables the realization of complex aperture openings on the free-standing stencil membrane. Continuous metallic patterns are achieved by taking advantage of the blurring effect, obtained by introducing an appropriate gap between the stencil and the substrate. The effects of applying narrow bridges to stabilize suspended membranes are detailed by characterizing the geometries of the patterns transferred through the apertures of stencils comprising several cantilevers. Spiral structures at the micrometer scale are firstly produced on both rigid and soft biodegradable PLGA substrates. SEM and AFM results indicate that metallic spiral patterns are successfully fabricated. Electrical characterization results show similar resistance values among the used substrate materials. A potential application of the fabricated spiral structure as heaters for biomedical implants is demonstrated with a DC breakdown characterization.

Furthermore, the bridge stencil is scaled down to the nanometer scale by utilizing a DUV stepper. Geometrical and electrical characterization results show that meandering metallic patterns at the nanometer scale are successfully fabricated on a large variety of substrate materials, including also biocompatible and biodegradable materials. The noticed thickness reduction is signaled by considering the effective evaporation source size during the metal deposition process. The distinct metal structure observed on the PLGA substrate is tentatively attributed to the low T_g of PLGA. Additional experiments conducted under different deposition parameters show different levels of reflow on the PLGA surface when it is exposed to the evaporated source atoms for a different amount of time. Notably, the electrical characterization results indicate that the observed irregular metal structures on PLGA substrates do not influence their electrical functionality. DC breakdown characterization results indicate a maximum temperature of about 120 °C on the fabricated nanomeanders using a Joule heating source, demonstrating a potential application as bioimplantable nanoheaters. Last, we apply the nanobridge stencil on a stretchable substrate having stiffness gradients. Electromechanical characterization results reveal that the produced nanomeanders are capable of sustaining strain up to 45% without electrical failure. However, the use of bridge stencils on a stretchable PDMS substrate shows an extremely low fabrication yield, which might be due to the cracks formed on metal films resulting from the huge CTE mismatch between deposited Au films and PDMS substrates. To solve this issue, we present in Chapter 4 the fabrication of liquid metal patterns on a PDMS substrate for stretchable electronic applications. To conclude, the concept demonstrated in this chapter can be applied to realize arbitrary structure designs on a broad range of substrates, a crucial step towards metal additive patterning on flexible and biodegradable material for implantable devices.

4 Stretchable conductors fabricated by SL and centrifugal force-assisted patterning of LM

Disclaimer: This chapter (4) is adapted from the following article with permissions of all co-authors:

Y.-C. Sun, G. Boero and J. Brugger, "Stretchable Conductors Fabricated by Stencil Lithography and Centrifugal Force-Assisted Patterning of Liquid Metal", *ACS Applied Electronic Materials*, 2021, 3, 5423-5432.

My contribution: conceptualization, design, fabrication, experiments, figures and writing.

This chapter aims to present the extended use of SL for the fabrication of high resolution liquid metal (LM) patterns on a stretchable substrate for stretchable electronic applications. First, the developed hybrid process combining SL and centrifugal force-assisted patterning of LM is presented. Then, the geometrical and electrical characterizations of the fabricated LM patterns are conducted and discussed. Finally, bridge stencils are implemented to produce stretchable LM serpentine resistors and interdigitated capacitors. Their electrical performance upon mechanical deformation is characterized.

4.1 Introduction

A stretchable conductor is an essential element in wearable and stretchable systems. Engineering thin metal films into serpentine patterns and incorporating nanomaterials into polymer matrix have enabled stretchable conductors with a large stretchability. However, the serpentine-patterned metal films consume a large portion of the usable density for functional devices. Also, the nanomaterial-polymer matrix normally has a relatively low electrical conductivity because the conductive traces are created by the percolation of nanomaterials. The limitations mentioned above hinder their use for wearable applications. Another strategy involves the use of intrinsically stretchable materials such as liquid metal for stretchable conductors.

Among the liquid metal candidates for stretchable conductors, the liquid gallium alloy such as eutectic gallium-indium (EGaIn, 75 wt% of Ga and 25 wt% of In) and gallium-indium-tin (Galinstan, 68.5 wt% of Ga, 21.5 wt% of In, and 10.0 wt% of Sn) are particularly attractive because of their non-toxicity, low electrical resistivity, negligible vapor pressure and low melting temperature. For example, EGaIn has a melting temperature of 15.5 °C and an electrical resistivity of $0.29 \Omega \cdot \mu\text{m}$ at room temperature (i.e., in liquid state) [85]. The electrical resistivity of EGaIn is one order of magnitude higher than bulk Cu but one order of magnitude lower than nanomaterial-embedded composites (e.g., AgNW) [67] and eight orders lower than ionic gels [77], which makes EGaIn an excellent candidate for stretchable conductors. One of the promising strategies for the use of liquid gallium alloy is to embed it into an elastomeric polymer [183, 184]. Being liquid at room temperature, liquid gallium alloy can deform into the shape of the microchannel and remain electrically conducting. These properties make liquid gallium alloy suitable for wearable applications.

The rigid thin oxide skin ($\approx 1\text{-}3 \text{ nm}$), formed on the surface of liquid gallium alloy when exposed to oxygen in the environment, allows for shape retainment at the micrometer scale and form stable freestanding structures [86, 185]. A broad range of manufacturing methods have been developed for structuring liquid gallium alloys at the micrometer or submicrometer scale by taking advantage of its moldability. For example, liquid gallium alloys can be structured at the micrometer scale by using picosecond laser ablation [186], printing directly on substrates via nozzles [185, 187], injecting into microfluidic channels [188, 189], screen printing [190] or spray deposition via stencils [126], or using PDMS stamps to transfer patterns [191, 192]. Although using PDMS stamps to transfer liquid metal patterns shows promising results, the substrate has to be molded to have desired channels, which prevents this approach from being applied to a wide range of substrate materials. Recently, a hybrid process utilizing electron-beam (E-beam) lithography and stamping has been developed to shape EGaIn at the sub-micrometer scale [193]. Therein, the patterned EGaIn is transferred to the desired substrate by immersing the device in DI water for more than six hours to laterally etch away the sacrificial layer. The transfer process makes the entire process time consuming.

Additional fabrication methods have been developed by taking advantage of the selective wetting property of oxide-removed liquid gallium alloy. The native oxide of liquid gallium alloy (Ga_2O_3) can be removed using aqueous acids (HCl) or bases (NaOH) [194]. Without the presence of Ga_2O_3 , liquid gallium alloy can selectively wet different metal surfaces such as Au and Cu due to the formation of intermetallic compounds (e.g., AuGa_2 and CuGa_2) [195]. Therefore, by having patterns of metal traces on the elastomer surface, where LM adheres, LM patterns can be produced by removing excess material by using a roller or by brief exposure to an aqueous acid/base to cause them to dewet the region without the metal traces [196–198]. However, in the reported literature, the metal traces are produced by resist-based photolithography processes, which puts a limit on what type of substrates can be used. Moreover, it remains challenging to fabricate liquid gallium alloy with lateral resolution smaller than $10\text{ }\mu\text{m}$ [196, 197]. The limitation presumably comes from the used acid (i.e., HCl) which etches the patterned metal layer or, alternatively, due to the non-controllable forces during the removal of excess liquid gallium alloy. To improve the resolution, a thick ($2\text{ }\mu\text{m}$) electroplated Cu has been applied as an adhesive layer for structuring liquid gallium alloys down to $2\text{ }\mu\text{m}$ [198]. However, this approach requires an additional electroplating process, which normally requires acid electrolyte and thus increases the overall fabrication costs and finally it is not suitable for chemical-sensitive substrate materials. Overall, a simple, versatile and cost-efficient process that enables patterning liquid gallium alloys at the micrometer scale on a broad range of substrates is still lacking.

For facile and reliable patterning, the selective deposition of materials utilizing the centrifugal force experienced from spinning the substrate is a well-established approach. It is normally used to create uniform films on the substrate by spinning off excess materials from the surface. Selective deposition of materials can be achieved by controlling interfacial interactions between the substrate and the deposited material. Patterns can be achieved by efficiently removing the excess materials by the well-controlled centrifugal force experienced from spinning the substrates [199, 200]. This approach provides a way for high-resolution and size-scalable manufacturing of patterned liquid structures.

In this chapter, we describe a hybrid process combining stencil lithography and centrifugal force-assisted patterning of LM to provide a simple but reliable method to shape LM on an elastomer surface at the micrometer scale. It allows for the creation of microscale EGaIn features on a stretchable PDMS substrate. We also adapt a bridge stencil concept to further enlarge the applicability of stencils for complex design patterns, such as long meanders and interdigitated electrodes. The EGaIn resistors with straight line and serpentine shapes are both fabricated on PDMS to demonstrate the electrical and electromechanical performances. Furthermore, we demonstrate the possibility of extending this approach to a stretchable and biodegradable poly(octamethylene maleate (anhydride) citrate) (POMaC) substrate. This represents an important enabling step towards its use in applications such as sustainable electronics [145, 201].

4.2 Results and discussions

4.2.1 Microfabrication based on a hybrid process

The fabrication process based on SL and centrifugal force-assisted patterning of LM to shape EGaIn at the micrometer scale is illustrated in Figure 4.1. The substrate is composed of a soft PDMS layer having a thickness of 1 mm with a lateral size of $30 \times 15 \text{ mm}^2$ on a $525 \mu\text{m}$ thick silicon wafer, which is coated with a self-assembled trimethylsilyl chloride silane (TMCS) (Sigma Aldrich) layer to enable the peeling of PDMS in the last step. The stencil mask used here consists of 500 nm thick low-stress silicon nitride (LS-SiN) membranes supported by a silicon frame. The stencils are fabricated by patterning the apertures on LS-SiN membranes, followed by the etching of the backside silicon carrier to release the nitride membranes. First, the fabricated stencil is brought into contact with the substrate and then 4 nm thick Cr and 60 nm thick Au are locally sputter deposited on the substrate via the apertures of the SiN stencil mask (Figure 4.1a). The deposition is performed using DC sputtering with a power of 350 W and 250 W for Cr and Au, respectively. Here, Cr is used as an adhesion layer for Au on PDMS and Au is used to have a selective wetting contrast with EGaIn. After the sputter deposition, the stencil mask is removed from the PDMS substrate by immersing the sample in isopropyl alcohol (IPA) (Figure 4.1b). Due to the sticky property of PDMS, we use IPA to assist the removal of the stencil without damaging the membrane. IPA swells PDMS, which increases the strain at the interface of the stencil and the PDMS, resulting in the PDMS film to peel off [116]. In a second experiment, we performed this method on a flexible POMaC substrate to validate the possibility of extending this approach on a biodegradable substrate. On POMaC substrate, the stencil can be released directly after sputter deposition without the use of IPA.

After the creation of the Cr/Au pattern and the removal of the stencil mask, $20 \mu\text{l}$ of 4% NaOH treated EGaIn is drop-casted onto the substrate to cover the entire Cr/Au patterns, followed by spinning the substrate (Figure 4.1c,d). The procedure starts by placing the chip on a vacuum sample holder in a spin-coater. Then, $20 \mu\text{l}$ of 4% NaOH and EGaIn (Gallium-Indium Eutectic, $\geq 99.99\%$, Sigma Aldrich) are drop-casted on the chip using a pipette, followed by spinning the chip. Here, 4% NaOH is applied to remove the native oxide of EGaIn (Ga_2O_3) so that it can selectively wet on the patterned Au surfaces. The spinning program is set up in three sequential steps using an in-built controller. Each step is defined by the target spinning speed and duration time. The time for acceleration is also included in the duration time. The parameters used for each step are as follows: (1) 100 rpm for 5 s with an acceleration rate of 82 rpm/s. (2) 500 rpm for 7 s with an acceleration rate of 82 rpm/s. (3) 0 rpm for 5 s with a deceleration rate of 410 rpm/s. In the end, the chip is rinsed with DI water. During the spinning, EGaIn wets the metal traces and the excess material is removed from the substrate by the centrifugal force (Figure 4.1e). The EGaIn confinement on the metal traces is attributed to the wetting contrast between PDMS and metal and the pinning effect on the metal mesa edge [202]. The competition between the adhesion forces between EGaIn and Au, the cohesion forces within EGaIn and the centrifugal force determines the geometry of the obtained EGaIn

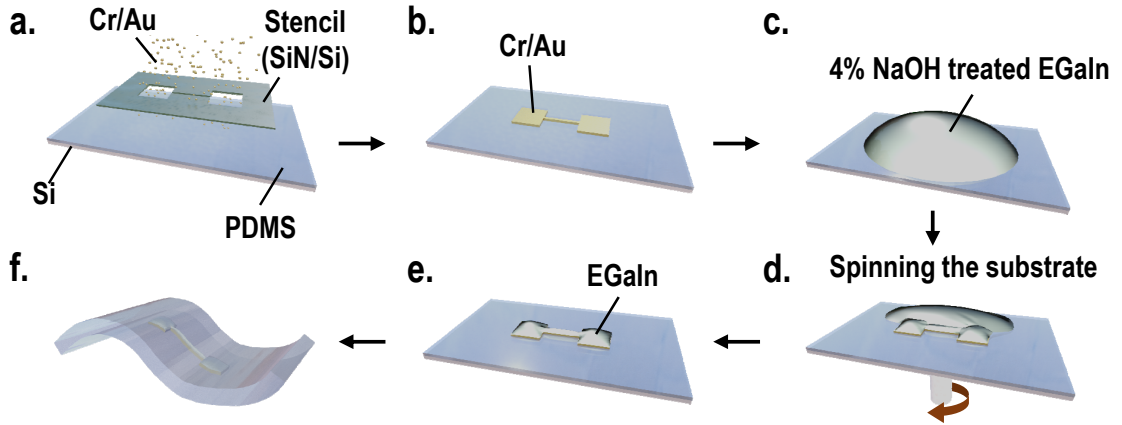


Figure 4.1: **Hybrid process for the fabrication of EGaln stretchable conductors.** Schematic pictures showing the liquid metal patterning process on a Si(0.5 mm)/PDMS(1 mm) substrate. **a.,b.** The fabricated stencil is placed on the substrate, followed by sputter deposition of Cr(4 nm) and Au(60 nm). **c.** EGaln treated with 4% NaOH is drop-casted onto the substrate. **d.,e.** EGaln wets the metal traces and the excess material is removed by spinning the substrate. **f.** Sealing with PDMS(1 mm) and peeling off from the Si support.

structures. The step-by-step images captured during the process detail the experimental procedure (Figure 4.2). Compared to the existing fabrication methods using a roller or manual shaking to remove excess materials [27, 196, 198], centrifugal force-assisted patterning of EGaln with microscale wetting contrast patterns provides a way to efficiently remove the excess material in a controllable manner and is size-scalable for large area manufacturing. Furthermore, the removed excess EGaln remains in the spin-coater as a droplet, which allows to be simply re-collected for further use (Figure 4.3). After the spinning, the device is rinsed in DI water to remove unwanted NaOH residues. Finally, the patterned LM device is sealed with a 1 mm thick layer of PDMS obtained by gently pouring a self-curing liquid PDMS solution over the device to protect LM patterns for the further stretching test. In the end, the encapsulated device is peeled off from the silicon carrier (Figure 4.1f). The developed hybrid process enables the creation of EGaln patterns on the substrate with minimal exposure to harsh chemicals. Only a few seconds of exposure to 4% NaOH and DI water is needed in the process, which allows the process to be extended to a wide range of substrates.

Chapter 4. Stretchable conductors fabricated by SL and centrifugal force-assisted patterning of LM

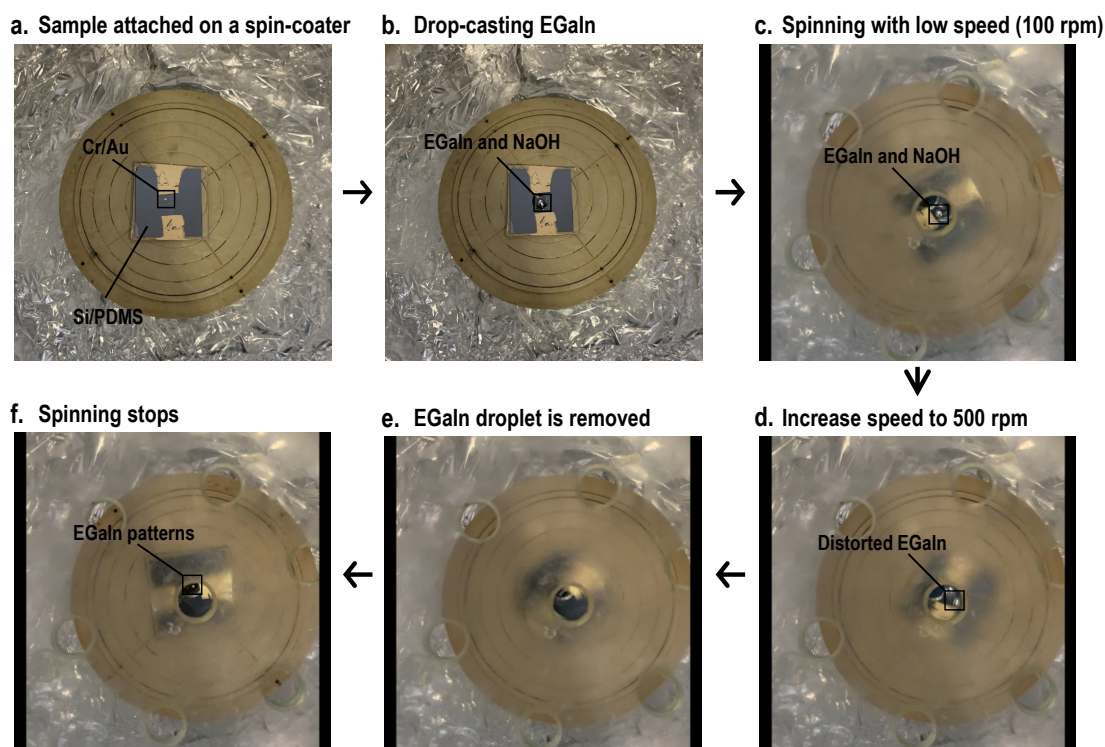


Figure 4.2: **Images showing the detailed procedure during the removal of EGaIn.** **a.** A Si/PDMS chip with stencil-defined metal patterns is attached on a spin-coater. **b.** EGaIn and NaOH are drop-casted on the metal patterns. **c.** With low spinning speed (100 rpm), EGaIn/NaOH stays on the initial place. The image is captured at 2 s of spinning. **d.** EGaIn droplet starts to distort with increased spinning speed before it has spun-off. The image is captured at 7 s of spinning. **e.,f.** Excess EGaIn is removed and EGaIn patterns are successfully produced on the chip. Images e. and f. are captured at 10 s and 16 s of spinning, respectively. In the images a. and b., there is no cover lid, and in the following there is.

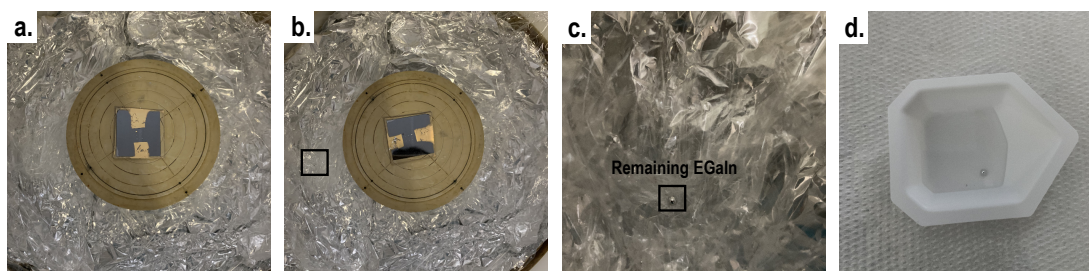


Figure 4.3: **Re-collection of the removed excess EGaIn after spinning.** **a.** A stencil patterned PDMS chip attached on a spin-coater. **b.** After spinning the substrate and the excess EGaIn remains in the spin-coater as a droplet. **c.** The zoom-in image of the black square in b. **d.** Re-collection of EGaIn into NaOH by using a pipette.

To elucidate the resolution limit, we have created on a PDMS substrate squares with a minimum side of $5\ \mu\text{m}$ and lines with a minimum width of $2\ \mu\text{m}$ (Figure 4.4a,b). In some cases, we observed distorted edges in the produced LM patterns, which might come from the corrosion of Au by EGaIn when EGaIn is in contact with Au patterns for a too long time. To have a clear picture, we have performed experiments under an extreme condition. After drop-casting EGaIn on the Au surface, we wait 1 min before spinning the substrate. After removing excess EGaIn, we observe that the Au surface (i.e., golden color shown in Figure 4.5a) is damaged, which results in irregular EGaIn patterns (Figure 4.5). The observation is tentatively attributed to the penetration of Ga into the Au layer from the top and the edges of metal mesas, thereby forming an intermetallic layer (AuGa_2) [196], which is suspected of having low adhesion to the other metal surfaces. Thereafter, a part of the Au layer is damaged during the removal of excess EGaIn. More detailed investigations are required to better understand the phenomenon. However, in most of our results with well-controlled experimental manipulation (i.e., less than 10 seconds between drop-casting EGaIn and spinning the substrate), the phenomenon is not significant. In addition to regular patterns, arbitrary patterns can be produced, such as the EPFL logo (Figure 4.4c). It is noted that in the stencil design, the letter "P" is connected with bridges because the suspended membrane in the stencil limits the production of a close-loop structure, as known as the 'Doughnut problem'. To solve this challenge, we report in the Section 4.2.3 a solution utilizing the blurring effect to achieve complex and continuous LM patterns. Arrays of lines and narrow lines with large contact pads with a width of $2\ \mu\text{m}$ are also successfully fabricated by the same method (Figure 4.6). The fabricated line patterns on a flexible and biodegradable POMaC substrate (Figure 4.7) demonstrate the possibility to apply the proposed approach on a wide range of substrates.

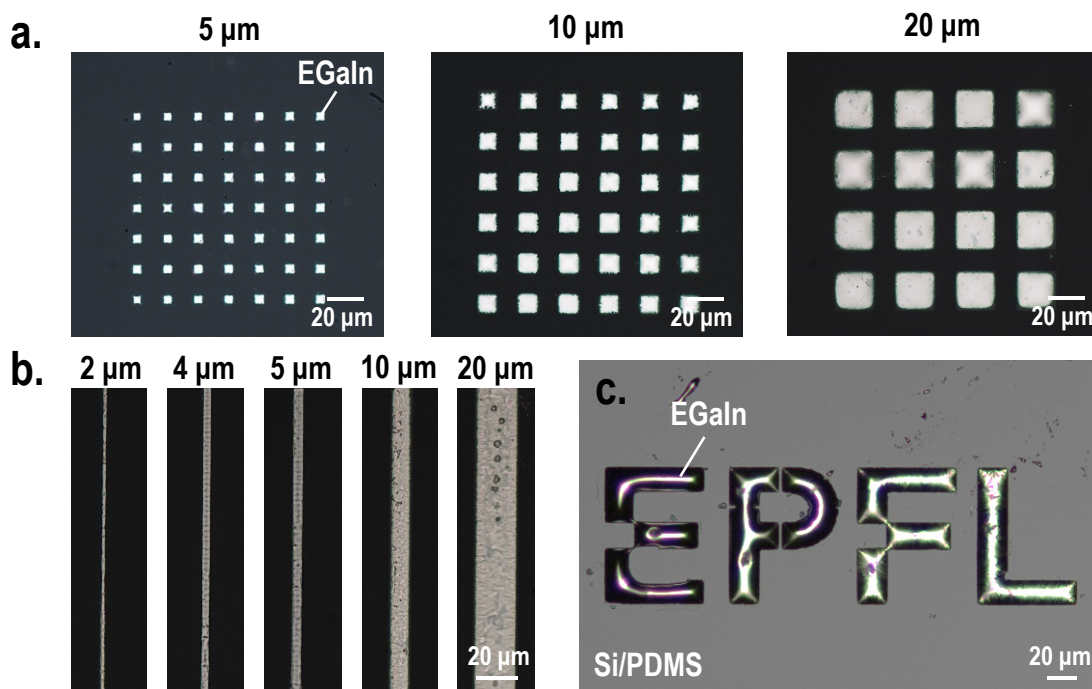


Figure 4.4: **Various EGaln patterns obtained by the proposed process.** **a.** Patterned EGaln square dot arrays with width from 5 μm to 20 μm . **b.** Patterned EGaln line patterns with width from 2 μm to 20 μm . **c.** Patterned EGaln EPFL logo. All patterns are imaged with an optical microscope at the step e. of the process shown in Figure 4.1.

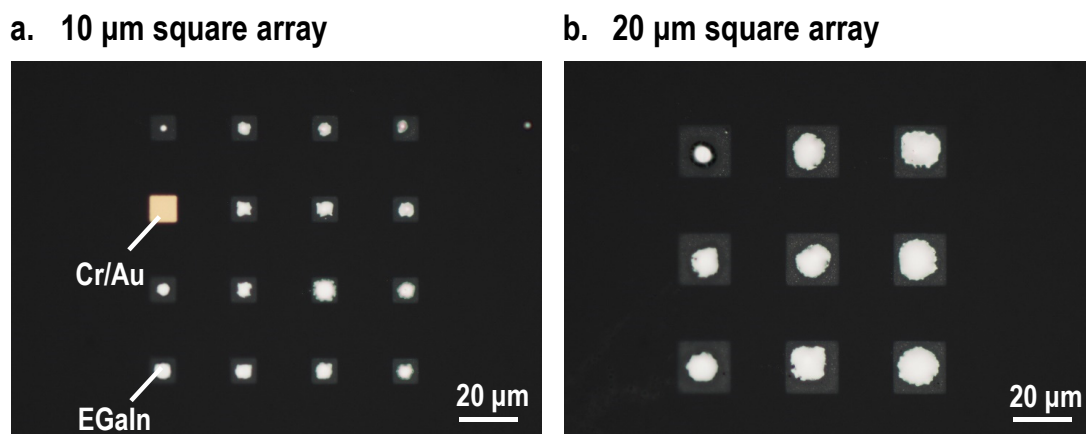


Figure 4.5: **The irregular EGaln patterns due to the corrosion of Au by EGaln.** The EGaln droplet is drop-casted on the Au surface and remains on it for 1 min before spinning the substrate. The images show that after spinning the excess EGaln off the substrate, the Au surface seems to be corroded, which results in irregular EGaln patterns.



Figure 4.6: **High resolution EGaIn patterns fabricated by the presented method.** a.,b. Line patterns with $2\ \mu\text{m}$ line width. In the optical image in a., the lines properly covered by EGaIn are clearly distinguishable from those where only the Au is present. c. $2\ \mu\text{m}$ wide lines connected to $100\ \mu\text{m}$ wide square contact pads. The defect comes from an incomplete Au pattern resulting from a broken stencil membrane

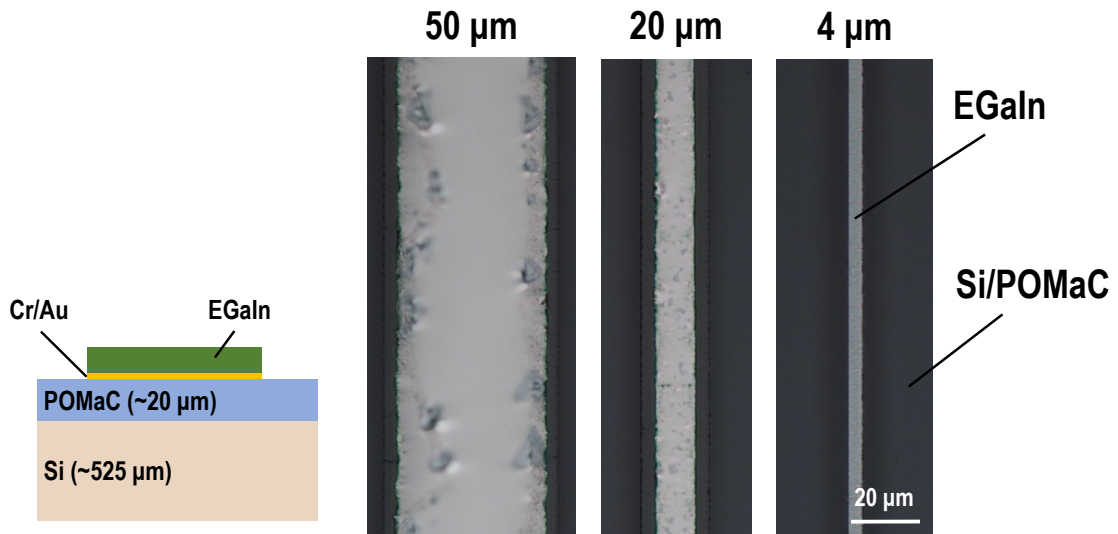


Figure 4.7: **Patterned EGaIn on POMaC, a flexible and biodegradable substrate.** EGaIn line patterns form on top of Cr (4 nm)/Au (60 nm) on a Si/POMaC substrate with widths from $50\ \mu\text{m}$ to $4\ \mu\text{m}$.

Chapter 4. Stretchable conductors fabricated by SL and centrifugal force-assisted patterning of LM

To assess the geometry of the fabricated EGaIn patterns on a PDMS substrate, confocal microscopy (S neox, Sensofar) is used to measure the profile of the patterned EGaIn square dots having different side widths (Figure 4.8). As expected, the height of each square pattern increases with its width (Figure 4.8a). The same result has been shown by using spin-coating to selectively deposit polymer thin film on a heterogeneous substrate [200]. Furthermore, a linear relationship can be obtained between the patterned EGaIn width and height (Figure 4.8b). The error bar shows the spread of data from three random samples, with each sample produced from a single 20 μ l NaOH treated EGaIn droplet. The process is performed under the same spinning parameters for all samples. Next, to study the effect of the spinning speed, which leads to different centrifugal forces on the geometry of the obtained EGaIn structure, geometrical analysis is carried out on samples fabricated with different spinning speed. Five spinning speeds ranging from 250 rpm to 4000 rpm are used to create EGaIn square array patterns, which consists of square patterns with side widths of 5 μ m, 10 μ m and 20 μ m, respectively. The results show a maximum standard deviation in heights of about 20% when applying different spinning speeds (Figure 4.9). This demonstrates that using centrifugal force experienced from spinning the substrate to structure LM provides not only promising results but also a large process window for reproducible manufacturing. Moreover, it shows the possibility to extend the presented method to the full wafer scale by adapting a well-established full wafer stencil [203]. After patterning metals on a wafer, several EGaIn droplets can be dispensed on the metal structures, followed by spinning the substrate to remove the excess materials. Although the centrifugal force differs based on the pattern location with respect to the rotation axis, the results shown in Figure 4.9 demonstrate a weak dependence of the patterned EGaIn structure dimensions on the spinning speed (i.e., on the centrifugal force), which paves a way for wafer scale patterning.

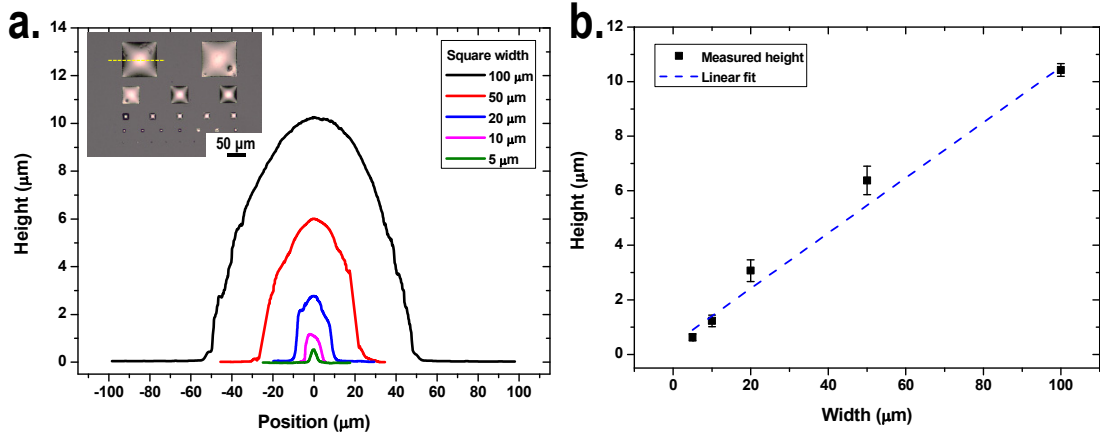


Figure 4.8: **Geometrical analysis of the patterned EGaIn on a PDMS substrate.** **a.** Profile of the patterned EGaIn square dots with different widths. The inset shows the optical image of the sample. Scale bar: 50 μm . **b.** Relationship between patterned EGaIn width and height and its linear fitting curve. The width and height values are taken from the stencil aperture size and the measured profile, respectively. Each data point contains measurement results from three random samples. The error bar represents the standard deviation.

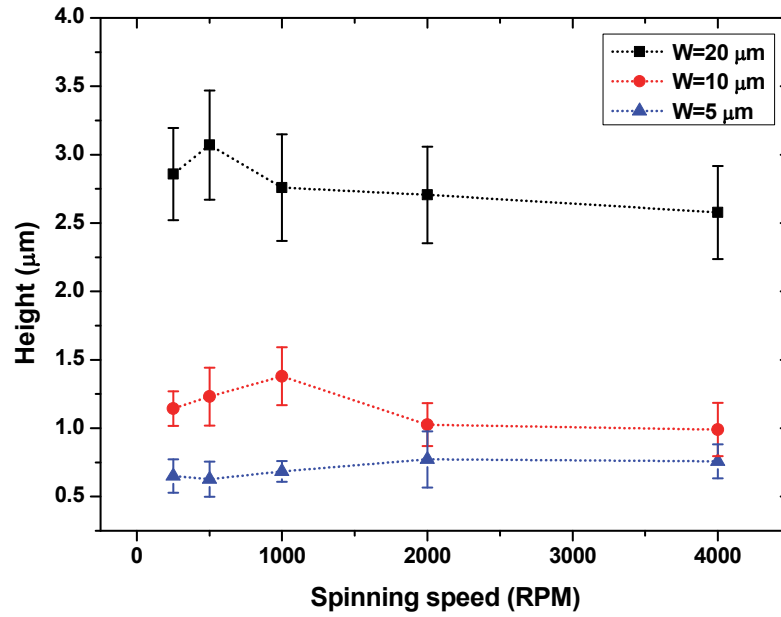


Figure 4.9: **Measured heights of the EGaIn square patterns fabricated with different spinning speed.** Five spinning speeds ranging from 250 rpm to 4000 rpm are carried out on square array patterns. For each experiment, different acceleration rate is used to keep the same process time. For all the experiments, the time for reaching the target speed is set to be about 4-5 s. Then, the devices rotate at the target speed for about 2-3 s and finally slow down to 0 speed in about 2 s. Each data point consists of measurement results from more than three square patterns taken from two random samples. Error bar represents the standard deviation. W indicates the width of the square.

4.2.2 Electrical characterization of the patterned EGaIn

Next we evaluate the electrical performance of the patterned EGaIn on a PDMS substrate. The devices used for resistance measurement contain lines with lengths of 50, 100 and 150 μm and widths of 2, 5 and 10 μm , and are connected by two square electrical pads having a width of 100 μm at their terminal ends. After patterning EGaIn with the method described above, the electrical measurements are performed before encapsulating the devices. The parasitic resistance, which consists of the resistance of the probes and the contact resistance between the probes and droplets, are quantified and subtracted from the measured total resistance. The parasitic resistance is measured by inserting two probes into the same droplet whereby the measured values varies between 5 to 10 Ω . The expected resistances of patterned EGaIn are calculated from a parallel circuit formed by the underneath adhesive Au layer and EGaIn structure. Here, because the thickness of Cr (4 nm) is ten times thinner than Au (60 nm) and Cr is six times more resistive than Au (0.12 $\Omega\cdot\mu\text{m}$ for Cr [170] and 0.02 $\Omega\cdot\mu\text{m}$ for Au [171]), the contribution of Cr to the electrical conductance is neglected. The resistivity of the adhesive Au layer is characterized by measuring the resistance of the sample before patterning EGaIn. The result shows a resistivity of 0.31 $\Omega\cdot\mu\text{m}$ for the sputter deposited Au by using a stencil mask (Figure 4.10). The measured resistivity of a sputtered Au thin film is more than ten times of the value of bulk Au, which is attributed to random cracks and surface wrinkles on the Au film formed during the sputtering process [204, 205] (Figure 4.11). To calculate the resistivity of patterned EGaIn, the resistance is plotted as a function of the inverse of the EGaIn cross-section area for different lengths (Figure 4.12a). The cross-section area of each device is calculated by integrating the profile measured by confocal microscopy (S neox, Sensofar) and subtracted from the area of the underneath adhesive layer. We observe variations in the cross-section area among different samples having the same device geometry. The variations can be explained by the resulting height differences of the patterned structures (Figure 4.8). The measured resistivity of EGaIn is $0.39 \pm 0.02 \Omega\cdot\mu\text{m}$ (Figure 4.12b), which is close to the reported resistivity of bulk EGaIn (0.29 $\Omega\cdot\mu\text{m}$) [85]. It is important to note that the calculation is based on a parallel circuit model without considering the occurring cracks on the Au film. If the cracks are filled with EGaIn, the effective resistivity of the Au film that contributes to the conduction is reduced. Therefore, the presence of such cracks would result in an underestimation of the calculated resistivity of EGaIn.

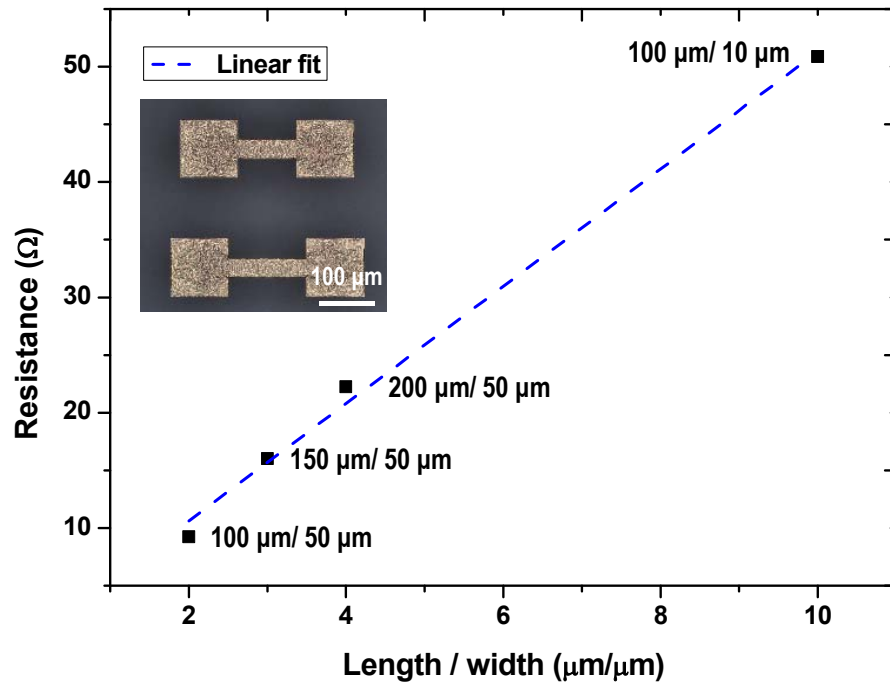


Figure 4.10: **Electrical characterization of the sputter deposited Au structures on a PDMS substrate.** Measured electrical resistance of Au with respect to the ratio of patterned length and width. The measured resistivity of the sputter deposited Au is about $0.31 \Omega \cdot \mu\text{m}$. Inset shows the optical image of the sample used for resistance measurement.

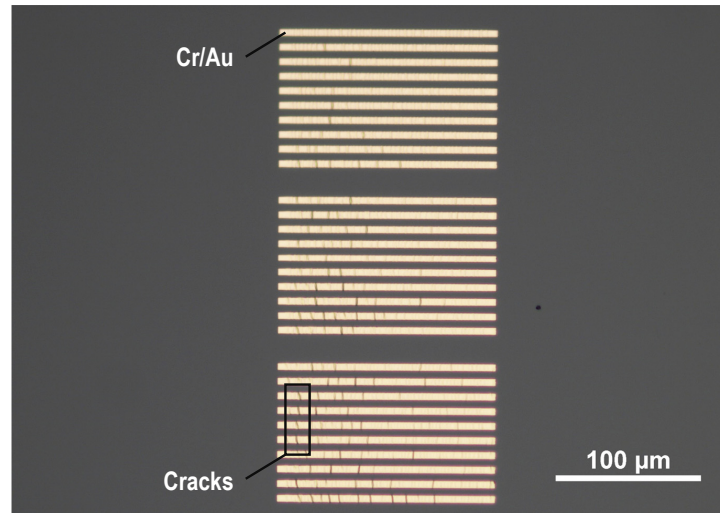


Figure 4.11: **Optical image of the sputtered Au surface on a PDMS substrate.** Optical image showing the presence of cracks on the Au surface after sputter deposition through a stencil on a PDMS substrate.

Chapter 4. Stretchable conductors fabricated by SL and centrifugal force-assisted patterning of LM

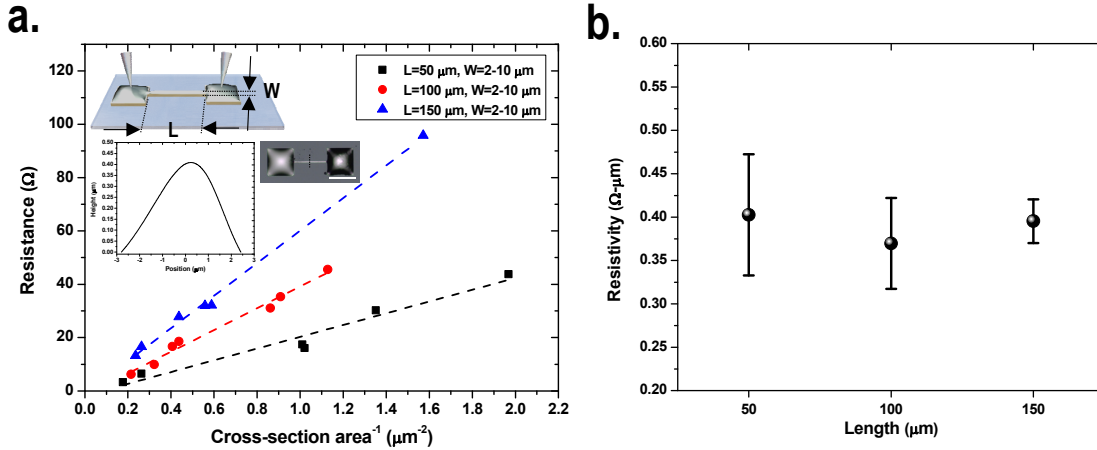


Figure 4.12: **Electrical characterization of the patterned EGaIn on a PDMS substrate.** **a.** Resistance measurement results as a function of the inverse of the cross-section area with different lengths and widths. The inset shows the geometry of the device and its measured cross-section profile together with a sketch of the two-point probe configuration used for the resistance measurement. Scale bar: 100 μm . **b.** Extracted resistivity of each measured data, which are 0.40, 0.37 and 0.39 $\Omega\cdot\mu\text{m}$ for lengths of 50, 100 and 150 μm , respectively.

In order to verify the suitability of the fabricated EGaIn structures as stretchable conductors, the measurement on the maximum operation current is performed. After patterning EGaIn on a PDMS substrate with the presented method, the terminal droplets are administered on the large electrical pads at the ends of the tested EGaIn wire. The terminal droplets allow copper wire to be added on to perform electrical measurements. The device is encapsulated by gently pouring a self-curing liquid PDMS solution on the device and curing it at room temperature for 48 hours. The experiment on the maximum operation current is conducted by measuring the electrical resistance with increased input currents. We observe that, at currents below 7 mA, no permanent modification of the device resistance is introduced. The resistance increases as a function of applied currents due to Joule heating but recovers to its initial value once the current is reduced (Figure 4.13). The measured resistance change indicates a temperature increase of around 65 $^{\circ}\text{C}$ based on the Equation 4.1, where R is the resistance, α the temperature coefficient of resistivity of EGaIn ($\sim 10^{-3}/^{\circ}\text{C}$) [206,207]. A COMSOL simulation coupling with Joule heating and heat transfer model is performed to verify the experimental results. The simulation result shows that when a current of 7 mA is applied, the embedded EGaIn is heated to around 79 $^{\circ}\text{C}$, which is similar to our experimental data of around 85 $^{\circ}\text{C}$, assuming room temperature of 20 $^{\circ}\text{C}$ (Figure 4.14).

$$\Delta T = \frac{\Delta R}{R_0 \alpha} \quad (4.1)$$

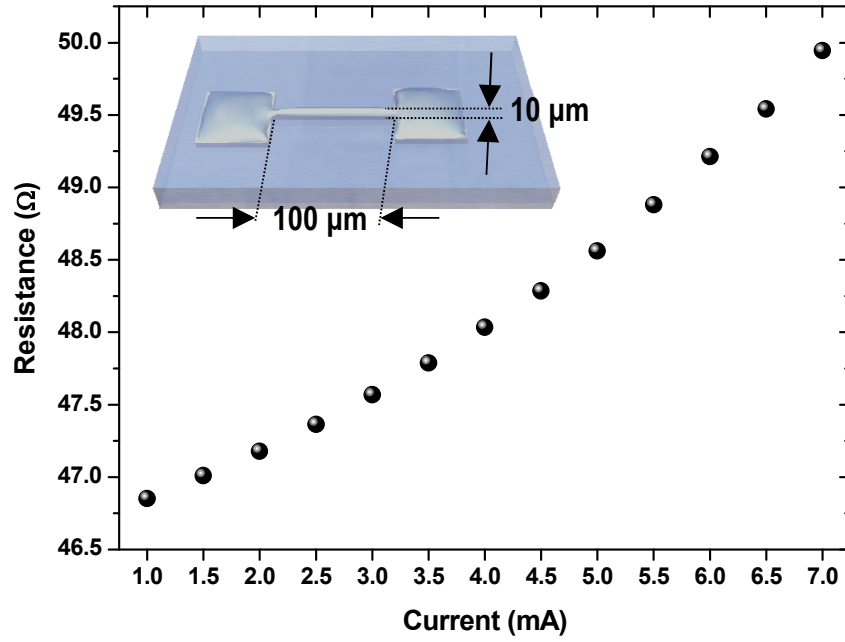


Figure 4.13: **Resistance versus applied currents.** The maximum current which does not produce irreversible damage is about 7 mA.

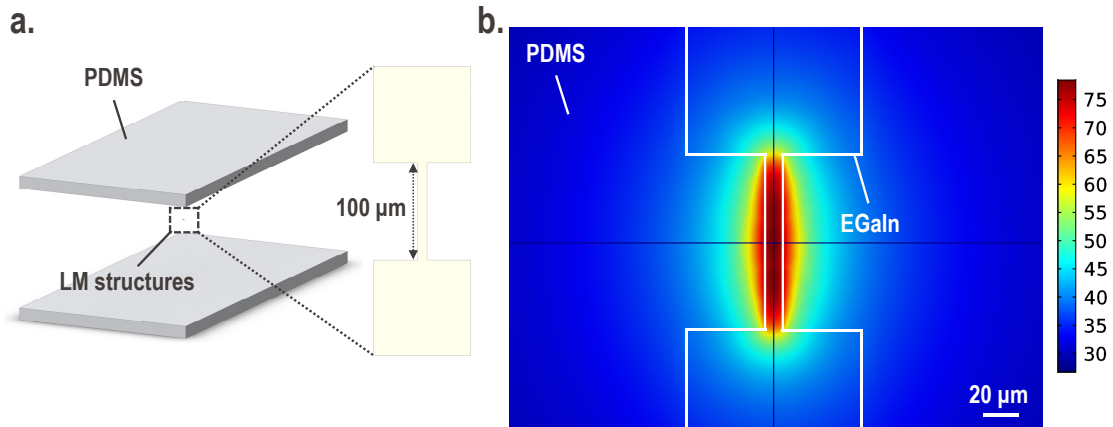


Figure 4.14: **Simulation of the Joule heating effect.** **a.** The simulation model contains a EGaln structure with the two-point probe configuration embedded in 2 mm thick PDMS. **b.** Simulation result shows that the embedded EGaln is heated to around 79 °C with an applied current of 7 mA. The thermal conductivity and heat capacity used for simulation are 26.4 W/m·K, 296 J/kg·K for EGaln and 0.16 W/m·K, 1460 J/kg·K for PDMS, respectively.

The result shows that LM conductors fabricated by the presented method could meet the requirements for wearable devices operating at least in a temperature range between 20 and 85 °C. At larger currents (7.5 mA), the resistance starts to gradually increase as a function of time and a permanent modification of the device resistance is observed. The phenomena is tentatively attributed to the void formation inside the embedded EGaln channel when the

Chapter 4. Stretchable conductors fabricated by SL and centrifugal force-assisted patterning of LM

device is heated up to a certain temperature [206,207]. The maximum operation current for the fabricated EGaIn sample is around 7 mA, which corresponds to a current density of around 2×10^9 A/m². The measured current density is about 4 orders of magnitude higher than the values for stretchable conductors based on the percolation of conductive silver nanowires [208].

Next, the electrical characterization of a EGaIn resistor under applied uniaxial deformation is performed. The sample chip is mounted on a commercial tensile testing stage (TST350, Linkam Scientific) with an in-built controller to actuate one of the two clamps moving along the horizontal plane. The electrical resistance is measured using the two-point probe method (2400 source-meter, Keithley) controlled by a LabVIEW program. The resistances are measured with an applied current of 1 mA. The results show an excellent electrical stability over one thousand cycles with 40% maximum applied strain in a sample with 10 μ m in width and 100 μ m in length (Figure 4.15). The electrical resistance increases from about 17 Ω to 45 Ω in the first 100 cycles and then remains constant up to at least 1300 cycles (8.6 hours). The mechanism of the observed phenomenon is not clear. In previous literature [209], the initial increase of the electrical resistance is tentatively attributed to the deformation and reformation of the oxide skin. Because PDMS is permeable to oxygen [210], oxygen might permeate inside the PDMS channel and results in the re-oxidation process, which forms a different amount of Ga₂O₃ within the wire [209]. Another possible explanation for the observed phenomenon is the increased crack density of the underneath Au during stretching [204]. In the first few cycles of stretching, EGaIn fills in the cracks produced on the Au film and the entire metal structures are stabilized afterwards. After 1300 cycles of stretching in 8.6 hours, the device is released to its original shape. To further study the stability of the fabricated device, three additional cycle tests are performed with different interval breaks. The second cycle test is performed after 15 hours from the first cycle test. The results of the second cycle indicates that there is no significant change in electrical resistance. The third and the fourth cycle tests are performed after 10 minutes and 1 hour from the second and the third cycles, respectively. No significant electrical resistance variations are observed (Figure 4.15). It can be concluded that after a certain number of stretching cycles, the electrical resistance of the fabricated device is no more affected by the subsequent stretching cycle. The calculated gauge factor of the fabricated device is 1.3 within the applied strain range from 0% to 40% (the inset in Figure 4.15) due to the geometrical change of the embedded liquid conductor, which is in agreement with previously reported values [187]. As an example for an application of the proposed process, we show the stretchable connection to a commercial LED chip. The connection to the LED chip can withstand bending and twisting and remains functional (Figure 4.16). These measurements demonstrate that the bilayer conductive pattern (Au/EGaIn) produced with the method proposed in this work has excellent and stable electrical properties and can be used to fabricate stretchable conductors.

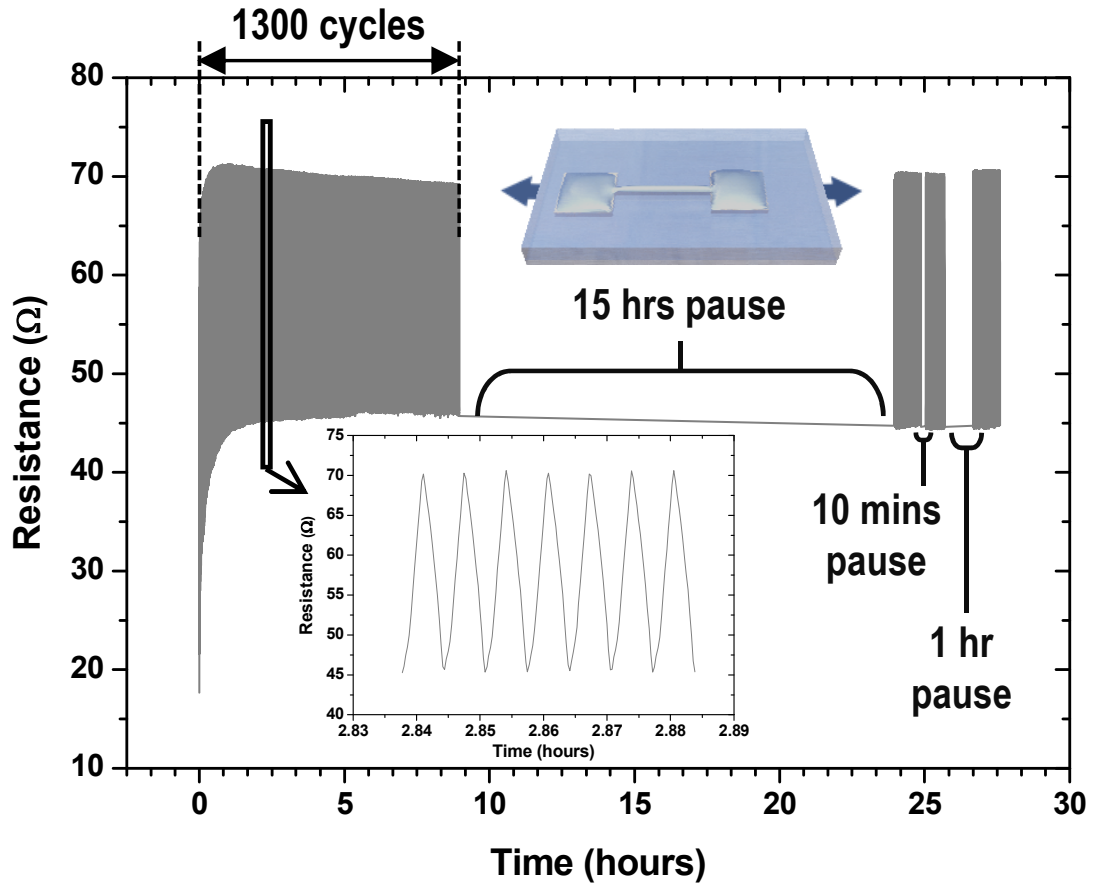


Figure 4.15: **Electrical characterization of the patterned EGaIn on a PDMS substrate under strain.** Long-term stability measurements on a sample with $10\ \mu\text{m}$ in width and $100\ \mu\text{m}$ in length. The strain is applied with a period of 24 seconds per cycle. Four cycle tests are performed on the same device under different interval periods. The inset shows detailed resistance changes under the maximum applied strain of 40% with an applied current of 1 mA.

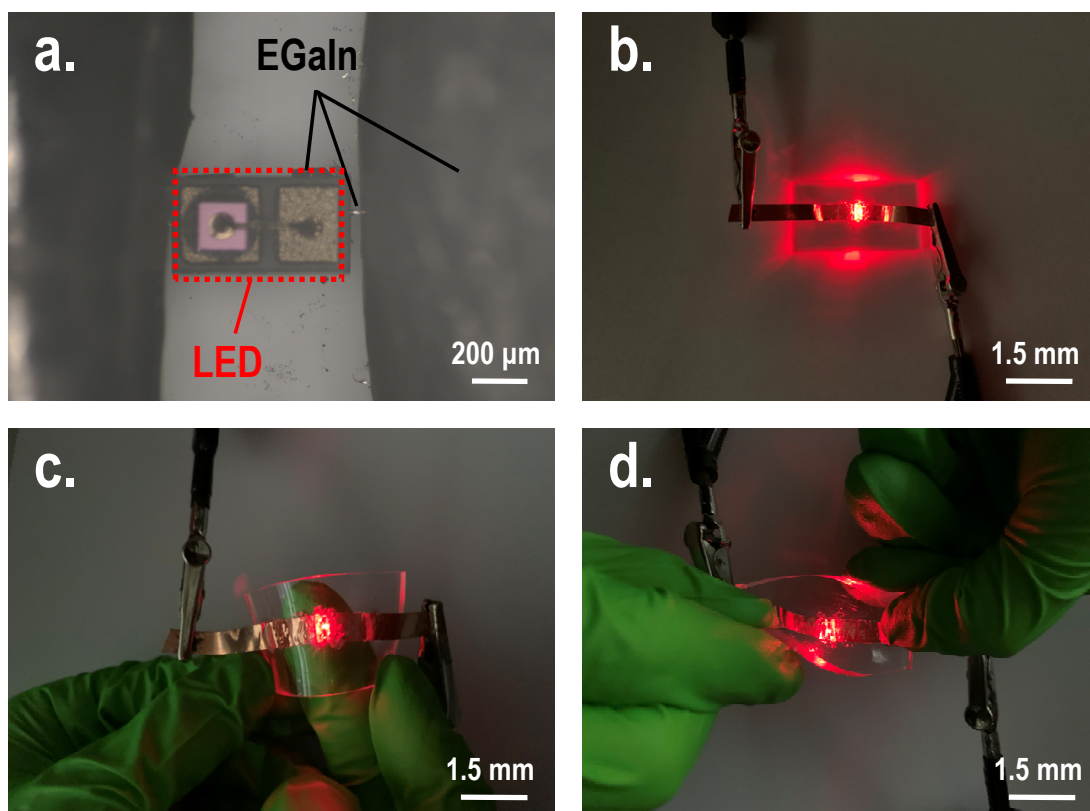


Figure 4.16: A LED chip connected with EGaIn/Au stretchable conductors. **a.,b.** Optical images showing the fabricated EGaIn conductors and the connected LED chip, which can withstand **c.** bending and **d.** twisting while remaining electrically functional.

4.2.3 Microbridge stencil for more complex patterns

Although stencil lithography has been demonstrated to enable the deposition of materials on a variety of substrates, the low mechanical robustness of the suspended thin SiN membrane limits its use for more complex patterns. To enable a wider variety of structures, we propose a microbridge stencil to enable geometries such as long serpentine and interdigitated structures. The proposed microbridge stencil consists of several bridges with a width of $1\ \mu\text{m}$ uniformly distributed across the entire structure to stabilize the suspended SiN membrane (Figure 4.17a). The applied microbridges result in a significant reduction of the membrane bending resulted from stresses and enable the realization of fragile serpentine structure (Figure 4.18). By lifting the microbridge stencil at a certain gap distance above the substrate surface, the line-of-sight evaporation results in material blurring and fills the shadowed bridge region (Figure 4.17b,c and Figure 4.19). In the last, EGaIn is formed on the stencil-patterned metal trace by spinning the excess EGaIn off the substrate (Figure 4.17d). The blurring effect causes pattern enlargement of the evaporated adhesive Au layer and consequently also of the final LM structure. For example, we observe LM pattern enlargements of $2.5\ \mu\text{m}$ per side when using a $70\ \mu\text{m}$ gap stencil-substrate distance. The result indicates that the best resolution of using microbridge stencil to pattern LM is around $6\ \mu\text{m}$, which results from the $1\ \mu\text{m}$ aperture opening plus the $5\ \mu\text{m}$ pattern enlargement. The optical images of the sample taken during the process indicate that the blurring underneath the microbridges in the stencil allows for a continuous metal pattern on the substrate surface (Figure 4.20a(i)) and enable a continuous LM pattern across the entire serpentine structure (Figure 4.20a(ii),(iii)). Comparing to the reported strategy of using a corrugated SiN [174] or an electroplated Cu [190] membrane to increase its mechanical robustness, the proposed microbridge stencil enables a wider variety of designs in the micrometer scale without introducing additional processes.

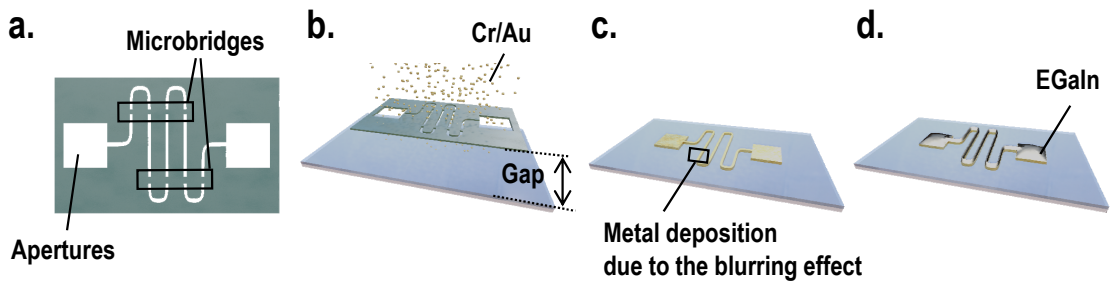


Figure 4.17: The use of a microbridge stencil for patterning EGaIn. **a.** Schematic drawings showing the concept of microbridge stencil and **b.-d.** fabrication processes. **b.** A microbridge stencil is attached above the Si/PDMS substrate with a certain gap distance ($70\ \mu\text{m}$) and fixed with Kapton tape. **c.** Cr(4 nm) and Au(150 nm) are evaporation deposited on the substrate. **d.** The EGaIn is structured by using the process mentioned in Figure 4.1.

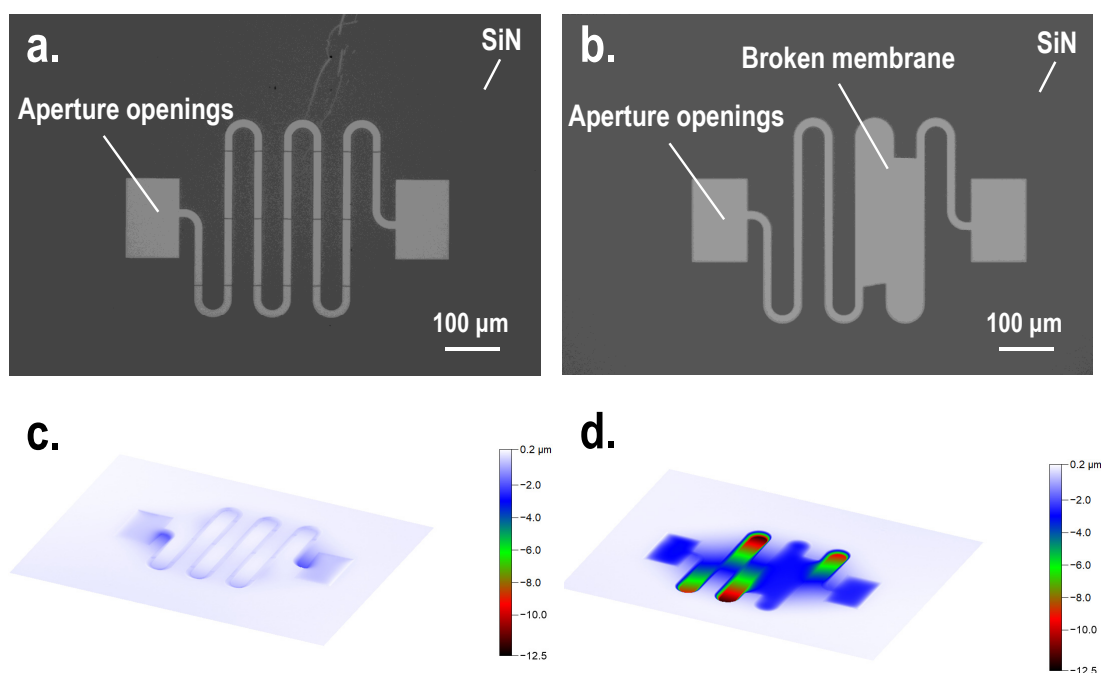


Figure 4.18: **Optical and confocal images of stencils with and without microbridges.** Optical images of stencils **a.** with and **b.** without microbridges. The confocal images showing the membrane bending after releasing the SiN membrane in stencils **c.** with and **d.** without microbridges.

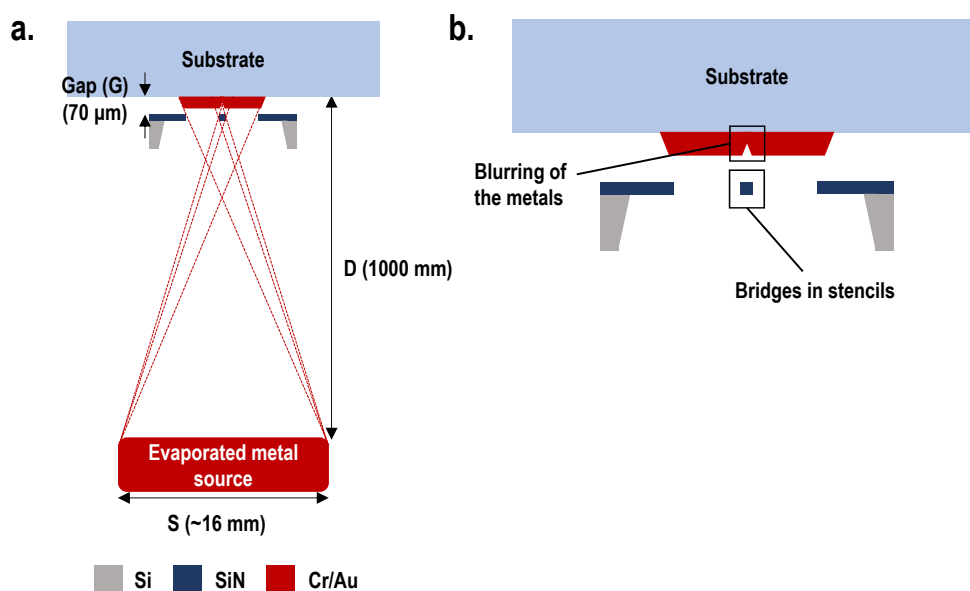


Figure 4.19: **Schematic drawings showing the blurring effect.** **a.** Schematic drawing showing the line-of-sight evaporation process. **b.** Zoom-in view of the substrate, deposited metals and the stencil, which shows the blurring of the metals under the shadowed bridge region.

The electromechanical characterization is performed on EGaIn resistors patterned with a microbridge stencil on a PDMS substrate. The serpentine EGaIn resistor is characterized by stretching the device up to 80% strain with a step of 10% strain. After each measurement, the device is released to its original shape. The results indicate that the resistance recovers to its initial value even after stretching to 80% strain (Figure 4.20b). A relative resistance change along with the applied strain shows a maximum relative resistance change of 106% with an applied strain of 80% (Figure 4.20c). In addition to meander shaped resistors, the proposed microbridge stencil also enables interdigitated structures in the suspended membrane (Figure 4.21a). The confocal image shows a greatly reduced membrane bending in the stencil (Figure 4.21b) and thus allows the realization of an interdigitated capacitor. The capacitance is measured using a LCR meter (4285A, HP) with an applied voltage of 500 mV and a frequency of 500 kHz. The measured initial capacitance is around 0.3 pF and the relative capacitance change shows a linear relationship with the applied strain having a slope of ~ 0.9 , which agrees well with the theoretical model derived by Fassler and Majidi [211] (Figure 4.21c). The equation used for the estimation of the relative capacitance change (ΔC) with the applied strain (ε) is derived in Ref. [211] and shown as Equation 4.2, where C_0 is the initial capacitance.

$$\varepsilon = \Delta C / C_0 \tag{4.2}$$

Chapter 4. Stretchable conductors fabricated by SL and centrifugal force-assisted patterning of LM

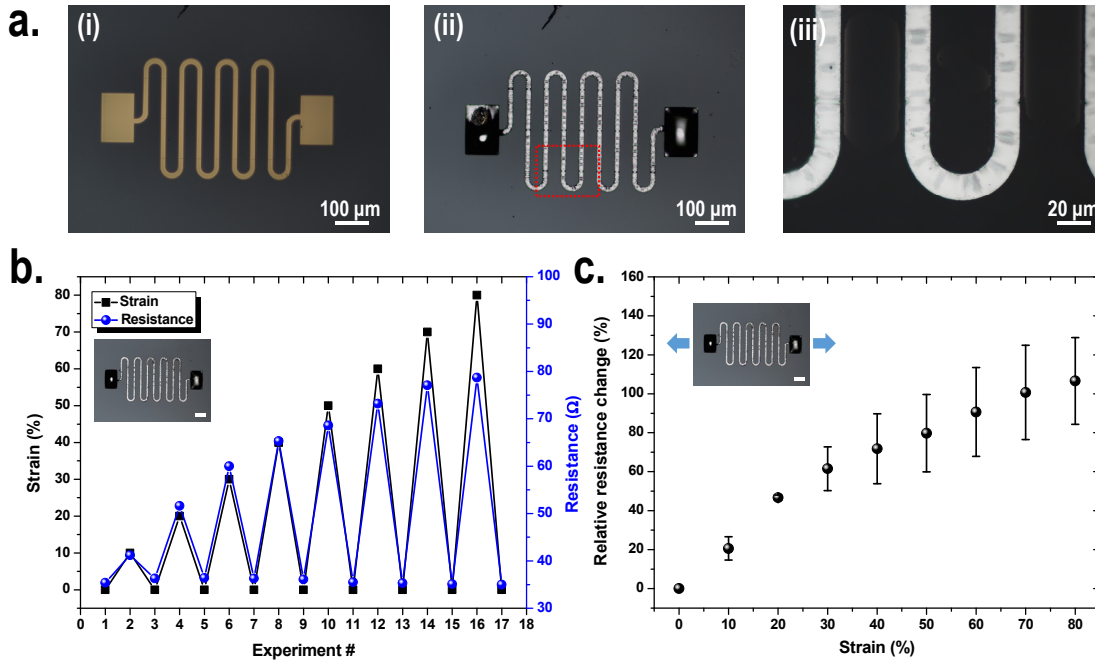


Figure 4.20: The fabrication results by the use of a microbridge stencil for patterning EGaIn.

a. Optical images of the sample during the fabrication steps: (i) Deposited continuous Cr/Au pattern after removing the stencil mask. (ii) Patterned EGaIn serpentine structure and (iii) its zoom-in view. **b.** Electromechanical characterization results of the patterned LM structures with a microbridge stencil. The inset shows the optical image of the tested sample. Scale bar: 100 μm . **c.** Relative resistance change as a function of the applied strain. Error bar shows the standard deviation of the measured two samples.

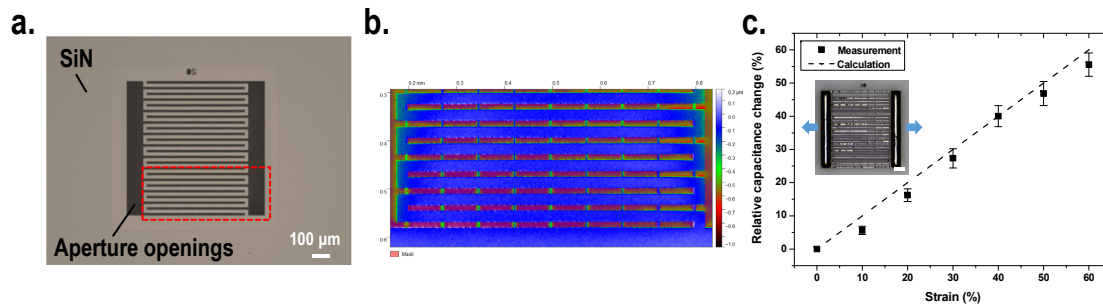


Figure 4.21: The use of a microbridge stencil with interdigitated apertures for an interdigitated EGaIn capacitor. **a.** An optical image of the fabricated microbridge stencil with interdigitated apertures. The red square indicates the region where a confocal image is taken. **b.** The confocal microscope image shows that the bending of the fabricated stencil is less than 0.2 μm . **c.** Measured and computed relative capacitance change as a function of the applied mechanical strain. The inset shows the optical image of the tested sample. Scale bar: 100 μm . Error bar shows the standard deviation of the measured two samples.

4.3 Conclusion

The results reported in this chapter demonstrate an original process that combines stencil lithography and centrifugal force-assisted patterning of liquid metal for the realization of EGaIn-based stretchable electronics. Using the selective wetting property of oxide-removed EGaIn, micrometer patterns with resolution down to $2\ \mu\text{m}$ can be obtained with micrometer scale wetting contrast patterns. Stencil lithography allows patterning metal traces, that EGaIn wets, without harsh chemical treatments and thus can be applied to soft, biodegradable polymer materials. The stencil can also be used several times to reduce fabrication costs. The centrifugal force experienced from spinning the substrate allows for the removal of excess materials in a highly controllable manner, thereby enabling micrometer EGaIn patterns. The patterned EGaIn on a flexible and biodegradable POMaC substrate demonstrates its suitability for a wider range of substrates. The presented method enables shaping EGaIn into a variety of patterns. Furthermore, the fabricated EGaIn patterns show low electrical resistivity ($0.39\ \Omega\cdot\mu\text{m}$) and excellent electromechanical response under large uniaxial deformation. In particular, it can endure an applied strain of 40% over thousands of cycles without significant change in its electrical performance. The proposed microbridge stencil broadens the design flexibility of stencil lithography. With a microbridge stencil, an EGaIn resistor with a serpentine structure and an interdigitated capacitor are demonstrated. The fabricated meander resistor can be stretched up to 80% strain and recovered to its original shape without significant change in its electrical resistance. The performance of the fabricated interdigitated capacitor under the applied strain agrees well with theoretical calculation. Comparing to the reported selective wetting process for patterning liquid gallium alloy, the presented work shows an improved pattern resolution without harsh chemical treatments and thus enables extending the method to a wide range of substrate materials such as biodegradable polymer materials (Table 4.1). The work presented here provides a simple and versatile method to fabricate liquid metal-based stretchable conductors.

Table 4.1: **Comparison of the reported selective wetting process**

	Adhesive layer	Resolution	Applied processes
Ref. [197]	Cr/Au	$10\ \mu\text{m}$	Resist-based lithography Manual rolling
Ref. [198]	Cr/Au/Cu	$2\ \mu\text{m}$	Resist-based lithography Electroplating process Manual rolling
Ref. [27]	Cr/Au	$50\ \mu\text{m}$	Resist-based lithography Manual shaking
Ref. [196]	Cr/Cu	$40\ \mu\text{m}$	Laser cutting Manual pipette jetting
This work	Cr/Au	$2\ \mu\text{m}$	Stencil lithography centrifugal force-assisted patterning

5 Stretchable silicon nanomembrane conductors enabled by liquid metal interconnections

The purpose of this chapter is to translate the fabrication processes developed in Chapter 4 to realize stretchable Si nanomembrane (NM) conductors. Research interests in Si NM are firstly introduced. The design considerations of the proposed device scheme are discussed with finite element simulation results. Next, the transfer printing technique for transferring single crystalline Si NMs to polymer substrates is presented, followed by the demonstration of the fabrication process for integrating liquid metal (LM) to Si NMs on a stretchable substrate. Finally, electrical characterizations are performed and the results are discussed.

5.1 Introduction

Single crystalline silicon (Si) has been widely used in advanced electronics due to its excellent electrical properties and easily-obtained high-quality dielectric materials (e.g., SiO₂). These properties make it an enabling building block for tremendous applications used in our daily life. Owing to the growing need for human healthcare, the development of flexible and wearable electronics has attracted significant attention. However, the brittle nature of Si hinders its potential application for wearable electronics.

The flexibility of materials can be described using the flexural rigidity (D). It can be expressed by Equation 5.1, where E is the Young's modulus, h is the thickness and ν is the Poisson's ratio of the material, where the strong relationship between the thickness and the flexural rigidity is presented. Therefore, a high degree of flexibility of materials can be obtained by reducing their thickness. Recently, nanometer-thick Si has been widely utilized for the realization of high performance flexible and stretchable electronics (Figure 5.1). The SEM image shown in Figure 5.1a illustrates the exceptional flexibility of Si NMs [212]. The theoretical calculation of the flexural rigidity and the energy release rate of Si elucidate the excellent bendability of Si when its thickness is reduced to the nanometer scale (Figure 5.1b) [212]. Additionally, it was experimentally demonstrated that the piezoresistive coefficient of Si NMs inversely increases as a function of the thickness (Figure 5.1c) [213, 214]. Moreover, the kinetics of hydrolysis of Si enables the dissolution of Si NMs in PBS solution at 37 °C (Figure 5.1d) [103]. These properties make Si NM an excellent candidate material for flexible and stretchable or bioresorbable electronics.

$$D = \frac{Eh^3}{12(1 - \nu^2)} \quad (5.1)$$

One of the most common approaches to realizing functional Si NM devices on various substrate materials is the transfer printing technique. The working principle of the transfer printing technique is to transfer functional devices prefabricated on a rigid substrate to the target substrate by using a viscoelastic stamp. Typically, the fabrication starts from a silicon-on-insulator (SOI) wafer where a thin single crystalline Si layer is bonded to an oxidized Si carrier wafer. Si electronics or integrated circuits are fabricated on a SOI wafer using the top Si layer as semiconducting material. Then, the buried oxide layer is etched to release the devices, followed by using an elastomer stamp (e.g., PDMS) to pick up the released devices and subsequently print them to the target substrate. To enable a high yield of the transfer printing, the adhesion control between stamps, Si devices and substrates is essential. The adhesion energy (i.e., the separation energy) can be evaluated by the energy release rate (G), which is defined as the energy dissipated to separate surfaces per unit area [24, 215]. It was reported that the energy release rate could be kinetically controlled by applying different peeling rates [24] and different bending radii of a stamp [215]. The fast peeling rate and

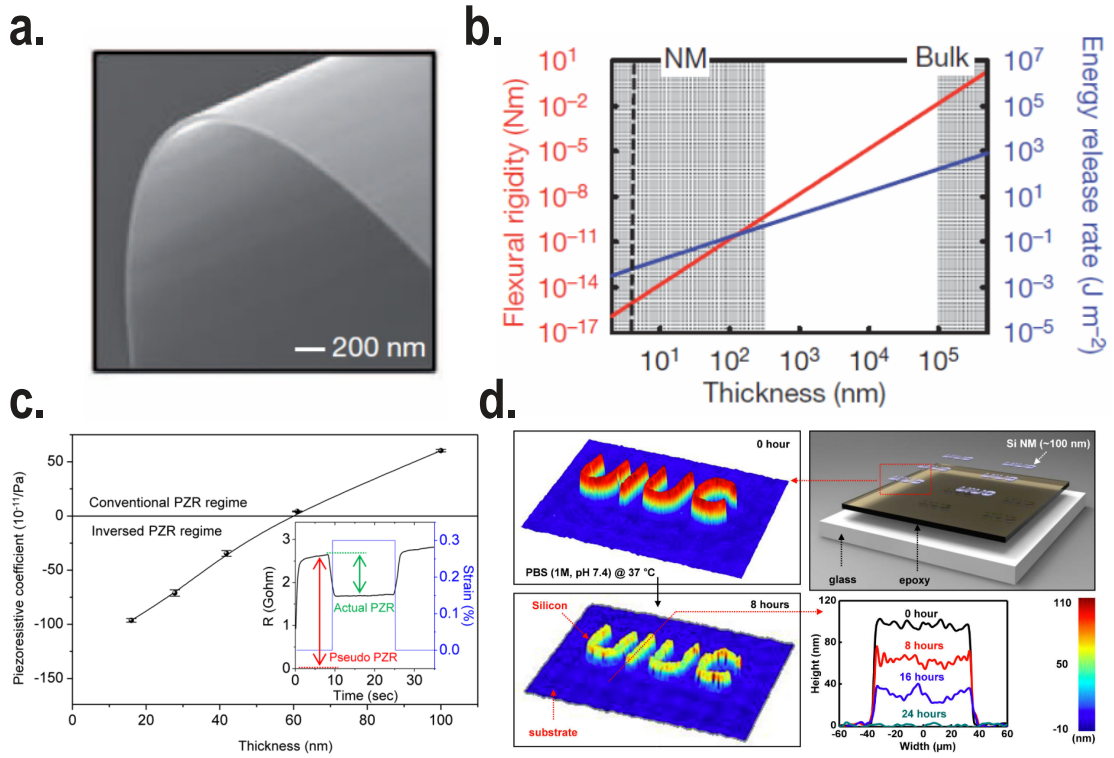


Figure 5.1: **Properties of Si nanomembranes (NMs).** **a.** SEM image showing a high degree of flexibility of Si NMs. Reprinted with permission from [212]. **b.** Theoretical calculation revealing the greatly decreased flexural rigidity with the reduced Si thickness. Reprinted with permission from [212]. **c.** The piezoresistive coefficient of Si NMs as a function of the thickness. Reprinted with permission from [214]. **d.** The resorbability of Si NMs. The thickness of Si NMs decreases with time when being immersed in PBS solution at 37 °C. Reprinted with permission from [103].

large bending radius of the stamp lead to the large energy release rate (i.e., relatively strong adhesion) between the elastomer stamp and solid objects and thus are applied for picking up the devices. On the other hand, the slower peeling rate and small bending radius of the stamp result in the smaller energy release rate (i.e., relatively weaker adhesion), thereby being used to print the devices. Using (3-mercaptopropyl)trimethoxysilane (MPTMS) as a molecular adhesive, the adhesion between Au films and the stamp was promoted through chemical reactions, enabling printing micrometer features with high yield [216]. Apart from the widely used PDMS stamp, a commercially available adhesive matrix with embedded expandable microspheres was employed as alternative stamp material. The switchable energy release rate induced by expandable microspheres was achieved by applying different temperatures to the stamp to enable a high yield in the transfer printing process [217].

Tremendous Si NM devices with different functionalities have been demonstrated by transferring prefabricated functional devices to various substrate materials. For example, embedding Si NM sensors in PI and subsequently transferring them to a stretchable PDMS substrate has

Chapter 5. Stretchable silicon nanomembrane conductors enabled by liquid metal interconnections

enabled a variety of stretchable Si NM devices, such as integrated circuits [101], pressure, strain and temperature sensors [105]. By functionalizing Si NM with Pd nanoparticles, flexible hydrogen sensors based on Si NM transistors were demonstrated [218]. Furthermore, the resorbability of Si NM paves an enabling step towards the realization of high performance bioresorbable electronics and integrated circuits. Bioresorbable Si NM pacemaker [219], gas sensor [220] and integrated electronic systems for monitoring brain activities [47, 221] were presented.

Regardless of the significant achievements in wearable and stretchable Si NM sensors and electronic devices, the stretchability of such devices mainly relies on the geometrical deformation of patterned metal conductors [48], which limits the usable density of the functional devices. To solve this challenge, in this chapter, we present a device scheme where functional Si NM devices are connected to intrinsically stretchable liquid metals (e.g., EGaIn) to enable decent stretchability in a small form factor. The proposed device scheme could serve as a building block to realize high density stretchable electronics based on single crystalline Si.

As a proof of concept, stretchable Si NM conductors are demonstrated in this chapter. The schematic drawings shown in Figure 5.2 describe the overview of the proposed stretchable Si NM conductors. Several Si NM ribbons are transferred to a PDMS substrate and are connected with EGaIn as electrical interconnections (Figure 5.2a). The cross-section reveals PI/Si NM islands and EGaIn interconnections embedded in PDMS. The PI layer is used to mitigate the mechanical strain on functional Si NMs and is bonded to the PDMS surface with the assistance of an intermediate Ti/SiO₂ layer. Cr and Au layers are used as adhesive for EGaIn conductors (Figure 5.2b).

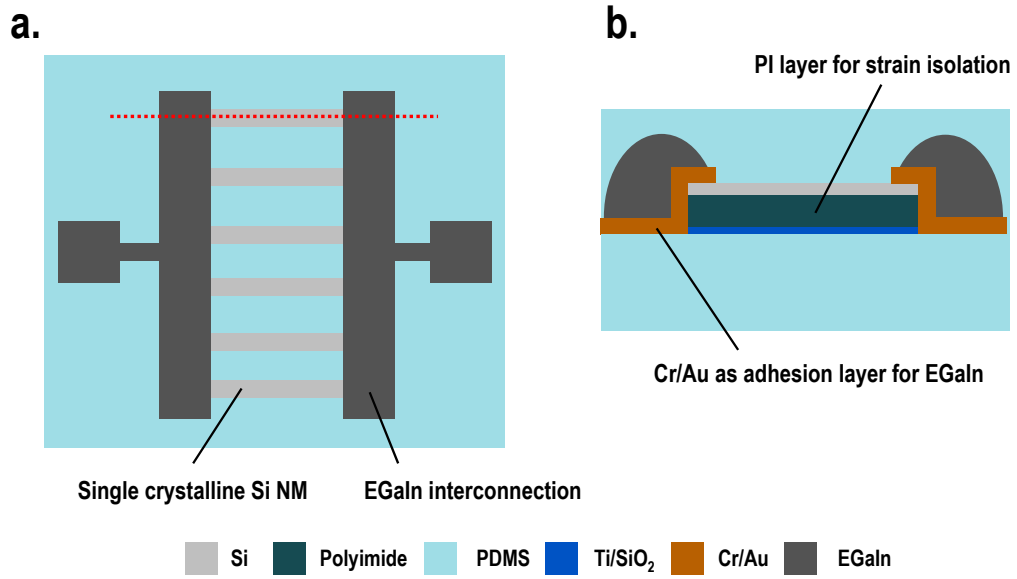


Figure 5.2: **Schematic drawings of the proposed stretchable Si NM conductors.** **a.** Schematic drawing showing the top view of the device containing single crystalline Si NMs and EGaIn interconnections. The red dashed line shows where the cross-section is extracted. **b.** Cross-section view of the device. A PI film is added underneath the Si NM for strain isolation. EGaIn adheres to Si NM and PDMS surface using Cr/Au as an adhesion layer. The entire device is embedded in PDMS. The drawings are not-to-scale.

5.2 Results and discussion

5.2.1 Simulation of the mechanical responses of stretchable Si NM conductors

Among all the design parameters for stretchable sensors, the strain and stress distribution is a crucial indicator that determines the mechanical responses of the sensors. For example, the strain on sensing materials determines the usable strain range. Sensors lose the ability to be elastically deformed when the experienced local stress/strain is larger than the yield strength/strain of materials [48]. Mismatches in the elastic modulus of materials result in the stress concentration at the interface, especially in regions where the elastic modulus changes abruptly, leading to lower resistance against local delamination upon stretching [180]. Due to these concerns, in this paragraph, we detail the mechanical responses of the proposed device by using finite element analysis (FEA) with simplified 2D models.

In the beginning, we investigate the effect on the thickness of a supporting PI layer. The structure used for simulation contains a Si NM having a thickness of $0.2\ \mu\text{m}$, supported by a thin PI layer with thicknesses ranging from 0 (i.e., no PI support) to $10\ \mu\text{m}$. The Si/PI structure is embedded in PDMS having a total thickness of 3 mm. A boundary load is applied on one side of the structure with the prescribed distance to have a global strain of 40%, while a fixed boundary is applied on the other side of the structure (Figure 5.3a). In this study, the von Mises stress is analyzed, which corresponds to the term "stress" in the following paragraphs. The simulation results indicate that the maximum strain and stress on the Si NM decrease as the PI thickness increases (Figure 5.3b). It is worth noting that without a PI layer (i.e., a thickness of $0\ \mu\text{m}$), the Si NM experiences a stress as large as 140 MPa, which is close to the yield strength of Si (165 MPa) [222]. The added PI layer dramatically reduces the local stress on Si NM and further extends its limit to sustain mechanical deformation. An example on the 2D strain contour map reveals an excellent capability of strain isolation with the applied PI supporting layer (Figure 5.3c). The strain distribution across the vertical centerline of the device shows the significantly reduced strain on Si/PI structures (Figure 5.3d). The zoom-in view of the strain distribution reveals the slightly decreased strain with the increased PI thickness (Figure 5.3e). The stress distribution provides an aspect concerning resistance against local delamination. The result points out the excessive stress concentration in regions where the elastic modulus changes dramatically (i.e., at the boundary between PI and Si NM, Z_{Si}) (Figure 5.3f). As indicated in the zoom-in view of the stress concentration, less abrupt changes and smaller maximum stress values are noticed when the supporting PI layer is thicker (Figure 5.3g). The results conclude that the thicker PI layer enables higher resistance against local delamination during stretching and the capability of withstanding higher global strain before exceeding its yield point.

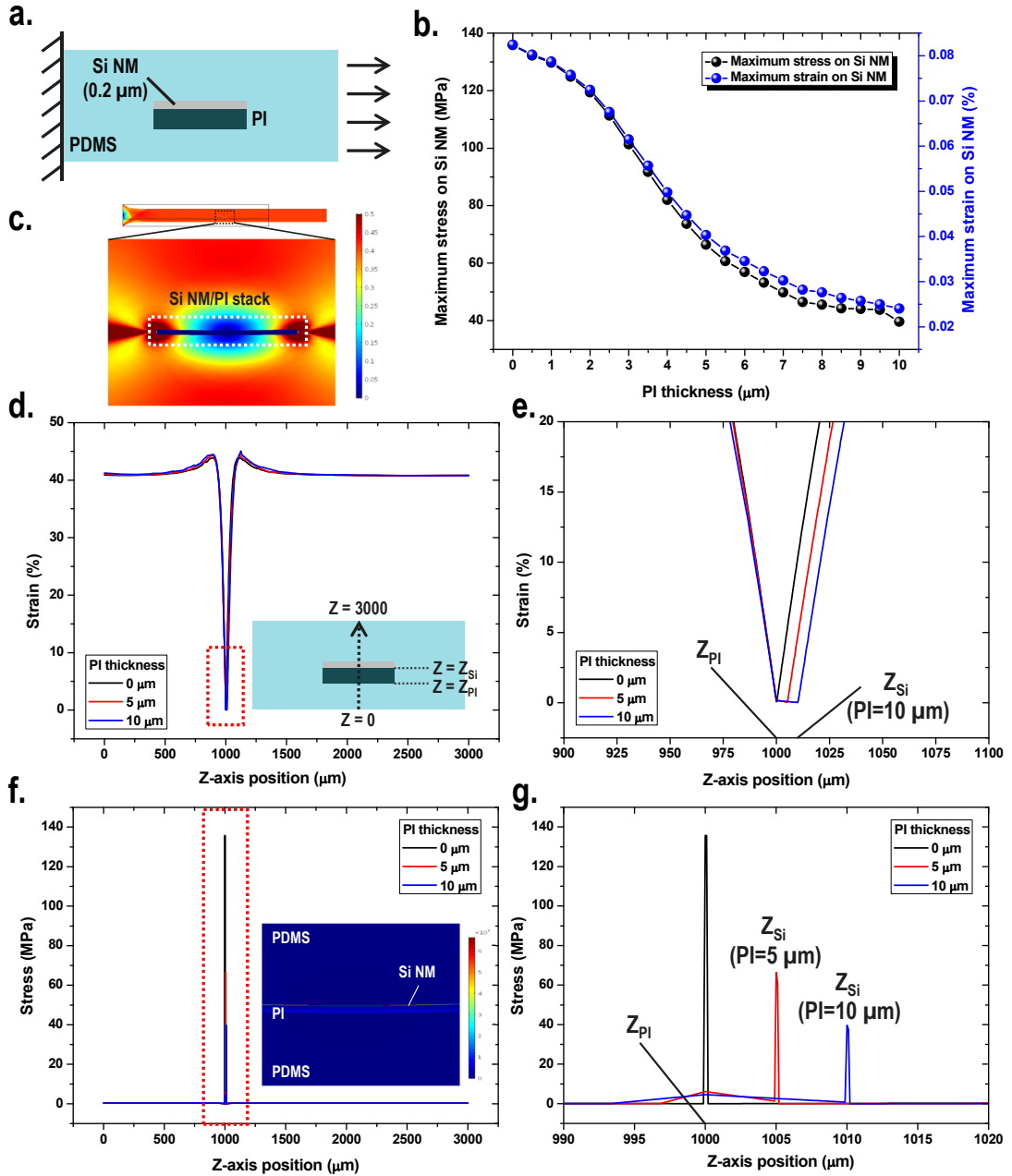


Figure 5.3: **FEA of the local mechanics of Si NM conductors with varying PI thickness.** **a.** Schematic drawing showing the simplified 2D model for FEA. The arrows show the direction of the applied prescribed displacement. A global strain of 40% is applied in the simulation. **b.** Summary of the maximum values of strain and von Mises stress on Si NMs as a function of PI thickness. **c.** 2D strain contour map showing the strain distribution under the applied global strain of 40%. A PI thickness of 5 μm is demonstrated here. **d.,e.** Strain and **f.,g.** von Mises stress profiles along the centerline of the device with varying PI thickness and their corresponding zoom-in views. The red dashed rectangles show regions where the zoom-in views are extracted. Inset in d. shows the cross-section view of the device. The black dashed arrow indicates where the strain and von Mises stress profiles are extracted. Inset in f. shows the 2D von Mises stress contour map of the sample having a PI thickness of 5 μm .

Chapter 5. Stretchable silicon nanomembrane conductors enabled by liquid metal interconnections

Next, we study the effect on the thickness of Si NM by fixing the PI thickness to $3.5\ \mu\text{m}$ under the consideration of the fabrication convenience (Figure 5.4a). The results indicate that the maximum strain and stress values on Si NM decrease as the thickness of Si NM increases. A considerable drop in strain and stress is observed when the thickness is less than 300 nm. Then, the changes in the thickness become less significant to the resulting strain and stress (Figure 5.4b). The strain distribution and its zoom-in view along the centerline of the device reveal a noticeable decrease in the strain on PI/Si NM (Figure 5.4c,d). The stress distribution indicates the smaller maximum values and less abrupt changes of the stress when Si NMs are thicker (Figure 5.4e,f).

To conclude, the simulation results indicate smaller strain and stress values on Si NMs when the thicknesses of both Si NM and PI increase. However, a few points need to be considered when designing the devices. First, the thickness of Si NM significantly influences the mechanical flexibility of devices, as indicated in Equation 5.1. To take advantage of the flexibility of Si NM and to consider the fabrication convenience, Si NMs with a thickness of about 200 nm are used, which can be easily obtained from commercially available SOI wafers. From the simulation results, a thickness of 200 nm could already provide a sufficient decrease in the local strain on Si NM (Figure 5.4b). Second, because LM needs to contact Si NMs located on the top of a PI layer, the thickness of the PI layer has to be thinner than a certain value. As a proof of concept and taking the process convenience into account, we choose a PI thickness of $3.5\ \mu\text{m}$ for the first attempt. The FEA results based on the selected geometrical parameters show a linear increase of the maximum strain and stress values on Si NM as a function of the applied global strain (Figure 5.5a). It reveals that the proposed device can endure a global mechanical strain up to 70%, which results in the local stress of about 160 MPa on Si NM (the yield strength of Si is 165 MPa [222]) (Figure 5.5a). In the last, we detail the stress distribution by plotting the local stress along the centerline of the device. The result shows a slight increase of the stress near the boundaries between PDMS/PI (i.e., Z_{PI}) and a larger increase at PI/Si NM interfaces (i.e., Z_{Si}) (Figure 5.5b). The results reveal that the proposed device might experience mechanical or electrical failure due to local delamination at the boundary between PI and Si NM or plastic deformation of Si NM under large strain.

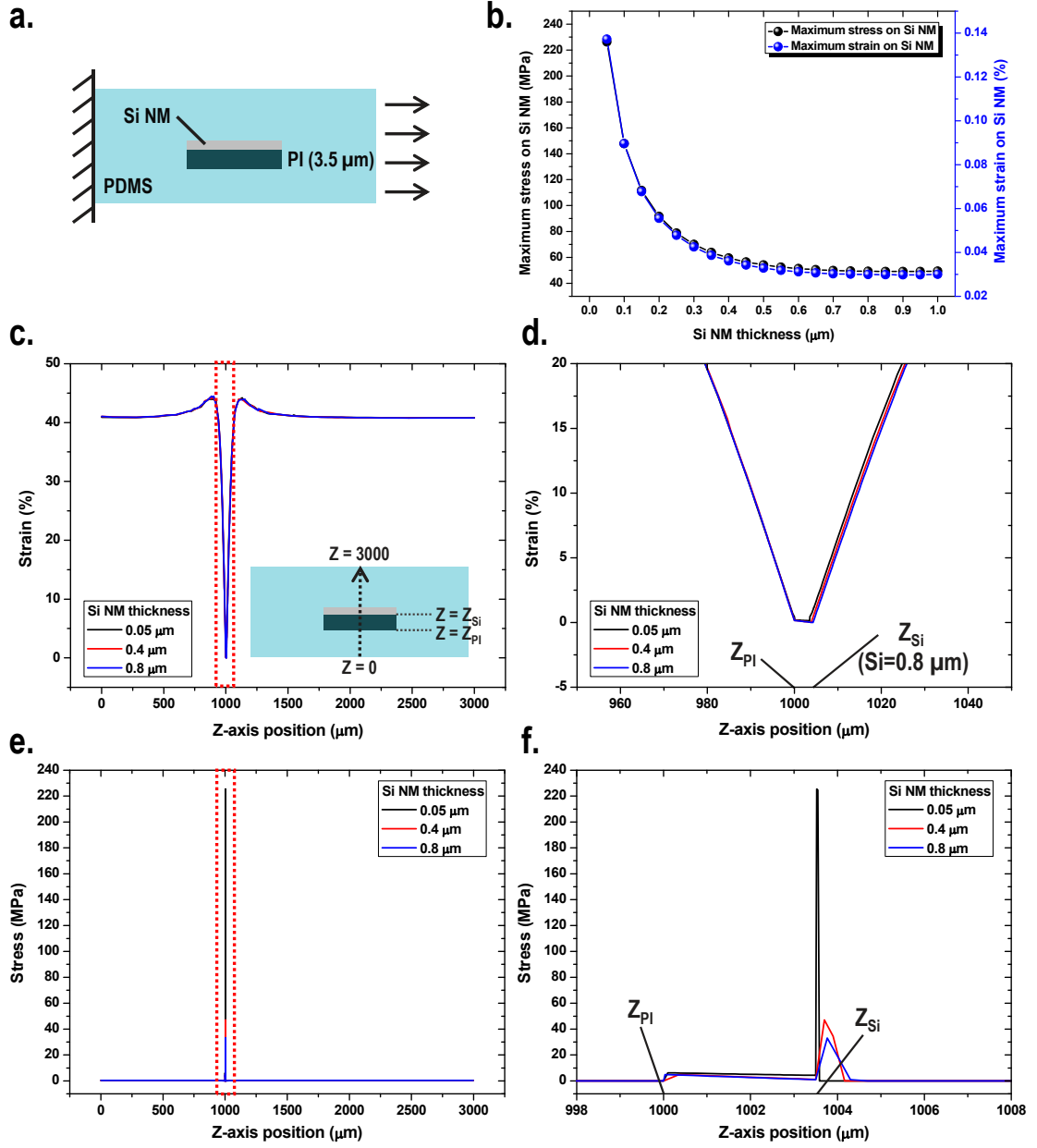


Figure 5.4: FEA of the local mechanics of Si NM conductors with varying Si NM thickness. **a.** Schematic drawing showing the simplified 2D model for FEA. The arrows show the direction of the applied prescribed displacement. A global strain of 40% is applied in the simulation. **b.** Summary of the maximum values of strain and von Mises stress on Si NMs as a function of Si NM thickness. **c., d.** Strain and **e., f.** von Mises stress profiles along the centerline of the device with varying Si NM thickness and their corresponding zoom-in views. The red dashed rectangles show regions where the zoom-in views are extracted. Inset in c. shows the cross-section view of the device. The black dashed arrow indicates where the strain and von Mises stress profiles are extracted.

Chapter 5. Stretchable silicon nanomembrane conductors enabled by liquid metal interconnections

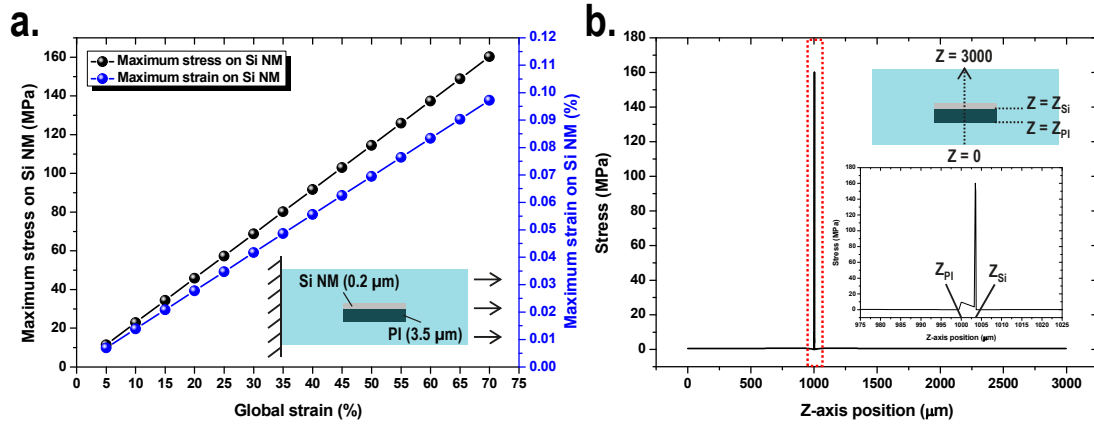


Figure 5.5: FEA of the mechanical responses of Si NM conductors under the applied strain.

a. Summary of the maximum strain and von Mises stress values on Si NMs as a function of the applied strain. Inset shows the schematic drawing of the simplified 2D model with geometrical parameters. **b.** Von Mises stress profiles along the centerline of the device under the applied strain of 70%. Inset shows the cross-section view of the device and the zoom-in view of the von Mises stress distribution.

5.2.2 Transfer printing of Si NMs to polymer substrates

To realize the proposed stretchable Si NM conductors, we start with the development of the transfer printing technique to transfer single crystalline Si NMs to polymer substrates. The process begins with patterning the top Si layer on a SOI chip, followed by etching through the buried oxide layer having a thickness of $2\ \mu\text{m}$ (Figure 5.6a-c). The released Si NMs are picked up by a PDMS slab and are subsequently printed to a PI substrate coated with a thin uncured PI layer as an adhesive (Figure 5.6d-f). During the printing procedure, a thin PI layer is firstly spin-coated on the PI substrate, followed by baking the film at $110\ ^\circ\text{C}$ for 40 s to have the semi-cured PI film. The PDMS stamp with Si NM structures is then gently brought into contact with the semi-cured PI film. Next, the PI substrate with the PDMS stamp attached is subjected to a thermal bake at $110\ ^\circ\text{C}$ for 30 s to facilitate the printing procedure. It has been reported that semi-cured epoxy flows around the edges of Si NM structures during the thermal baking process, thereby enhancing the bonding forces between the Si structures and the soft epoxy layer to enable the successful printing [223]. Finally, the PDMS stamp is peeled off from the PI substrate to finish the transfer printing process. However, in the presented process, after etching through the buried oxide layer using HF, the released structures leave the original substrate and are randomly distributed in the HF solution. The step-by-step optical images taken during the process show that some of the released Si NMs randomly fall on the handling Si substrate, leading to the unsuccessful printing results on the target PI substrate (Figure 5.7b-d).

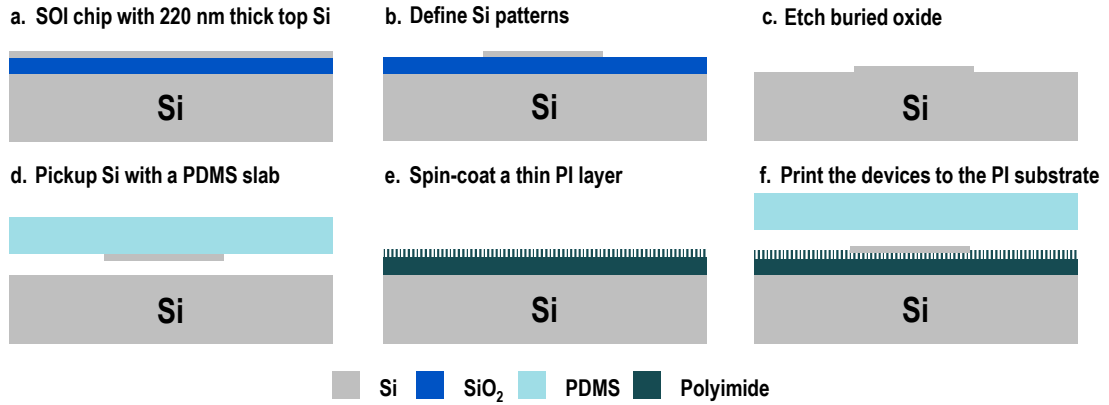


Figure 5.6: **Transfer printing of Si NMs to a PI substrate.** **a.,b.** Patterning Si NMs with photolithography and dry etching. **c.,d.** Releasing the patterned Si NMs using HF and subsequently picking up the released Si structures with a PDMS slab. **e.,f.** Printing the Si NM structures to a PI substrate coated with a thin uncured PI layer as an adhesive.

The results shown in Figure 5.7 indicate the necessity of having anchor points on patterned Si NMs in order to keep the released structures remaining on the handling Si substrate. The revised process utilizes photoresist (PR) coated under the periphery of Si NMs to keep the released structures staying at the original position (Figure 5.8) [224]. The space under the periphery of Si NMs is created by short under-etching of the buried oxide in 49% HF for 2

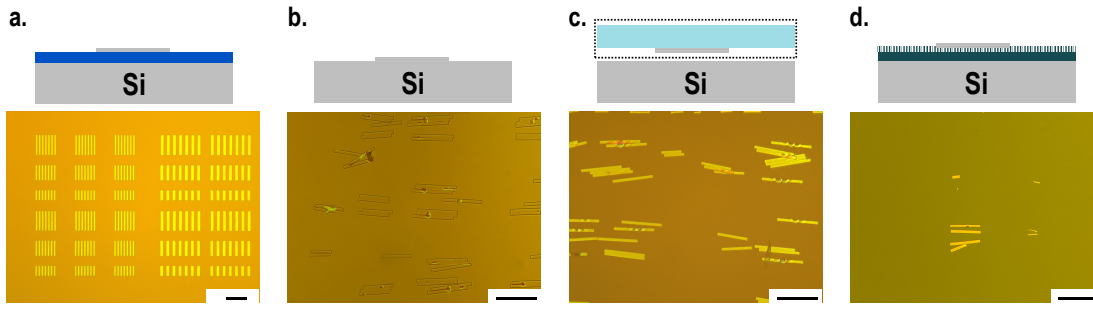


Figure 5.7: Optical images showing the process of transferring Si NMs to a PI substrate. a. Patterned Si NMs on a SOI chip. **b.-d.** After etching through the buried oxide layer, the released structures randomly fall on the handling Si substrate, resulting in the unsuccessful printing results. Scale bar: 200 μm .

mins to have a $\sim 2 \mu\text{m}$ undercut (Figure 5.8c). Subsequently, PR is spin-coated to cover the entire sample, including the region under the periphery of the patterned Si NMs. Because the entire Si surfaces are covered by PR after spin-coating, several openings are defined on the Si surfaces to provide the access for HF solution to etch the buried oxide layer. The openings are transferred to the Si NMs using plasma dry etching (Figure 5.8d). Anisotropic etching is then performed using O_2 plasma to remove the excess PR outside the Si NMs (Figure 5.8e). In this step, since the PR under the periphery of the Si NMs is protected by Si, it remains intact after O_2 plasma etching. In the following, the buried oxide layer is removed by HF via the opened release holes on the Si surfaces (Figure 5.8f). Thanks to the designed PR-surrounded anchors, the released structures remain on the original substrate. The released structures are picked up by a PDMS slab and then transferred to a PI substrate coated with an uncured PI layer as an adhesive (Figure 5.8g-i). The optical images show that the PR-surrounded anchors effectively keep the released structures remaining on the handling Si substrate after the buried oxide layer is completely removed, leading to the successful transfer printing of Si NMs having different geometries and sizes to a PI substrate (Figure 5.9).

The process reported in Figure 5.9 demonstrates that PR works as an excellent material for anchoring released Si NM structures. However, the formation of PR-surrounded anchors requires additional process steps, which makes the process not cost-efficient and time-consuming. To reduce the process complexity, we report on the use of strip-shaped PR to keep the released Si NMs remaining on the handling substrate. The anchors are formed by patterning PR to several strips on the top of Si NMs, which serve as a constraint to keep the structures remaining on the original substrate after etching through the buried oxide (Figure 5.10a-d). Through a detailed experimental study on the size and gap of PR strips, the strips having a width of $5 \mu\text{m}$ and a gap of $70 \mu\text{m}$ in between sufficiently bound the Si NMs on the handling Si substrate after the buried oxide layer is removed. The released Si NMs are then picked up by a PDMS slab and transferred to a PI substrate (Figure 5.10e,f). The optical images taken during the process verify the effectiveness of PR strip anchors, which perfectly bound the released Si NMs to stay on the underlying substrate (Figure 5.11a,b). Finally, the released structures are successfully

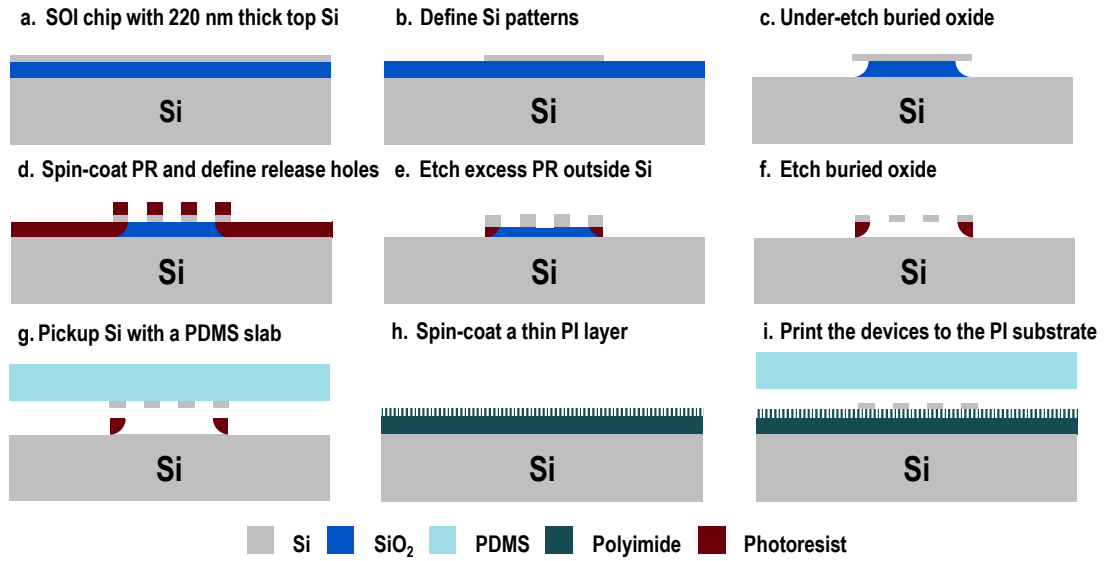


Figure 5.8: **Transfer printing of Si NMs to a PI substrate with PR-surrounded anchors.** Process flow of using PR-surrounded anchors to keep patterned Si NMs remaining on the handling Si substrate after the buried oxide layer is removed. The space under the periphery of Si NMs is created by short under-etching of the buried oxide using HF.

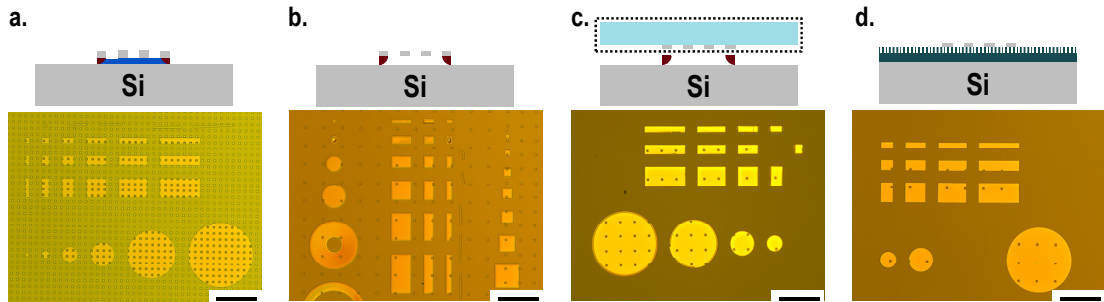


Figure 5.9: **Optical images showing the process of transferring Si NMs to a PI substrate with PR-surrounded anchors.** **a.** Patterned Si NMs with PR coated under the periphery of the Si NMs. Several holes are created on the Si surface to facilitate the etching of the buried oxide layer. **b.** After etching through the buried oxide layer, the released Si NMs remain on the handling Si substrate due to the presence of PR-surrounded anchors. **c.,d.** The successful transfer printing of Si NMs to a PI substrate. Scale bar: 100 μm .

transferred to a PI substrate via transfer printing (Figure 5.11c,d). The PR residues are observed but can be easily removed by dipping the sample in acetone afterwards.

It is important to note that a successful transfer printing process mandates the control of the peeling rate and radius of curvature of a PDMS slab. The pickup procedure is enabled by the fast peeling rate and the large radius of curvature of the PDMS slab. In contrast, the printing procedure requires the relatively slow peeling rate and the small radius of curvature of the

Chapter 5. Stretchable silicon nanomembrane conductors enabled by liquid metal interconnections

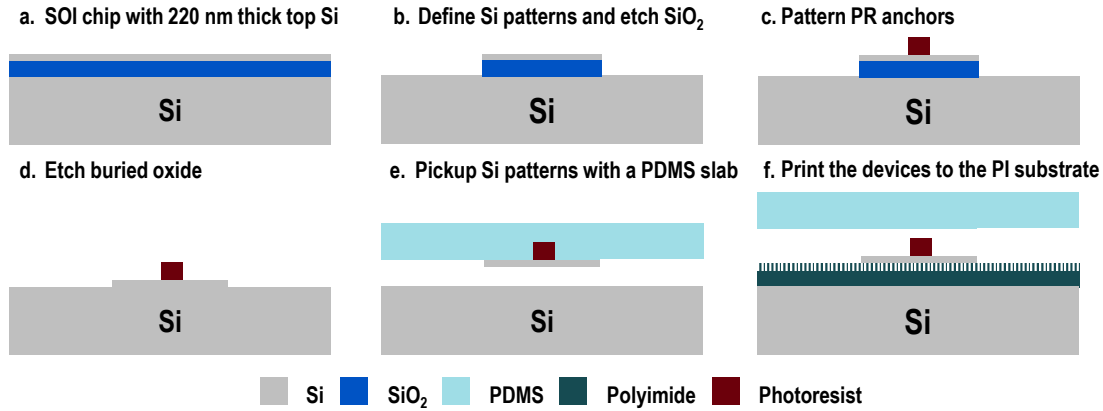


Figure 5.10: **Transfer printing of Si NMs to a PI substrate with strip-shaped PR anchors.** Process flow of using strip-shaped PR anchors to bound the released Si NMs to remain on the handling Si substrate.

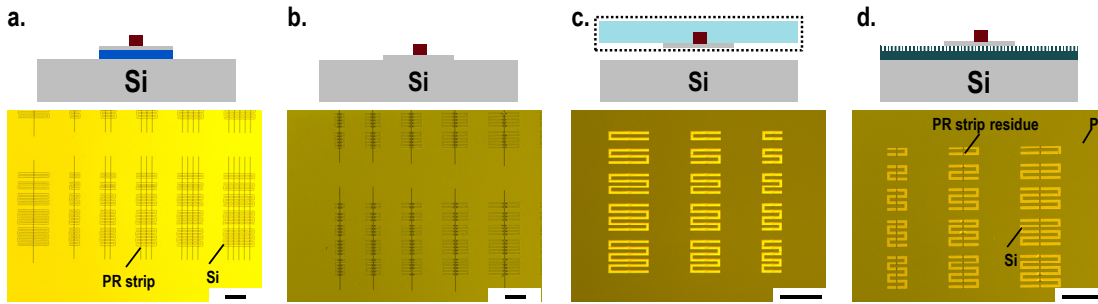


Figure 5.11: **Optical images showing the process of transferring Si NMs to a PI substrate with strip-shaped PR anchors.** **a.** Patterned Si NMs with PR strip anchors. **b.** After etching through the buried oxide layer, the released Si NMs remain on the handling Si substrate due to the presence of PR strips. **c.,d.** The successful transfer printing of Si NMs to a PI substrate. Scale bar: 200 μm .

slab. Due to the lack of an automatic transferring tool, the presented process is controlled by manual operations. Therefore, the applied peeling rate and radius of curvature of the PDMS slab are not stable among different batches, resulting in an unstable transfer yield.

5.2.3 Microfabrication of silicon NM conductors with LM interconnections

The transfer printing process developed in Section 5.2.2 has been experimentally demonstrated as an effective method to transfer the patterned Si NMs to a PI substrate. We utilize the developed process to realize stretchable Si NM devices using liquid metal as interconnections. As a proof of concept, we demonstrate stretchable Si NM conductors with heavily doped Si NMs as conducting material. A SOI wafer consisting of a buried oxide layer with a thickness of 2 μm sandwiched between a 220 nm thick Si device layer and a handling Si substrate is used. To obtain heavily doped Si NMs, POCl_3 diffusion doping process is performed on the entire SOI wafer. In the beginning, POCl_3 precursor is brought into a furnace to form phosphosilicate glass (PSG) through the oxidation process. The deposited PSG layer provides a phosphorus source that diffuses into Si through the following diffusion process. Afterwards, the formed PSG layer is removed using HF. Because Si is consumed during the oxidation process, the thickness of the Si NM is measured before and after the doping process. The result shows a thickness reduction on the Si device layer of about 30 nm (i.e., from 220 nm to 190 nm). After the doping process, the Si NMs are patterned into several microribbons having a width of 15 μm and a length of 180 μm using a laser writer and plasma dry etching (Figure 5.12a,b), followed by patterning PR anchors on the Si structures (Figure 5.12c). An uncured thin PI layer is spin-coated on a PI substrate, which contains a 300 nm thick Al layer underneath PI as a sacrificial layer, as an adhesive between the Si NMs and the substrate, followed by transferring the patterned Si NMs to the PI substrate (Figure 5.12d,e). After the printing process, PR anchor residues are removed by immersing the wafer in Acetone for 6 hrs (Figure 5.12f). In the following, the adhesive PI film is cured in an oven at 300 °C for 1 hr with N_2 flow (Figure 5.12g).

Next, a PDMS slab is covered on the sample, followed by etching through the sacrificial Al layer in diluted HCl ($\text{HCl}:\text{DI water}=1:6$) for at least 24 hours to release the Si/PI devices (Figure 5.12h,i). The applied PDMS slab ensures the flat surface of the released Si/PI films. The released thin film is subsequently bonded to another PDMS substrate. To facilitate the bonding process, thin Ti(5 nm)/ SiO_2 (30 nm) is sputter deposited on the backside of the sample (Figure 5.12j). The bonding is achieved by activating the bonding sides using UV-ozone for 3 mins, followed by manually laminating the sample on the PDMS substrate [101]. The bonded sample is then baked in an oven at 80 °C for 2 hrs (Figure 5.12k). In the following, anisotropic O_2 etching is applied to remove the exposed PI and thus, only PI underneath the Si NMs remains (Figure 5.12l).

The metallization process starts with dipping the device in dilute HF (10% HF) to remove Si native oxide. Then, a chip stencil is manually aligned on the device. Cr(4 nm)/ Au(60 nm) are sputtered deposited through the apertures of the stencil (Figure 5.12m). The removal of the chip stencil is assisted by using IPA, which swells PDMS to enable the successful removal of the stencil without damage. Next, EGaln is selectively deposited on the sputtered metal regions using the patterning technique developed in Chapter 4 (Figure 5.12n). Thereafter, big droplets of EGaln are administered on the contact pads of the device to allow the insertion of Cu wires for electrical characterization. Eventually, the device is encapsulated by gently

Chapter 5. Stretchable silicon nanomembrane conductors enabled by liquid metal interconnections

pouring liquid PDMS solution on the device and the PDMS is cured at room temperature for at least 48 hrs to complete the process (Figure 5.12o). The proposed device configuration and the presented process flow exhibit the following merits. First, the fabricated functional device is insensitive to mechanical deformation thanks to the applied intermediate PI layer, making it suitable for wearable applications. Second, the interconnection is formed by intrinsically stretchable materials (i.e., liquid metal, EGaIn), avoiding serpentine-patterned metal films. Thus, the usable density for functional devices increases. Third, the presented process flow utilizes stencils as a shadow mask to define metal films on the device, leading to reduced fabrication costs thanks to the reusability of stencils.

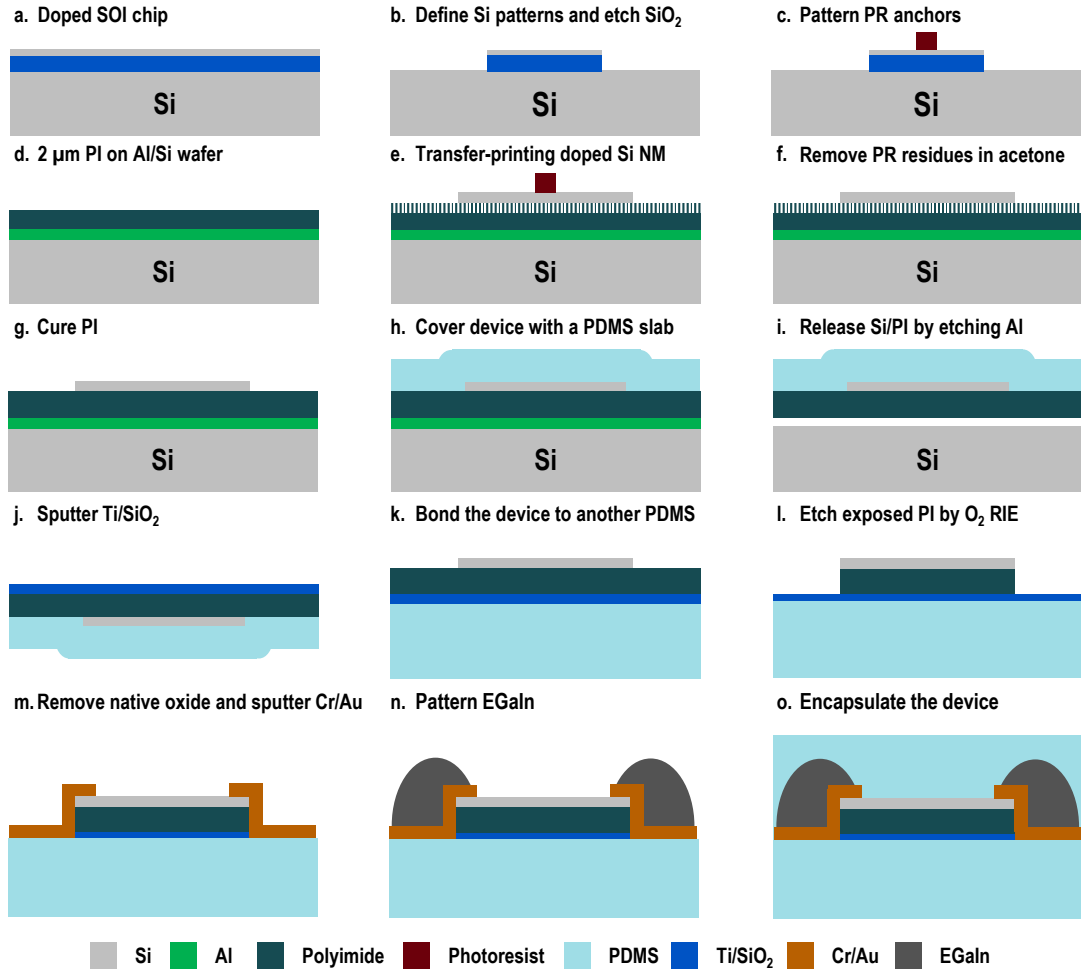


Figure 5.12: **Fabrication process of stretchable Si NM conductors with LM interconnections.**

a. A fresh SOI wafer is heavily doped using the POCl₃ diffusion process and is diced into square chips having a side of 12.5 mm. **b.** Defining Si NM structures and transferring the patterns to the SiO₂ layer. **c.** Patterning PR strip anchors. **d.,e.** Transfer printing of the patterned Si NMs to a PI substrate. **f.** Removing PR anchor residues by immersing the sample in acetone. **g.** Curing the PI adhesion layer. **h.,i.** Covering the device with a PDMS slab and releasing the PI film by etching through the Al sacrificial layer. **j.** Sputter deposition of Ti(5 nm)/ SiO₂(30 nm) on the backside of the device. **k.** Activating the bonding surfaces with UV-ozone and laminating the device to another PDMS substrate. The sample is then baked at 80 °C for 2 hours to finish the bonding process. **l.** Etching the exposed PI with O₂ plasma using Si NMs as a hard mask. **m.** Dip the device in diluted HF to remove Si native oxide, followed by sputter deposition of Cr(4 nm)/ Au(60 nm) through a chip stencil. **n.** Selective deposition of EGaIn on the Cr/Au patterns. **o.** Encapsulating the device with PDMS to complete the process.

Chapter 5. Stretchable silicon nanomembrane conductors enabled by liquid metal interconnections

Technical challenges While optimizing the presented process flow, two main challenges are encountered. First, during the removal of Si native oxide, Si NMs and PDMS surface are both exposed to dilute HF. The HF treatment turns the PDMS surface hydrophobic, resulting in a weaker adhesion to sputtered metal films. The weak adhesion between metals and PDMS leads to the peeling of the sputtered metal films during the removal of excess EGaIn. As shown in Figure 5.13, EGaIn only remains on the Si NM surface where the adhesion is supposed to be stronger. In contrast, metals deposited on the PDMS surface are mostly removed during the removal of excess EGaIn due to the weak adhesion between the metal films and the PDMS surface. The issue is resolved by decreasing the dipping time in 10% HF from 4 mins to 1 min. From the reported SiO₂ etching rate in 10% HF (~60 nm per min), an etching time of 1 min is enough to remove Si native oxide, which is typically less than 2 nm [225]. Second, due to the lack of stencil alignment equipment and the sticky nature of PDMS surfaces, the alignment of a chip stencil to the device, as shown in Figure 5.12m, remains challenging. When a stencil is brought into contact with a PDMS surface, the stencil adheres to the surface and cannot be moved for fine adjustment and re-alignment.

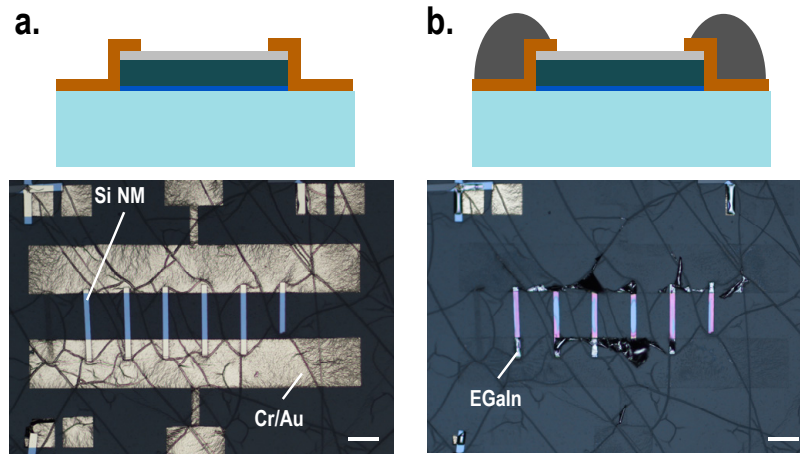


Figure 5.13: **Optical images showing the failures during the patterning of EGaIn.** **a.** After dipping the device in 10% HF for 4 mins, Cr(4 nm)/ Au(60 nm) are sputter deposited through an aligned chip stencil. **b.** After patterning EGaIn, most of the metals deposited on the PDMS surface are removed during the removal of excess EGaIn, whereas EGaIn remains on the Si NM surface. Scale bar: 100 μm .

Fabrication results with the optimized process parameters The optical images shown in Figure 5.14 detail the presented fabrication process. Si NM is firstly structured into several microribbons with a width of 15 μm and a length of 180 μm . PR anchors are patterned on the structures, which are used to keep the structures remaining on the underlying Si substrate after the buried oxide layer is fully etched (Figure 5.14a). Next, the Si microribbons are transfer-printed to a PI substrate coated with a semi-cured PI adhesive. The resist residues are removed by immersing the wafer in acetone for over 6 hours. The PI adhesive is then cured in an oven at the maximum temperature of 300 $^{\circ}\text{C}$ (Figure 5.14b). Afterwards, the PI film is released

by etching through the Al sacrificial layer with a PDMS stamp attached to the device. The released PI film is laminated to another PDMS substrate with a sputtered Ti/SiO₂ film as a bonding layer (Figure 5.14c). The applied PDMS stamp supports the released thin PI film and enables the successful printing of the film to another PDMS substrate. The optical image indicates the successful transfer of the thin PI film without any damage (Figure 5.14c). Later, O₂ plasma RIE is applied to etch the exposed PI using the Si microribbons as a hard mask (Figure 5.14d). Cracks on the PDMS surface are observed after RIE due to the bombardment of O₂ plasma. However, the cracks have a minor influence on the final device performance due to the following reasons. First, the electrical interconnections are made of an intrinsically stretchable material (i.e., LM). The electrical functionality of LMs remains intact even with the presence of cracks on the surface. Second, because functional Si ribbons are supported by PI films, no cracks are translated to the Si structures. The profile of the formed Si NM/PI island is characterized using a mechanical profilometer. The result points out a height of $\sim 3.5 \mu\text{m}$ of the fabricated Si NM/PI islands (Figure 5.15). Afterwards, a chip stencil is manually aligned on the device after dipping the sample in 10% HF for 1 min to remove Si native oxide. 4 nm Cr and 60 nm Au are subsequently sputter deposited through the apertures of the applied chip stencil. After the metal deposition, the stencil is removed by dipping the sample in IPA to keep the stencil membranes intact (Figure 5.14e). In the last, EGaln is patterned on the device by using the sputtered Cr/Au as an adhesion layer (Figure 5.14f). The result clearly shows that the shortened dipping time in 10% HF maintains a sufficient adhesion between the sputtered metals and the PDMS surface and enables the successful patterning of EGaln.

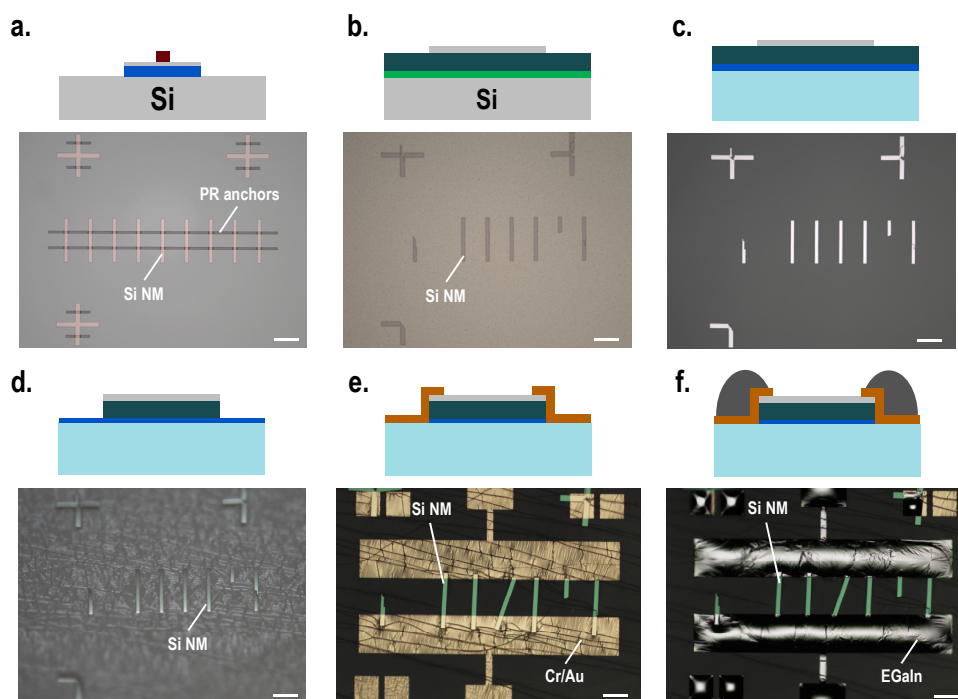


Figure 5.14: **Schematic drawings and the corresponding optical images showing the detailed process steps.** **a.** The fabricated Si NM microribbons and PR anchors. **b.** Transfer printing of Si NM microribbons to a PI substrate. **c.** PI film is released and transferred to another PDMS substrate. **d.** Excess PI is etched by using Si as hard masks. **e.** Removing Si native oxide in 10% HF for 1 min. Then, a chip stencil is manually aligned on the sample, followed by sputter deposition of Cr(4 nm)/ Au(60 nm). **f.** Patterning EGaln using the method presented in Chapter 4. Scale bar: 100 μm .

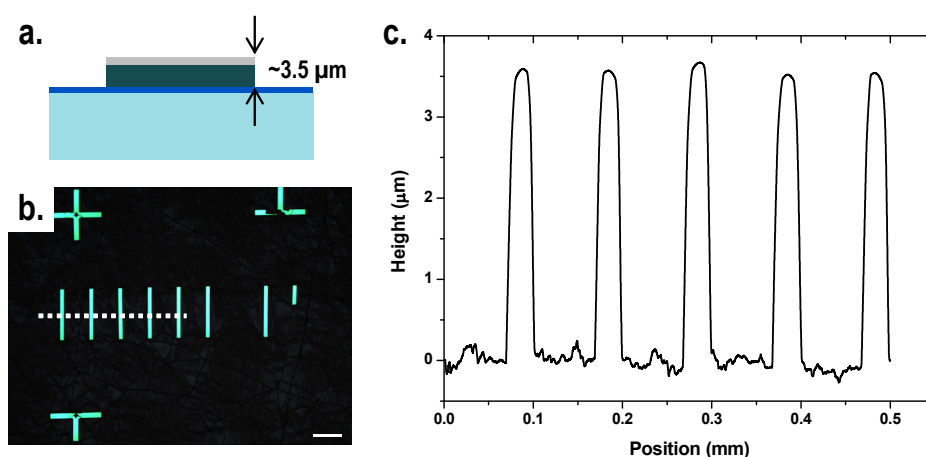


Figure 5.15: **Profile of Si NM/PI islands.** **a.,b.** Schematic drawing and the corresponding optical image showing the Si NM/PI island. The white dashed line indicates where the profile is extracted. Scale bar: 100 μm . **c.** The profile of the Si NM/PI islands measured using a mechanical profilometer.

5.2.4 Electrical characterization

The electrical characterization starts with extracting the resistivity of doped Si NMs using the four-point probe method. Cr/Au electrical contacts with an equal distance of 2000 μm are patterned on a doped SOI chip using the lift-off process. The sheet resistance is measured and calculated using the Equation 5.2 [226]. The results indicate a sheet resistance of $22.8 \pm 0.5 \Omega/\text{sq}$ from the measured 6 data sets. The resistivity is obtained by applying Equation 5.3, where t is the thickness of Si NMs, $F(t/s)$ is the correction factor and s is the distance between the measurement probes [226]. The calculated resistivity is $4.3 \pm 0.1 \Omega \cdot \mu\text{m}$, assuming the correction factor of 1 by considering the geometry of the measured sample, where s (2000 μm) is much larger than t (0.19 μm). The extracted resistivity corresponds to a doping level of about 10^{20} cm^{-3} [227]. The obtained high doping level is reasonable compared to the reported resistivity values of Si wafers doped using the POCl_3 doping process at the temperature similar to our case [228, 229]. In the presented case, the process is performed at 1050 $^\circ\text{C}$ for 5 and 15 mins for deposition and diffusion, respectively. Next, the electrical functionality of the transferred Si NM ribbons is characterized by measuring the resistance values before encapsulating the device (as shown in Figure 5.12n). Two big droplets of EGaIn are administered to the electrical contact pads to facilitate the resistance characterization. The optical images show the patterned Si NM device for resistance measurement (Figure 5.16a). The measurement is conducted by measuring the resistance of the sample with 4 Si ribbons using a digital multimeter (34401A, Keysight) with the applied current of 1 mA. Then, the resistance values of different numbers of Si ribbons are measured after manually scratching the ribbons. The measured resistance values follow the hyperbola relation, which agrees well with the resistance values calculated using the measured resistivity and the parallel circuit model (Figure 5.16b). The linear IV curve obtained using a source meter (2400, Keithley) confirms an adequate contact between EGaIn and Si NMs (Figure 5.16c). The results presented here confirm the successful connection of LMs to Si NM structures on a stretchable PDMS substrate.

$$R_s = \frac{\pi}{\ln(2)} \frac{\Delta V}{I} = 4.53236 \frac{\Delta V}{I} \quad (5.2)$$

$$\rho = R_s t = 4.53236 \frac{\Delta V}{I} t F\left(\frac{t}{s}\right) \quad (5.3)$$

Next, the electromechanical responses of the fabricated devices are characterized. Cu wires are placed on large EGaIn droplets as external connections to measurement instruments to enable real-time measurements of electrical signals during mechanical stretching. The device is then encapsulated with self-cured PDMS. After curing the encapsulated PDMS layer at room temperature for over 48 hours, the device is mechanically clamped at both ends on a commercial stretcher and electrical signals are measured through the inserted Cu wires

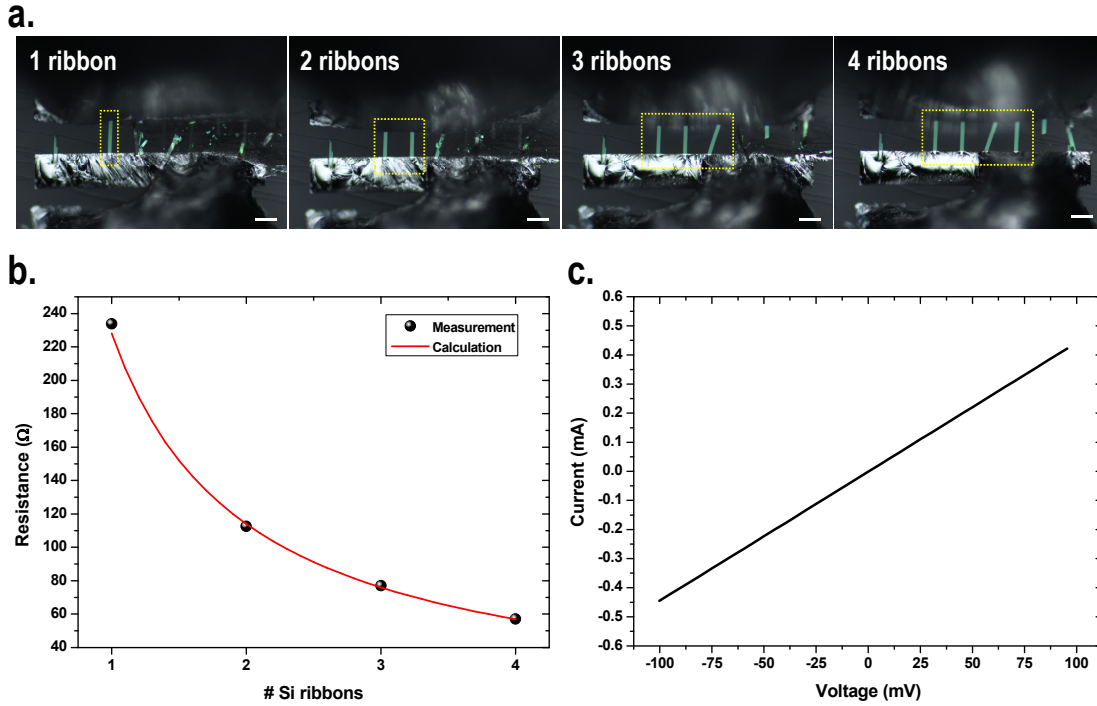


Figure 5.16: Resistance measurements of Si NM ribbons with LM interconnections. a. Optical images showing the measured device with different numbers of Si NM ribbons. The yellow dashed squares indicate the transferred Si ribbons. Scale bar: 100 μm . **b.** Measured and calculated resistance values as a function of different numbers of Si ribbons. **c.** The measured linear IV curve of the device with one Si ribbon.

(Figure 5.17a). The optical image details the fabricated Si NM ribbons connected to EGaIn interconnections (Figure 5.17b). The device is subjected to stretching cycles with a maximum strain of 40%. Electrical resistance values are captured during the cycling test by a source meter (2400, Keithley) with a sampling rate of 1 s. The optical images taken during the stretching test show the deformation of the sample under different applied strains, which presents the excellent stretchability of the device (Figure 5.18a). The measured resistance change during the cycling test is plotted as a function of time (Figure 5.18b). We observe continuously decreased resistance values in the first 50 cycles. Then, the resistance values become stable (i.e., without significant change from one cycle to another). The observed unstable resistance changes in the first few cycles are also observed in Section 4.2.2, where the resistance increases in the first few cycles of stretching, then the electrical responses become stable. In Section 4.2.2, we attribute the phenomenon to the crack formation on the adhesive Au surface or the re-oxidation of EGaIn. However, here we observe the decreases in the resistance values, so the reason behind the presented phenomenon might be different from the previous case reported in Section 4.2.2. The difference between the two cases is that in Si NM conductors, the resistance is dominated by Si NM ribbons instead of EGaIn interconnections. Therefore, we tentatively ascribed the phenomenon to the poor connection between the patterned EGaIn and the Si NM ribbons. Due to the added PI layers, there is a height difference of $\sim 3.5 \mu\text{m}$ between the Si ribbons and

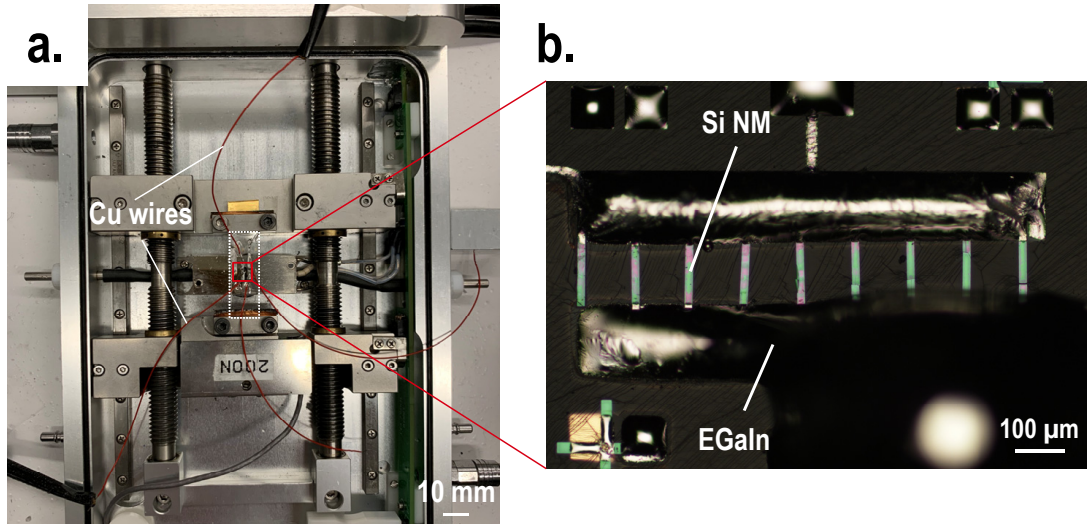


Figure 5.17: **Measurement setup for electromechanical characterization of stretchable Si NM conductors.** **a.** The sample is mechanically clamped on a commercial stretcher and is connected with Cu wires for real-time electrical characterization. The white dashed rectangle indicates the device under test. **b.** The optical image showing the zoom-in view of the red square in **a.**, indicating the Si NM structures connected with EGaIn interconnections. The image is captured before encapsulating the sample.

PDMS surface. After the first few stretching cycles, the connections between EGaIn and Si/PI mesas are stabilized and provide stable electrical signal outputs afterwards.

We observe that the device provides stable electrical outputs without significant changes in resistance between each cycle after the first few cycles of stretching. The device then remains electrically functional under the applied maximum strain of 40% for 1000 cycles (Figure 5.18b). To verify the stability of the device, after 1000 cycles of stretching, the device is released to its original state (i.e., 0% strain) and rested for 15 hrs, followed by the second cycling test. The results show similar resistance changes in the second cycling test without significant deviation from the first cycles (Figure 5.18b). The measurement data certifies that the device becomes stable after the first few stretching cycles and no longer experiences significant changes in its electrical functionality. Moreover, the result demonstrates that the fabricated Si NM conductors can sustain the applied strain of 40% for at least 1200 cycles without electrical degradation.

In the previous paragraph, we verify the excellent long-term stability of the fabricated Si NM conductors. However, the detailed view of the resistance change shows an irregular variation under applied strains (Figure 5.18c). The resistance decreases when the device is stretched and increases back to the original resistance value upon release. The resistance change follows the same trend throughout the entire cycling test. To elucidate the observation, the resistance variation during one cycle of stretching and releasing is plotted as a function of strain (Figure 5.18d). We observe serious hysteresis in resistance upon mechanical stretching and

Chapter 5. Stretchable silicon nanomembrane conductors enabled by liquid metal interconnections

releasing. Typically, the hysteresis of strain-resistance behavior results from the viscoelastic property of polymeric substrates and their interaction with the active materials (e.g., PDMS, PI and Si NM conductor in our case). It has been reported that high hysteresis originates from the weak binding between conducting materials and polymer substrates, which retards the fast recovery of conducting materials during the release of the device [230]. In the presented device, because the main contribution of the electrical resistance comes from Si NMs supported by PI films, the weak binding between the PDMS substrate and the PI supporting layer might contribute to the observed hysteresis, assuming strong bonding between Si NM and PI. We also notice an irregular resistance change with the applied strain (Figure 5.18d). The reason is tentatively attributed to unexpected bending of the device that occurs during stretching and releasing the device since Si NM conductors are not located at the neutral plane. However, it is essential to note that the observed resistance change during the cycling test is less than 2.5%, so the unstable contact between the inserted Cu wires and the device might also contribute to the observed phenomenon. Last, a step strain of 5% is applied to characterize the maximum strain capability of the fabricated Si NM conductor. The trend of the resistance change agrees with the data presented in the cycling test. It demonstrates that the device is capable of sustaining mechanical strain up to 50% with a maximum resistance change of about 3% (Figure 5.18e).

In short, here we present the electromechanical characterizations of the fabricated Si NM conductors. Regardless of the observed high hysteresis and irregular resistance changes with the applied strain, the device remains electrically functional under the maximum applied strain of 40% for at least 1200 cycles. Furthermore, due to the added PI layer underneath Si NM conductors, the device shows tiny resistance variation under large strain (e.g., 3% at the applied strain of 50%). The data presented here is a case study on stretchable Si conductors. The proposed device scheme and the developed process can be extended to realize strain-insensitive stretchable Si electronics.

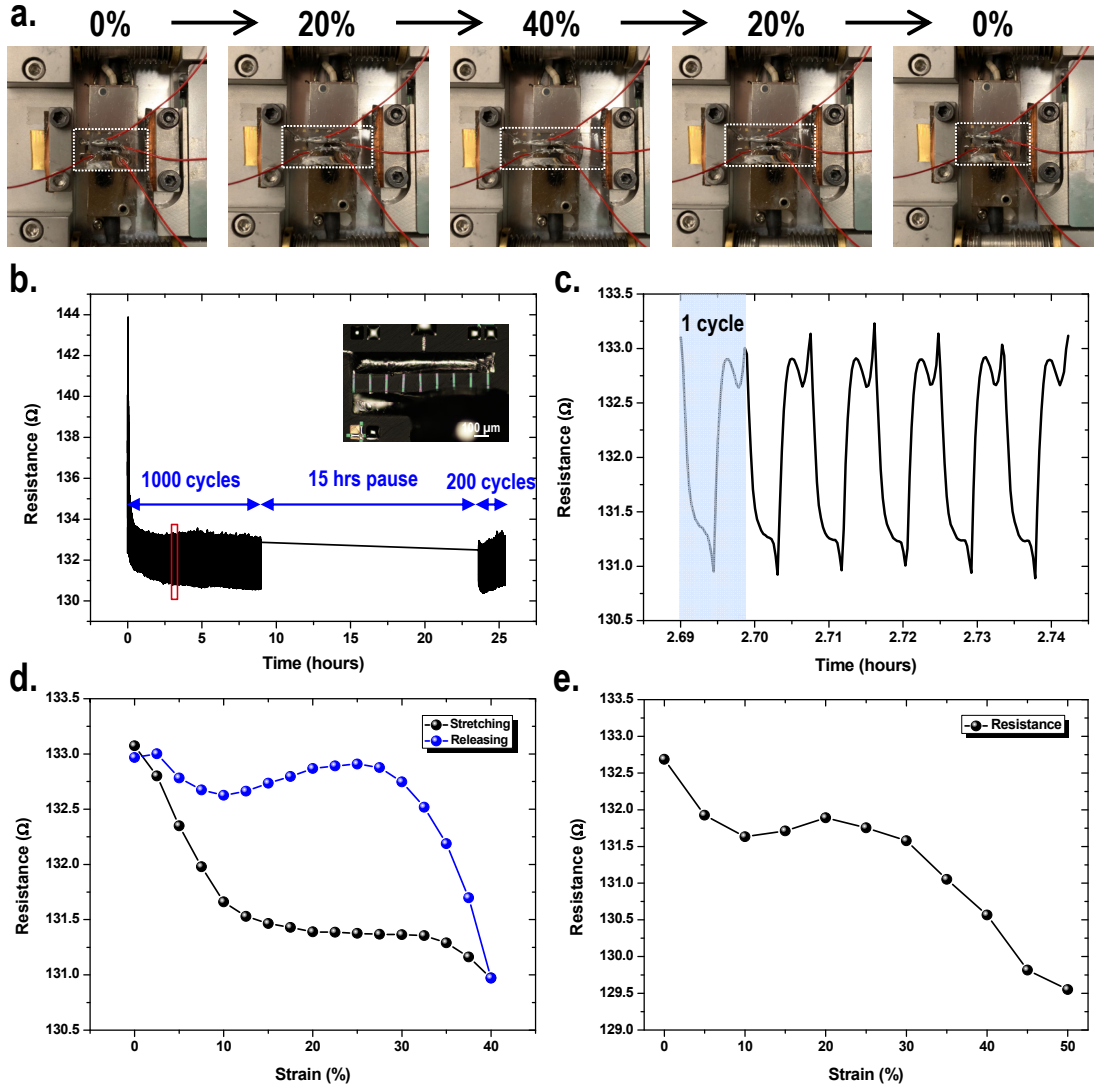


Figure 5.18: **Electromechanical characterization of the fabricated Si NM conductors.** **a.** Optical images showing the stretchable Si NM conductors subjected to mechanical strains. The white dashed rectangles indicate the fabricated sample under one stretching cycle. **b.** Electromechanical behavior of the fabricated Si NM conductor under stretching cycling test with the maximum applied strain of 40%. The strain is applied with a period of 32 s per cycle. Electrical resistance values are measured using a source meter with a sampling rate of 1 s. Inset shows the optical image of the measured device before PDMS encapsulation. The red rectangle indicates where the detailed resistance values are extracted. **c.** Zoom-in view of the resistance changes. **d.** Comparison of the resistance changes between the stretching and releasing of the device. **e.** Electromechanical characterizations of the Si NM conductor under the maximum applied strain of 50% with a step strain of 5%.

5.3 Conclusion

In this chapter, we present a novel concept for the realization of stretchable Si NM conductors. Single crystalline Si supported by a PI layer is transferred to a PDMS substrate and intrinsically stretchable liquid metals are connected to Si as interconnections. Compared to the state-of-the-art of stretchable Si devices, where Si is connected to serpentine-patterned metal films, liquid metal interconnections significantly increase the usable density for functional devices. PI layers applied underneath Si NMs isolate the strain on the Si structures, enabling the device to remain electrically functional under large mechanical deformation. Various transfer printing techniques are studied and discussed. The challenges in the transfer printing process are conquered, including introducing PR anchors to keep the released structures remaining at the original position and applying different radii of curvatures on a PDMS stamp during the transfer and printing steps. A fabrication platform combining the transfer printing and the liquid metal patterning techniques is developed to realize stretchable Si NM conductors on a stretchable PDMS substrate. Several fabrication challenges are discussed and improved. Static electrical characterization results indicate the successful formation of electrical contacts between transferred Si NM conductors and EGaln. The measured resistance values agree well with the theoretical calculation results. The stretching cycling characterization on the encapsulated sample shows steady electrical performance under the maximum applied strain of 40% for at least 1200 cycles. The observed hysteresis is discussed and is tentatively attributed to the weak binding between the PDMS substrate and the PI supporting layer. In the last, the electrical characterization under different applied strains shows that the device can sustain strains up to 50% without electrical failure. The results presented here demonstrate a case study of stretchable Si NM conductors with intrinsically stretchable liquid metals as interconnections. The concept can be extended to a wide range of Si NM electronics and circuits, paving a crucial enabling step towards high-density stretchable Si electronics.

6 Conclusion and perspectives

This chapter presents the main outcomes of the thesis and discusses possible future developments.

6.1 Conclusion

In this thesis, a systematic study on the deposition of metals on various substrate materials using stencil lithography is firstly introduced. Next, to overcome the limitation in the geometrical design flexibility of stencil membranes, a new stencil concept utilizing bridges to stabilize the suspended membrane is presented. The resolution of the proposed bridge stencil is improved to the nanometer scale by using a DUV stepper. The micro- and nanobridge stencils are applied on various substrate materials to demonstrate their versatility. The implementation of SL is further extended to pattern intrinsically stretchable liquid metals to realize high resolution stretchable LM electronic. Last, stretchable Si NM conductors are proposed and demonstrated using LM as electrical interconnections to Si NMs. The contribution of this thesis is summarized in the following.

A systematic study on the deposition of metals on polymer substrates using stencil lithography First, a detailed study on the deposition of metals on various polymer substrates using stencil lithography is presented. The selected polymer substrates include biocompatible PI, parylene, biodegradable PLGA and metastable PPA. The geometrical and electrical characterizations of the deposited metal structures are performed and discussed. The results show that the deposited metal patterns have similar geometries on the polymers except for PLGA. The distinct metal patterns on PLGA substrates are surrounded by PLGA fences built during the evaporation deposition process. The reason is attributed to the low T_g of PLGA. The high temperature evaporated source atoms transfer thermal energy to the PLGA surface, resulting in a temperature increase above its T_g and further triggering local reflow of PLGA. The electrical characterization results present similar resistivity values of the deposited metal films on polymer substrates, indicating that the observed irregular metal geometry on PLGA

substrates does not influence the electrical functionality. The study presented in this chapter describes the use of a resistless process to fabricate metal structures on different kinds of polymer substrates. The results presented here pave an important step for realizing wearable or implantable systems using a simple but versatile stencil technique.

Bridge stencils enabling almost arbitrary apertures on stencil membranes Next, a new stencil concept utilizing bridges to stabilize suspended membrane is proposed to conquer the challenge in SL, where the membrane stability constraints the geometrical design flexibility of aperture designs. The narrow bridges bound the suspended membrane to remain in the same plane as the surrounding membrane, allowing the realization of almost arbitrary apertures. Continuous metal traces are obtained by taking advantage of the blurring effect. When the stencil is lifted to an appropriate gap distance above the substrate, the line-of-sight evaporation process results in the material deposition under the shadowed bridge regions. Spiral structures at the micrometer scale are demonstrated on rigid and soft polymer substrates. A potential application for implantable heaters is investigated. Furthermore, the resolution of the proposed bridge stencil is improved to the sub-micrometer scale by using a DUV stepper. Sub-micrometer meandering structures are successfully fabricated on a variety of polymer substrates. The observed thickness reduction with the use of nanobridge stencils is explained by the reduced evaporation source size. The reflow behaviour observed on PLGA substrates is discussed with additional experiments performed using different deposition parameters. The more prolonged exposure of PLGA surfaces to evaporated source atoms results in more significant reflow behaviour. Last, nanobridge stencils are applied on stretchable substrates with material stiffness gradients to demonstrate their versatility. The results show the successful fabrication of sub-micrometer structures on a stretchable substrate composed of materials with different rigidity. The results presented in this chapter demonstrate the potential of producing almost arbitrary patterns by utilizing bridge stencils on a large variety of substrate materials, laying a solid foundation for the realization of multifunctional devices on various polymers.

High resolution stretchable LM electronics enabled by SL The use of SL is further explored to pattern intrinsically stretchable LMs. A hybrid process combining SL and centrifugal force-assisted patterning of LM is proposed to shape LM at the micrometer scale. The oxide-removed EGaIn selectively wets on metal traces produced using SL and the excess EGaIn is removed by the well-controlled centrifugal force. The developed process enables high resolution EGaIn patterns on a stretchable PDMS substrate with significantly reduced process complexity. Bridge stencils are applied to shape EGaIn into serpentine and interdigitated patterns for stretchable passive devices. Additionally, the proposed hybrid process enables high resolution EGaIn patterns on a biodegradable substrate for recyclable electronic applications. The results presented in this chapter show an essential step toward high resolution stretchable or recyclable LM electronics.

Stretchable Si NM conductors enabled by LM interconnections Last, stretchable Si NM conductors enabled by LM interconnections are proposed and realized. Single crystalline Si NM supported by a PI layer is transferred to a stretchable PDMS substrate and LM is connected to Si NM as electrical interconnections. The strain on Si NM is significantly reduced by the added PI layer and thus can sustain large global deformation. The applied LM conductors considerably reduce the required space for interconnections and provide high stretchability and excellent electrical conductivity compared to serpentine-patterned metal films. As a proof of concept, stretchable Si NM conductors are demonstrated using highly doped Si NMs as functional materials. FEA results provide design guidelines for the proposed devices. The fabrication platform to achieve such devices is developed, including the transfer printing technique for transferring single crystalline Si NMs to flexible PI substrates, the transfer of Si NM/PI films to a stretchable PDMS substrate and the integration of LM interconnections to Si NMs. The electrical characterization results show that the fabricated device can ensure 40% strain for at least 1200 cycles. However, a low process yield and serious electrical hysteresis under mechanical deformation are noticed. The serious hysteresis is tentatively attributed to the weak adhesion between PI and PDMS. More studies are required to improve the device performance and the fabrication yield. Overall, the results described in this chapter demonstrate a case study of stretchable Si NM conductors enabled by LM interconnections. The concept can be further extended to realize stretchable Si NM electronics for a wide range of applications.

In summary, the results presented in this thesis provide guidelines for the fabrication of functional devices on various substrate materials by using a simple and cost-efficient stencil technique. The bridge stencil addresses the challenges in the realization of complex aperture openings on the stencil membrane, extending the applications of SL. The developed hybrid process for high resolution LM patterns opens a new route for stretchable or recyclable electronic applications. Last, the demonstration of stretchable Si NM conductors enabled by LM interconnections provides an insight into the development of high density and high performance stretchable Si electronics.

6.2 Perspectives

Multifunctional wearable systems enabled by SL Combining with the results presented in Chapter 2 and 3, the developed stencil technique can be applied to achieve various kinds of structures on a wide range of substrate materials. The capability of bridge stencils has been demonstrated to realize commonly used structures for potential sensor applications. For instance, serpentine structures can be utilized as temperature and strain sensors. Spiral structures can be applied as an antenna for wireless power transmission. Thanks to the reusability of stencils, SL provides a cost-efficient method for high resolution manufacturing. Therefore, a multifunctional system containing temperature, strain and pressure sensors as well as wireless power transmission antennas for skin prosthetics can be realized by applying one single bridge stencil on polymer substrates with reduced fabrication complexity and costs.

Process and performance improvement of stretchable Si devices with LM interconnections

As discussed in Chapter 5, the low fabrication yield of stretchable Si conductors limits the study of device performance in detail and their applications. The low yield of transfer printing of single crystalline Si NM to a PI substrate can be improved by designing a customized automatic transferring tool. The tool enables well-controlled bending radii of stamps and peeling rates for device pick-up and printing (Figure 6.1). Additionally, in the presented process flow, the alignment of a chip stencil to a PDMS substrate remains challenging. It can be addressed by having a customized 3-axis microstage. Thanks to the sticky nature of a PDMS surface, the stencil adheres to the surface right after being brought into contact with PDMS, avoiding an extra step of tape fixing. Moreover, sometimes we observe that in the last PDMS encapsulation step, the hydrophobic property of HF-treated PDMS surface results in poor adhesion between the PDMS substrate and the PDMS encapsulation layer. An additional O_2 plasma treatment can be performed to increase its hydrophilicity before encapsulation.

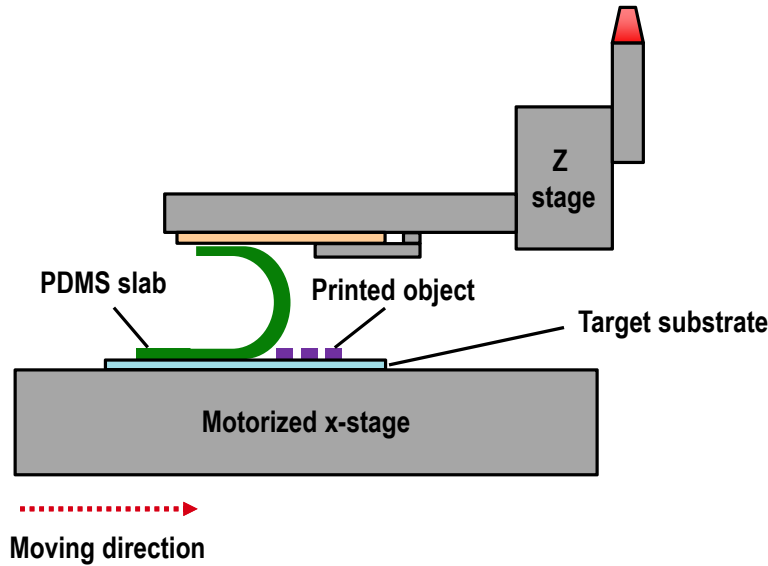


Figure 6.1: **Schematic drawing showing a customized tool for transfer printing.** The target substrate is fixed on the bottom motorized X-stage by a vacuum or mechanical system. The radius of curvature of a PDMS slab is controlled by bending the PDMS with a Z-stage. The peeling rate is controlled by moving the substrate with a motorized X-stage.

Regarding the device performance, the measurement results indicate serious hysteresis of the fabricated stretchable Si conductors, which is tentatively attributed to the weak bonding between PI and PDMS. The quantitative characterization of the adhesion between these interfaces (Si NM, PI and PDMS) is of great importance to understand the root cause and further improve the device hysteresis. Furthermore, in the current structure design, Si NMs are not located at the neutral plane, which results in unwanted resistance changes due to the bending of the devices. A proper design with the neutral plane on Si NMs is a critical aspect to improve the device performance.

High density stretchable Si electronics enabled by LM interconnections The results demonstrated in Chapter 5 provide an insight into the realization of stretchable Si conductors. The concept and the fabrication process can be extended to realize stretchable Si electronics having a variety of functionalities. Using the transfer printing technique, semiconducting Si NMs with selectively doped electrical contacts can be transferred to a PI substrate. Electronic circuits can be fabricated on the PI substrate using conventional fabrication processes thanks to the excellent thermal and chemical resistant properties of PI. The stretchable Si electronics can be eventually obtained by following the rest of the process reported in Chapter 5. The developed fabrication process, including transferring Si NM/PI films to PDMS and the integration of LM interconnections, avoids the use of harsh chemicals and thus can be generally used even with the presence of other materials (e.g., dielectric SiO₂). Due to the intrinsically unlimited stretchability of LMs, high density and high performance stretchable Si electronics can be realized for various wearable applications.

Bibliography

- [1] “Apple Watch Series 7.” [Online]. Available: <https://www.apple.com/apple-watch-series-7/>
- [2] “Garmin vivosmart 4 | Fitness Activity Tracker | Pulse Ox.” [Online]. Available: <https://www.garmin.com/en-US/p/605739>
- [3] “Xsensio | Lab-on-Skin Sensing Platform.” [Online]. Available: <https://xsensio.com/>
- [4] T. R. Cox and J. T. Erler, “Remodeling and homeostasis of the extracellular matrix: implications for fibrotic diseases and cancer,” *Disease Models & Mechanisms*, vol. 4, no. 2, pp. 165–178, mar 2011. [Online]. Available: <https://journals.biologists.com/dmm/article/4/2/165/53523/Remodeling-and-homeostasis-of-the-extracellular>
- [5] R. Das, F. Moradi, and H. Heidari, “Biointegrated and Wirelessly Powered Implantable Brain Devices: A Review,” *IEEE Transactions on Biomedical Circuits and Systems*, vol. 14, no. 2, pp. 343–358, apr 2020. [Online]. Available: <https://ieeexplore.ieee.org/document/8960457/>
- [6] Y. Liu, M. Pharr, and G. A. Salvatore, “Lab-on-Skin: A Review of Flexible and Stretchable Electronics for Wearable Health Monitoring,” *ACS Nano*, vol. 11, no. 10, pp. 9614–9635, oct 2017. [Online]. Available: <https://pubs.acs.org/doi/10.1021/acsnano.7b04898>
- [7] G. Acar, O. Ozturk, A. J. Golparvar, T. A. Elboshra, K. Böhringer, and M. K. Yapici, “Wearable and Flexible Textile Electrodes for Biopotential Signal Monitoring: A review,” *Electronics*, vol. 8, no. 5, p. 479, apr 2019. [Online]. Available: <https://www.mdpi.com/2079-9292/8/5/479>
- [8] P. J. Derbyshire, H. Barr, F. Davis, and S. P. J. Higson, “Lactate in human sweat: a critical review of research to the present day,” *The Journal of Physiological Sciences*, vol. 62, pp. 429–440, 11 2012.
- [9] J. Moyer, D. Wilson, I. Finkelshtein, B. Wong, and R. Potts, “Correlation between sweat glucose and blood glucose in subjects with diabetes,” *Diabetes Technology & Therapeutics*, vol. 14, pp. 398–402, 5 2012.

Bibliography

- [10] D.-H. Kim, J. Viventi, J. J. Amsden, J. Xiao, L. Vigeland, Y.-S. Kim, J. A. Blanco, B. Panilaitis, E. S. Frechette, D. Contreras, D. L. Kaplan, F. G. Omenetto, Y. Huang, K.-C. Hwang, M. R. Zakin, B. Litt, and J. A. Rogers, "Dissolvable films of silk fibroin for ultrathin conformal bio-integrated electronics," *Nature Materials*, vol. 9, pp. 511–517, 6 2010.
- [11] S. Park, S. W. Heo, W. Lee, D. Inoue, Z. Jiang, K. Yu, H. Jinno, D. Hashizume, M. Sekino, T. Yokota, K. Fukuda, K. Tajima, and T. Someya, "Self-powered ultra-flexible electronics via nano-grating-patterned organic photovoltaics," *Nature*, vol. 561, no. 7724, pp. 516–521, sep 2018. [Online]. Available: <http://www.nature.com/articles/s41586-018-0536-x>
- [12] J. Kim, H. J. Shim, J. Yang, M. K. Choi, D. C. Kim, J. Kim, T. Hyeon, and D.-H. Kim, "Ultra-thin quantum dot display integrated with wearable electronics," *Advanced Materials*, vol. 29, p. 1700217, 10 2017.
- [13] M. Kaltenbrunner, T. Sekitani, J. Reeder, T. Yokota, K. Kuribara, T. Tokuhara, M. Drack, R. Schwödiauer, I. Graz, S. Bauer-Gogonea, S. Bauer, and T. Someya, "An ultra-lightweight design for imperceptible plastic electronics," *Nature*, vol. 499, no. 7459, pp. 458–463, jul 2013. [Online]. Available: <http://www.nature.com/articles/nature12314>
- [14] Y. S. Lee, S. M. Yang, D. Y. Park, W. J. Lee, J. Y. Park, and S.-H. Choa, "Characteristics of mechanical behavior and environmental reliability of ultra-stretchable ecoflex substrates," *Nanoscience and Nanotechnology Letters*, vol. 9, pp. 1153–1158, 8 2017.
- [15] N. Naserifar, S. S. Yerneni, L. E. Weiss, and G. K. Fedder, "Inkjet printing of curing agent on thin pdms for local tailoring of mechanical properties," *Macromolecular Rapid Communications*, vol. 41, p. 1900569, 3 2020.
- [16] D. Qi, K. Zhang, G. Tian, B. Jiang, and Y. Huang, "Stretchable electronics based on pdms substrates," *Advanced Materials*, vol. 33, p. 2003155, 2 2021.
- [17] N. Lucas, C. Bieniaime, C. Belloy, M. Queneudec, F. Silvestre, and J.-E. Nava-Saucedo, "Polymer biodegradation: Mechanisms and estimation techniques – a review," *Chemosphere*, vol. 73, pp. 429–442, 9 2008.
- [18] Y. Cao and K. E. Uhrich, "Biodegradable and biocompatible polymers for electronic applications: A review," *Journal of Bioactive and Compatible Polymers*, vol. 34, pp. 3–15, 1 2019.
- [19] R. C. Webb, A. P. Bonifas, A. Behnaz, Y. Zhang, K. J. Yu, H. Cheng, M. Shi, Z. Bian, Z. Liu, Y.-S. Kim, W.-H. Yeo, J. S. Park, J. Song, Y. Li, Y. Huang, A. M. Gorbach, and J. A. Rogers, "Ultrathin conformal devices for precise and continuous thermal characterization of human skin," *Nature Materials*, vol. 12, no. 10, pp. 938–944, oct 2013. [Online]. Available: <http://www.nature.com/articles/nmat3755>
- [20] "Information about dow corning brand silicone encapsulants." [Online]. Available: <http://bdml.stanford.edu/twiki/pub/Rise/PDMSProceSS/PDMSdatasheet.pdf>

- [21] J. Carvill, *Mechanical Engineer's Data Handbook*. Elsevier, 1993.
- [22] N. Chou, J. Jeong, and S. Kim, "Crack-free and reliable lithographical patterning methods on pdms substrate," *Journal of Micromechanics and Microengineering*, vol. 23, p. 125035, 12 2013.
- [23] G. Mattana, A. Loi, M. Woytasik, M. Barbaro, V. Noël, and B. Piro, "Inkjet-printing: A new fabrication technology for organic transistors," *Advanced Materials Technologies*, vol. 2, p. 1700063, 10 2017.
- [24] M. A. Meitl, Z.-T. Zhu, V. Kumar, K. J. Lee, X. Feng, Y. Y. Huang, I. Adesida, R. G. Nuzzo, and J. A. Rogers, "Transfer printing by kinetic control of adhesion to an elastomeric stamp," *Nature Materials*, vol. 5, no. 1, pp. 33–38, jan 2006. [Online]. Available: <http://www.nature.com/articles/nmat1532>
- [25] S. Lee, S. Franklin, F. A. Hassani, T. Yokota, M. O. G. Nayeem, Y. Wang, R. Leib, G. Cheng, D. W. Franklin, and T. Someya, "Nanomesh pressure sensor for monitoring finger manipulation without sensory interference," *Science*, vol. 370, no. 6519, pp. 966–970, nov 2020. [Online]. Available: <https://www.science.org/doi/10.1126/science.abc9735>
- [26] A. Miyamoto, H. Kawasaki, S. Lee, T. Yokota, M. Amagai, and T. Someya, "Highly Precise, Continuous, Long-term Monitoring of Skin Electrical Resistance by Nanomesh Electrodes," *Advanced Healthcare Materials*, p. 2102425, jan 2022. [Online]. Available: <https://onlinelibrary.wiley.com/doi/10.1002/adhm.202102425>
- [27] Y. R. Jeong, J. Kim, Z. Xie, Y. Xue, S. M. Won, G. Lee, S. W. Jin, S. Y. Hong, X. Feng, Y. Huang, J. A. Rogers, and J. S. Ha, "A skin-attachable, stretchable integrated system based on liquid GaInSn for wireless human motion monitoring with multi-site sensing capabilities," *NPG Asia Materials*, vol. 9, no. 10, pp. e443–e443, oct 2017. [Online]. Available: <http://www.nature.com/articles/am2017189>
- [28] N. Rodeheaver, R. Herbert, Y. Kim, M. Mahmood, H. Kim, J. Jeong, and W. Yeo, "Strain-isolating materials and interfacial physics for soft wearable bioelectronics and wireless, motion artifact-controlled health monitoring," *Advanced Functional Materials*, vol. 31, p. 2104070, 9 2021.
- [29] Y. S. Oh, J.-H. Kim, Z. Xie, S. Cho, H. Han, S. W. Jeon, M. Park, M. Namkoong, R. Avila, Z. Song, S.-U. Lee, K. Ko, J. Lee, J.-S. Lee, W. G. Min, B.-J. Lee, M. Choi, H. U. Chung, J. Kim, M. Han, J. Koo, Y. S. Choi, S. S. Kwak, S. B. Kim, J. Kim, J. Choi, C.-M. Kang, J. U. Kim, K. Kwon, S. M. Won, J. M. Baek, Y. Lee, S. Y. Kim, W. Lu, A. Vazquez-Guardado, H. Jeong, H. Ryu, G. Lee, K. Kim, S. Kim, M. S. Kim, J. Choi, D. Y. Choi, Q. Yang, H. Zhao, W. Bai, H. Jang, Y. Yu, J. Lim, X. Guo, B. H. Kim, S. Jeon, C. Davies, A. Banks, H. J. Sung, Y. Huang, I. Park, and J. A. Rogers, "Battery-free, wireless soft sensors for continuous multi-site measurements of pressure and temperature from patients at risk for pressure injuries," *Nature Communications*, vol. 12, p. 5008, 12 2021.

Bibliography

- [30] H. Kim, Y. Kim, M. Mahmood, S. Kwon, N. Zavanelli, H. S. Kim, Y. S. Rim, F. Epps, and W. Yeo, "Fully integrated, stretchable, wireless skin-conformal bioelectronics for continuous stress monitoring in daily life," *Advanced Science*, vol. 7, p. 2000810, 8 2020.
- [31] S. Jadoon, S. Karim, M. R. Akram, A. Kalsoom Khan, M. A. Zia, A. R. Siddiqi, and G. Murtaza, "Recent Developments in Sweat Analysis and Its Applications," *International Journal of Analytical Chemistry*, vol. 2015, pp. 1–7, 2015. [Online]. Available: <http://www.hindawi.com/journals/ijac/2015/164974/>
- [32] T. R. Ray, J. Choi, A. J. Bandodkar, S. Krishnan, P. Gutruf, L. Tian, R. Ghaffari, and J. A. Rogers, "Bio-Integrated Wearable Systems: A Comprehensive Review," *Chemical Reviews*, vol. 119, no. 8, pp. 5461–5533, apr 2019. [Online]. Available: <https://pubs.acs.org/doi/10.1021/acs.chemrev.8b00573>
- [33] W. Gao, S. Emaminejad, H. Y. Y. Nyein, S. Challa, K. Chen, A. Peck, H. M. Fahad, H. Ota, H. Shiraki, D. Kiriya, D.-H. Lien, G. A. Brooks, R. W. Davis, and A. Javey, "Fully integrated wearable sensor arrays for multiplexed in situ perspiration analysis," *Nature*, vol. 529, pp. 509–514, 1 2016.
- [34] H. Lee, T. K. Choi, Y. B. Lee, H. R. Cho, R. Ghaffari, L. Wang, H. J. Choi, T. D. Chung, N. Lu, T. Hyeon, S. H. Choi, and D.-H. Kim, "A graphene-based electrochemical device with thermoresponsive microneedles for diabetes monitoring and therapy," *Nature Nanotechnology*, vol. 11, pp. 566–572, 6 2016.
- [35] K. Kwon, J. U. Kim, Y. Deng, S. R. Krishnan, J. Choi, H. Jang, K. Lee, C.-J. Su, I. Yoo, Y. Wu, L. Lipschultz, J.-H. Kim, T. S. Chung, D. Wu, Y. Park, T. il Kim, R. Ghaffari, S. Lee, Y. Huang, and J. A. Rogers, "An on-skin platform for wireless monitoring of flow rate, cumulative loss and temperature of sweat in real time," *Nature Electronics*, vol. 4, pp. 302–312, 4 2021.
- [36] H. Y. Y. Nyein, M. Bariya, B. Tran, C. H. Ahn, B. J. Brown, W. Ji, N. Davis, and A. Javey, "A wearable patch for continuous analysis of thermoregulatory sweat at rest," *Nature Communications*, vol. 12, p. 1823, 12 2021.
- [37] J. Kim, Y. Wu, H. Luan, D. S. Yang, D. Cho, S. S. Kwak, S. Liu, H. Ryu, R. Ghaffari, and J. A. Rogers, "A skin-interfaced, miniaturized microfluidic analysis and delivery system for colorimetric measurements of nutrients in sweat and supply of vitamins through the skin," *Advanced Science*, vol. 9, p. 2103331, 1 2022.
- [38] S. Mosaed, J. H. Liu, and R. N. Weinreb, "Correlation between office and peak nocturnal intraocular pressures in healthy subjects and glaucoma patients," *American Journal of Ophthalmology*, vol. 139, no. 2, pp. 320–324, feb 2005. [Online]. Available: <https://linkinghub.elsevier.com/retrieve/pii/S000293940401164X>
- [39] J. Kim, M. Kim, M.-S. Lee, K. Kim, S. Ji, Y.-T. Kim, J. Park, K. Na, K.-H. Bae, H. Kyun Kim, F. Bien, C. Young Lee, and J.-U. Park, "Wearable smart sensor systems integrated on soft

- contact lenses for wireless ocular diagnostics,” *Nature Communications*, vol. 8, no. 1, p. 14997, apr 2017. [Online]. Available: <http://dx.doi.org/10.1038/ncomms14997>
<http://www.nature.com/articles/ncomms14997>
- [40] S. Guo, K. Wu, C. Li, H. Wang, Z. Sun, D. Xi, S. Zhang, W. Ding, M. E. Zaghloul, C. Wang, F. A. Castro, D. Yang, and Y. Zhao, “Integrated contact lens sensor system based on multifunctional ultrathin MoS₂ transistors,” *Matter*, vol. 4, no. 3, pp. 969–985, mar 2021. [Online]. Available: <https://linkinghub.elsevier.com/retrieve/pii/S2590238520306718>
- [41] J. Park, J. Kim, S.-Y. Kim, W. H. Cheong, J. Jang, Y.-G. Park, K. Na, Y.-T. Kim, J. H. Heo, C. Y. Lee, J. H. Lee, F. Bien, and J.-U. Park, “Soft, smart contact lenses with integrations of wireless circuits, glucose sensors, and displays,” *Science Advances*, vol. 4, no. 1, jan 2018. [Online]. Available: <https://www.science.org/doi/10.1126/sciadv.aap9841>
- [42] R. Yin, Z. Xu, M. Mei, Z. Chen, K. Wang, Y. Liu, T. Tang, M. K. Priyadarshi, X. Meng, S. Zhao, B. Deng, H. Peng, Z. Liu, and X. Duan, “Soft transparent graphene contact lens electrodes for conformal full-cornea recording of electroretinogram,” *Nature Communications*, vol. 9, no. 1, p. 2334, dec 2018. [Online]. Available: <http://www.nature.com/articles/s41467-018-04781-w>
- [43] J.-K. Chang, H. Fang, C. A. Bower, E. Song, X. Yu, and J. A. Rogers, “Materials and processing approaches for foundry-compatible transient electronics,” *Proceedings of the National Academy of Sciences*, vol. 114, 7 2017.
- [44] C. M. Boutry, L. Beker, Y. Kaizawa, C. Vassos, H. Tran, A. C. Hinckley, R. Pfattner, S. Niu, J. Li, J. Claverie, Z. Wang, J. Chang, P. M. Fox, and Z. Bao, “Biodegradable and flexible arterial-pulse sensor for the wireless monitoring of blood flow,” *Nature Biomedical Engineering*, vol. 3, pp. 47–57, 1 2019.
- [45] S.-W. Hwang, C. H. Lee, H. Cheng, J.-W. Jeong, S.-K. Kang, J.-H. Kim, J. Shin, J. Yang, Z. Liu, G. A. Ameer, Y. Huang, and J. A. Rogers, “Biodegradable elastomers and silicon nanomembranes/nanoribbons for stretchable, transient electronics, and biosensors,” *Nano Letters*, vol. 15, pp. 2801–2808, 5 2015.
- [46] W. Bai, J. Shin, R. Fu, I. Kandela, D. Lu, X. Ni, Y. Park, Z. Liu, T. Hang, D. Wu, Y. Liu, C. R. Haney, I. Stepien, Q. Yang, J. Zhao, K. R. Nandoliya, H. Zhang, X. Sheng, L. Yin, K. MacRenaris, A. Brikha, F. Aird, M. Pezhouh, J. Hornick, W. Zhou, and J. A. Rogers, “Bioresorbable photonic devices for the spectroscopic characterization of physiological status and neural activity,” *Nature Biomedical Engineering*, vol. 3, pp. 644–654, 8 2019.
- [47] S.-K. Kang, R. K. J. Murphy, S.-W. Hwang, S. M. Lee, D. V. Harburg, N. A. Krueger, J. Shin, P. Gamble, H. Cheng, S. Yu, Z. Liu, J. G. McCall, M. Stephen, H. Ying, J. Kim, G. Park, R. C. Webb, C. H. Lee, S. Chung, D. S. Wie, A. D. Gujar, B. Vemulapalli, A. H. Kim, K.-M. Lee, J. Cheng, Y. Huang, S. H. Lee, P. V. Braun, W. Z. Ray, and J. A. Rogers, “Bioresorbable silicon electronic sensors for the brain,” *Nature*, vol. 530, no. 7588, pp. 71–76, feb 2016. [Online]. Available: <http://www.nature.com/articles/nature16492>

- [48] J. A. Fan, W.-H. Yeo, Y. Su, Y. Hattori, W. Lee, S.-Y. Jung, Y. Zhang, Z. Liu, H. Cheng, L. Falgout, M. Bajema, T. Coleman, D. Gregoire, R. J. Larsen, Y. Huang, and J. A. Rogers, "Fractal design concepts for stretchable electronics," *Nature Communications*, vol. 5, no. 1, p. 3266, may 2014. [Online]. Available: <http://www.nature.com/articles/ncomms4266>
- [49] Q. Hua, J. Sun, H. Liu, R. Bao, R. Yu, J. Zhai, C. Pan, and Z. L. Wang, "Skin-inspired highly stretchable and conformable matrix networks for multifunctional sensing," *Nature Communications*, vol. 9, no. 1, p. 244, dec 2018. [Online]. Available: <http://www.nature.com/articles/s41467-017-02685-9>
- [50] K.-I. Jang, K. Li, H. U. Chung, S. Xu, H. N. Jung, Y. Yang, J. W. Kwak, H. H. Jung, J. Song, C. Yang, A. Wang, Z. Liu, J. Y. Lee, B. H. Kim, J.-H. Kim, J. Lee, Y. Yu, B. J. Kim, H. Jang, K. J. Yu, J. Kim, J. W. Lee, J.-W. Jeong, Y. M. Song, Y. Huang, Y. Zhang, and J. A. Rogers, "Self-assembled three dimensional network designs for soft electronics," *Nature Communications*, vol. 8, no. 1, p. 15894, aug 2017. [Online]. Available: <http://www.nature.com/articles/ncomms15894>
- [51] K. Li, X. Cheng, F. Zhu, L. Li, Z. Xie, H. Luan, Z. Wang, Z. Ji, H. Wang, F. Liu, Y. Xue, C. Jiang, X. Feng, L. Li, J. A. Rogers, Y. Huang, and Y. Zhang, "A Generic Soft Encapsulation Strategy for Stretchable Electronics," *Advanced Functional Materials*, vol. 29, no. 8, p. 1806630, feb 2019. [Online]. Available: <http://doi.wiley.com/10.1002/adfm.201806630>
- [52] N. Qaiser, A. N. Damdam, S. M. Khan, N. Elatab, and M. M. Hussain, "Mechanical reliability of self-similar serpentine interconnect for fracture-free stretchable electronic devices," *Journal of Applied Physics*, vol. 130, p. 014902, 7 2021.
- [53] Y. Morikawa, S. Yamagiwa, H. Sawahata, R. Numano, K. Koida, M. Ishida, and T. Kawano, "Ultrastretchable kirigami bioprobes," *Advanced Healthcare Materials*, vol. 7, p. 1701100, 2 2018.
- [54] J.-H. Lee, P.-S. Chee, E.-H. Lim, J.-H. Low, and N.-T. Nguyen, "A stretchable kirigami-inspired self-powered electroactive sensor for tensile strain and torsion sensing," *Advanced Engineering Materials*, p. 2100961, 11 2021.
- [55] N. An, A. G. Domel, J. Zhou, A. Rafsanjani, and K. Bertoldi, "Programmable hierarchical kirigami," *Advanced Functional Materials*, vol. 30, p. 1906711, 2 2020.
- [56] N. Vachicouras, C. M. Tringides, P. B. Campiche, and S. P. Lacour, "Engineering reversible elasticity in ductile and brittle thin films supported by a plastic foil," *Extreme Mechanics Letters*, vol. 15, pp. 63–69, 9 2017.
- [57] O. Graudejus, P. Görrn, and S. Wagner, "Controlling the morphology of gold films on poly(dimethylsiloxane)," *ACS Applied Materials & Interfaces*, vol. 2, pp. 1927–1933, 7 2010.

- [58] O. Akogwu, D. Kwabi, S. Midturi, M. Eleruja, B. Babatope, and W. Soboyejo, "Large strain deformation and cracking of nano-scale gold films on pdms substrate," *Materials Science and Engineering: B*, vol. 170, pp. 32–40, 6 2010.
- [59] S. Lacour, J. Jones, S. Wagner, T. Li, and Z. Suo, "Stretchable interconnects for elastic electronic surfaces," *Proceedings of the IEEE*, vol. 93, pp. 1459–1467, 8 2005.
- [60] S. P. Lacour, D. Chan, S. Wagner, T. Li, and Z. Suo, "Mechanisms of reversible stretchability of thin metal films on elastomeric substrates," *Applied Physics Letters*, vol. 88, p. 204103, 5 2006.
- [61] N. Matsuhisa, Y. Jiang, Z. Liu, G. Chen, C. Wan, Y. Kim, J. Kang, H. Tran, H. Wu, I. You, Z. Bao, and X. Chen, "High-transconductance stretchable transistors achieved by controlled gold microcrack morphology," *Advanced Electronic Materials*, vol. 5, p. 1900347, 8 2019.
- [62] Q. Wang and X. Zhao, "Phase Diagrams of Instabilities in Compressed Film-Substrate Systems," *Journal of Applied Mechanics*, vol. 81, no. 5, may 2014. [Online]. Available: <https://asmedigitalcollection.asme.org/appliedmechanics/article/doi/10.1115/1.4025828/473461/Phase-Diagrams-of-Instabilities-in-Compressed>
- [63] —, "A three-dimensional phase diagram of growth-induced surface instabilities," *Scientific Reports*, vol. 5, no. 1, p. 8887, aug 2015. [Online]. Available: <http://www.nature.com/articles/srep08887>
- [64] M. Drack, I. Graz, T. Sekitani, T. Someya, M. Kaltenbrunner, and S. Bauer, "An Imperceptible Plastic Electronic Wrap," *Advanced Materials*, vol. 27, no. 1, pp. 34–40, jan 2015. [Online]. Available: <https://onlinelibrary.wiley.com/doi/10.1002/adma.201403093>
- [65] G. Chen, N. Matsuhisa, Z. Liu, D. Qi, P. Cai, Y. Jiang, C. Wan, Y. Cui, W. R. Leow, Z. Liu, S. Gong, K.-Q. Zhang, Y. Cheng, and X. Chen, "Plasticizing Silk Protein for On-Skin Stretchable Electrodes," *Advanced Materials*, vol. 30, no. 21, p. 1800129, may 2018. [Online]. Available: <https://onlinelibrary.wiley.com/doi/10.1002/adma.201800129>
- [66] R. Nur, N. Matsuhisa, Z. Jiang, M. O. G. Nayeem, T. Yokota, and T. Someya, "A Highly Sensitive Capacitive-type Strain Sensor Using Wrinkled Ultrathin Gold Films," *Nano Letters*, vol. 18, no. 9, pp. 5610–5617, sep 2018. [Online]. Available: <https://pubs.acs.org/doi/10.1021/acs.nanolett.8b02088>
- [67] F. Xu and Y. Zhu, "Highly Conductive and Stretchable Silver Nanowire Conductors," *Advanced Materials*, vol. 24, no. 37, pp. 5117–5122, sep 2012. [Online]. Available: <http://doi.wiley.com/10.1002/adma.201201886>
- [68] S. Wang, J. Xu, W. Wang, G.-J. N. Wang, R. Rastak, F. Molina-Lopez, J. W. Chung, S. Niu, V. R. Feig, J. Lopez, T. Lei, S.-K. Kwon, Y. Kim, A. M. Foudeh, A. Ehrlich, A. Gasperini, Y. Yun, B. Murmann, J. B.-H. Tok, and Z. Bao, "Skin electronics from scalable fabrication

- of an intrinsically stretchable transistor array,” *Nature*, vol. 555, no. 7694, pp. 83–88, mar 2018. [Online]. Available: <http://www.nature.com/articles/nature25494>
- [69] M. O. Tas, M. A. Baker, M. G. Masteghin, J. Bentz, K. Boxshall, and V. Stolojan, “Highly stretchable, directionally oriented carbon nanotube/pdms conductive films with enhanced sensitivity as wearable strain sensors,” *ACS Applied Materials & Interfaces*, vol. 11, pp. 39 560–39 573, 10 2019.
- [70] X. Wang, J. Li, H. Song, H. Huang, and J. Gou, “Highly stretchable and wearable strain sensor based on printable carbon nanotube layers/polydimethylsiloxane composites with adjustable sensitivity,” *ACS Applied Materials & Interfaces*, vol. 10, pp. 7371–7380, 2 2018.
- [71] R. Zhang, J. Ding, C. Liu, and E.-H. Yang, “Highly stretchable supercapacitors enabled by interwoven cnts partially embedded in pdms,” *ACS Applied Energy Materials*, vol. 1, pp. 2048–2055, 5 2018.
- [72] Y. Chen, R. S. Carmichael, and T. B. Carmichael, “Patterned, flexible, and stretchable silver nanowire/polymer composite films as transparent conductive electrodes,” *ACS Applied Materials & Interfaces*, vol. 11, pp. 31 210–31 219, 8 2019.
- [73] Q. Che, Q. Zhao, M. Hu, R. Qin, G. Shan, and J. Yang, “Ag nanowire-based stretchable electrodes and wearable sensor arrays,” *ACS Applied Nano Materials*, vol. 4, pp. 12 726–12 736, 11 2021.
- [74] S. Wu, Z. Cui, G. L. Baker, S. Mahendran, Z. Xie, and Y. Zhu, “A biaxially stretchable and self-sensing textile heater using silver nanowire composite,” *ACS Applied Materials & Interfaces*, vol. 13, pp. 59 085–59 091, 12 2021.
- [75] Y. Wang, X. Kong, J. Gao, M. Gong, X. Lin, L. Zhang, M. Guo, and D. Wang, “Customizable stretchable transparent electrodes based on agnw/cnt hybrids via tailoring sizes of building blocks,” *ACS Applied Electronic Materials*, p. acsaelm.1c01258, 2 2022.
- [76] C. Keplinger, J.-Y. Sun, C. C. Foo, P. Rothemund, G. M. Whitesides, and Z. Suo, “Stretchable, Transparent, Ionic Conductors,” *Science*, vol. 341, no. 6149, pp. 984–987, aug 2013. [Online]. Available: <https://www.sciencemag.org/lookup/doi/10.1126/science.1240228>
- [77] J. Wang, C. Yan, G. Cai, M. Cui, A. Lee-Sie Eh, and P. See Lee, “Extremely Stretchable Electroluminescent Devices with Ionic Conductors,” *Advanced Materials*, vol. 28, no. 22, pp. 4490–4496, jun 2016. [Online]. Available: <http://doi.wiley.com/10.1002/adma.201504187>
- [78] C.-C. Kim, H.-H. Lee, K. H. Oh, and J.-Y. Sun, “Highly stretchable, transparent ionic touch panel,” *Science*, vol. 353, pp. 682–687, 8 2016.

- [79] K. Parida, V. Kumar, W. Jiangxin, V. Bhavanasi, R. Bendi, and P. S. Lee, "Highly transparent, stretchable, and self-healing ionic-skin triboelectric nanogenerators for energy harvesting and touch applications," *Advanced Materials*, vol. 29, p. 1702181, 10 2017.
- [80] L. Shi, T. Zhu, G. Gao, X. Zhang, W. Wei, W. Liu, and S. Ding, "Highly stretchable and transparent ionic conducting elastomers," *Nature Communications*, vol. 9, p. 2630, 12 2018.
- [81] Y. Wang, Z. Yu, G. Mao, Y. Liu, G. Liu, J. Shang, S. Qu, Q. Chen, and R.-W. Li, "Printable liquid-metal@pdms stretchable heater with high stretchability and dynamic stability for wearable thermotherapy," *Advanced Materials Technologies*, vol. 4, p. 1800435, 2 2019.
- [82] K. Yamagishi, W. Zhou, T. Ching, S. Y. Huang, and M. Hashimoto, "Ultra-deformable and tissue-adhesive liquid metal antennas with high wireless powering efficiency," *Advanced Materials*, vol. 33, p. 2008062, 7 2021.
- [83] E. J. Markvicka, M. D. Bartlett, X. Huang, and C. Majidi, "An autonomously electrically self-healing liquid metal–elastomer composite for robust soft-matter robotics and electronics," *Nature Materials*, vol. 17, pp. 618–624, 7 2018.
- [84] F. Krisnadi, L. L. Nguyen, Ankit, J. Ma, M. R. Kulkarni, N. Mathews, and M. D. Dickey, "Directed assembly of liquid metal–elastomer conductors for stretchable and self-healing electronics," *Advanced Materials*, vol. 32, p. 2001642, 7 2020.
- [85] L. Zhu, B. Wang, S. Handschuh-Wang, and X. Zhou, "Liquid Metal–Based Soft Microfluidics," *Small*, vol. 16, no. 9, p. 1903841, mar 2020. [Online]. Available: <https://onlinelibrary.wiley.com/doi/abs/10.1002/sml.201903841>
- [86] M. D. Dickey, "Stretchable and Soft Electronics using Liquid Metals," *Advanced Materials*, vol. 29, no. 27, p. 1606425, jul 2017. [Online]. Available: <http://doi.wiley.com/10.1002/adma.201606425>
- [87] Q. Gao, H. Li, J. Zhang, Z. Xie, J. Zhang, and L. Wang, "Microchannel structural design for a room-temperature liquid metal based super-stretchable sensor," *Scientific Reports*, vol. 9, p. 5908, 12 2019.
- [88] Y. Zhang, S. Liu, Y. Miao, H. Yang, X. Chen, X. Xiao, Z. Jiang, X. Chen, B. Nie, and J. Liu, "Highly stretchable and sensitive pressure sensor array based on icicle-shaped liquid metal film electrodes," *ACS Applied Materials & Interfaces*, vol. 12, pp. 27 961–27 970, 6 2020.
- [89] Y. Yang, N. Sun, Z. Wen, P. Cheng, H. Zheng, H. Shao, Y. Xia, C. Chen, H. Lan, X. Xie, C. Zhou, J. Zhong, X. Sun, and S.-T. Lee, "Liquid-metal-based super-stretchable and structure-designable triboelectric nanogenerator for wearable electronics," *ACS Nano*, vol. 12, pp. 2027–2034, 2 2018.

Bibliography

- [90] Z. Ma, Q. Huang, Q. Xu, Q. Zhuang, X. Zhao, Y. Yang, H. Qiu, Z. Yang, C. Wang, Y. Chai, and Z. Zheng, "Permeable superelastic liquid-metal fibre mat enables biocompatible and monolithic stretchable electronics," *Nature Materials*, vol. 20, pp. 859–868, 6 2021.
- [91] C. Xu, B. Ma, S. Yuan, C. Zhao, and H. Liu, "High-resolution patterning of liquid metal on hydrogel for flexible, stretchable, and self-healing electronics," *Advanced Electronic Materials*, vol. 6, p. 1900721, 1 2020.
- [92] J. W. Boley, E. L. White, and R. K. Kramer, "Mechanically sintered gallium-indium nanoparticles," *Advanced Materials*, vol. 27, pp. 2355–2360, 4 2015.
- [93] S. Liu, S. N. Reed, M. J. Higgins, M. S. Titus, and R. Kramer-Bottiglio, "Oxide rupture-induced conductivity in liquid metal nanoparticles by laser and thermal sintering," *Nanoscale*, vol. 11, pp. 17 615–17 629, 2019.
- [94] L. Mou, J. Qi, L. Tang, R. Dong, Y. Xia, Y. Gao, and X. Jiang, "Highly stretchable and biocompatible liquid metal-elastomer conductors for self-healing electronics," *Small*, vol. 16, p. 2005336, 12 2020.
- [95] Q. Huang and Y. Zhu, "Printing conductive nanomaterials for flexible and stretchable electronics: A review of materials, processes, and applications," *Advanced Materials Technologies*, vol. 4, p. 1800546, 5 2019.
- [96] J. Li, J. Liu, W. Huo, J. Yu, X. Liu, M. Haslinger, M. Muehlberger, P. Kulha, and X. Huang, "Micro and nano materials and processing techniques for printed biodegradable electronics," *Materials Today Nano*, vol. 18, p. 100201, 6 2022.
- [97] R. Su, S. H. Park, X. Ouyang, S. I. Ahn, and M. C. McAlpine, "3d-printed flexible organic light-emitting diode displays," *Science Advances*, vol. 8, 1 2022.
- [98] J. J. Adams, E. B. Duoss, T. F. Malkowski, M. J. Motala, B. Y. Ahn, R. G. Nuzzo, J. T. Bernhard, and J. A. Lewis, "Conformal printing of electrically small antennas on three-dimensional surfaces," *Advanced Materials*, vol. 23, pp. 1335–1340, 3 2011.
- [99] Y.-G. Park, H. S. An, J.-Y. Kim, and J.-U. Park, "High-resolution, reconfigurable printing of liquid metals with three-dimensional structures," *Science Advances*, vol. 5, 6 2019.
- [100] D. F. Fernandes, C. Majidi, and M. Tavakoli, "Digitally printed stretchable electronics: a review," *Journal of Materials Chemistry C*, vol. 7, pp. 14 035–14 068, 2019.
- [101] D.-H. Kim, J.-H. Ahn, W. M. Choi, H.-S. Kim, T.-H. Kim, J. Song, Y. Y. Huang, Z. Liu, C. Lu, and J. A. Rogers, "Stretchable and Foldable Silicon Integrated Circuits," *Science*, vol. 320, no. 5875, pp. 507–511, apr 2008. [Online]. Available: <https://www.science.org/doi/10.1126/science.1154367>
- [102] L. Tian, B. Zimmerman, A. Akhtar, K. J. Yu, M. Moore, J. Wu, R. J. Larsen, J. W. Lee, J. Li, Y. Liu, B. Metzger, S. Qu, X. Guo, K. E. Mathewson, J. A. Fan, J. Cornman,

- M. Fatina, Z. Xie, Y. Ma, J. Zhang, Y. Zhang, F. Dolcos, M. Fabiani, G. Gratton, T. Bretl, L. J. Hargrove, P. V. Braun, Y. Huang, and J. A. Rogers, "Large-area MRI-compatible epidermal electronic interfaces for prosthetic control and cognitive monitoring," *Nature Biomedical Engineering*, vol. 3, no. 3, pp. 194–205, mar 2019. [Online]. Available: <http://www.nature.com/articles/s41551-019-0347-x>
- [103] S.-W. Hwang, G. Park, C. Edwards, E. A. Corbin, S.-K. Kang, H. Cheng, J.-K. Song, J.-H. Kim, S. Yu, J. Ng, J. E. Lee, J. Kim, C. Yee, B. Bhaduri, Y. Su, F. G. Omennetto, Y. Huang, R. Bashir, L. Goddard, G. Popescu, K.-M. Lee, and J. A. Rogers, "Dissolution Chemistry and Biocompatibility of Single-Crystalline Silicon Nanomembranes and Associated Materials for Transient Electronics," *ACS Nano*, vol. 8, no. 6, pp. 5843–5851, jun 2014. [Online]. Available: <http://pubs.acs.org/doi/10.1021/nn500847g>
- [104] J. Lee, H. R. Cho, G. D. Cha, H. Seo, S. Lee, C.-K. Park, J. W. Kim, S. Qiao, L. Wang, D. Kang, T. Kang, T. Ichikawa, J. Kim, H. Lee, W. Lee, S. Kim, S.-T. Lee, N. Lu, T. Hyeon, S. H. Choi, and D.-H. Kim, "Flexible, sticky, and biodegradable wireless device for drug delivery to brain tumors," *Nature Communications*, vol. 10, no. 1, p. 5205, dec 2019. [Online]. Available: <http://www.nature.com/articles/s41467-019-13198-y>
- [105] J. Kim, M. Lee, H. J. Shim, R. Ghaffari, H. R. Cho, D. Son, Y. H. Jung, M. Soh, C. Choi, S. Jung, K. Chu, D. Jeon, S.-T. Lee, J. H. Kim, S. H. Choi, T. Hyeon, and D.-H. Kim, "Stretchable silicon nanoribbon electronics for skin prosthesis," *Nature Communications*, vol. 5, no. 1, p. 5747, dec 2014. [Online]. Available: <http://www.nature.com/articles/ncomms6747>
- [106] T.-H. Kim, K.-S. Cho, E. K. Lee, S. J. Lee, J. Chae, J. W. Kim, D. H. Kim, J.-Y. Kwon, G. Amaratunga, S. Y. Lee, B. L. Choi, Y. Kuk, J. M. Kim, and K. Kim, "Full-colour quantum dot displays fabricated by transfer printing," *Nature Photonics*, vol. 5, no. 3, pp. 176–182, mar 2011. [Online]. Available: <http://www.nature.com/articles/nphoton.2011.12>
- [107] K. Sim, S. Chen, Z. Li, Z. Rao, J. Liu, Y. Lu, S. Jang, F. Ershad, J. Chen, J. Xiao, and C. Yu, "Three-dimensional curvy electronics created using conformal additive stamp printing," *Nature Electronics*, vol. 2, no. 10, pp. 471–479, oct 2019. [Online]. Available: <http://www.nature.com/articles/s41928-019-0304-4>
- [108] S. Heo, J. Ha, S. J. Son, I. S. Choi, H. Lee, S. Oh, J. Jekal, M. H. Kang, G. J. Lee, H. H. Jung, J. Yea, T. Lee, Y. Lee, J.-W. Choi, S. Xu, J. H. Choi, J.-W. Jeong, Y. M. Song, J.-C. Rah, H. Keum, and K.-I. Jang, "Instant, multiscale dry transfer printing by atomic diffusion control at heterogeneous interfaces," *Science Advances*, vol. 7, no. 28, jul 2021. [Online]. Available: <https://www.science.org/doi/10.1126/sciadv.abh0040>
- [109] W. Lee, Y. Liu, Y. Lee, B. K. Sharma, S. M. Shinde, S. D. Kim, K. Nan, Z. Yan, M. Han, Y. Huang, Y. Zhang, J.-H. Ahn, and J. A. Rogers, "Two-dimensional materials in functional three-dimensional architectures with applications in photodetection and imaging," *Nature Communications*, vol. 9, no. 1, p. 1417, dec 2018. [Online]. Available: <http://www.nature.com/articles/s41467-018-03870-0>

- [110] B. H. Kim, K. Li, J.-T. Kim, Y. Park, H. Jang, X. Wang, Z. Xie, S. M. Won, H.-J. Yoon, G. Lee, W. J. Jang, K. H. Lee, T. S. Chung, Y. H. Jung, S. Y. Heo, Y. Lee, J. Kim, T. Cai, Y. Kim, P. Prasopsukh, Y. Yu, X. Yu, R. Avila, H. Luan, H. Song, F. Zhu, Y. Zhao, L. Chen, S. H. Han, J. Kim, S. J. Oh, H. Lee, C. H. Lee, Y. Huang, L. P. Chamorro, Y. Zhang, and J. A. Rogers, "Three-dimensional electronic microfliers inspired by wind-dispersed seeds," *Nature*, vol. 597, no. 7877, pp. 503–510, sep 2021. [Online]. Available: <https://www.nature.com/articles/s41586-021-03847-y>
- [111] P. S. Taçon, M. Langley, S. May, R. Lamilami, W. Brennan, and D. Guse, "Ancient bird stencils discovered in arnhem land, northern territory, australia," *Antiquity*, vol. 84, pp. 416–427, 6 2010.
- [112] O. Vazquez-Mena, L. Gross, S. Xie, L. Villanueva, and J. Brugger, "Resistless nanofabrication by stencil lithography: A review," *Microelectronic Engineering*, vol. 132, pp. 236–254, jan 2015. [Online]. Available: <http://dx.doi.org/10.1016/j.mee.2014.08.003><https://linkinghub.elsevier.com/retrieve/pii/S0167931714003359>
- [113] V. Flauraud, T. S. van Zanten, M. Mivelle, C. Manzo, M. F. Garcia Parajo, and J. Brugger, "Large-Scale Arrays of Bowtie Nanoaperture Antennas for Nanoscale Dynamics in Living Cell Membranes," *Nano Letters*, vol. 15, no. 6, pp. 4176–4182, jun 2015. [Online]. Available: <https://pubs.acs.org/doi/10.1021/acs.nanolett.5b01335>
- [114] L. G. Villanueva, O. Vazquez-Mena, C. Martin-Olmos, V. Savu, K. Sidler, J. Montserrat, P. Langlet, C. Hibert, P. Vettiger, J. Bausells, and J. Brugger, "All-stencil transistor fabrication on 3D silicon substrates," *Journal of Micromechanics and Microengineering*, vol. 22, no. 9, p. 095022, sep 2012. [Online]. Available: <https://iopscience.iop.org/article/10.1088/0960-1317/22/9/095022>
- [115] K. Tanahashi, M. Moriya, K. Shirasawa, and H. Takato, "Stencil-masked phosphorus-implanted silicon for solar cell applications," *Materials Science in Semiconductor Processing*, vol. 124, p. 105589, 3 2021.
- [116] S. Aksu, M. Huang, A. Artar, A. A. Yanik, S. Selvarasah, M. R. Dokmeci, and H. Altug, "Flexible Plasmonics on Unconventional and Nonplanar Substrates," *Advanced Materials*, vol. 23, no. 38, pp. 4422–4430, oct 2011. [Online]. Available: <http://doi.wiley.com/10.1002/adma.201102430>
- [117] O. Vazquez-Mena, T. Sannomiya, M. Tosun, L. G. Villanueva, V. Savu, J. Voros, and J. Brugger, "High-Resolution Resistless Nanopatterning on Polymer and Flexible Substrates for Plasmonic Biosensing Using Stencil Masks," *ACS Nano*, vol. 6, no. 6, pp. 5474–5481, jun 2012. [Online]. Available: <https://pubs.acs.org/doi/10.1021/nn301358n>
- [118] U. Zschieschang, J. W. Borchert, M. Geiger, F. Letzkus, J. N. Burghartz, and H. Klauk, "Stencil lithography for organic thin-film transistors with a channel length of 300 nm," *Organic Electronics*, vol. 61, pp. 65–69, oct 2018. [Online]. Available: <https://linkinghub.elsevier.com/retrieve/pii/S1566119918303446>

- [119] S.-W. Hwang, H. Tao, D.-H. Kim, H. Cheng, J.-K. Song, E. Rill, M. A. Brenckle, B. Panilaitis, S. M. Won, Y.-S. Kim, Y. M. Song, K. J. Yu, A. Ameen, R. Li, Y. Su, M. Yang, D. L. Kaplan, M. R. Zakin, M. J. Slepian, Y. Huang, F. G. Omenetto, and J. A. Rogers, "A Physically Transient Form of Silicon Electronics," *Science*, vol. 337, no. 6102, pp. 1640–1644, sep 2012. [Online]. Available: <https://www.sciencemag.org/lookup/doi/10.1126/science.1226325>
- [120] C. Dagdeviren, S.-W. Hwang, Y. Su, S. Kim, H. Cheng, O. Gur, R. Haney, F. G. Omenetto, Y. Huang, and J. A. Rogers, "Transient, Biocompatible Electronics and Energy Harvesters Based on ZnO," *Small*, vol. 9, no. 20, pp. 3398–3404, oct 2013. [Online]. Available: <https://onlinelibrary.wiley.com/doi/10.1002/sml.201300146>
- [121] W. Song, L. Kong, Q. Tao, Q. Liu, X. Yang, J. Li, H. Duan, X. Duan, L. Liao, and Y. Liu, "High-Resolution Van der Waals Stencil Lithography for 2D Transistors," *Small*, vol. 17, no. 29, p. 2101209, jul 2021. [Online]. Available: <https://onlinelibrary.wiley.com/doi/10.1002/sml.202101209>
- [122] K. Sidler, N. V. Cvetkovic, V. Savu, D. Tsamados, A. M. Ionescu, and J. Brugger, "Organic thin film transistors on flexible polyimide substrates fabricated by full-wafer stencil lithography," *Sensors and Actuators A: Physical*, vol. 162, no. 2, pp. 155–159, aug 2010. [Online]. Available: <https://linkinghub.elsevier.com/retrieve/pii/S0924424710001925>
- [123] H.-J. Kim, H. Oh, T. Kim, D. Kim, and M. Park, "Stretchable photodetectors based on electrospun polymer/perovskite composite nanofibers," *ACS Applied Nano Materials*, vol. 5, pp. 1308–1316, 1 2022.
- [124] X. P. Hao, C. Y. Li, C. W. Zhang, M. Du, Z. Ying, Q. Zheng, and Z. L. Wu, "Self-shaping soft electronics based on patterned hydrogel with stencil-printed liquid metal," *Advanced Functional Materials*, vol. 31, p. 2105481, 11 2021.
- [125] K.-d. Seong, J.-Y. Jung, J. Kang, D.-S. Kim, L. Lyu, S. Seo, J.-H. Kim, and Y. Piao, "Direct printing of high-performance micro-supercapacitors on flexible substrates using polymeric stencil masks with highly precise interdigitated patterns," *Journal of Materials Chemistry A*, vol. 8, no. 48, pp. 25 986–25 994, 2020. [Online]. Available: <http://xlink.rsc.org/?DOI=D0TA09811F>
- [126] T. H. Park, J. Kim, and S. Seo, "Facile and Rapid Method for Fabricating Liquid Metal Electrodes with Highly Precise Patterns via One-Step Coating," *Advanced Functional Materials*, vol. 30, no. 35, p. 2003694, aug 2020. [Online]. Available: <https://onlinelibrary.wiley.com/doi/10.1002/adfm.202003694>
- [127] H. Cai, Q. Meng, H. Ding, K. Zhang, Y. Lin, W. Ren, X. Yu, Y. Wu, G. Zhang, M. Li, N. Pan, Z. Qi, Y. Tian, Y. Luo, and X. Wang, "Utilization of Resist Stencil Lithography for Multidimensional Fabrication on a Curved Surface," *ACS Nano*, vol. 12, no. 9, pp. 9626–9632, sep 2018. [Online]. Available: <https://pubs.acs.org/doi/10.1021/acsnano.8b06534>

Bibliography

- [128] H. Cai, Q. Meng, Q. Chen, H. Ding, Y. Dai, S. Li, D. Chen, Q. Tan, N. Pan, C. Zeng, Z. Qi, G. Liu, Y. Tian, W. Gao, and X. Wang, "Fabricating 3D Metastructures by Simultaneous Modulation of Flexible Resist Stencils and Basal Molds," *Advanced Materials*, p. 2002570, jul 2020. [Online]. Available: <https://onlinelibrary.wiley.com/doi/10.1002/adma.202002570>
- [129] V. Savu, M. A. F. van den Boogaart, J. Brugger, J. Arcamone, M. Sansa, and F. Perez-Murano, "Dynamic stencil lithography on full wafer scale," *Journal of Vacuum Science & Technology B: Microelectronics and Nanometer Structures*, vol. 26, no. 6, pp. 2054–2058, nov 2008. [Online]. Available: <http://scitation.aip.org/content/avs/journal/jvstb/26/6/10.1116/1.2987953>
- [130] O. Vazquez-Mena, G. Villanueva, V. Savu, K. Sidler, M. A. F. van den Boogaart, and J. Brugger, "Metallic nanowires by full wafer stencil lithography," *Nano Letters*, vol. 8, pp. 3675–3682, 11 2008.
- [131] P. Schüffegen, D. Rosenbach, C. Li, T. W. Schmitt, M. Schleenvoigt, A. R. Jalil, S. Schmitt, J. Kölzer, M. Wang, B. Bennemann, U. Parlak, L. Kibkalo, S. Trellenkamp, T. Grap, D. Meertens, M. Luysberg, G. Mussler, E. Berenschot, N. Tas, A. A. Golubov, A. Brinkman, T. Schäpers, and D. Grützmacher, "Selective area growth and stencil lithography for in situ fabricated quantum devices," *Nature Nanotechnology*, vol. 14, pp. 825–831, 9 2019.
- [132] A. Enrico, V. Dubois, F. Niklaus, and G. Stemme, "Scalable manufacturing of single nanowire devices using crack-defined shadow mask lithography," *ACS Applied Materials & Interfaces*, vol. 11, pp. 8217–8226, 2 2019.
- [133] O. Vazquez-Mena, L. G. Villanueva, V. Savu, K. Sidler, P. Langlet, and J. Brugger, "Analysis of the blurring in stencil lithography," *Nanotechnology*, vol. 20, no. 41, p. 415303, oct 2009. [Online]. Available: <https://iopscience.iop.org/article/10.1088/0957-4484/20/41/415303>
- [134] Z. Racz and A. Seabaugh, "Characterization and control of unconfined lateral diffusion under stencil masks," *Journal of Vacuum Science & Technology B: Microelectronics and Nanometer Structures*, vol. 25, no. 3, p. 857, 2007. [Online]. Available: <http://scitation.aip.org/content/avs/journal/jvstb/25/3/10.1116/1.2737437>
- [135] P. Fesenko, V. Flauraud, S. Xie, J. Brugger, J. Genoe, P. Heremans, and C. Rolin, "Arrays of pentacene single crystals by stencil evaporation," *Crystal Growth & Design*, vol. 16, pp. 4694–4700, 8 2016.
- [136] P. Fesenko, V. Flauraud, S. Xie, E. Kang, T. Uemura, J. Brugger, J. Genoe, P. Heremans, and C. Rolin, "Growth Of Organic Semiconductor Thin Films with Multi-Micron Domain Size and Fabrication of Organic Transistors Using a Stencil Nanosieve," *ACS Applied Materials & Interfaces*, vol. 9, no. 28, pp. 23 314–23 318, jul 2017. [Online]. Available: <https://pubs.acs.org/doi/10.1021/acsami.7b06584>

- [137] K. Sidler, L. G. Villanueva, O. Vazquez-Mena, V. Savu, and J. Brugger, "Compliant membranes improve resolution in full-wafer micro/nanostencil lithography," *Nanoscale*, vol. 4, no. 3, pp. 773–778, 2012. [Online]. Available: <http://xlink.rsc.org/?DOI=C2NR11609J>
- [138] O. Vázquez-Mena, G. Villanueva, M. van den Boogaart, V. Savu, and J. Brugger, "Reusability of nanostencils for the patterning of Aluminum nanostructures by selective wet etching," *Microelectronic Engineering*, vol. 85, no. 5-6, pp. 1237–1240, may 2008. [Online]. Available: <https://linkinghub.elsevier.com/retrieve/pii/S0167931707007940>
- [139] S. Xie, A. V. Savu, and J. Brugger, "In-situ actuated gap reduction and clogging-free apertures for quasi-dynamic stencil lithography," in *The 7th Annual IEEE International Conference on Nano/Micro Engineered and Molecular Systems*, no. CONF, 2012.
- [140] S. Joo, J.-H. Kim, and S. Seo, "Direct fabrication of electrochromic devices with complex patterns on three-dimensional substrates using polymeric stencil films," *RSC Advances*, vol. 7, no. 68, pp. 43 283–43 288, 2017. [Online]. Available: <http://xlink.rsc.org/?DOI=C7RA08336J>
- [141] S. Xie, V. Savu, and J. Brugger, "Heated membranes prevent clogging of apertures in nanostencil lithography," in *2011 16th International Solid-State Sensors, Actuators and Microsystems Conference*. IEEE, jun 2011, pp. 998–1001. [Online]. Available: <http://ieeexplore.ieee.org/document/5969501/>
- [142] M. Kölbel, R. W. Tjerkstra, J. Brugger, C. J. M. van Rijn, W. Nijdam, J. Huskens, and D. N. Reinhoudt, "Shadow-Mask Evaporation through Monolayer-Modified Nanostencils," *Nano Letters*, vol. 2, no. 12, pp. 1339–1343, dec 2002. [Online]. Available: <https://pubs.acs.org/doi/10.1021/nl025784o>
- [143] F. Yesilkoy, V. Flauraud, M. Rüegg, B. J. Kim, and J. Brugger, "3D nanostructures fabricated by advanced stencil lithography," *Nanoscale*, vol. 8, no. 9, pp. 4945–4950, 2016. [Online]. Available: <http://xlink.rsc.org/?DOI=C5NR08444J>
- [144] K. Xu, S. Li, S. Dong, S. Zhang, G. Pan, G. Wang, L. Shi, W. Guo, C. Yu, and J. Luo, "Bioresorbable Electrode Array for Electrophysiological and Pressure Signal Recording in the Brain," *Advanced Healthcare Materials*, vol. 8, no. 15, p. 1801649, aug 2019. [Online]. Available: <https://onlinelibrary.wiley.com/doi/10.1002/adhm.201801649>
- [145] Q. Guo, J. Koo, Z. Xie, R. Avila, X. Yu, X. Ning, H. Zhang, X. Liang, S. B. Kim, Y. Yan, M. R. MacEwan, H. M. Lee, A. Song, Z. Di, Y. Huang, Y. Mei, and J. A. Rogers, "A Bioresorbable Magnetically Coupled System for Low-Frequency Wireless Power Transfer," *Advanced Functional Materials*, vol. 29, no. 46, p. 1905451, nov 2019. [Online]. Available: <https://onlinelibrary.wiley.com/doi/10.1002/adfm.201905451>
- [146] C. M. Boutry, Y. Kaizawa, B. C. Schroeder, A. Chortos, A. Legrand, Z. Wang, J. Chang, P. Fox, and Z. Bao, "A stretchable and biodegradable strain and pressure sensor for

Bibliography

- orthopaedic application,” *Nature Electronics*, vol. 1, no. 5, pp. 314–321, may 2018. [Online]. Available: <http://www.nature.com/articles/s41928-018-0071-7>
- [147] H. Ouyang, Z. Li, M. Gu, Y. Hu, L. Xu, D. Jiang, S. Cheng, Y. Zou, Y. Deng, B. Shi, W. Hua, Y. Fan, Z. Li, and Z. Wang, “A Bioresorbable Dynamic Pressure Sensor for Cardiovascular Postoperative Care,” *Advanced Materials*, vol. 33, no. 39, p. 2102302, oct 2021. [Online]. Available: <https://onlinelibrary.wiley.com/doi/10.1002/adma.202102302>
- [148] K. Sidler, O. Vazquez-Mena, V. Savu, G. Villanueva, M. van den Boogaart, and J. Brugger, “Resistivity measurements of gold wires fabricated by stencil lithography on flexible polymer substrates,” *Microelectronic Engineering*, vol. 85, no. 5-6, pp. 1108–1111, may 2008. [Online]. Available: <https://linkinghub.elsevier.com/retrieve/pii/S0167931707008283>
- [149] D. N. Kapoor, A. Bhatia, R. Kaur, R. Sharma, G. Kaur, and S. Dhawan, “PLGA: a unique polymer for drug delivery,” *Therapeutic Delivery*, vol. 6, no. 1, pp. 41–58, jan 2015. [Online]. Available: <http://www.future-science.com/doi/10.4155/tde.14.91>
- [150] “HD MicroSystems Product Selection Guide.” [Online]. Available: <http://web.mit.edu/scholvin/www/nt245/Documents/resists.PI.ProductSelectorGuide.pdf>
- [151] B. Rubehn and T. Stieglitz, “In vitro evaluation of the long-term stability of polyimide as a material for neural implants,” *Biomaterials*, vol. 31, pp. 3449–3458, 5 2010.
- [152] H. L. Hernandez, S.-K. Kang, O. P. Lee, S.-W. Hwang, J. A. Kaitz, B. Inci, C. W. Park, S. Chung, N. R. Sottos, J. S. Moore, J. A. Rogers, and S. R. White, “Triggered Transience of Metastable Poly(phthalaldehyde) for Transient Electronics,” *Advanced Materials*, vol. 26, no. 45, pp. 7637–7642, dec 2014. [Online]. Available: <https://onlinelibrary.wiley.com/doi/10.1002/adma.201403045>
- [153] C. W. Park, S.-K. Kang, H. L. Hernandez, J. A. Kaitz, D. S. Wie, J. Shin, O. P. Lee, N. R. Sottos, J. S. Moore, J. A. Rogers, and S. R. White, “Thermally Triggered Degradation of Transient Electronic Devices,” *Advanced Materials*, vol. 27, no. 25, pp. 3783–3788, jul 2015. [Online]. Available: <https://onlinelibrary.wiley.com/doi/10.1002/adma.201501180>
- [154] C. Wu, J. Jiang, H. Guo, X. Pu, L. Liu, W. Ding, P. A. Kohl, and Z. L. Wang, “Sunlight-Triggerable Transient Energy Harvester and Sensors Based on Triboelectric Nanogenerator Using Acid-Sensitive Poly(phthalaldehyde),” *Advanced Electronic Materials*, vol. 5, no. 12, p. 1900725, dec 2019. [Online]. Available: <https://onlinelibrary.wiley.com/doi/10.1002/aelm.201900725>
- [155] J. Ortigoza-Diaz, K. Scholten, C. Larson, A. Cobo, T. Hudson, J. Yoo, A. Baldwin, A. Weltman Hirschberg, and E. Meng, “Techniques and Considerations in the Microfabrication of Parylene C Microelectromechanical Systems,” *Micromachines*, vol. 9, no. 9, p. 422, aug 2018. [Online]. Available: <http://www.mdpi.com/2072-666X/9/9/422>

- [156] S. Kuppusami and R. H. Oskouei, "Parylene Coatings in Medical Devices and Implants: A Review," *Universal Journal of Biomedical Engineering*, vol. 3, no. 2, pp. 9–14, may 2015. [Online]. Available: <http://www.hrpub.org/journals/article{ }info.php?aid=2572>
- [157] M. Kim, D. M. Mackenzie, W. Kim, K. Isakov, and H. Lipsanen, "All-parylene flexible wafer-scale graphene thin film transistor," *Applied Surface Science*, vol. 551, p. 149410, jun 2021. [Online]. Available: <https://linkinghub.elsevier.com/retrieve/pii/S0169433221004864>
- [158] S.-W. Hwang, J.-K. Song, X. Huang, H. Cheng, S.-K. Kang, B. H. Kim, J.-H. Kim, S. Yu, Y. Huang, and J. A. Rogers, "High-Performance Biodegradable/Transient Electronics on Biodegradable Polymers," *Advanced Materials*, vol. 26, no. 23, pp. 3905–3911, jun 2014. [Online]. Available: <https://onlinelibrary.wiley.com/doi/10.1002/adma.201306050>
- [159] Q. Zheng, Y. Zou, Y. Zhang, Z. Liu, B. Shi, X. Wang, Y. Jin, H. Ouyang, Z. Li, and Z. L. Wang, "Biodegradable triboelectric nanogenerator as a life-time designed implantable power source," *Science Advances*, vol. 2, no. 3, mar 2016. [Online]. Available: <https://www.science.org/doi/10.1126/sciadv.1501478>
- [160] X. Yu, W. Shou, B. K. Mahajan, X. Huang, and H. Pan, "Materials, Processes, and Facile Manufacturing for Bioresorbable Electronics: A Review," *Advanced Materials*, vol. 30, no. 28, p. 1707624, jul 2018. [Online]. Available: <https://onlinelibrary.wiley.com/doi/10.1002/adma.201707624>
- [161] N. Bowden, S. Brittain, A. G. Evans, J. W. Hutchinson, and G. M. Whitesides, "Spontaneous formation of ordered structures in thin films of metals supported on an elastomeric polymer," *Nature*, vol. 393, no. 6681, pp. 146–149, may 1998. [Online]. Available: <http://www.nature.com/articles/30193>
- [162] F. Wang and C. E. Diesendruck, "Polyphthalaldehyde: Synthesis, Derivatives, and Applications," *Macromolecular Rapid Communications*, vol. 39, no. 2, p. 1700519, jan 2018. [Online]. Available: <https://onlinelibrary.wiley.com/doi/10.1002/marc.201700519>
- [163] M. Warner, A. Engler, and P. A. Kohl, "Improvement in the transience and mechanical performance of flexible poly(phthalaldehyde) substrates," *Polymer*, vol. 202, p. 122588, 8 2020.
- [164] "Thermal Properties of Parylene C." [Online]. Available: https://www.paryleneengineering.com/thermal_properties_of_parylene.htm
- [165] "Parylene Properties, VSi Parylene." [Online]. Available: <https://vsiparylene.com/parylene-properties/{#}mechanical-properties>
- [166] "PLGA | CAS#:34346-01-5 | Chemsrsrc." [Online]. Available: https://www.chemsrc.com/en/cas/34346-01-5_1470921.html#wuHuaDiv

Bibliography

- [167] P. Gentile, V. Chiono, I. Carmagnola, and P. Hatton, "An overview of poly(lactic-co-glycolic) acid (plga)-based biomaterials for bone tissue engineering," *International Journal of Molecular Sciences*, vol. 15, pp. 3640–3659, 2 2014.
- [168] H. Schiff, C. Spreu, A. Schleunitz, and J. Lee, "Shape control of polymer reflow structures fabricated by nanoimprint lithography," *Microelectronic Engineering*, vol. 88, no. 1, pp. 87–92, jan 2011. [Online]. Available: <https://linkinghub.elsevier.com/retrieve/pii/S0167931710003321>
- [169] C. Dai, K. Agarwal, and J.-H. Cho, "Ion-Induced Localized Nanoscale Polymer Reflow for Three-Dimensional Self-Assembly," *ACS Nano*, vol. 12, no. 10, pp. 10 251–10 261, oct 2018. [Online]. Available: <https://pubs.acs.org/doi/10.1021/acsnano.8b05283>
- [170] J. P. Moore, R. K. Williams, and R. S. Graves, "Thermal conductivity, electrical resistivity, and Seebeck coefficient of high-purity chromium from 280 to 1000 K," *Journal of Applied Physics*, vol. 48, no. 2, pp. 610–617, feb 1977. [Online]. Available: <http://aip.scitation.org/doi/10.1063/1.323697>
- [171] R. A. Matula, "Electrical resistivity of copper, gold, palladium, and silver," *Journal of Physical and Chemical Reference Data*, vol. 8, no. 4, pp. 1147–1298, oct 1979. [Online]. Available: <http://aip.scitation.org/doi/10.1063/1.555614>
- [172] R. Lüthi, R. R. Schlittler, J. Brugger, P. Vettiger, M. E. Welland, and J. K. Gimzewski, "Parallel nanodevice fabrication using a combination of shadow mask and scanning probe methods," *Applied Physics Letters*, vol. 75, pp. 1314–1316, 8 1999.
- [173] S. Kuiper, C. van Rijn, W. Nijdam, and M. Elwenspoek, "Development and applications of very high flux microfiltration membranes," *Journal of Membrane Science*, vol. 150, pp. 1–8, 11 1998.
- [174] M. A. F. van den Boogaart, L. M. Doeswijk, and J. Brugger, "Silicon-Supported Membranes for Improved Large-Area and High-Density Micro/Nanostencil Lithography," *Journal of Microelectromechanical Systems*, vol. 15, no. 6, pp. 1663–1670, dec 2006. [Online]. Available: <http://ieeexplore.ieee.org/document/4020297/>
- [175] M. A. van den Boogaart, M. Lishchynska, L. M. Doeswijk, J. C. Greer, and J. Brugger, "Corrugated membranes for improved pattern definition with micro/nanostencil lithography," *Sensors and Actuators A: Physical*, vol. 130-131, pp. 568–574, aug 2006. [Online]. Available: <https://linkinghub.elsevier.com/retrieve/pii/S0924424705005066>
- [176] O. Vazquez-Mena, K. Sidler, V. Savu, C. W. Park, L. Guillermo Villanueva, and J. Brugger, "Reliable and Improved Nanoscale Stencil Lithography by Membrane Stabilization, Blurring, and Clogging Corrections," *IEEE Transactions on Nanotechnology*, vol. 10, no. 2, pp. 352–357, mar 2011. [Online]. Available: <http://ieeexplore.ieee.org/document/5415675/>

- [177] A. Tixier, Y. Mita, J. P. Gouy, and H. Fujita, "A silicon shadow mask for deposition on isolated areas," *Journal of Micromechanics and Microengineering*, vol. 10, pp. 157–162, 6 2000.
- [178] M. A. F. v. d. Boogaart, "Stencil lithography an ancient technique for advanced micro- and nano-patterning," p. 191, 2006. [Online]. Available: <http://infoscience.epfl.ch/record/86075>
- [179] M. Rüegg, R. Blum, G. Boero, and J. Brugger, "Biodegradable Frequency-Selective Magnesium Radio-Frequency Microresonators for Transient Biomedical Implants," *Advanced Functional Materials*, vol. 29, no. 39, p. 1903051, sep 2019. [Online]. Available: <https://onlinelibrary.wiley.com/doi/10.1002/adfm.201903051>
- [180] R. Libanori, R. M. Erb, A. Reiser, H. Le Ferrand, M. J. Süess, R. Spolenak, and A. R. Studart, "Stretchable heterogeneous composites with extreme mechanical gradients," *Nature Communications*, vol. 3, no. 1, p. 1265, jan 2012. [Online]. Available: <http://www.nature.com/articles/ncomms2281>
- [181] N. Naserifar, P. R. LeDuc, and G. K. Fedder, "Material gradients in stretchable substrates toward integrated electronic functionality," *Advanced Materials*, vol. 28, pp. 3584–3591, 5 2016.
- [182] W. Wang, S. Wang, R. Rastak, Y. Ochiai, S. Niu, Y. Jiang, P. K. Arunachala, Y. Zheng, J. Xu, N. Matsuhisa, X. Yan, S.-K. Kwon, M. Miyakawa, Z. Zhang, R. Ning, A. M. Foudeh, Y. Yun, C. Linder, J. B.-H. Tok, and Z. Bao, "Strain-insensitive intrinsically stretchable transistors and circuits," *Nature Electronics*, vol. 4, no. 2, pp. 143–150, feb 2021. [Online]. Available: <http://www.nature.com/articles/s41928-020-00525-1>
- [183] J. Yoon, S. Y. Hong, Y. Lim, S.-J. Lee, G. Zi, and J. S. Ha, "Design and Fabrication of Novel Stretchable Device Arrays on a Deformable Polymer Substrate with Embedded Liquid-Metal Interconnections," *Advanced Materials*, vol. 26, no. 38, pp. 6580–6586, oct 2014. [Online]. Available: <http://doi.wiley.com/10.1002/adma.201402588>
- [184] J. Park, S. Wang, M. Li, C. Ahn, J. K. Hyun, D. S. Kim, D. K. Kim, J. A. Rogers, Y. Huang, and S. Jeon, "Three-dimensional nanonetworks for giant stretchability in dielectrics and conductors," *Nature Communications*, vol. 3, no. 1, p. 916, jan 2012. [Online]. Available: <http://www.nature.com/articles/ncomms1929>
- [185] C. Ladd, J.-H. So, J. Muth, and M. D. Dickey, "3D Printing of Free Standing Liquid Metal Microstructures," *Advanced Materials*, vol. 25, no. 36, pp. 5081–5085, sep 2013. [Online]. Available: <http://doi.wiley.com/10.1002/adma.201301400>
- [186] C. Pan, K. Kumar, J. Li, E. J. Markvicka, P. R. Herman, and C. Majidi, "Visually Imperceptible Liquid-Metal Circuits for Transparent, Stretchable Electronics with Direct Laser Writing," *Advanced Materials*, vol. 30, no. 12, p. 1706937, mar 2018. [Online]. Available: <http://doi.wiley.com/10.1002/adma.201706937>

Bibliography

- [187] J. W. Boley, E. L. White, G. T.-C. Chiu, and R. K. Kramer, "Direct Writing of Gallium-Indium Alloy for Stretchable Electronics," *Advanced Functional Materials*, vol. 24, no. 23, pp. 3501–3507, jun 2014. [Online]. Available: <http://doi.wiley.com/10.1002/adfm.201303220>
- [188] J. Yang, T. Zhou, L. Zhang, D. Zhu, S. Handschuh-Wang, Z. Liu, T. Kong, Y. Liu, J. Zhang, and X. Zhou, "Defect-free, high resolution patterning of liquid metals using reversibly sealed, reusable polydimethylsiloxane microchannels for flexible electronic applications," *Journal of Materials Chemistry C*, vol. 5, no. 27, pp. 6790–6797, 2017. [Online]. Available: <http://xlink.rsc.org/?DOI=C7TC01918A>
- [189] Y. Lin, O. Gordon, M. R. Khan, N. Vasquez, J. Genzer, and M. D. Dickey, "Vacuum filling of complex microchannels with liquid metal," *Lab on a Chip*, vol. 17, no. 18, pp. 3043–3050, 2017. [Online]. Available: <http://xlink.rsc.org/?DOI=C7LC00426E>
- [190] N. Lazarus, S. S. Bedair, and I. M. Kierzewski, "Ultrafine Pitch Stencil Printing of Liquid Metal Alloys," *ACS Applied Materials & Interfaces*, vol. 9, no. 2, pp. 1178–1182, jan 2017. [Online]. Available: <https://pubs.acs.org/doi/10.1021/acsami.6b13088>
- [191] E. P. Yalcintas, K. B. Ozutemiz, T. Cetinkaya, L. Dalloro, C. Majidi, and O. B. Ozdoganlar, "Soft Electronics Manufacturing Using Microcontact Printing," *Advanced Functional Materials*, vol. 29, no. 51, pp. 1–13, 2019.
- [192] M.-g. Kim, H. Alrowais, S. Pavlidis, and O. Brand, "Size-Scalable and High-Density Liquid-Metal-Based Soft Electronic Passive Components and Circuits Using Soft Lithography," *Advanced Functional Materials*, vol. 27, no. 3, p. 1604466, jan 2017. [Online]. Available: <http://doi.wiley.com/10.1002/adfm.201604466>
- [193] M.-g. Kim, D. K. Brown, and O. Brand, "Nanofabrication for all-soft and high-density electronic devices based on liquid metal," *Nature Communications*, vol. 11, no. 1, p. 1002, dec 2020. [Online]. Available: <http://www.nature.com/articles/s41467-020-14814-y>
- [194] S.-Y. Tang, Y. Lin, I. D. Joshipura, K. Khoshmanesh, and M. D. Dickey, "Steering liquid metal flow in microchannels using low voltages," *Lab on a Chip*, vol. 15, no. 19, pp. 3905–3911, 2015. [Online]. Available: <http://xlink.rsc.org/?DOI=C5LC00742A>
- [195] Y. Cui, F. Liang, Z. Yang, S. Xu, X. Zhao, Y. Ding, Z. Lin, and J. Liu, "Metallic bond-enabled wetting behavior at the liquid Ga/CuGa₂ interfaces," *ACS Applied Materials & Interfaces*, vol. 10, pp. 9203–9210, 3 2018.
- [196] K. B. Ozutemiz, J. Wissman, O. B. Ozdoganlar, and C. Majidi, "EGaIn-Metal Interfacing for Liquid Metal Circuitry and Microelectronics Integration," *Advanced Materials Interfaces*, vol. 5, no. 10, p. 1701596, may 2018. [Online]. Available: <http://doi.wiley.com/10.1002/admi.201701596>
- [197] G. Li, X. Wu, and D.-W. Lee, "Selectively plated stretchable liquid metal wires for transparent electronics," *Sensors and Actuators B: Chemical*, vol. 221, pp.

- 1114–1119, dec 2015. [Online]. Available: <https://linkinghub.elsevier.com/retrieve/pii/S0925400515301192>
- [198] G. Li and D.-W. Lee, “An advanced selective liquid-metal plating technique for stretchable biosensor applications,” *Lab on a Chip*, vol. 17, no. 20, pp. 3415–3421, 2017. [Online]. Available: <http://xlink.rsc.org/?DOI=C7LC00768J>
- [199] W. Lee, J. Lee, H. Yun, J. Kim, J. Park, C. Choi, D. C. Kim, H. Seo, H. Lee, J. W. Yu, W. B. Lee, and D.-H. Kim, “High-Resolution Spin-on-Patterning of Perovskite Thin Films for a Multiplexed Image Sensor Array,” *Advanced Materials*, vol. 29, no. 40, p. 1702902, oct 2017. [Online]. Available: <http://doi.wiley.com/10.1002/adma.201702902>
- [200] Y. Zhang, C. A. D’Ambra, R. Katsumata, R. L. Burns, M. H. Somervell, R. A. Segalman, C. J. Hawker, and C. M. Bates, “Rapid and Selective Deposition of Patterned Thin Films on Heterogeneous Substrates via Spin Coating,” *ACS Applied Materials & Interfaces*, vol. 11, no. 23, pp. 21 177–21 183, jun 2019. [Online]. Available: <https://pubs.acs.org/doi/10.1021/acsami.9b05190>
- [201] L. Teng, S. Ye, S. Handschuh-Wang, X. Zhou, T. Gan, and X. Zhou, “Liquid Metal-Based Transient Circuits for Flexible and Recyclable Electronics,” *Advanced Functional Materials*, vol. 29, no. 11, p. 1808739, mar 2019. [Online]. Available: <http://doi.wiley.com/10.1002/adfm.201808739>
- [202] M. Mastrangeli, Q. Zhou, V. Sariola, and P. Lambert, “Surface tension-driven self-alignment,” *Soft Matter*, vol. 13, no. 2, pp. 304–327, 2017. [Online]. Available: <http://xlink.rsc.org/?DOI=C6SM02078J>
- [203] V. Savu, J. Kivioja, J. Ahopelto, and J. Brugger, “Quick and Clean: Stencil Lithography for Wafer-Scale Fabrication of Superconducting Tunnel Junctions,” *IEEE Transactions on Applied Superconductivity*, vol. 19, no. 3, pp. 242–244, jun 2009. [Online]. Available: <http://ieeexplore.ieee.org/document/5067231/>
- [204] T. Adrega and S. P. Lacour, “Stretchable gold conductors embedded in PDMS and patterned by photolithography: fabrication and electromechanical characterization,” *Journal of Micromechanics and Microengineering*, vol. 20, no. 5, p. 055025, may 2010. [Online]. Available: <https://iopscience.iop.org/article/10.1088/0960-1317/20/5/055025>
- [205] M. Watanabe, R. Hatano, and C. Koizumi, “Spontaneous formation of interdigitated array pattern in wrinkled gold films deposited on poly(dimethylsiloxane) elastomer,” *Polymer Journal*, vol. 47, no. 4, pp. 320–327, 2015.
- [206] Jinsol Je and Jungchul Lee, “Design, Fabrication, and Characterization of Liquid Metal Microheaters,” *Journal of Microelectromechanical Systems*, vol. 23, no. 5, pp. 1156–1163, oct 2014. [Online]. Available: <http://ieeexplore.ieee.org/document/6766649/>
- [207] L. Zhang, P. Zhang, R. Wang, R. Zhang, Z. Li, W. Liu, Q. Wang, M. Gao, and L. Gui, “A Performance-Enhanced Liquid Metal-Based Microheater with Parallel Ventilating

Bibliography

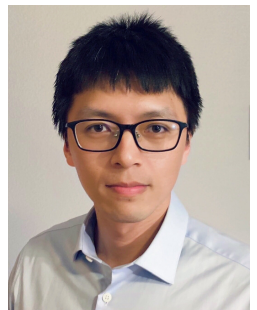
- Side-Channels," *Micromachines*, vol. 11, no. 2, p. 133, jan 2020. [Online]. Available: <https://www.mdpi.com/2072-666X/11/2/133>
- [208] F. N. Kholid, H. Huang, Y. Zhang, and H. J. Fan, "Multiple electrical breakdowns and electrical annealing using high current approximating breakdown current of silver nanowire network," *Nanotechnology*, vol. 27, no. 2, p. 025703, jan 2016. [Online]. Available: <https://iopscience.iop.org/article/10.1088/0957-4484/27/2/025703>
- [209] B. A. Gozen, A. Tabatabai, O. B. Ozdoganlar, and C. Majidi, "High-density soft-matter electronics with micron-scale line width," *Advanced Materials*, vol. 26, no. 30, pp. 5211–5216, 2014.
- [210] H.-X. Rao, F.-N. Liu, and Z.-Y. Zhang, "Preparation and oxygen/nitrogen permeability of PDMS crosslinked membrane and PDMS/tetraethoxysilicone hybrid membrane," *Journal of Membrane Science*, vol. 303, no. 1-2, pp. 132–139, oct 2007. [Online]. Available: <https://linkinghub.elsevier.com/retrieve/pii/S037673880700470X>
- [211] A. Fassler and C. Majidi, "Soft-matter capacitors and inductors for hyperelastic strain sensing and stretchable electronics," *Smart Materials and Structures*, vol. 22, no. 5, p. 055023, may 2013. [Online]. Available: <https://iopscience.iop.org/article/10.1088/0964-1726/22/5/055023>
- [212] J. a. Rogers, M. G. Lagally, and R. G. Nuzzo, "Synthesis, assembly and applications of semiconductor nanomembranes," *Nature*, vol. 477, no. 7362, pp. 45–53, sep 2011. [Online]. Available: <http://www.nature.com/articles/nature10381>
- [213] Y. Yang and X. Li, "Giant piezoresistance of p-type nano-thick silicon induced by interface electron trapping instead of 2D quantum confinement," *Nanotechnology*, vol. 22, no. 1, p. 015501, jan 2011. [Online]. Available: <https://iopscience.iop.org/article/10.1088/0957-4484/22/1/015501>
- [214] H. Jang, J. Kim, M.-S. Kim, J. H. Cho, H. Choi, and J.-H. Ahn, "Observation of the Inverse Giant Piezoresistance Effect in Silicon Nanomembranes Probed by Ultrafast Terahertz Spectroscopy," *Nano Letters*, vol. 14, no. 12, pp. 6942–6948, dec 2014. [Online]. Available: <https://pubs.acs.org/doi/10.1021/nl503186u>
- [215] S. Cho, N. Kim, K. Song, and J. Lee, "Adhesiveless Transfer Printing of Ultrathin Microscale Semiconductor Materials by Controlling the Bending Radius of an Elastomeric Stamp," *Langmuir*, vol. 32, no. 31, pp. 7951–7957, aug 2016. [Online]. Available: <https://pubs.acs.org/doi/10.1021/acs.langmuir.6b01880>
- [216] I. Byun, A. W. Coleman, and B. Kim, "Transfer of thin au films to polydimethylsiloxane (pdms) with reliable bonding using (3-mercaptopropyl)trimethoxysilane (mptms) as a molecular adhesive," *Journal of Micromechanics and Microengineering*, vol. 23, p. 085016, 8 2013.


- [217] C. Wang, C. Linghu, S. Nie, C. Li, Q. Lei, X. Tao, Y. Zeng, Y. Du, S. Zhang, K. Yu, H. Jin, W. Chen, and J. Song, "Programmable and scalable transfer printing with high reliability and efficiency for flexible inorganic electronics," *Science Advances*, vol. 6, no. 25, jun 2020. [Online]. Available: <https://www.science.org/doi/10.1126/sciadv.abb2393>
- [218] M. Cho, I. Cho, K. Kim, and I. Park, "Fast Flexible Bottom-Gated Hydrogen Sensor Based on Silicon Nanomembrane," *Advanced Materials Technologies*, vol. 6, no. 5, p. 2000847, may 2021. [Online]. Available: <https://onlinelibrary.wiley.com/doi/10.1002/admt.202000847>
- [219] Y. S. Choi, R. T. Yin, A. Pfenniger, J. Koo, R. Avila, K. Benjamin Lee, S. W. Chen, G. Lee, G. Li, Y. Qiao, A. Murillo-Berlitz, A. Kiss, S. Han, S. M. Lee, C. Li, Z. Xie, Y.-Y. Chen, A. Burrell, B. Geist, H. Jeong, J. Kim, H.-J. Yoon, A. Banks, S.-K. Kang, Z. J. Zhang, C. R. Haney, A. V. Sahakian, D. Johnson, T. Efimova, Y. Huang, G. D. Trachiotis, B. P. Knight, R. K. Arora, I. R. Efimov, and J. A. Rogers, "Fully implantable and bioresorbable cardiac pacemakers without leads or batteries," *Nature Biotechnology*, vol. 39, no. 10, pp. 1228–1238, oct 2021. [Online]. Available: <https://www.nature.com/articles/s41587-021-00948-x>
- [220] G.-J. Ko, S. D. Han, J.-K. Kim, J. Zhu, W. B. Han, J. Chung, S. M. Yang, H. Cheng, D.-H. Kim, C.-Y. Kang, and S.-W. Hwang, "Biodegradable, flexible silicon nanomembrane-based NO_x gas sensor system with record-high performance for transient environmental monitors and medical implants," *NPG Asia Materials*, vol. 12, no. 1, p. 71, dec 2020. [Online]. Available: <http://www.nature.com/articles/s41427-020-00253-0>
- [221] K. J. Yu, D. Kuzum, S.-W. Hwang, B. H. Kim, H. Juul, N. H. Kim, S. M. Won, K. Chiang, M. Trumpis, A. G. Richardson, H. Cheng, H. Fang, M. Thompson, H. Bink, D. Talos, K. J. Seo, H. N. Lee, S.-K. Kang, J.-H. Kim, J. Y. Lee, Y. Huang, F. E. Jensen, M. A. Dichter, T. H. Lucas, J. Viventi, B. Litt, and J. A. Rogers, "Bioresorbable silicon electronics for transient spatiotemporal mapping of electrical activity from the cerebral cortex," *Nature Materials*, vol. 15, no. 7, pp. 782–791, jul 2016. [Online]. Available: <http://www.nature.com/articles/nmat4624>
- [222] "Silicon – Strength – Hardness – Elasticity – Crystal Structure." [Online]. Available: <https://material-properties.org/silicon-mechanical-properties-strength-hardness-crystal-structure/>
- [223] E. Menard, R. G. Nuzzo, and J. A. Rogers, "Bendable single crystal silicon thin film transistors formed by printing on plastic substrates," *Applied Physics Letters*, vol. 86, p. 093507, 2 2005.
- [224] Y. Yang, Y. Hwang, H. A. Cho, J.-H. Song, S.-J. Park, J. A. Rogers, and H. C. Ko, "Arrays of Silicon Micro/Nanostructures Formed in Suspended Configurations for Deterministic Assembly Using Flat and Roller-Type Stamps," *Small*, vol. 7, no. 4, pp. 484–491, feb 2011. [Online]. Available: <https://onlinelibrary.wiley.com/doi/10.1002/sml.201001633>

Bibliography

- [225] M. Morita, T. Ohmi, E. Hasegawa, M. Kawakami, and M. Ohwada, "Growth of native oxide on a silicon surface," *Journal of Applied Physics*, vol. 68, no. 3, pp. 1272–1281, aug 1990. [Online]. Available: <http://aip.scitation.org/doi/10.1063/1.347181>
- [226] F. M. Smits, "Measurement of Sheet Resistivities with the Four-Point Probe," *Bell System Technical Journal*, vol. 37, no. 3, pp. 711–718, may 1958. [Online]. Available: <https://ieeexplore.ieee.org/document/6773368>
- [227] F. Mousty, P. Ostojka, and L. Passari, "Relationship between resistivity and phosphorus concentration in silicon," *Journal of Applied Physics*, vol. 45, no. 10, pp. 4576–4580, oct 1974. [Online]. Available: <http://aip.scitation.org/doi/10.1063/1.1663091>
- [228] R. I. Hegde, "Surface topography of phosphorus doped polysilicon," *Journal of Vacuum Science & Technology B: Microelectronics and Nanometer Structures*, vol. 13, no. 4, p. 1434, jul 1995. [Online]. Available: <http://scitation.aip.org/content/avs/journal/jvstb/13/4/10.1116/1.588167>
- [229] R. Charavel, P. Gassot, A. Suvkhanov, and T. Mexnier, "N-sinker formation by phosphorous silicon glass diffusion," in *14th annual conference, ON Semiconductor Technical Paper*, 2011, pp. 1–5.
- [230] H. Souri, H. Banerjee, A. Jusufi, N. Radacsi, A. A. Stokes, I. Park, M. Sitti, and M. Amjadi, "Wearable and Stretchable Strain Sensors: Materials, Sensing Mechanisms, and Applications," *Advanced Intelligent Systems*, vol. 2, no. 8, p. 2000039, aug 2020. [Online]. Available: <https://onlinelibrary.wiley.com/doi/10.1002/aisy.202000039>

Yi-Chiang Sun



 Avenue du Tir-Fédéral 92, 1024 Ecublens, Switzerland

 +41 77 988 30 93  jackyichiang.sun@gmail.com

SUMMARY Detail-oriented MEMS/IC packaging engineer with extensive experience in design, processing and characterization techniques in MEMS devices as well as advanced IC package platforms. Skills in sensor and IC package design, process development, failure analysis, reverse engineering, project coordination, collaboration and leadership.

CAREER

2014 - 2017

Taiwan Semiconductor Manufacturing Company (TSMC), Taiwan
R&D engineer at 3DIC department

- Led projects with a cross-functional team to develop 2.5D IC package platforms
- Integral to the success of over 5 products into mass production/commercialization, all used by global clients including Google, Nvidia, Xilinx and Broadcom
- Evaluated new IC package schemes for modulating package structure stress and providing superior device performances, while reducing process and material costs
- Attained extensive experience in the integration of chip, TSV interposer and substrate
- Patented an innovative package design for improving the device reliability performance
- Consultant role to regularly manage customer projects with demanding schedules, communicating with customers in handling spontaneous changes and adapting the development plan accordingly

EDUCATION

2017 - 2022

École Polytechnique Fédérale de Lausanne (EPFL), Switzerland
Ph.D. candidate at Microsystems and Microelectronics

- Designed, fabricated and characterized flexible and stretchable sensors for human healthcare/medical applications
- Conducted FEM simulations for designing stretchable sensors, especially on their mechanical interactions and thermal responses
- Experienced in conceptualizing and prototyping stretchable sensors

2012 - 2014

National Tsing Hua University (NTHU), Taiwan
M.S. at Department of Power Mechanical Engineering

- Introduced a new design for a CMOS-MEMS vacuum gauge to increase the sensitivity by 50%, while reducing the power consumption by 75%
- Engaged in industrial projects for the development of vacuum MEMS package platforms and MEMS pressure sensors

SKILLS

- Rigid and soft MEMS sensor design (pressure/vacuum sensor, microphone, stretchable strain sensor, etc.) with mathematical analysis, structure design (Solidworks), FEM simulation (COMSOL) and layout (Klayout)
- Fabrication process flow development including photolithography, etching, thin film deposition, bonding, grinding, dicing, die attach, underfill, backend assembly, etc.
- Project coordination, management and customer communication
- Methods for failure analysis, root cause finding (e.g., fishbone diagram), process analysis, control and improvement (e.g., Six Sigma)